



TECHNISCHE
UNIVERSITÄT
WIEN

DISSERTATION

Numerical Simulation of Core-Level Spectroscopies of Correlated Materials

Ausgeführt zum Zwecke der Erlangung des akademischen Grades des
Doktors der Naturwissenschaften (Dr. rer. nat.)

am Institut für Festkörperphysik der
Technischen Universität Wien

unter Anleitung von:

Prof. Dr. Jan Kuneš
(Technische Universität Wien, Wien)

Prof. Dr. Atsushi Hariki
(Osaka Prefecture University, Osaka)

durch

Dipl.-Ing. Mathias Winder, BSc
Matrikelnummer: 1230412

Wien, July 6, 2020



Die approbierte gedruckte Originalversion dieser Dissertation ist an der TU Wien Bibliothek verfügbar.
The approved original version of this doctoral thesis is available in print at TU Wien Bibliothek.

Kurzfassung

Eine der zentralen Aufgaben der Festkörperphysik ist die Untersuchung der elektronischen Struktur von stark korrelierten Materialien. Eine tragende Rolle spielt dabei die lokale Wechselwirkung von Valenzelektronen, welche zu Metall-Isolator-Übergängen, magnetischer Ordnung und vielen weiteren Effekten führt. Für die Untersuchung der elektronischen Struktur von korrelierten Materialien sind Kernröntgenspektroskopien weit verbreitet. In Kernröntgenspektroskopien emittiert ein eingehendes Photon ein Kernelektron oder regt dieses in einen freien Valenzzustand an. Die Resonanz des Systems auf das erzeugte positiv geladene Kernloch liefert umfassende Informationen zur elektronischen Struktur der untersuchten Materialien. Die vorliegende Dissertation umfasst die theoretische und numerische Modellierung von Kernröntgenspektroskopien. Wir entwickeln theoretische Kernröntgenspektroskopiemethoden, basierend auf lokaler Dichtenäherung und dynamischer Molekularfeldtheorie. Dazu verwenden wir die Configuration-Interaction-Methode und exakte Diagonalisierung. Dies ermöglicht uns eine gleichzeitige Behandlung von lokalisierten ($d-d$) und nicht lokalisierten (ungebundene Elektron-Loch Paare) Anregungen, welche in den Spektren beobachtet werden. Wir vergleichen unsere Resultate mit Experimenten und anderen etablierten Methoden (z.B. Clustermodell). In unseren Studien verwenden wir Röntgenphotoelektronenspektroskopie, Röntgenabsorptionsspektroskopie oder resonante inelastische Röntgenspektroskopie. Jede dieser Spektroskopien hat individuelle Vorteile und eine Kombination dieser liefert ein umfassendes Verständnis zur elektronischen Struktur der Materialien. Wir untersuchen eine breite Auswahl von stark korrelierten Materialien, wie zum Beispiel: NiO, Fe₂O₃, Kobaltite, Kuprate und Nickelate Seltener Erden.

Abstract

Understanding the electronic structure of strongly correlated materials is one of the main ambitions of solid state physics. Local interactions of valence electrons play an important role in correlated materials, leading to metal-insulator transitions, magnetic orderings and a variety of other effects. The proper interpretation of these effects is theoretically and computationally challenging. Core-level X-ray spectroscopy techniques are widely used for the investigation of the electronic structure of correlated materials. In core-level X-ray spectroscopies an incident photon excites (emits) a core-electron to an empty valence state. The response of the system to the positively charged core-hole provides rich information about the electronic structure of the studied compound. We study the theoretical and numerical modeling of core-level X-ray spectroscopies and develop a theoretical core-level X-ray spectroscopy approach based on local density approximation and dynamical mean-field theory. For calculating the core-level spectra, we use the configuration-interaction scheme and exact diagonalization. In contrast to other available methods, this approach enables us to describe simultaneously localized ($d-d$) and delocalized (unbound electron-hole pair) excitations observed in the core-level X-ray spectra. Within our material studies we use various core-level X-ray spectroscopies; X-ray photoemission spectroscopy, X-ray absorption spectroscopy and resonant inelastic X-ray scattering. Each kind has its own advantages; by combining them we obtain a comprehensive understanding of the electronic structure of the studied compounds. The main purpose of this thesis is the generalization of our core-level spectroscopy code to lower symmetries and its application to a broad variety of strongly correlated materials, in particular transition metal oxides, e.g. NiO, Fe₂O₃, cobaltites, cuprates and rare-earth nickelates.

Acknowledgements

I owe my deepest gratitude to Jan who supervised me on this comprehensive study in the field of solid state physics and core-level spectroscopy. Jan guided and taught me the various details of solid state physics and always tried to keep my view on the bigger picture. It is amazing how many brilliant ideas Jan has and it is unfortunate that I can no longer work on them.

I would like to show my greatest appreciation to Atsushi who guided me with endless patience throughout my Phd. He taught me his comprehensive spectroscopy knowledge and never got tired to answer my many (often repetitive) questions. I have never met such a hard working person in my life. His guidance supported me to increase my efficiency in approaching and solving new problems, which will assist me in my future career.

My gratitude also belongs to my colleagues in our office. Special thanks to Michael and Josef who discussed with me the many topics of solid states physics. Patrick, Paul, Christian, Clemens and Abdu, we had an excellent time together with many wonderful discussions. The happy atmosphere in our office and the occasional after work beer have been marvelous and motivated me to keep going. Our best investment was the couch in our office, which was of course just for reading papers...

Then I want to thank all others in our group. Dominique, your visits were always a pleasure and it is unfortunate to not collaborate with you anymore. Your programming skills are excellent and I could have learned so much more from you. Juan, you gave me a lot of inputs especially in the beginning of my Phd. You guided me through the numerous often overwhelming details of DFT calculations. Kyo-Hoon, you are such a generous person and your DFT skills are way over the top.

I want to thank all members of Karsten Held's group and Alessandro Toschi's group. Especially Anna, you always gave me new inputs on how to approach things (also how to approach Jan) during our wonderful lunch times in the Cafe 'Schrödinger'. Matthias, we always had fruitful discussions and you were always open for my many questions. Then, I want to thank Kathi, Severino and Benjamin, who shared an office with me at the beginning of my Phd. We had a great time together.

My deepest gratitude belongs to my family, friends and especially my partner Marita. Without you Marita, this thesis would not have been possible. It is one thing to work hard but you gave me the space to relax, refresh my energy and a

shoulder in difficult times. The same belongs to my parents Monika and Richard as well as my second parents Mamaklaudia and Röbi. Johannes and Theresa, Dominik and Sarah, and Andreas, I am so grateful that I was always welcome during my holidays in Vorarlberg. Furthermore I want to thank my sisters Christina, Isabell and also Nadin. Without all of you I would not be the person who I am today. Thank you!

List of Publications

Below is a complete list of all publications of the author, listed by date in descending order. Some chapters are based on the these publications. These are listed explicitly at the beginning of the corresponding chapter.

[1] "X-ray spectroscopy of rare-earth nickelate LuNiO_3 : LDA+DMFT study"

M. Winder, A. Hariki, and J. Kuneš
arXiv:2004.01428 (2020).

[2] "LDA+DMFT approach to resonant inelastic X-ray scattering in correlated materials"¹

A. Hariki, M. Winder, T. Uozumi, and J. Kuneš
Phys. Rev. B **101**, 115130 (2020).

[3] "Metal-insulator transition in $\text{CaCu}_3\text{Fe}_4\text{O}_{12}$ "

A. Hariki, M. Winder and J. Kuneš
arXiv:1909.12126 (2019).

[4] "Charge-transfer effect in hard X-ray 1s and 2p photoemission spectra: LDA+DMFT and cluster-model analysis"

M. Ghiasi, A. Hariki, M. Winder, J. Kuneš, A. Regoutz, T.-L. Lee, Y. Hu, J.-P. Rueff, and F. M. F. de Groot
Phys. Rev. B **100**, 075146 (2019).

[5] "Continuum Charge Excitations in High-Valence Transition-Metal Oxides Revealed by Resonant Inelastic X-ray Scattering"

A. Hariki, M. Winder and J. Kuneš
Phys. Rev. Lett. **121**, 126403 (2018).

The author contributed mainly to core-level spectroscopy calculations, as well as to band structure calculations and Wannierization of the studied materials throughout all the listed publications. The author extended the impurity solver used for the spectroscopy calculations, which consisted mainly in the extension of the configuration interaction basis, its application to lower symmetries, and in the parallelization

¹Editors' Suggestion, A.H and M.W contributed equally to this work.

of the treatment of the incident photon energies used for resonant inelastic X-ray scattering calculations. The extended basis provides a more realistic description of X-ray absorption, core-level X-ray photoemission and resonant inelastic X-ray scattering in correlated materials.

Foreword

Quantum mechanics is the description of the behavior of matter and light in all its details and, in particular, of the happenings on an atomic scale. Things on a very small scale behave like nothing that you have any direct experience about. They do not behave like waves, they do not behave like particles, they do not behave like clouds, or billiard balls, or weights on springs, or like anything that you have ever seen.

— R. P. Feynman [6]

The understanding of Nature had to be redefined with the development of quantum mechanics in the early 20th century. Processes happening on the quantum scale were completely contradictory to the perception of the physical world at that time. The discovery of quantum processes led to the development of novel technology influencing all fields of our modern society. For example the realization of semiconducting transistors by Bardeen, Brattain and Shockley in 1947. Semiconducting transistors were initially large sized and were first applied to radio machines. Once their size shrunk, transistors became integrated in circuits, and laid the foundation of modern computers. Today, application of quantum mechanics can be found in all fields of modern technology, such as displays, smartphones, fibreoptics, internet devices, or even in simple things like laser pointers. It must nevertheless be noted that all these remarkable achievements came at the cost of severe exploitation of natural resources. Nowadays, the research and development of new technologies is necessary in order to provide a high-living standard within our society, while the impact on our environment is kept at a sustainable level.

To continue the rapid development of sustainable technology, quantum mechanics needs to be adapted to new and also numerically accessible theories. For example real materials do not simply contain single particles, but rather an aggregate of interacting particles, generating collective quantum mechanical phenomena. Real materials contain 10^{23} particles in a size of just a cubic millimeter, which prevents the description of their electronic structure by standard quantum mechanical methods. A big breakthrough on the theory side was the development of density functional theory (DFT) by Kohn and Sham in the 1960's [7, 8]. DFT describes the electronic structure of a material by a charge distribution, which encodes the

electrons of a system in a simplified form. This approach enabled the numerical calculation of electronic properties of large systems. It allowed for the theoretical description of the electronic properties of many complex materials, e.g. semiconductors, metals and some insulators. DFT and its extensions (e.g. LDA [9], GGA [10], LDA+U [11]) often provide a correct quantitative description of crystal, magnetic and orbital structures. However, they fail to describe the correct electronic structure of a specific group of complex materials, in particular the group of strongly correlated materials [12].

Dynamical mean field theory [13] (DMFT) was developed in the last three decades and is a well established method to describe the electronic structure of correlated materials today. DMFT takes into account the essential Coulomb interaction between localized valence electrons in strongly correlated materials, which is often treated by a static mean field within standard electronic structure methods. The local correlations may lead to metal-insulator transitions or lead to countless other interesting physical phenomena. The combination of DMFT and density functional theory (DFT+DMFT) into a first principle calculation tool was a further step towards the accurate description of the electronic structure of real materials [14]. Although there are numerous experimental methods to compare DFT+DMFT results with experiments, there is still a missing link between X-ray spectroscopy experiments of correlated materials and first principle calculations. Recent experimental progress in energy resolution has led to the observation of correlated effects in the spectra, often happening in a very low-energy regime. However, the extraction of electronic information from the spectra, and thus the theoretical modeling of core-level X-ray spectroscopy, is a challenging task. We demonstrate how to combine DFT+DMFT with core-level X-ray spectroscopies, and study various core-level X-ray spectra of correlated materials.

Contents

1	Introduction	1
1.1	Transition Metal Oxides	1
1.2	Core-Level X-ray Spectroscopy	3
1.2.1	X-ray Photoemission Spectroscopy	4
1.2.2	X-ray Absorption Spectroscopy	6
1.2.3	Resonant Inelastic X-ray Scattering	7
1.3	Studied Materials: Transition Metal Oxides	11
1.3.1	NiO	11
1.3.2	Fe ₂ O ₃	12
1.3.3	Cuprates	13
1.3.4	Cobaltites	13
1.3.5	Rare-Earth Nickelates	14
1.4	Motivation	16
2	Theory	19
2.1	Spectral Functions of Core-Level X-ray Spectroscopy	20
2.1.1	X-ray Photoemission Spectroscopy	20
2.1.2	X-ray Absorption Spectroscopy	21
2.1.3	Resonant Inelastic X-ray Scattering	21
2.1.4	Core-Level Spectral Functions in Thermal Equilibrium	22
2.2	Atomic Model	22
2.2.1	Crystal Field Splitting	24
2.2.2	Spin-Orbit Coupling	26
2.2.3	Coulomb Interaction	27
2.3	Cluster Model	30
2.3.1	Charge-Transfer Energy	30
2.3.2	Molecular Orbitals	31
2.4	Double-Cluster Model	32
2.5	Anderson Impurity Model	34
2.5.1	Hybridization Function	35
2.6	First Principle Calculations	36
2.6.1	Density Functional Theory	36
2.6.2	Bloch Functions and Band Structure	38

2.6.3	Wannier Functions	39
2.6.4	Tight-Binding Representation	42
2.6.5	Hubbard Model and dp Model	44
2.6.6	Dynamical Mean-Field Theory	46
2.6.7	Double Counting and Charge-Transfer Energy	49
2.7	Computational Details of Core-Level X-ray Spectroscopy	49
2.7.1	Fermi's Golden Rule	49
2.7.2	Kramers-Heisenberg Formula	50
2.7.3	Scattering Geometry	52
2.7.4	Transition Operator	53
2.7.5	Configuration Interaction Scheme	54
2.7.6	Numerical Many-Body Basis	56
2.8	Workflow	59
3	1s and 2p X-ray Photoemission Spectroscopy of Correlated Materials	63
3.1	Introduction	63
3.2	Computational Details	64
3.3	Ni 1s and Ni 2p X-ray Photoemission Spectroscopy of NiO	65
3.3.1	Hybridization Dependence	67
3.4	Co 1s and Co 2p X-ray Photoemission Spectroscopy of CoO	69
3.5	Fe 1s and Fe 2p X-ray Photoemission Spectroscopy of Fe ₂ O ₃	70
3.6	Fe 1s and Fe 2p X-ray Photoemission Spectroscopy of FeTiO ₃	72
3.7	Conclusions	74
4	L₃-Edge X-ray Absorption Spectroscopy and Resonant Inelastic X-ray Scattering of Correlated Materials	77
4.1	Introduction	78
4.2	Ni L ₃ -Edge X-ray Absorption Spectroscopy and Resonant Inelastic X-ray Scattering of NiO	78
4.2.1	Double-Counting Dependence	81
4.3	Fe L ₃ -Edge X-ray Absorption Spectroscopy and Resonant Inelastic X-ray Scattering of Fe ₂ O ₃	84
4.3.1	Double-Counting Dependence	85
4.4	Cu L ₃ -Edge X-ray Absorption Spectroscopy and Resonant Inelastic X-ray Scattering of Cuprates	87
4.4.1	Fluorescence-like Feature	90
4.4.2	Double-Counting Dependence	92
4.4.3	Cluster Model	94
4.5	Co L ₃ -Edge X-ray Absorption Spectroscopy and Resonant Inelastic X-ray Scattering of Cobaltites	96
4.6	Conclusions	99

5	<i>L</i>₃-Edge X-ray Absorption Spectroscopy and Resonant Inelastic X-ray Spectroscopy of Rare-Earth Nickel Oxides	101
5.1	Introduction	102
5.2	Computational Details	103
5.3	Configuration-Interaction Scheme for Different Charge Sectors . . .	105
5.4	Valence Spectra and Hybridization	107
5.5	Ni 2 <i>p</i> X-ray Absorption and Resonant Inelastic X-ray Spectroscopy of LuNiO ₃	108
5.5.1	Metal-Insulator Transition	111
5.5.2	Charge Sector Resolved Spectra	112
5.6	Double-Counting Dependence	113
5.7	Conclusions	114
6	Summary and Outlook	115
	Appendices	117
A	Methods	119
A.1	Lanczos Algorithm	119
A.2	Continued Fraction Expansion	121
A.3	Resolvent Formalism of Electronic Systems	122
B	Tensor Operators	125
B.1	Crystal Field Potential	125
B.2	Spin-Orbit Coupling	126
B.3	Coulomb Interaction	127
	Bibliography	129
	Curriculum Vitae	147

Chapter 1

Introduction

Strongly correlated materials exhibit a broad variety of electronic phenomena, such as high-temperature superconductivity, magnetism or metal-insulator transitions. They show a strong response to external parameters like temperature, pressure, magnetic and electric fields. The high-degeneracy of low-energy states, i.e. the degeneracy of orbital, spin and lattice degrees of freedom, in correlated materials leads to instabilities and rich phase diagrams with various ordered phases. These phenomena have been attracting much attention [12, 15–17] and are intriguing for fundamental science as well as their possible application in technology. We mean by ‘strongly correlated’, that one or two particle correlation functions cannot be described by independent electrons (even in an effective model). Typically, for the correlations to be manifested, one needs a strong Coulomb interaction and a phase space available for electron dynamics, e.g. in partially filled *d*- or *f*-shells. The Coulomb interaction is strong compared to the kinetic energy of the electrons, which hinders the description of valence electrons as free particles as described in classical mean-field theories. This is contrary to other metallic compounds where local interactions are weak. Thus, more sophisticated approaches, which take the strong local interaction into account, are needed to describe to electronic structure of correlated materials. Experimental core-level X-ray spectroscopy studies revealed intriguing fine spectral features in the electronic structure of strongly correlated materials. We focus on the core-level spectra of transition metal oxides which are an important class of correlated materials and show how to combine first principle calculations with core-level X-ray spectroscopy studies. We discuss various kinds of core-level X-ray spectroscopies, where each reveals different features of the electronic structure of correlated materials.

1.1 Transition Metal Oxides

Transition metal oxides (TMOs) are strongly correlated materials with partially filled transition metal (TM) *d*-shells. The partially filled TM shells form chemical bonds with neighboring oxygen atoms. TMOs contain divalent O^{2-} anions, where

each oxygen ion deducts two additional electrons from the transition metal cation. TMOs show phases with entirely different electronic or magnetic properties [12]. In 1937, de Boer and Verwey [18] pointed out the astonishing properties of $3d$ TMOs. Mott and Peierls [19] discussed these properties, which gave rise to a whole new field in solid state physics which is one of the core subjects of modern material science and condensed matter physics. A famous TMO is NiO, which is predicted to be metallic by band structure calculations [20], but experimentally observed to be an insulator. The local correlations are the driving mechanism for the metal-insulator transition, similar to many other correlated materials.

A quantitative description of the electronic structure of TMOs requires models which include the local Coulomb interaction of the partially filled orbitals. The Hubbard model is a paradigm model for describing local correlations. It takes into account the hopping of electrons between different TM sites $d_i^n d_j^n \rightarrow d_i^{n-1} d_j^{n+1}$, where i, j denote the position of TM atoms in the lattice, as well as the local Coulomb interaction U_{dd} of the valence electrons on the same site. The gap opening takes place when the energy gain of the electron hopping between different sites becomes smaller than the energy loss due to the Coulomb repulsion of two electrons on the same site. Then the initially metallic band, which crosses the Fermi energy E_F , splits into two separate bands: the lower Hubbard band (LHB) below E_F and the upper Hubbard band (UHB) above E_F [21, 22].

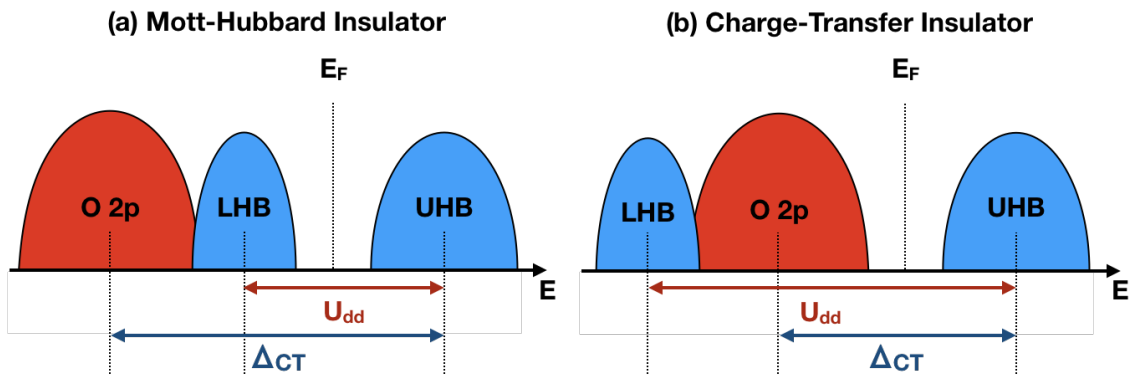


Figure 1.1: (a) Mott insulator: the upper (lower) Hubbard band is situated above (below) the Fermi-level E_F , the O $2p$ states are below the lower Hubbard band (b) charge-transfer insulator: the O $2p$ states are situated above the lower Hubbard band but below the Fermi-level [22]. Figure adapted from [21] with permission of the author.

Zaanen, Sawatzky and Allen [23] classified Mott insulators into Mott-Hubbard and charge-transfer types, see Fig. 1.1. Both types are classified by the local Coulomb interaction of the valence electrons and the charge-transfer energy Δ_{CT} . Δ_{CT} is the energy cost of an electron transfer from O $2p$ to the Ni $3d$ states. In

order to take into account the p - d hopping in the Hubbard model, it has to be extended by the inclusion of O sites with the hopping process $d_{\text{TM}}^n p_{\text{O}}^i \rightarrow d_{\text{TM}}^{n+1} p_{\text{O}}^{i-1}$. In the Mott-Hubbard type, see Fig. 1.1a, the O $2p$ bands are situated below the lower Hubbard band, which means that the Coulomb repulsion energy U_{dd} is smaller than the energy cost of a charge transfer Δ_{CT} from oxygen to the TM ion. In charge-transfer type insulators, see Fig. 1.1b, the bands formed by the O $2p$ electrons are situated between the lower and upper Hubbard band. The energy cost of the charge transfer from oxygen to the TM ion is lower than the energy cost of the local Coulomb repulsion [21, 22].

1.2 Core-Level X-ray Spectroscopy

Core-level X-ray spectroscopies present a powerful set of tools to study materials with a complex electronic structure, such as strongly correlated materials. The excitation spectrum characterizes the electronic properties of the studied compound. Core-level spectroscopies are element sensitive, due to the strong energy dependence of X-ray absorption edges on the proton number. Different valence states of the same elements can be observed in the spectra due to their typical shapes and their shifts on eV scale.

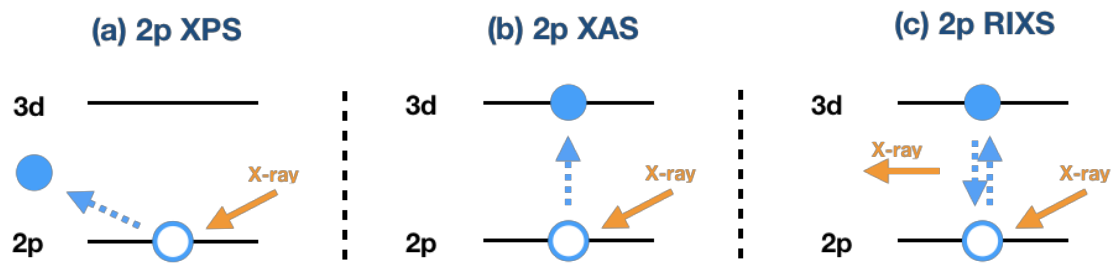


Figure 1.2: Schematic picture of $2p$ core-level excitation processes: (a) X-ray photoemission spectroscopy (XPS), (b) X-ray absorption spectroscopy (XAS), (c) resonant inelastic X-ray scattering (RIXS). Figure adapted from [21] with permission of the author.

We present three types of core-level X-ray spectroscopies: X-ray photoemission spectroscopy (XPS), X-ray absorption spectroscopy (XAS) and resonant inelastic X-ray scattering (RIXS), see Fig. 1.2. They share the absorption of an incident X-ray, which creates a positively charged core-hole either by emitting or by excitation of an electron from a $1s$ or $2p$ core-shell to a valence shell. The generated positively charged core-hole is strongly bound to the core-excited atom and the response of the system provides rich information about the electronic structure which can be observed in the spectra. For example, local valence electrons forming multiplet structures as a result of the Coulomb interaction with the core-hole, or screening effects from neighboring ligand electrons.

The spectroscopy types vary with the excitation process and the underlying selection rules as well as with the electron number of the system. In XPS, see Fig. 1.2a, the incident photons emit core-electrons from the system and generate an electron emission spectrum. XAS provides an absorption spectrum of incident photons, see Fig. 1.2b, retaining the electron number of the system constant. The excitation process of RIXS is similar to the one of XAS, but followed by a relaxation process where a photon is emitted, see Fig. 1.2c.

1.2.1 X-ray Photoemission Spectroscopy

Core-level X-ray photoemission spectroscopy is a widely used tool to study the electronic properties of transition-metal compounds. XPS is a first-order optical process in which a core-electron is emitted from the system by absorption of an incident photon. The emitted electrons undergo scatterings in the bulk, leading to a smearing of spectral features. Recent experimental progress reduces the impact of these smearing effects by using hard X-ray sources in the energy range of >5.0 keV. Hard X-ray photoemission spectroscopy (HAXPES) is capable of probing the bulk states [24, 25] with an improved energy resolution, e.g., ≈ 200 meV in $2p$ HAXPES for $3d$ TMOs. This makes it possible to study fine spectral features which reflect the low-energy states near the Fermi energy [26–31].

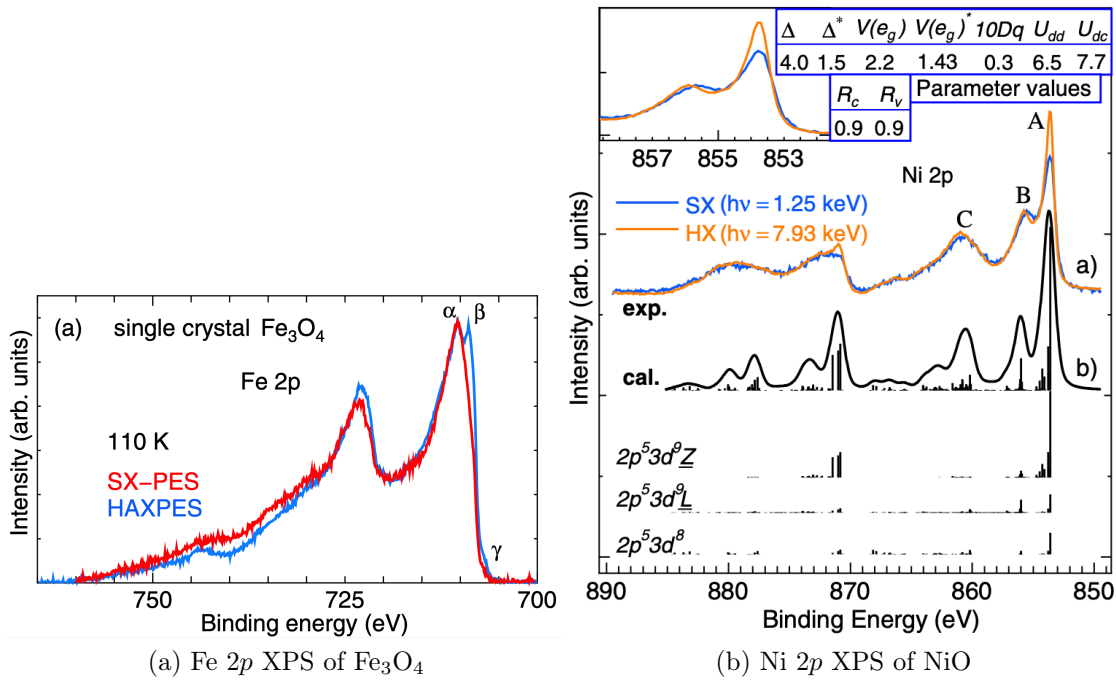


Figure 1.3: Experimental TM $2p$ XPS spectra of (a) Fe_3O_4 [28] and (b) NiO [32]. Figures taken from [28] and [32].

Fig. 1.3a shows the $\text{Fe } 2p$ XPS spectra of Fe_3O_4 [28]. One can clearly distinguish

two separated parts, $2p_{3/2}$ (between 706 – 720 eV) and $2p_{1/2}$ (between 721 and 735 eV), due to spin-orbit (SO) coupling in the Fe $2p$ states. The peak α (≈ 710.5 eV) is called the main line (ML) and observed in the soft X-ray photoemission (PES) and HAXPES spectrum. The peaks β (≈ 708.5 eV) and γ (≈ 707.0 eV) are only seen in the bulk-sensitive HAXPES spectrum indicating the importance of HAXPES. In Ni $2p$ XPS of NiO [32], see Fig. 1.3b, we see two well-separated parts, $2p_{3/2}$ (between 853 – 869 eV) and $2p_{1/2}$ (between 870 – 886 eV), due to spin-orbit coupling in the Ni $2p$ states. The $2p_{3/2}$ main line shows a double peak structure (peak A and peak B) at ≈ 856 eV. The $2p_{1/2}$ main line at ≈ 872 eV is enhanced in the bulk-sensitive HAXPES spectrum compared to the soft X-ray PES spectrum. In Ni $2p$ XPS of NiO, fine spectral features are observed. The emission of a core-electron breaks the local charge neutrality and induces a strong charge response from neighboring ligand electrons. This effect is called charge-transfer (CT) screening and is visible in peak C, in the $2p_{3/2}$ part, and in the peaks of the $2p_{1/2}$ part in the region between 876 and 885 eV. HAXPES enabled the clear observation of charge transfer from distant transition metals and the rest of the crystal, which is traditionally called non-local screening (NLS) [33, 34]. Soft X-ray PES cannot probe the bulk properly and non-local screening effects are suppressed on the surface states. Peak B in Fig. 1.3b reflects the charge transfer from distant atoms. These non-local screening features are sensitive to various aspects of inter-site physics, e.g. the long-range magnetic or orbital ordering, or even to the metal-insulator transition [4, 21, 31, 32, 34–41].

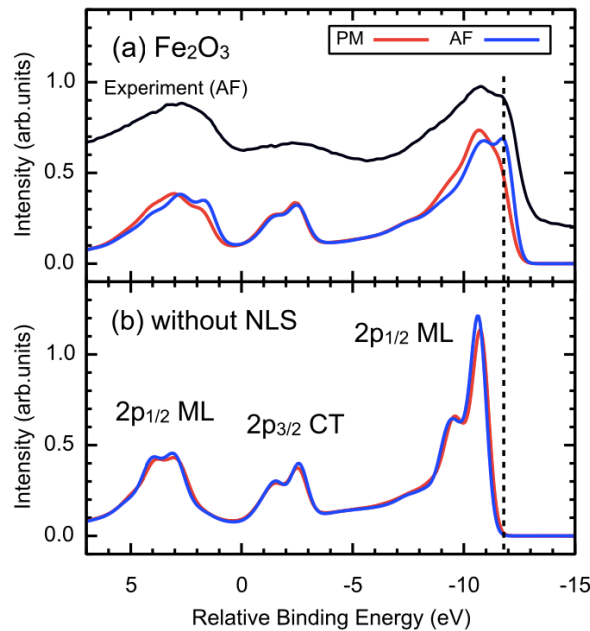


Figure 1.4: Fe $2p$ XPS of Fe_2O_3 in paramagnetic metal (PM) and antiferromagnetic (AF) insulating phase, blue and red line are calculated with LDA+DMFT approach, the experimental (black curve) data is taken from Ref. [42]. Figure taken from [31].

Fig. 1.4a shows the Fe $2p$ XPS of Fe_2O_3 in the antiferromagnetic and paramagnetic phases [31]. We distinguish two well separated parts, $2p_{3/2}$ (between $-15 - 0$ eV) and $2p_{1/2}$ (between $1 - 6$ eV). The $2p_{3/2}$ main line at ≈ -9 eV exhibits an internal fine-structure as a result of non-local screening effects. The $2p_{3/2}$ charge-transfer satellite is formed between -4 and 0 eV. A theoretical investigation without the non-local screening channel from the Fe $3d$ bands is provided in Fig. 1.4b. The $2p_{3/2}$ main line in Fig. 1.4b consists of a sharp peak with a high-binding energy E_B shoulder (in some spectra observable as satellite), which is due to intra-atomic Coulomb multiplets. These Coulomb multiplet shoulders (satellites) result from unscreened final states and are well separated from the charge-transfer satellites. The low- E_B peak, which is observed in Fig. 1.4a and marked by the dashed line, disappears if non-local screening effects are excluded, see Fig. 1.4b.

1.2.2 X-ray Absorption Spectroscopy

X-ray absorption spectroscopy (XAS) can be used to estimate the valence state of an ion in mixed-valence materials. XAS in localized electron systems, e.g. L -edge ($2p \rightarrow 3d$) in $3d$ TMOs, show complex spectra due to the rich core-valence Coulomb multiplets. The charge-transfer screening from electrons of surrounding ions can be also observed in the spectra. However, the charge transfer effects in XAS are not as dominant compared to XPS. This is because the charge-neutrality is preserved in the system and the core-excited electron screens the positively charged core-hole. This hampers a direct access to the details of the ground as well as excited states in the XAS spectra. In XAS the Coulomb multiplet effects and the crystal field excitations are dominant [2, 30].

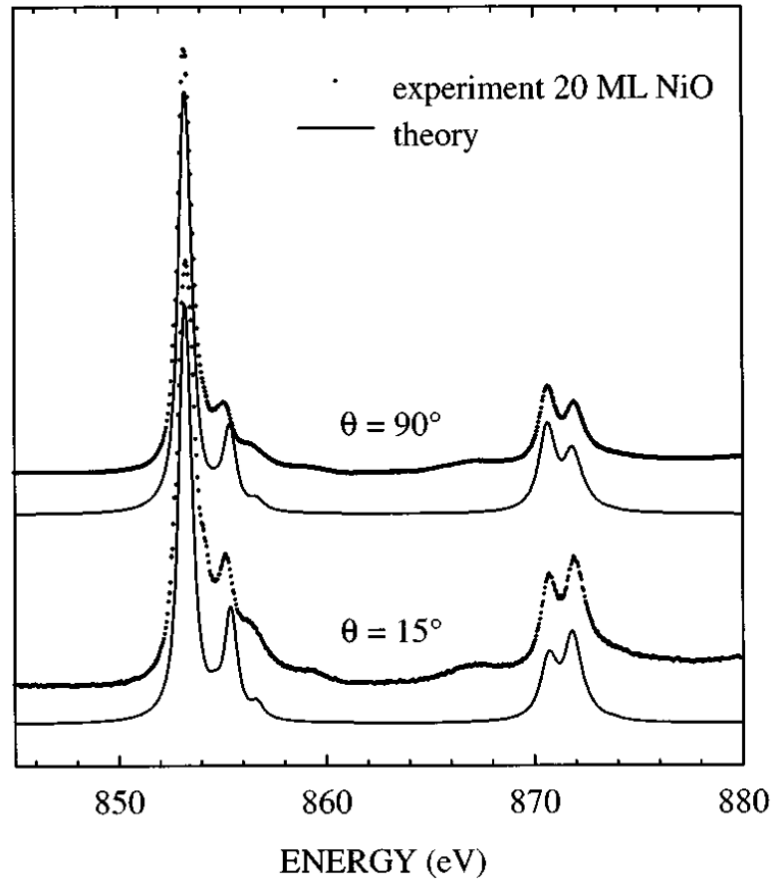


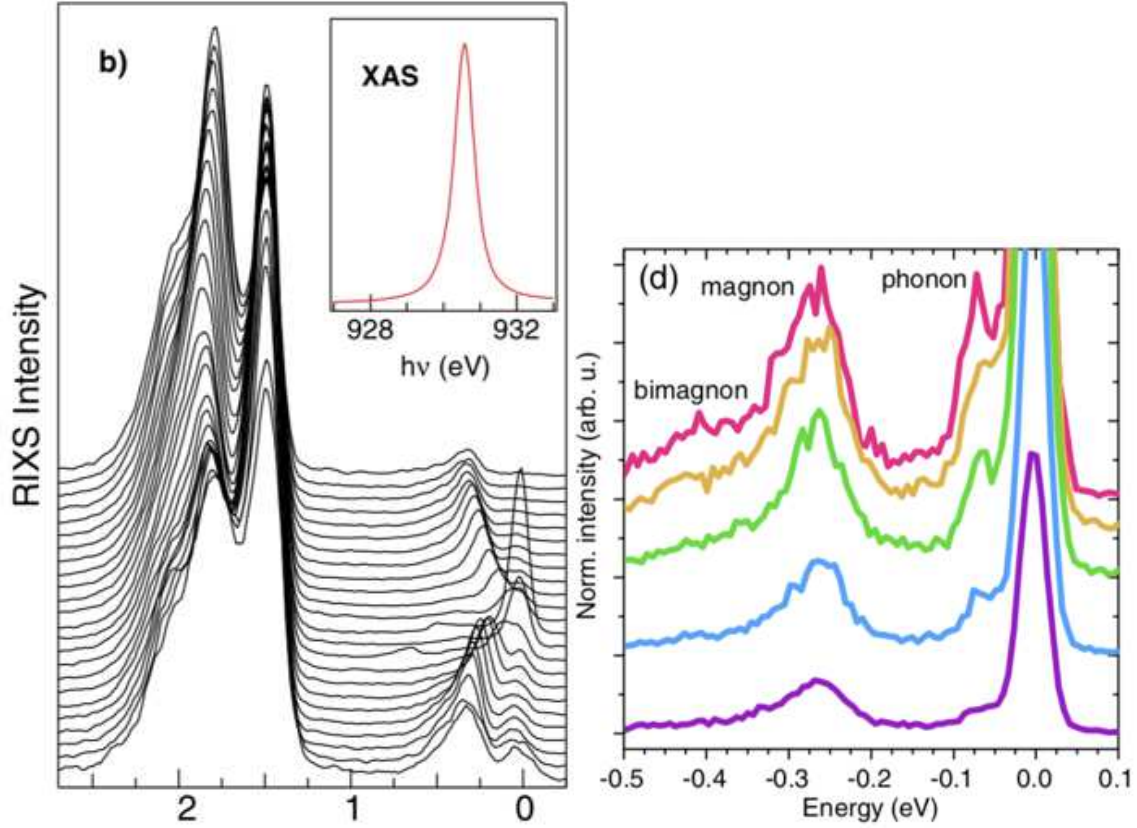
Figure 1.5: Ni L -edge XAS of NiO. Figure taken from [43].

Fig. 1.5 shows the experimental spectra of Ni L -edge XAS of NiO [43]. The spin-orbit coupling in the Ni $2p$ states gives rise to two separated edges: L_3 -edge ($2p_{3/2}$) at ≈ 855 eV and L_2 -edge ($2p_{1/2}$) at ≈ 872 eV. The dominant peak at the L_3 -edge contains an unscreened excitation. The shoulder at ≈ 855 eV arises from Coulomb multiplets and not from charge-transfer or non-local screening effects observable in XPS spectra. Charge transfer effects from neighboring ligands are just faintly observed at ≈ 857 eV.

1.2.3 Resonant Inelastic X-ray Scattering

Thanks to remarkable improvements in energy resolution, resonant inelastic X-ray scattering (RIXS) has become a powerful tool to study strongly correlated materials [2, 44]. RIXS is a second-order optical process, in which an incident photon with energy ω_{in} excites a core-electron to a valence state, followed by a deexcitation process with emitted photon energy ω_{out} . The dipole selection rules in the second-order optical process enable the observation of various two-particle excitations with lattice, spin, orbital and charge degrees of freedom in the low-energy

loss $\omega_{\text{loss}} = \omega_{\text{in}} - \omega_{\text{out}}$ regime (≈ 100 meV) [45–48]. RIXS is also sensitive to high- ω_{loss} excitations (between 1 – 10 eV), like charge transfer or atomic multiplet ($d-d$) excitations [30, 49, 50]. Furthermore RIXS can resolve the momentum dependence, which is not accessible by XPS and XAS.



(a) Cu L_3 -edge RIXS of $\text{Sr}_2\text{CuO}_2\text{Cl}_2$ of (2010) (b) Cu L_3 -edge RIXS of $\text{NdBa}_2\text{Cu}_3\text{O}_6$ (2019)

Figure 1.6: Experimental momentum resolved L_3 -edge RIXS of Cuprates. Figure (a) taken from [51] and Figure (b) taken from [52].

Fig. 1.6a shows a momentum resolved Cu L_3 -edge ($2p \rightarrow 3d \rightarrow 2p$) RIXS study of the compound $\text{Sr}_2\text{CuO}_2\text{Cl}_2$ from the year 2010. The horizontal axis denotes the energy loss ω_{loss} , whereas the vertical axis corresponds to the momentum transfer. The peaks within the range of 1.25 – 2 eV ω_{loss} are $d-d$ multiplet excitations. The inset shows a Cu L_3 -edge XAS spectrum with a single absorption peak at ≈ 830 eV. Here, we see the limitations of extracting detailed information about the electronic structure from XAS spectra. The resolution of RIXS allows for a more detailed study of the elementary excitations near the elastic peak in the low- ω_{loss} regime. Fig. 1.6b shows a momentum-resolved Cu L_3 -edge RIXS study from the year 2019. Due to improvements of the energy resolution, the elementary excitations are resolved, whereas initially they were merged with the elastic peak. The elementary excitations consist of phonons, magnons or bimagnons. Recent experi-

mental progress of RIXS also enabled the study of even more degrees of freedom, e.g. tuning the incident photon energy ω_{in} . This allows for scanning across the X-ray absorption edges, facilitating the study of non-local charge excitations.

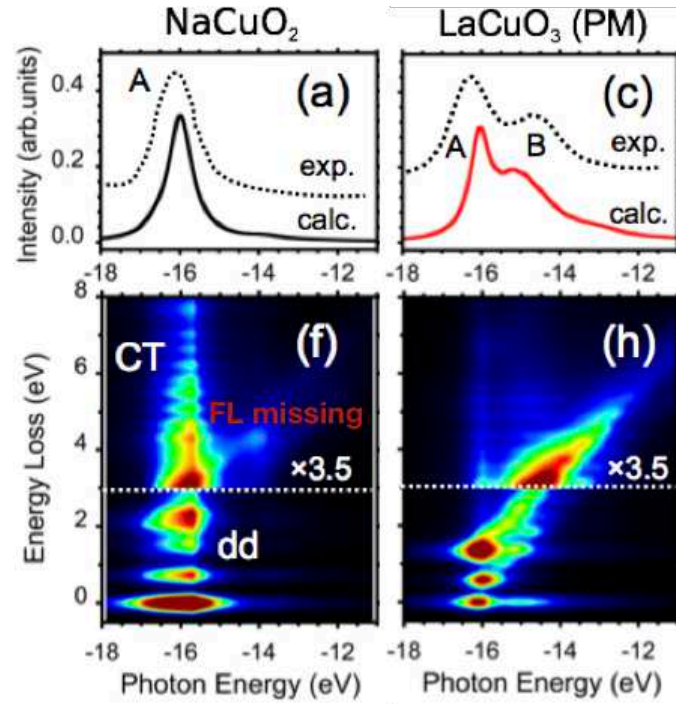


Figure 1.7: Cu L_3 -edge XAS and RIXS of NaCuO₂ and LaCuO₃. LaCuO₃ shows a continuous fluorescence-like feature in RIXS spectrum. Figure adapted from [5].

Figs. 1.7a,c show theoretical Cu L_3 -edge XAS spectra of NaCuO₂ and LaCuO₃. In NaCuO₂ we see a single peak at the incident photon energy $\omega_{\text{in}} \approx -16$ eV, whereas in the XAS spectrum of LaCuO₃ there is a dominant peak at $\omega_{\text{in}} \approx -16$ eV with a broad shoulder at higher ω_{in} due to non-local charge excitations. Figs. 1.7f,h show theoretical Cu L_3 -edge RIXS spectra of NaCuO₂ and LaCuO₃. The abscissa corresponds to the incident photon energy ω_{in} and the ordinate to the energy loss ω_{loss} . In both spectra we observe bound $d-d$ excitations in the ω_{loss} regime between 0.5 and 3.0 eV at $\omega_{\text{in}} \approx -16$ eV. The charge-transfer excitations are more dominant in NaCuO₂ with $\omega_{\text{loss}} > 3.0$ eV. But the RIXS spectrum of LaCuO₃ exhibits an intriguing continuous fluorescence-like feature which is not observed in NaCuO₂. This feature is due to unbound electron-hole pairs propagating through the crystal [5]. Generally we distinguish two main features observed in the spectra by scanning the incident photon energy: Raman-like (RL) signals with constant ω_{loss} , and continuous fluorescence-like (FL) signals with a constant emission energy ω_{out} . The energy of the emitted photon has a linear dependence of ω_{loss} on ω_{in} [44, 50, 53–56].

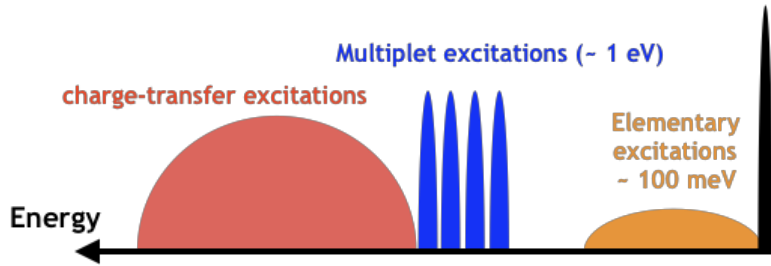


Figure 1.8: Typical excitations observed in RIXS spectra. Figure adapted from [44].

Fig. 1.8 shows a cartoon of typical excitations that are observed in the RIXS spectra of strongly correlated materials. The drawback of the sensitivity of this technique to various excitations is that the interpretation of the spectra is complex, due to possible overlap or interference between excitations. Through the analysis of the material-specific excitations, questions about the itinerancy of charge carriers as well as localization of charge excitations arise [54, 56, 57]. But while several experimentally motivated interpretations were put forward, a unified description of atomic-like RL and itinerant FL features poses a theoretical challenge [2, 58, 59]. Thus, the goal of the theoretical description of RIXS would be to cover the multi-energy-scale excitations on the same footing, while eliminating uncertainties in disentangling RL and FL excitations.

In order to provide a better understanding of RIXS, we discuss the excitation process on the example of a compound with a TM d^8 configuration in the ground state, e.g. Cuprates or NiO.

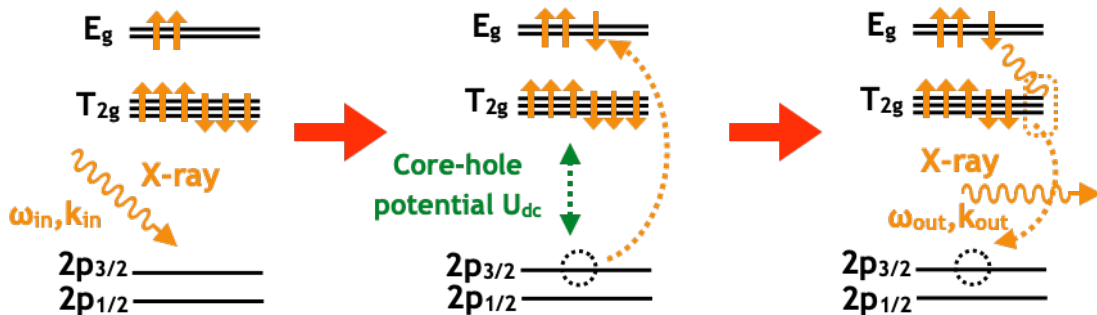


Figure 1.9: TM L_3 -edge RIXS process with a d^8 configuration in ground state.

Fig. 1.9 shows an L_3 -edge RIXS process with completely filled T_{2g} orbitals and two electrons in the E_g orbitals in the ground state of the compound. RIXS consists of two steps, connecting three types of states: initial, intermediate (with active core-hole) and final states. The incident photon excites a core-electron in the initial state to an empty E_g orbital. The core orbitals are localized, thus the positively

charged core-hole remains at the impurity and renormalizes the energies of the TM $3d$ states in the intermediate state. TM $3d$ valence electrons can be transferred from the impurity into the crystal host within the intermediate state. The spin-orbit coupling on the $2p$ core-level is also critical for the excitation of $3d$ multiplets. The intermediate states of RIXS can be seen as the final states of XAS. Then, a valence electron deexcites into the core-hole by emission of a photon, building the final states.

1.3 Studied Materials: Transition Metal Oxides

In the following, we show the various transition metal compounds which were studied in this thesis. First we discuss NiO and Fe_2O_3 , followed by cuprates, cobaltites and rare-earth nickelates. We also introduce high-valence transition metal compounds.

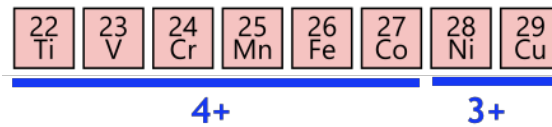


Figure 1.10: High-valence transition metals.

High-valence transition metal oxides possess interesting physics and share a small or even negative charge-transfer energy. Since there is no strict definition, we consider tetravalent Ti^{4+} to Co^{4+} and trivalent Ni^{3+} and Cu^{3+} high-valence transition metals, see Fig. 1.10.

1.3.1 NiO

NiO has a rocksalt crystal structure with Fm-3m (225) space group, see Fig. 1.11. The divalent Ni^{2+} cation is surrounded by six equidistant O^{2-} anions forming an NiO_6 cluster in O_h point group symmetry. The ground state mainly consists of Ni d^8 configurations.

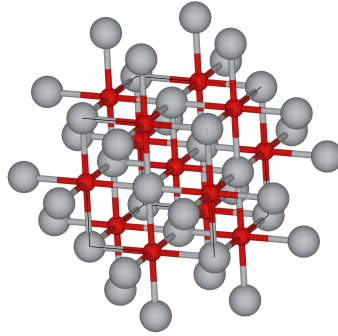


Figure 1.11: Crystal structure of NiO, visualized by VESTA [60].

NiO is an type-II antiferromagnet (AF), with a staggered order in all three spatial directions. The Néel temperature is $T_N \approx 523$ K, with a paramagnetic insulating phase above T_N . NiO has a large charge gap $E_{\text{gap}} \approx 4$ eV and a magnetic moment of $\approx 2\mu_B$, where μ_B is the Bohr magneton. NiO is an extensively studied compound and can be seen as a prototype material for studying electronic correlations. Standard band structure calculations predict NiO to be metallic [20] or small-gap AF insulator [61]. Band structure calculations severely underestimate the charge gap as well as the magnetic moment. The lowest excited state in NiO is formed by an electron transfer from O $2p$ bands to the upper Hubbard band. Thus, NiO is a charge-transfer type insulator which can be captured by DFT+DMFT calculations.

1.3.2 Fe_2O_3

$\alpha\text{-Fe}_2\text{O}_3$, also known as hematite, has a corundum structure with R-3c h (167) space group. The AF insulating phase develops at the Néel temperature $T_N \approx 956$ K with paramagnetic insulating phase above T_N . The iron has a formal Fe^{3+} valence where mainly d^5 configurations contribute to the ground state. This gives rise to a local high-spin state. Recently, the pressure dependence of $\alpha\text{-Fe}_2\text{O}_3$ was investigated by Kuneš *et al.* [62]. As the volume decreases with higher pressure, a simultaneous first-order insulator-metal and high-spin to low-spin transition occurs close to the experimental value of the critical volume. The high-spin insulating phase is destroyed by a progressive reduction of the charge gap with increasing pressure. The high-pressure phase is characterized by metallic conductivity and the absence of magnetic long-range ordering and a high-spin local moment [63]. Similar to many transition metal oxides, DFT fails to reproduce the ground state under ambient conditions. DFT severely underestimates the charge gap and the magnetic moment on iron. Fe_2O_3 is similar to NiO a charge-transfer type insulator. More recently, the site-selective Mott transition was reported in Fe_2O_3 under pressure [64].

1.3.3 Cuprates

We study the two compounds LaCuO_3 and NaCuO_2 with perovskite structure with $P4/m$ space group and a monoclinic $C2/m$ space group, respectively. The Cu^{3+} ions in both compounds are trivalent with dominant d^8 configurations in the ground state. The original motivation to study cuprates was the discovery of high- T_c superconductivity [65]. However, both compounds can also be used as model systems for high-valence TMOs [5]. They share a tiny charge-transfer energy [66–70] which leads to a small or even absent charge gap [66, 68, 69, 71, 72]. NaCuO_2 ($E_{\text{gap}} \approx 0.5$ eV) is a band-insulator with a gap present already in the LDA solution [73, 74]. The main difference between these compounds is the lattice geometry. LaCuO_3 has a corner-sharing structure with CuO_6 octahedra, whereas NaCuO_2 has edge-sharing CuO_6 octahedra, see Fig. 1.12. The different lattice geometry is the key element of the presence or absence of the FL-feature observed in the Cu L_3 -edge RIXS spectra of these compounds.

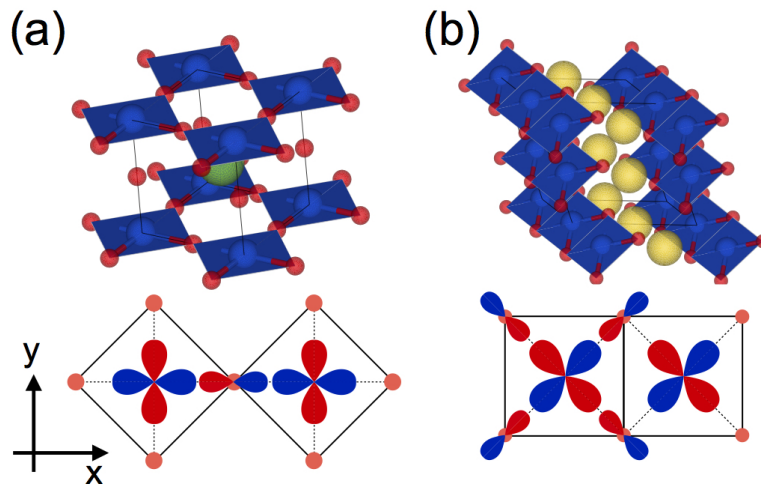


Figure 1.12: The crystal structures of (a) LaCuO_3 with $P4/m$ and $C2/m$ space groups in paramagnetic and antiferromagnetic states, respectively [71] (b) NaCuO_2 [75] visualized by VESTA [60]. The blue, red, green, and yellow circles represent Cu, O, La and Na atoms, respectively. Figure and caption taken from [5].

1.3.4 Cobaltites

We study various kinds of cobaltites: LaCoO_3 , SrCoO_3 , LiCoO_3 and CoO . The compound LaCoO_3 with trivalent Co^{3+} is a diamagnetic insulator at low temperatures, where the T_{2g}^6 orbitals are fully filled and the E_g^0 bands are empty. Thus, LaCoO_3 has a singlet $3d^6$ ground state. It undergoes a transition to a paramagnetic insulating phase with increasing temperature, at $T_C \approx 100$ K, which was originally attributed to the thermal population of atomic multiplets. Recently, this has been questioned and the importance of either the intermediate-spin (IS, $S = 1, T_{2g}^5 E_g^1, {}^3 T_{1g}$) or the

high-spin ($HS, S = 2, T_{2g}^4 E_g^2, {}^5 T_{2g}$) states for the phase transition are discussed [76–93]. SrCoO_3 crystallizes like LaCoO_3 in corner-sharing perovskite structure with a formal valence of Co^{4+} . The ground state has a mixed $3d^5 +$ dominant $d^6 \underline{L}^1$ configuration with a hole in the ligands, denoted as \underline{L} , due to a small charge-transfer energy. While LiCoO_2 crystallizes in a quasi-two-dimensional structure with edge-sharing CoO_6 octahedra, it has a trivalent ground state similar to LaCoO_3 . The $\text{Co } d^6$ manifolds have rich low-energy multiplets characterized by low-spin ($S = 0$), intermediate-spin ($S = 1$), and high-spin ($S = 2$) states. LaCoO_3 and LiCoO_2 are band insulators with a charge gap of $E_{\text{gap}} \approx 0.5$ eV. They share a LS configuration in the ground state, while SrCoO_3 is a ferromagnetic metal with an admixture of the HS state and charge fluctuations around it [2, 94]. CoO is a typical TMO with divalent Co^{2+} and d^7 configuration in the ground state. CoO has a large charge gap of $E_{\text{gap}} \approx 3.6$ eV.

1.3.5 Rare-Earth Nickelates

The RNiO_3 family shows a concomitant metal-insulator and structural transition followed by an unusual magnetic ordering resulting in a rich phase diagram [57, 95–103], see Fig. 1.13.

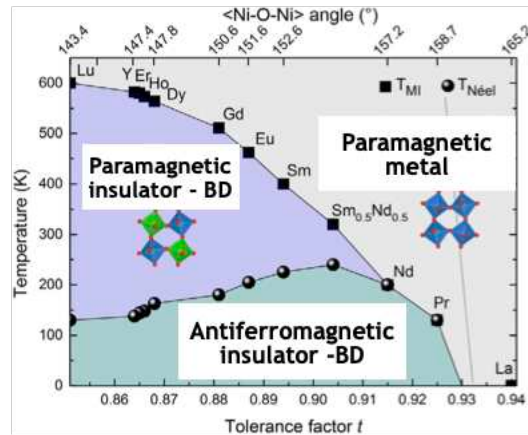


Figure 1.13: Phase diagram of ReNiO_3 family. Figure taken from [104].

At low temperatures a magnetically ordered region with antiferromagnetic insulating behaviour is observed. As the temperature increases, we move from the magnetic ordered phase to a paramagnetic insulating phase. The paramagnetic insulating phase shows a bond disproportionation (BD) with two inequivalent Ni sites. The sites are forming a NiO_6 cluster with shrunked and expanded NiO_6 octahedra which are called short-bond (SB) and long-bond (LB) site, respectively, see Fig. 1.14.

Bond disproportionated system

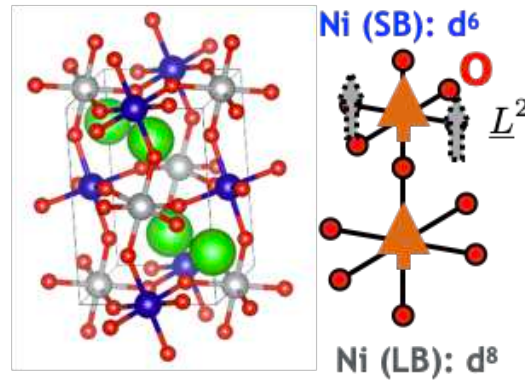


Figure 1.14: Crystal structure of LuNiO₃, visualized by VESTA [60].

The disproportionation of the Ni-O bonds leads to a structural deformation of the crystal. This bond disproportionation induces a charge disproportionation, see Fig. 1.15. The Ni ions have a formal valence of Ni³⁺ in RNiO₃. Starting from this ionic picture, initially a charge disproportionation from $2d^7 \rightarrow d^6 + d^8$ was proposed by Mazin *et al.* [95]. By taking ligand holes into account explicitly, a state with a $d^8 \underline{L}^2$ configuration at the SB site and a d^8 configuration at the LB site develops, which was discussed recently by Park *et al.* [97]. The d^8 state formed at the LB site shows a local moment with a triplet ground state, while the $d^8 \underline{L}^2$ state at the shrunk Ni-O site forms a singlet ground state.

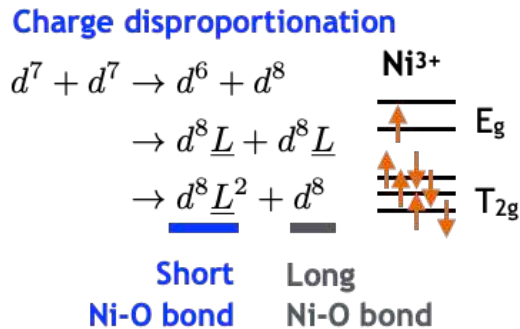


Figure 1.15: Charge disproportionation in rare-earth nickelates.

At high temperatures on the other hand, a paramagnetic-metal (PMM) phase with equivalent NiO₆ octahedra is observed. The mechanism of the metal-insulator transition is the object of an active debate. Recently, DFT+DMFT studies pointed out the importance of the electronic correlations and proposed a site-selective Mott transition scenario [97, 105]. Lee *et al.* [96] used the band picture to argue that a Peierls-like distortion originating in Fermi surface nesting explains the physics of rare-earth nickelates. This view is supported by LDA+U calculations of Mercy *et*

al. [102] in the magnetically ordered state. They pointed out the importance of octahedral rotations for tuning the Peierls-like instability. Thus, the metal-insulator transition is connected with the magnetic ordering, which is at odds with the paramagnet-to-paramagnet metal-insulator transition in a number of rare-earth nickelates. The question of Peierls vs. site-selective Mott mechanism [106] remains open [3].

1.4 Motivation

Recent experimental progress of various core-level X-ray spectroscopy methods have opened opportunities to study the electronic structure of correlated materials. Additional degrees of freedom in experiment, such as the tuning of the incident photon energy in RIXS and a drastic improvement of energy resolution revealed fine features in the core-level spectra of correlated materials. The use of core-level X-ray spectroscopies for investigating the electronic structure is advantageous compared to other methods. For example RIXS reaches dipole transitions which are not accessible by other methods, e.g. neutron scattering. These dipole transitions encode various information about the fine features observed in the spectra. The non-local screening effects and itinerant electron-hole pairs observed in the spectra of transition metal compounds are intriguing for the development of theoretical models. The recent experimental advances are a challenge for the established models, which oversimplify the studied compounds. We have developed a core-level X-ray spectroscopy code, based on the Anderson impurity model description [5, 22, 31], which resolves a number of problems in the field and provides a quantitative agreement with state-of-the-art experiments. We use DFT+DMFT to obtain a realistic electronic structure of the studied compounds and apply the hybridization function obtained by DMFT to an Anderson impurity model augmented by core-orbitals to calculate core-level spectra. We optimize the spectroscopy code to increase the number of basis functions which is necessary to obtain realistic spectra including their fine spectral features. In detail, we extend the number of possible bath states, encoded in the hybridization function. The fine energy mesh of the hybridization function allows us to study the metal-insulator transition in LuNiO_3 . Furthermore, we extend the code to lower symmetries which allows for using a different hybridization function for each valence orbital. This enables us to study a broad variety of real materials with distorted MO_6 octahedra. We use a combination of XPS, XAS and RIXS to provide a detailed study of the electronic structure hidden in the spectra of real materials. We compare the spectra with experimental core-level studies and several commonly used impurity models, e.g. the cluster model. We highlight the importance of the Anderson impurity model description and give insight into some features of the electronic structure. One of the core topics is the investigation of bond disproportionated systems, e.g. LuNiO_3 . We show that the metal-insulator transition is connected to the presence or absence of the fluorescence-like feature

observed in the low-energy loss regime of RIXS spectra.

Chapter 2

Theory

Theoretical studies of core-level X-ray spectroscopies are crucial for extracting electronic information hidden in the experimental spectra. The theoretical modelling is based on spectral functions which simulate core-excited spectra of electronic systems. We discuss the spectral functions of X-ray photoemission spectroscopy (XPS), X-ray absorption spectroscopy (XAS) and resonant inelastic X-ray scattering (RIXS). Calculating spectral functions requires the choice of proper model Hamiltonians which encode the electronic structure of real materials in an effective way. Naively, one would use the full Hamiltonian of a system, but due to the exponentially increasing size of the Hamiltonian with the number of particles and thus computational limitations, one has to limit oneself to models which reduce the size of the Hamiltonian. The core-level excitation is a local process because of the negligible overlaps of TM $1s$ and TM $2p$ core orbitals between neighboring sites. Thus, impurity models are applicable for the calculation of core-level spectra. We discuss the atomic model, where the electron exchange between atom and the crystal is neglected. The atomic model is not the most appropriate model to describe real materials, it fails to reproduce even simple features of the spectra. A natural extension of the atomic model are impurity models. The cluster model includes the charge transfer between an impurity and its nearest-neighbor ligands and has been widely used in core-level spectroscopies of real materials. The cluster model can be extended by a second cluster including the charge transfer between distinct TM sites. This extension is the so-called double-cluster model [107] and can be applied in order to describe bond disproportionated systems like RNiO_3 [108]. These impurity models have many adjustable parameters and show limitations in the description of real materials. The Anderson impurity model is a generalization of the cluster model that encodes the electronic structure of the crystal host by a so-called hybridization function. The hybridization function can be seen as hopping amplitude between impurity and the electronic structure of the rest of the crystal host. First principle calculations provide the hybridization function with almost no parameters as input.

We use first principle calculations in our core-level spectroscopy approach to calculate the electronic structure of real materials, see Sec. 2.6. In Sec. 2.7 we discuss the computational details of core-level spectroscopies. The core-level spectroscopy calculations are based on exact diagonalization. We reformulate spectral functions in terms of resolvents, which are numerically accessible. Furthermore we study the scattering geometry and the transition operator as well as the configuration-interaction scheme, which is widely used to generate optimized basis sets in theoretical core-level spectroscopy studies. The theoretical modelling of core-level spectroscopies includes a large variety of tools. In the last part of the theory chapter we show the workflow of our core-level X-ray spectroscopy approach and discuss the used parameters and software.

2.1 Spectral Functions of Core-Level X-ray Spectroscopy

Spectral functions of core-level X-ray spectroscopy provide the theoretical description of the absorption of an incident photon in materials. This absorption process depends on the energy of the incident photon resulting in either an emission (XPS) or excitation (XAS) of a core-electron. RIXS encodes the excitation of a core-electron to a valence state followed by a relaxation process. Thus, the spectral function of RIXS encodes additionally the emission of a photon. In this section we study the spectral functions of core-level spectroscopy and the consideration of finite temperature in core-level studies.

2.1.1 X-ray Photoemission Spectroscopy

The theoretical description of the core-level photoemission process is given by Fermi's golden rule [30]. Here, Fermi's golden rule describes the transition from an initial state $|n\rangle$ to a set of final states $\{|f\rangle\}$ by emission of a photoelectron. The transition is triggered by the incident photon

$$F_{\text{XPS}}^{(n)}(\omega) = \sum_f \left| \langle f | \hat{T}_D | n \rangle \right|^2 \delta(E_n + \omega - E_f), \quad (2.1)$$

where ω is the energy of the emitted photoelectron. The initial state $|n\rangle$ is described by a many-body wave function with n_v electrons in its valence states and fully occupied core states with n_p electrons. The valence states consist of partially filled valence shells, e.g. for transition metal (TM) oxides TM $3d$ orbitals as well as oxygen (O) $2p$ orbitals. The core states consist of orbitals from TM $1s$, TM $2s$ or TM $2p$ shells. The initial state is often the (degenerate) ground state of the system but for finite temperatures we use a thermodynamical ensemble consisting of multiple initial states. The number of valence electrons is conserved in the XPS process, thus the set of final states $\{|f\rangle\}$ has n_v electrons in their valence

orbitals. Due to the emission of a photoelectron the number of electrons in the core states is reduced, having ‘ n_p-1 ’ core electrons compared to the initial state. The missing electron in the core shell behaves as a positively charged core-hole. The system’s response to the incident photon, i.e. the emitted electron, is encoded in the transition operator \hat{T}_D , which connects the subspaces of the initial states $|n\rangle$ with the subspace of the set of final states $\{|f\rangle\}$. The transition operator encodes the propagation of the photoelectron described as plane wave in the high energy regime and can be approximated as a dipole moment $\hat{T}_D \sim \boldsymbol{\varepsilon} \cdot \hat{\mathbf{r}}$, with the photon polarization vector $\boldsymbol{\varepsilon}$ and the position operator $\hat{\mathbf{r}}$. The delta function represents the energy conserving process. The energies E_n and E_f are the eigenenergies of the eigenstates $|n\rangle$ and $\{|f\rangle\}$ of the system, respectively. The initial eigenstate $|n\rangle$ is calculated by diagonalizing model Hamiltonians which are introduced below.

2.1.2 X-ray Absorption Spectroscopy

The spectral function of core-level X-ray absorption spectroscopy describes the absorption process of an incident photon, where the incident photon excites a core electron to an empty valence orbital. The spectral function is described by Fermi’s golden rule, similar to that of XPS, and reads

$$F_{\text{XAS}}^{(n)}(\omega) = \sum_f \left| \langle f | \hat{T}_D | n \rangle \right|^2 \delta(E_n + \omega - E_f), \quad (2.2)$$

where ω is the energy of the incident photon. The initial state $|n\rangle$ has n_v electrons in the valence orbitals and n_p electrons in the core orbitals. However, the set of final states $\{|f\rangle\}$ differ from XPS. The final states contain ‘ n_v+1 ’ valence electrons and ‘ n_p-1 ’ electrons in the core states due to the excitation of a core electron to a valence orbital. The response of the system to the incident photon is encoded in the transition operator and approximated as dipole operator $\hat{T}_D \sim \boldsymbol{\varepsilon} \cdot \hat{\mathbf{r}}$.

2.1.3 Resonant Inelastic X-ray Scattering

The numerical simulations of RIXS usually start from either two limits, the non-interacting solid or the atomic limit. In the former limit one is able to apply the Bethe-Salpeter approach based on band theory with effectively non-interacting electrons [109, 110]. This approach provides only a crude approximation of many-body effects in correlated materials. In the latter limit one applies exact diagonalization which provides an accurate description of atomic multiplet excitations. The spectral function of RIXS includes two optical processes. The excitation of a core electron to an empty valence state by absorption of an incident photon followed by a relaxation process, where a local valence electron deexcites into the core-hole by emission of a photon. The sequence of the RIXS process reads

$$\underbrace{|n\rangle}_{\text{initial state}} \rightarrow \underbrace{\hat{T}_I}_{\text{absorption}} \rightarrow \underbrace{|m\rangle}_{\text{intermediate state}} \rightarrow \underbrace{\hat{T}_E}_{\text{emission}} \rightarrow \underbrace{|f\rangle}_{\text{final state}},$$

where two transition operators couple the initial state $|n\rangle$ to a set of intermediate states $\{|m\rangle\}$ which are then coupled to a set of final states $\{|f\rangle\}$. The first transition operator \hat{T}_I encodes the excitation of the core electron to an empty valence state. The second transition operator \hat{T}_E encodes the relaxation process. The theoretical description of RIXS is given by Kramers-Heisenberg formula [111]

$$F_{\text{RIXS}}^{(n)}(\omega_{\text{in}}, \omega_{\text{out}}) = \sum_f \left| \sum_m \frac{\langle f | \hat{T}_E | m \rangle \langle m | \hat{T}_I | n \rangle}{\omega_{\text{in}} + E_n - E_m + i\Gamma_L} \right|^2 \delta(\omega_{\text{in}} - \omega_{\text{out}} + E_f - E_n), \quad (2.3)$$

where ω_{in} and ω_{out} are the energies of the incident and emitted photons, respectively. The states $|n\rangle$ and $|f\rangle$ are the initial and final states with energy E_n and E_f , respectively. Both states have n_v electrons in the valence orbitals and fully occupied core shells with n_p electrons. The set of intermediate states have ' n_v+1 ' electrons in its valence orbitals and ' n_p-1 ' electrons in its core shells, similar to XAS. Initial, intermediate and final states are eigenstates of the system. The transition operators \hat{T}_I and \hat{T}_E are approximated as dipoles $\hat{T}_D \sim \boldsymbol{\varepsilon} \cdot \hat{\mathbf{r}}$. The delta function corresponds to the energy conservation of the RIXS process. The term in the square of the absolute value propagates the state $\hat{T}_I |n\rangle$ within the system

$$G(\omega_{\text{in}}) = \sum_m \frac{1}{\omega_{\text{in}} + E_n - E_m + i\Gamma_L} |m\rangle \langle m|, \quad (2.4)$$

where Γ_L is the inverse of the lifetime (scattering rate) of the core-hole in the intermediate state.

2.1.4 Core-Level Spectral Functions in Thermal Equilibrium

The spectral functions provide the core-level spectra for a given initial state. By considering finite temperatures $T > 0$ K one has to take into account the thermodynamical ensemble that includes a set of initial states $\{|n\rangle\}$. The contribution of each initial state to the spectra is then weighted by the Boltzmann factor $e^{-E_n/k_B T}$ with the Boltzmann constant k_B . The thermal average is calculated by the trace of the density matrix resulting in

$$F_{\text{XPS/XAS/RIXS}}(\omega) = \sum_n \frac{e^{-E_n/(k_B T)}}{Z} \times F_{\text{XPS/XAS/RIXS}}^{(n)}(\omega), \quad (2.5)$$

with the partition function $Z = \sum_m e^{-E_m/(k_B T)}$. By summing over the weighted spectral functions $F_{\text{XPS/XAS/RIXS}}^{(n)}$ for different initial states we obtain the spectrum for finite temperatures.

2.2 Atomic Model

The atomic model describes an atom in a crystal host, in which the electron transfer between the atom and the host is neglected. The TM atom, which we call impurity

from now on, still feels an effective electric field generated by the rest of the crystal ions. This field is the so-called crystal field, which lifts the energy degeneracy of the partially filled valence orbitals of the impurity, see Fig. 2.1.

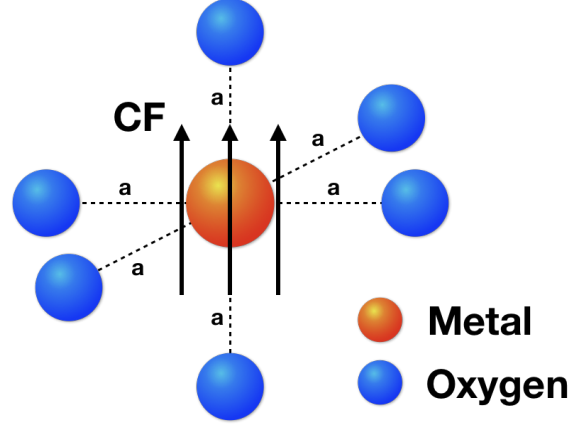


Figure 2.1: Decoupled atom in a octahedral crystal field, generated by neighboring oxygen ions.

The atomic model describes the intra-atomic interactions explicitly, which include the spin-orbit coupling on outer and inner (core) shells of the TM ion and the Coulomb multiplet interaction between electrons in the outer shell, e.g. the partially filled TM $3d$ shells. When a hole is created in the core shell, e.g. TM $1s$ or $2p$, by X-ray absorption or emission, the multiplet interaction between the outer and the excited core shell becomes important. In the formulas below (and in the rest of this chapter) we focus on TM $2p$ and $3d$ shells for simplicity. The (impurity) Hamiltonian of the atomic model reads

$$\hat{H}_{\text{imp}} = \sum_{\gamma\gamma'} h_{\gamma\gamma'}^{1P} \hat{d}_{\gamma}^{\dagger} \hat{d}_{\gamma'} + U_{dd} \sum_{\gamma>\gamma'} \hat{d}_{\gamma}^{\dagger} \hat{d}_{\gamma} \hat{d}_{\gamma'}^{\dagger} \hat{d}_{\gamma'} - U_{dc} \sum_{\gamma,\eta} \hat{d}_{\gamma}^{\dagger} \hat{d}_{\gamma} (1 - \hat{c}_{\eta}^{\dagger} \hat{c}_{\eta}) + \hat{H}_C. \quad (2.6)$$

Here, $\hat{d}_{\gamma}^{\dagger}$ (\hat{d}_{γ}) and \hat{c}_{η}^{\dagger} (\hat{c}_{η}) are creation (annihilation) operators for Ni $3d$ and $2p$ electrons, respectively. The indices γ and η denote the TM $3d$ and TM $2p$ orbitals including spin, respectively. The term $h_{\gamma\gamma'}^{1P}$ are the matrix elements of the single-particle Hamiltonian and reads

$$h_{\gamma\gamma'}^{1P} = \langle \phi_{\gamma} | \hat{O}^{1P} | \phi_{\gamma'} \rangle = \int d\mathbf{r} \phi_{\gamma}^*(\mathbf{r}) O^{1P}(\mathbf{r}) \phi_{\gamma'}(\mathbf{r}), \quad (2.7)$$

where \hat{O}^{1P} can be a crystal field or a spin-orbit coupling operator. The $\phi_{\gamma}(\mathbf{r}) = R_{\gamma}(r)Y_{\gamma}(\theta, \phi)$ are single-particle wave functions, e.g. atomic-like or Wannier functions, with radial $R_{\gamma}(r)$ and angular part $Y_{\gamma}(\theta, \phi)$. The isotropic part, i.e. the averaged Coulomb interaction, of the valence $3d$ - $3d$ (U_{dd}) and core-valence $2p$ - $3d$ (U_{dc}) interactions are shown explicitly in the Hamiltonian \hat{H}_{imp} . The core-valence

interaction U_{dc} becomes important in the case of an existing core-hole in the TM $2p$ shell. The term \hat{H}_C contains the multipole parts of the Coulomb interaction represented by higher-order Slater integrals. The energies of the TM $2p$ states are not included explicitly, because they provide just a constant energy shift.

2.2.1 Crystal Field Splitting

The crystal field lifts the degeneracy of the TM $3d$ states in TMOs and depends on the local symmetry (point group). The crystal field splitting is basis dependent, where the cubic harmonics d_i form a real-valued eigenbasis of the crystal field Hamiltonian. The cubic harmonics are expressed in terms of atomic-like orbitals $\phi_{kq} = R_k Y_{kq}$, where $k = 2$ is the angular momentum of the TM $3d$ shells and q the corresponding magnetic quantum number, and read

$$d_{3z^2-r^2} = \phi_{20}, \quad d_{x^2-y^2} = \frac{1}{\sqrt{2}}(\phi_{22} + \phi_{2-2})$$

$$d_{xy} = -\frac{i}{\sqrt{2}}(\phi_{22} - \phi_{2-2}), \quad d_{yz} = \frac{i}{\sqrt{2}}(\phi_{21} - \phi_{2-1}), \quad d_{zx} = -\frac{1}{\sqrt{2}}(\phi_{21} - \phi_{2-1}).$$

The ϕ_{kq} are complex-valued wave functions. A real-valued basis can be obtained by performing a transformation $\hat{H} = \hat{U} \hat{H} \hat{U}^\dagger$ within the irreducible representations of the diagonalized crystal field Hamiltonian. The diagonal elements are the eigenvalues of the crystal field splitting in the corresponding symmetry.

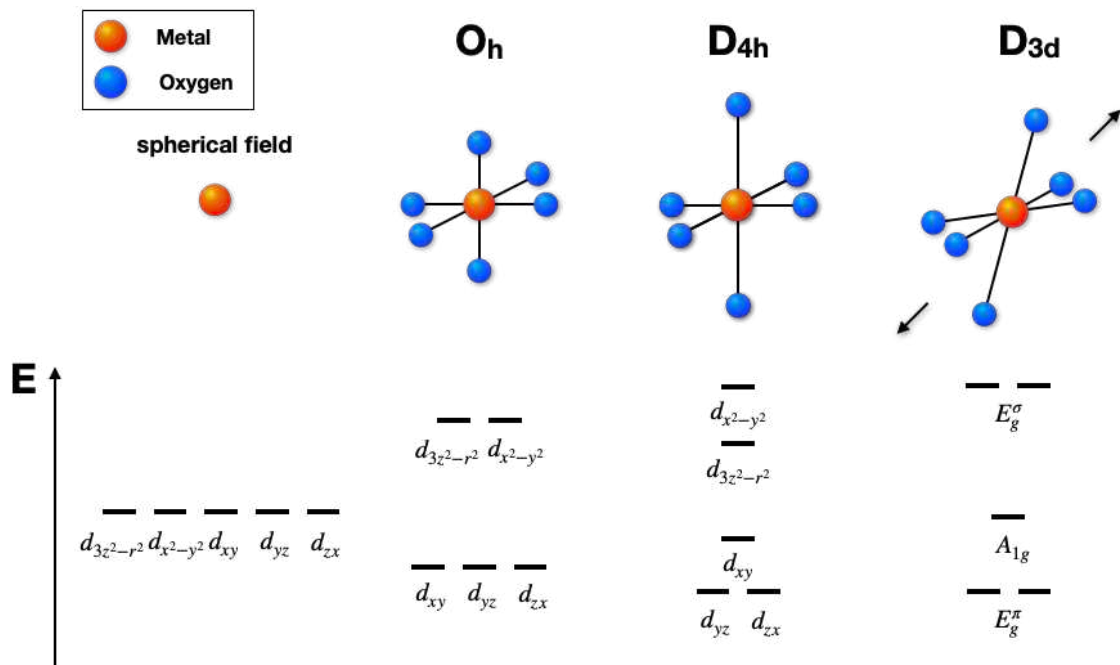


Figure 2.2: Schematic picture of the crystal field splitting for different point groups in the basis of cubic harmonics.

Fig. 2.2 shows a schematic picture of the energy splitting in different point groups. The left part shows an atom in a spherical field leaving the energies of the cubic harmonics degenerate. In the O_h point group the six nearest-neighbor oxygen ions are equally distributed along the orthogonal \mathbf{x} , \mathbf{y} and \mathbf{z} axes, see Fig. 2.1. The former degenerate energies split and form two irreducible representations, a two-fold E_g : $d_{3z^2-r^2}$, $d_{x^2-y^2}$ and a three-fold T_{2g} : d_{xy} , d_{yz} , d_{zx} . In the D_{4h} point group the oxygen ligands in \mathbf{z} -direction are further apart than the ions in \mathbf{x} - and \mathbf{y} -direction which results in an additional splitting of the energies. The lowest two-fold degenerate orbitals have E_g symmetry, followed by singlet B_{2g} , A_{1g} and B_{1g} states in ascending order of the energy. The right part of Fig. 2.2 includes the D_{3d} point group. In the D_{3d} point group the former cubic lattice is distorted in $[1,1,1]$ -direction. Thus, the initially diagonal crystal field Hamiltonian in the representation of cubic harmonics has off-diagonal elements. In the D_{3d} point group the triple-degenerate T_{2g} states split into double-degenerate E_g^π states and a singlet A_{1g} state. A derivation of the crystal field potential generated by a general electron density is given in Appendix. B.1.

Crystal Field Splitting in Octahedral Symmetry

Here we show the crystal field potential generated by neighboring oxygen ligands in the octahedral (O_h) point group. The electrons of the ligand ions are treated as point charges for simplicity. The crystal field potential takes the form [21, 22, 112]

$$O(\mathbf{r}) = v_{\text{cf}} = \frac{Ze^2}{a} \left\{ 6 + \frac{7}{2} \left(\frac{r}{a} \right)^4 \left[C_0^4(\theta, \phi) + \sqrt{\frac{5}{14}} (C_4^4(\theta, \phi) + C_{-4}^4(\theta, \phi)) \right] + \dots \right\}, \quad (2.8)$$

where $C_q^k(\theta, \phi) = \sqrt{\frac{4\pi}{2k+1}} Y_{kq}(\theta, \phi)$ are renormalized spherical harmonics, which can be regarded as spherical tensor operators, see Appendix. B.1. The application of $C_q^k(\theta, \phi)$ to a given atomic-like orbital can be understood as rotation of the orbital. The first term, corresponding to $k = 0$, provides no rotation of the atomic-like orbital due to its spherical character and thus provides a constant energy shift of the TM $3d$ levels. The renormalized spherical harmonic $C_0^4(\theta, \phi)$ in the second term corresponds to $k = 4$ which acts on the diagonal elements. The $C_4^4(\theta, \phi)$ and $C_{-4}^4(\theta, \phi)$ rotate the atomic-like orbitals in a way such that it connect states with magnetic quantum number $\Delta q = \pm 4$. The remaining terms with $k \geq 6$ do not affect the TM $3d$ energy levels due to the selection rules in the coupling of the spherical functions. This results in an energy splitting of the initially degenerate $3d$ levels into double-degenerate E_g states and triple-degenerate T_{2g} states represented with a historical parameter Dq . We rewrite Eq. 2.8 as

$$v_{\text{cf}} = 21Dq \left[C_0^4(\theta, \phi) + \sqrt{\frac{5}{14}} (C_4^4(\theta, \phi) + C_{-4}^4(\theta, \phi)) \right], \quad (2.9)$$

where we neglected the term corresponding to the constant energy shift and considered only the terms that induce the energy splitting of the initially degenerate orbitals. The energies of the E_g and T_{2g} states read

$$\varepsilon_d(E_g) = \varepsilon_d + 6Dq \quad (2.10)$$

$$\varepsilon_d(T_{2g}) = \varepsilon_d - 4Dq, \quad (2.11)$$

with the energy $\varepsilon_d = \varepsilon_0 + \frac{6Ze^2}{a}$ of the $3d$ orbitals in a spherical field, where ε_0 is the energy of the degenerate TM $3d$ orbitals without the octahedral crystal field. The induced energy splitting $10Dq$ is obtained from the radial parts of the wave functions. The parameter $10Dq$ is treated as an adjustable parameter in a conventional impurity model analysis of core-level spectra, while it is determined by first principle calculations in this study.

2.2.2 Spin-Orbit Coupling

Spin-orbit (SO) coupling is active for shells with angular momentum $l > 0$ and couples the orbital angular momentum with the spin momentum $\frac{1}{2}$. The SO coupling lifts the energy degeneracy within the shells. It becomes more effective in inner shells but decreases with increasing l , e.g. within TM $2p$ shells (≈ 10 eV), TM $3p$ shells (≈ 1 eV), TM $3d$ shells (≈ 0.01 eV). The SO coupling in the TM $2p$ core shells yields the splitting of the core-level spectra into two main parts, e.g. L_2 ($2p_{1/2}$) and L_3 -edge ($2p_{3/2}$) XAS, see Fig. 1.5. The SO Hamiltonian reads [21, 22]

$$\hat{H}_{\text{SO}} = \sum_l \zeta_l \sum_{m,m',s,s'} \langle lm, \frac{1}{2}s | \mathbf{l} \cdot \mathbf{s} | lm', \frac{1}{2}s' \rangle \hat{a}_{lms}^\dagger \hat{a}_{lm's'}, \quad (2.12)$$

where \mathbf{l} and \mathbf{s} are the orbital and spin angular momentum operators, respectively. The m and s are the magnetic quantum numbers of the orbital (l) and spin ($\frac{1}{2}$) angular momentum, respectively. The operators \hat{a}_{lms}^\dagger and \hat{a}_{lms} create and annihilate an electron with quantum numbers l , m and s , respectively. The spin-orbit coupling constant includes the radial part of SO coupling and reads [21]

$$\zeta_l = \frac{1}{2}\alpha^2 \int_0^\infty dr R_l^2(r) \frac{1}{r} \frac{dV}{dr} r^2. \quad (2.13)$$

The coupling constant represents the strength of the spin-orbit coupling (splitting) within the shells. α is the relativistic fine-structure constant. The electronic potential $V(r)$ with radial part $R_l(r)$ acts on electrons in the l -th shell. The dot-product $\mathbf{l} \cdot \mathbf{s}$ between the orbital and spin angular momentum operators can be expanded in terms of tensor operators, see Appendix. B.2. Using the Wigner-Eckhart theorem, the matrix elements in Eq. 2.12 can be expressed with $3J$ symbols and reduced

matrix elements of angular momentum and spin

$$\begin{aligned}
& \langle lm, \frac{1}{2}s | \mathbf{l} \cdot \mathbf{s} | lm', \frac{1}{2}s' \rangle \\
&= \langle l || \mathbf{l} || l \rangle \langle \frac{1}{2} || \mathbf{s} || \frac{1}{2} \rangle \sum_q (-1)^{q+l-m+\frac{1}{2}-s} \begin{pmatrix} l & 1 & l \\ -m & -q & m' \end{pmatrix} \begin{pmatrix} \frac{1}{2} & 1 & \frac{1}{2} \\ -s & q & s' \end{pmatrix} \\
&= (-1)^{l+\frac{1}{2}-m'-s} \sqrt{\frac{3}{2}l(l+1)(2l+1)} \begin{pmatrix} l & 1 & l \\ -m & m-m' & m' \end{pmatrix} \begin{pmatrix} \frac{1}{2} & 1 & \frac{1}{2} \\ -s & s-s' & s' \end{pmatrix}.
\end{aligned} \tag{2.14}$$

Here, we used the selection rules of the $3J$ symbols, see Eqs. B.13, B.14, and the definition of the reduced matrix elements (e.g. $\langle l || \mathbf{l} || l \rangle$) for angular momentum operators, see Eq. B.12. Since the SO coupling couples spin and orbital momentum, the SO coupling results in the total angular momentum quantum number $J = l + \frac{1}{2}$ which is a good quantum number for SO systems. A basis transformation to the J -basis can be obtained by either $3J$ symbols or equivalently by Clebsch-Gordan coefficients [113]. The Clebsch-Gordan coefficients can be given by the $3J$ symbols

$$\langle lm, \frac{1}{2}s | Jj \rangle = (-1)^{-l+\frac{1}{2}-j} \sqrt{2J+1} \begin{pmatrix} l & \frac{1}{2} & J \\ m & s & -j \end{pmatrix}, \tag{2.15}$$

where the total angular momentum J is in the range from $|l - \frac{1}{2}| \leq J \leq l + \frac{1}{2}$ in steps of one. The z -component j of the total angular momentum J is in the range of $-J, J+1, \dots, J$ for a given J . The diagonal Hamiltonian in the basis of the total angular momentum provides the energy splitting induced by the spin-orbit interaction [21]

$$\varepsilon(J) = \begin{cases} \zeta_l \cdot l/2 & (J = l + 1/2) \\ -\zeta_l \cdot (l+1)/2 & (J = l - 1/2). \end{cases} \tag{2.16}$$

2.2.3 Coulomb Interaction

Here we discuss the Coulomb interaction between electrons in partially filled TM $3d$ shells as well as between partially filled TM $3d$ and TM $2p$ shells. In the previous sections we introduced single-particle operators, e.g. crystal field and spin-orbit coupling. The Coulomb interaction between two electrons on the contrary contains two-particle operators. Matrix elements of a general two-particle operator \hat{O}^{2p} read

$$h_{ijkl}^{2p} = \langle ij | \hat{O}^{2p} | kl \rangle = \int \int d^3r d^3r' \Psi_i^*(\mathbf{r}) \Psi_j^*(\mathbf{r}') O^{2p}(\mathbf{r}, \mathbf{r}') \Psi_l(\mathbf{r}') \Psi_k(\mathbf{r}), \tag{2.17}$$

where Ψ are orbitals with index i, j, k, l . In the real space, the Coulomb interaction is represented as

$$O^{2p}(\mathbf{r}, \mathbf{r}') = \frac{1}{|\mathbf{r}' - \mathbf{r}|} = \sum_k \frac{r_{<}^k}{r_{>}^{k+1}} \sum_{q=-k}^k (-1)^q C_{-q}^k(\theta, \phi) C_q^k(\theta', \phi'), \tag{2.18}$$

where we factorized the potential into radial and angular parts in the basis of spherical harmonics, similar to the crystal field potential, see Appendix. B.1. The C_q^k are renormalized spherical harmonics, see Eq. B.4. The angles θ, ϕ and θ', ϕ' denote the position of particle 1 and 2, respectively. The $r_< = \min(r, r')$ and $r_> = \max(r, r')$ are the lesser and greater ones of r and r' . Here, we investigate the Coulomb interaction including its multipole effects. The Hamiltonian of the Coulomb interaction used in our calculations reads [21, 22]

$$\hat{H}_C = \hat{H}_{3d-3d} + \hat{H}_{2p-3d}, \quad (2.19)$$

where the Coulomb Hamiltonian includes a TM $3d-3d$ valence and a TM $2p-3d$ core-valence term. First, we focus on the TM $3d-3d$ valence interaction. We keep in mind that the orbital momentum of TM $3d$ shells is $l = 2$, thus we neglect the orbital momentum index. The Coulomb interaction of the $3d-3d$ valence interaction reads

$$\begin{aligned} \hat{H}_{3d-3d} &= \sum_{\substack{m_1 < m_2 \\ m_3 < m_4}} \left[\langle m_1 m_2 | \frac{1}{|\mathbf{r}' - \mathbf{r}|} | m_3 m_4 \rangle - \langle m_1 m_2 | \frac{1}{|\mathbf{r}' - \mathbf{r}|} | m_4 m_3 \rangle \right] \hat{d}_{m_1}^\dagger \hat{d}_{m_2}^\dagger \hat{d}_{m_4} \hat{d}_{m_3} \\ &= \sum_{k=2,4} F^k(3d, 3d) \sum_{\substack{m_1 < m_2 \\ m_3 < m_4}} \left[f^k(m_1 m_2, m_3 m_4) - f^k(m_1 m_2, m_4 m_3) \right] \hat{d}_{m_1}^\dagger \hat{d}_{m_2}^\dagger \hat{d}_{m_4} \hat{d}_{m_3}, \end{aligned} \quad (2.20)$$

where the first term is the direct and the second term is the exchange part of the Coulomb interaction. The monopole part $k = 0$ of the Coulomb interaction is already included in the isotropic part of the Coulomb interaction U_{dd} of the atomic model Hamiltonian, see Eq. 2.6. The $\hat{d}_{m_j}^\dagger$ (\hat{d}_{m_j}) are creation (annihilation) operators for TM $3d$ electrons with orbital momentum $l = 2$ and the corresponding magnetic quantum number m_j . We use Eq. 2.18 to factorize the potential into radial $F^k(3d, 3d)$, so-called Slater integrals, and angular parts

$$\begin{aligned} f^k(m_1 m_2, m_3 m_4) &= \delta_{s_1, s_3} \delta_{s_2, s_4} (-1)^{2+2-m_2-m_4} \langle 2 || \mathbf{C}^k || 2 \rangle \langle 2 || \mathbf{C}^k || 2 \rangle \\ &\times \begin{pmatrix} 2 & k & 2 \\ -m_1 & m_1 - m_3 & m_3 \end{pmatrix} \begin{pmatrix} 2 & k & 2 \\ -m_2 & m_2 - m_4 & m_4 \end{pmatrix}, \end{aligned} \quad (2.21)$$

where the spin s_i is conserved. Additionally, we used the Wigner-Eckhard theorem and the reduced matrix elements, see Appendix. B.3. Only terms with $k = 0, 2, 4$ satisfy the selection rules of the $3J$ symbols in the TM $3d-3d$ valence interaction. We note that m_4 and m_3 are interchanged in the exchange part of the Coulomb interaction. The radial parts $F^k(3d, 3d)$ are shown in Appendix. B.3.

The reformulation of the Coulomb interaction between the $2p-3d$ core-valence electrons into a numerically accessible form follows similarly to the valence-valence

interaction. The Hamiltonian of the core-valence interaction reads

$$\begin{aligned}
\hat{H}_{2p-3d} &= \sum_{\eta_1, m_1, \eta_2, m_2} \left[\langle \eta_1 m_1 | \frac{1}{|\mathbf{r}' - \mathbf{r}|} | \eta_2 m_2 \rangle - \langle \eta_1 m_1 | \frac{1}{|\mathbf{r}' - \mathbf{r}|} | m_2 \eta_2 \rangle \right] \hat{c}_{\eta_1}^\dagger \hat{c}_{\eta_2} \hat{d}_{m_1}^\dagger \hat{d}_{m_2} \\
&= F^2(2p, 3d) \sum_{\eta_1, m_1, \eta_2, m_2} f^2(\eta_1 m_1, \eta_2 m_2) \hat{c}_{\eta_1}^\dagger \hat{c}_{\eta_2} \hat{d}_{m_1}^\dagger \hat{d}_{m_2} \\
&\quad - \sum_{k=1,3} G^k(2p, 3d) \sum_{\eta_1, m_1, \eta_2, m_2} f^k(\eta_1 m_1, m_2 \eta_2) \hat{c}_{\eta_1}^\dagger \hat{c}_{\eta_2} \hat{d}_{m_1}^\dagger \hat{d}_{m_2},
\end{aligned} \tag{2.22}$$

where $\hat{d}_{m_j}^\dagger$ (\hat{d}_{m_j}) are creation (annihilation) operators for TM $3d$ electrons with orbital momentum l_i and magnetic quantum number m_j . The $\hat{c}_{\eta_j}^\dagger$ (\hat{c}_{η_j}) are creation (annihilation) operators for TM $2p$ core electrons with orbital momentum $l = 1$ and magnetic quantum number η_j . The first and second term represent the direct and exchange term of the core-valence Coulomb interaction, respectively. The monopole part is already considered in the averaged core-valence interaction U_{dc} in the atomic model Hamiltonian, see Eq. 2.6. The angular part of the direct core-valence interaction reads

$$\begin{aligned}
f^k(\eta_1 m_1, \eta_2 m_2) &= \delta_{s_1, s_3} \delta_{s_2, s_4} (-1)^{1+2-m_1-m_2} \langle 1 || \mathbf{C}^k || 1 \rangle \langle 2 || \mathbf{C}^k || 2 \rangle \\
&\quad \times \begin{pmatrix} 1 & k & 1 \\ -\eta_1 & \eta_1 - \eta_2 & \eta_2 \end{pmatrix} \begin{pmatrix} 2 & k & 2 \\ -m_1 & m_1 - m_2 & m_2 \end{pmatrix},
\end{aligned} \tag{2.23}$$

where the reduced matrix elements and a general form of the radial parts $F^k(2p, 3d)$ and $G^k(2p, 3d)$ are shown in Appendix. B.3.

In practice, the monopole parts of the Coulomb interaction are substantially screened from their bare values [30, 114]. The screened value of the averaged Coulomb interaction U_{dd} can be estimated by constrained random-phase approximation [115] (cRPA) or by fitting the experimental valence photoemission spectra. The averaged Coulomb interaction U_{dc} is hard to be determined in an *ab-initio* way. We fix $U_{dc} = x \times U_{dd}$ with $1.1 < x < 1.3$ in our core-level spectroscopy calculations, which is empirically established by comparison with various $2p$ core-level XPS and XAS spectra in $3d$ transition metal oxides [30, 50, 116–119]. In general the screening is less effective for higher-order Slater-integrals, and cRPA provides reasonable estimates for Hund's J which relates to the Slater integrals of the TM $3d$ – $3d$ valence interaction by $J = (F^2 + F^4)/14$. We use the relation $F^4 = 0.625 \times F^2$ [115, 120]. The multipole parts of the core-valence interaction are calculated with an atomic Hartree-Fock code [121]. The F_{pd}^2 , G_{pd}^1 and G_{pd}^3 values in the core-valence (p – d) interaction are scaled down between 20 - 30% of their actual values to simulate the effect of intra-atomic configuration interaction from higher basis configurations neglected in the atomic calculation [30, 122].

2.3 Cluster Model

The cluster model includes the electron transfer between impurity states and ligands. Thus, it is able to reproduce spectral features, arising from the charge transfer from neighboring ligands to the impurity, which are missing in the description of the atomic model.

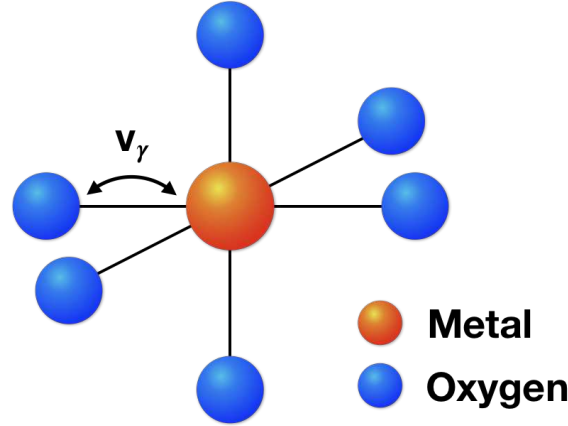


Figure 2.3: Cluster model with electron hopping between metal and ligand ions.

The MO_6 cluster includes the impurity with its six nearest-neighbor ligands in a three dimensional material, see Fig. 2.3. The Hamiltonian of the cluster model reads

$$\hat{H}_{\text{clu}} = \hat{H}_{\text{imp}} + \sum_{\gamma} \varepsilon_p(\gamma) \hat{b}_{\gamma}^{\dagger} \hat{b}_{\gamma} + \sum_{\gamma} v_{\gamma} (\hat{d}_{\gamma}^{\dagger} \hat{b}_{\gamma} + \hat{b}_{\gamma}^{\dagger} \hat{d}_{\gamma}), \quad (2.24)$$

where the first term is the impurity Hamiltonian \hat{H}_{imp} , see Eq. 2.6. The $\hat{b}_{\gamma}^{\dagger}$ and \hat{b}_{γ} are creation and annihilation operators of the ligand states with energy ε_p . The ligand states are described as molecular orbitals with same symmetry as the TM $3d$ states. There are as many possible molecular orbitals as TM $3d$ orbitals, thus we use the same index γ as for the TM $3d$ orbitals. The hopping amplitude v_{γ} between TM $3d$ states and the ligand states can be either tuned by hand or calculated by first principle calculations. We use cluster models constructed from *ab-initio* lattice models. By comparison with the more realistic Anderson impurity model one is able to identify non-local screening contributions missing in the cluster model.

2.3.1 Charge-Transfer Energy

The charge-transfer energy Δ_{CT} is the average energy cost of an electron transfer from a ligand state, e.g. O $2p$ state, to an impurity valence state, e.g. TM $3d$ state [22, 30],

$$\Delta_{\text{CT}} = E(|d^{n+1}\underline{L}\rangle) - E(|d^n\rangle). \quad (2.25)$$

Here n is the number of electrons in the TM $3d$ shell and \underline{L} denotes a hole in the O $2p$ shells. An estimate for the charge-transfer energy for n electrons in its valence orbitals is given by

$$\Delta_{\text{CT}} = \binom{n+1}{2} U_{dd} + (n+1)\epsilon_{d_0} - 35\epsilon_p - \left[\binom{n}{2} U_{dd} + n\epsilon_{d_0} - 36\epsilon_p \right], \quad (2.26)$$

where ϵ_{d_0} and ϵ_p are the average energies of the TM $3d$ states and the ligand $2p$ states, respectively. These energies provide a constant energy shift and can be determined by first principle calculations. U_{dd} is the isotropic part of the Coulomb interaction. By including the six neighboring oxygen ligands with fully filled O $2p$ shells in the $|d^n\rangle$ configuration, we obtain $6 \times 6 = 36$ electrons in the ligands. The charge-transfer energy can be used as a parameter to fix the energy splitting $\epsilon_{d_0} - \epsilon_p$, and hence fit the calculated spectra to the experiment.

2.3.2 Molecular Orbitals

The TM ion contains ten $3d$ orbitals including spin, whereas the oxygen ligands contain six O $2p$ orbitals resulting in a total of $10 + 36 = 46$ valence orbitals in the cluster. Describing all orbitals separately exponentially increases computationally costs [123]. Slater and Koster [124] showed that only some of the O $2p$ orbitals have a finite coupling intensity with the TM $3d$ orbitals. Thus, by creating molecular orbitals out of the coupling ones, the computational costs are substantially reduced. For example in the left panel of Fig. 2.4, the TM $3d_{x^2-y^2}$ orbital couples with only four neighboring O $2p$ orbitals, denoted as p^i . These can be determined by applying the symmetry operations of the TM $3d$ orbital to a given O $2p$ orbital. By superposing the O $2p$ orbitals obtained by the symmetry operations of the TM $3d$ orbital, one constructs a molecular orbital with the same symmetry as the TM $3d$ orbital. It turns out that out of the 46 ligand orbitals, just 20 orbitals couple to the TM $3d$ orbitals. In O_h point group symmetry this results to three (with spin: six) T_{2g} symmetric and two (with spin: four) E_g symmetric molecular orbitals. The molecular orbitals can be used as basis functions. The coupling between molecular orbitals and the TM $3d$ orbitals results in a bonding and anti-bonding solution of the Hamiltonian. All other possible superpositions of O $2p$ orbitals result in so-called non-bonding states which have no finite coupling. Thus, for creating an effective model Hamiltonian, the non-bonding states can be neglected.

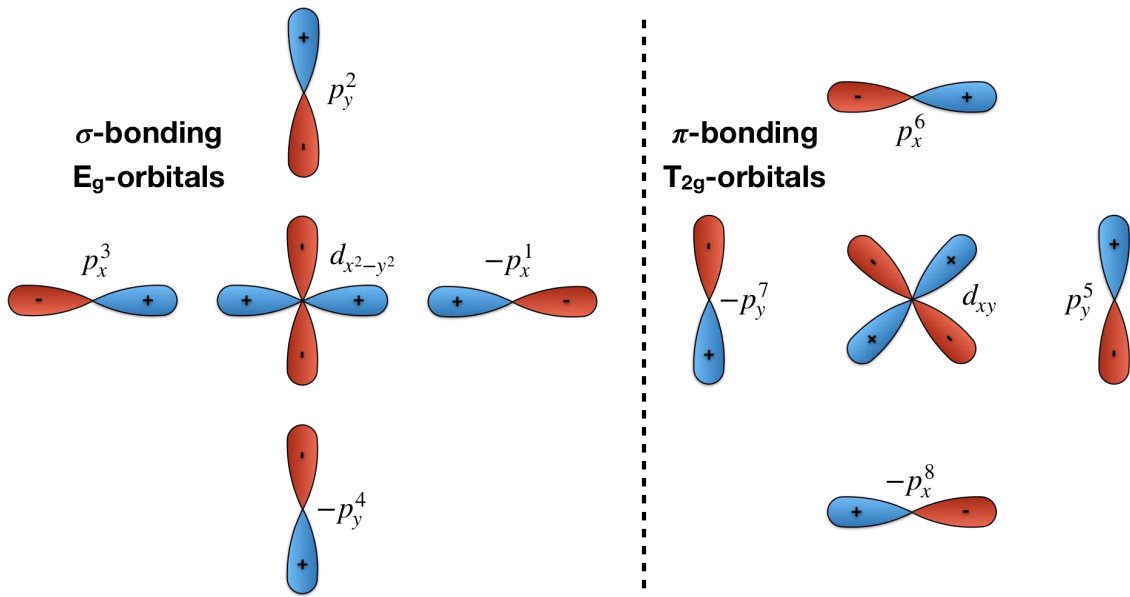
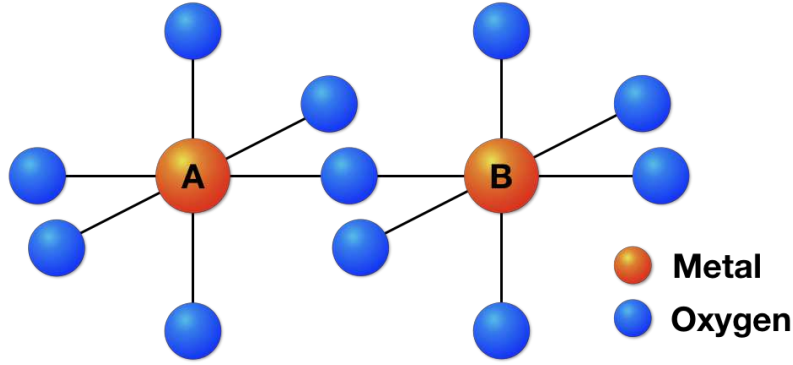


Figure 2.4: Bonding molecular orbitals with E_g (left) and T_{2g} (right) symmetry in the xy-plane. Figure adapted from [123].

Fig. 2.4 shows the bonding solution between the TM $3d$ orbitals and the molecular orbitals in E_g (left) and T_{2g} (right) symmetry. The E_g orbitals form so-called σ -bonds, whereas the T_{2g} orbitals form so-called π -bonds. The hopping amplitude between the TM $3d$ orbitals and the O $2p$ orbitals can be expressed by the sum of the Slater-Koster parameters $pd\sigma$ and $pd\pi$ [124] for atomic orbitals. The σ -bonds have usually a greater overlap and thus a larger hopping amplitude than the π -bonds.

2.4 Double-Cluster Model

Initially the multi-site cluster model was introduced by Veenendal and Sawatzky to study core-level XPS in cuprates and NiO [33]. The double-cluster model is the smallest variant of a multi-site cluster model and consists of a M_2O_{11} cluster with two metallic sites and eleven surrounding ligand ions, see Fig. 2.5. The oxygen orbitals are included as molecular orbitals, similar to the single-cluster model description. Out of the ligand orbitals five (with spin: ten) molecular orbitals can be formed. Although the global symmetry of the molecular orbitals is broken by inclusion of just one neighboring cluster, the approach leads to reasonable results by tuning the hopping parameters between the TM ions and the molecular orbitals as well as between the different TM ions.

Figure 2.5: M_2O_{11} cluster.

Here we adapt the full Coulomb-multiplet form of the double-cluster model, which was employed by Agui *et al* to study Ti L_3 -RIXS in $FeTiO_3$ [125], and subsequently applied to Ni L_3 -XAS and RIXS analyzes of $RNiO_3$ [108]. The Hamiltonian of the double-cluster model reads

$$\begin{aligned} \hat{H}_{dc} = & \hat{H}_{imp}^{(A)} + \hat{H}_{imp}^{(B)} + \hat{H}_{IM} \\ & + \sum_{\gamma} \varepsilon_{\gamma} \hat{b}_{\gamma}^{\dagger} \hat{b}_{\gamma} + \sum_{i \in \{A, B\}} \sum_{\gamma} v_{i, \gamma} (\hat{d}_{i, \gamma}^{\dagger} \hat{b}_{\gamma} + \hat{b}_{\gamma}^{\dagger} \hat{d}_{i, \gamma}), \end{aligned} \quad (2.27)$$

where $\hat{H}_{imp}^{(A)}$ and $\hat{H}_{imp}^{(B)}$ are the impurity Hamiltonians, see Eq. 2.6, for impurities A and B, respectively. The ε_{γ} are the energies of the molecular orbitals with index γ denoting orbital and spin. The $\hat{d}_{i, \gamma}^{\dagger}$ ($\hat{d}_{i, \gamma}$) and $\hat{b}_{\gamma}^{\dagger}$ (\hat{b}_{γ}) are creation (annihilation) operators for TM $3d$ electrons on site $i = \{A, B\}$ and electrons on the molecular orbitals, respectively. The metal-ligand hopping amplitudes $v_{i, \gamma}$ are constructed by Slater-Koster parameters which can be obtained from first principle calculations.

The double-cluster model incorporates a metal-metal charge-transfer (MMCT), by the inclusion of inter-metal hopping between the TMs on site A and TM on site B. The Hamiltonian of the inter-metal hopping reads

$$\hat{H}_{IM} = \sum_{\gamma, \gamma'} u_{\gamma \gamma'} (\hat{d}_{A, \gamma}^{\dagger} \hat{d}_{B, \gamma'} + \hat{d}_{B, \gamma'}^{\dagger} \hat{d}_{A, \gamma}), \quad (2.28)$$

where the indices γ and γ' denote the orbital and spin of the TM on site A and the TM on site B, respectively. The $u_{\gamma \gamma'}$ is the hopping amplitude between the two TM sites. Although the double-cluster model incorporates MMCT, only a single metal-metal bond is considered due to the symmetry of the double-cluster. This simplification needs an adjustment of the MMCT amplitude obtained by first principle calculations, to mimic contributions of the other five bonds in a real crystal. Thus, the MMCT hopping amplitude is tuned to reproduce experimental core-level spectra.

2.5 Anderson Impurity Model

The Anderson impurity model (AIM) is a single-impurity model and takes into account the hybridization, i.e. hopping, between an impurity embedded in a crystal host and the electronic states of the host, so-called bath states, see Fig. 2.6. The AIM allows to include unbound electron-hole pair excitations which propagate in the crystal host. These unbound excitations cannot be captured by a cluster model analysis. We employ two kinds of AIMs in this thesis: (1) Within first principle DMFT calculations, where a lattice model is mapped onto the AIM self-consistently. This AIM contains just valence states around the Fermi energy E_F . (2) Within the calculation of spectral functions, where the AIM is extended by core orbitals to explicitly take into account the core-valence interaction.

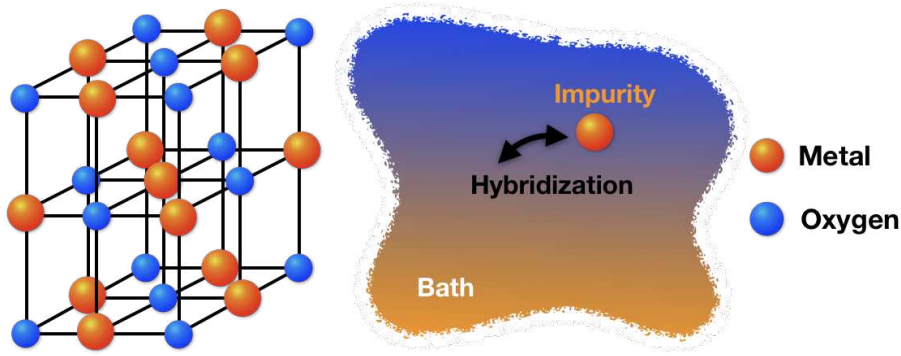


Figure 2.6: Anderson impurity model with hybridization to the crystal host bath states. Figure adapted from [21].

The AIM Hamiltonian consists of the on-site term, i.e. impurity, and the hybridization term, which includes the energy of bath states. The Hamiltonian reads

$$\hat{H}_{\text{AIM}} = \hat{H}_{\text{imp}} + \hat{H}_{\text{hyb}}, \quad (2.29)$$

where the impurity term is equivalent to the Hamiltonian of the atomic model, see Eq. 2.6. The hybridization term reads [1]

$$\begin{aligned} \hat{H}_{\text{hyb}} &= \hat{H}_{\text{host}} + \hat{H}_{\text{imp-host}} \\ &= \sum_{\alpha, \gamma \sigma} \varepsilon_{\alpha, \gamma \sigma} \hat{v}_{\alpha, \gamma \sigma}^\dagger \hat{v}_{\alpha, \gamma \sigma} + \sum_{\alpha, \gamma \sigma} V_{\alpha, \gamma \sigma} (\hat{d}_{\gamma \sigma}^\dagger \hat{v}_{\alpha, \gamma \sigma} + \hat{v}_{\alpha, \gamma \sigma}^\dagger \hat{d}_{\gamma \sigma}). \end{aligned} \quad (2.30)$$

The first term \hat{H}_{host} represents the energies of the bath states $\varepsilon_{\alpha, \gamma \sigma}$. The operator $\hat{v}_{\alpha, \gamma \sigma}^\dagger$ ($\hat{v}_{\alpha, \gamma \sigma}$) creates (annihilates) an electron of the bath state with energy $\varepsilon_{\alpha, \gamma \sigma}$. The index α denotes the energy levels for each orbital γ and spin σ . The second term $\hat{H}_{\text{imp-host}}$ contains the hybridization between the impurity and bath states. The hybridization amplitude $V_{\alpha, \gamma \sigma}$ relates to the hybridization function $\Delta_{\gamma \sigma}(\varepsilon)$.

2.5.1 Hybridization Function

The hybridization function $\Delta_{\gamma\sigma}(\varepsilon)$ is the core element of the Anderson impurity model. It describes a density which encodes the hopping amplitude between the impurity states and the bath states. The bath consists of auxiliary states which describe the electronic structure of the rest of the crystal host, see Fig. 2.7.

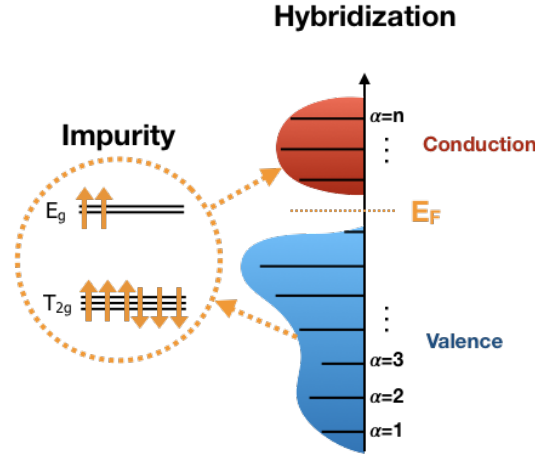


Figure 2.7: Anderson impurity model for TM $3d$ states with a schematic hybridization intensity in continuous and discrete (black bars) form.

The hybridization function of the Anderson impurity model is often assumed to be semi-elliptical or triangular shaped for spectroscopy calculations [30]. This assumption does not reflect the electronic structure of a real material. The hybridization function obtained by first principle calculations, describes a realistic hopping between impurity and bath states. We distinguish two parts of the hybridization function. The hybridization intensities above E_F are denoted as conduction, whereas the hybridization intensities below E_F are denoted as valence. The hybridization function is a general function of energy ε for each valence orbital γ of the impurity with spin σ

$$\Delta_{\gamma\sigma}(\varepsilon) = \sum_{\alpha} \frac{V_{\alpha,\gamma\sigma}^2}{\varepsilon^+ - \varepsilon_{\alpha,\gamma\sigma}}. \quad (2.31)$$

Here, $\Delta_{\gamma\sigma}(\varepsilon)$ describes a continuous hybridization function with hopping intensities (amplitudes) $V_{\alpha,\gamma\sigma}^2$. The energy $\varepsilon^+ = \varepsilon + i0^+$ shifts the poles to the lower half of the complex plane. The hybridization function, which is continuous in real materials, takes the form of a Dirac delta function for the special case of the cluster model and reads

$$\Im\Delta_{\gamma\sigma}(\varepsilon) = -\pi|V_{\gamma\sigma}|^2 \times \delta(\varepsilon - \varepsilon_{\gamma\sigma}^p), \quad (2.32)$$

where $V_{\gamma\sigma}$ is the hopping amplitude between the E_g and T_{2g} orbitals of the TM ion, denoted by γ with spin σ , and its surrounding molecular orbitals with energy $\varepsilon_{\gamma\sigma}^p$.

2.6 First Principle Calculations

First principle calculations are used to calculate the electronic structure of real materials with almost no parameters. First we use density functional theory to create Bloch functions which describe the electronic structure of a periodic lattice without explicit local interactions. The Bloch functions are transformed into Wannier functions which are atomic-like orbitals centered on the lattice sites. We construct a tight-binding representation in the Wannier basis which contains the hopping amplitudes between Wannier orbitals on the same and on different lattice sites. Then we construct a lattice model with local interactions, e.g. dp model, where we add the Coulomb interaction U_{dd} to the TM $3d$ valence orbitals which is active only locally on the lattice sites. The U_{dd} can be evaluated by e.g. constrained random phase approximation (cRPA) [115]. There are two approaches to calculate electronic structure of correlated materials in general; Green's function based methods and wave function based methods. Green's function based methods work with correlation functions directly, whereas wave function based methods use the interacting Hamiltonian in terms of a resolvent to calculate the electronic properties. The resolvent formalism is computationally more challenging because it uses the description of many-body wave functions. But the resolvent formalism is applicable for the impurity models we are using for the calculation of core-level X-ray spectral functions. To calculate the electronic structure from lattice based models we use dynamical mean-field theory (DMFT) [13]. DMFT is a Green's function based method which maps the lattice model with local interaction onto an Anderson impurity model.

2.6.1 Density Functional Theory

Density functional theory (DFT) is a powerful method to calculate the electronic structure of a many-body system. DFT allows the calculation of basic characteristics of interacting systems, such as charge and spin density on the ground state level, by mapping it onto an effective non-interacting problem. The experience shows that DFT band structures provide an excellent description of weakly correlated materials as well as a good starting point for many-body treatment of strongly correlated materials. With this methodological simplification it is possible to study real materials in continuous space where only the positions of atomic nuclei have to be provided as input. DFT for solids was introduced by Hohenberg and Kohn [7] as well as Kohn and Sham [8]. They showed that the ground state of the N -electron Schrödinger equation is uniquely determined by a non-interacting electron density $n(\mathbf{r})$ [7, 22]:

- There is a one-to-one mapping between an external potential $V(\mathbf{r})$ and the ground state particle density $n(\mathbf{r})$.
- The ground state of a system characterized by the external potential $V(\mathbf{r})$

can be obtained by the minimization of a functional $E[n(\mathbf{r})]$.

The energy of the ground state can be calculated by the variational principle

$$\left. \frac{\partial E[n(\mathbf{r})]}{\partial n(\mathbf{r})} \right|_{n(\mathbf{r})=n_0(\mathbf{r})} = 0, \quad (2.33)$$

with the use of self-consistent single-particle Kohn-Sham equations. The Ansatz $n(\mathbf{r}) = \sum_i f_i |\Psi_i(\mathbf{r})|^2$ is used, together with constraining the particle number conservation $N = \int n(\mathbf{r}) d^3r$ and the mutual orthogonality of the single-particle wave functions $\Psi_i(\mathbf{r})$. The energy functional can be written as

$$E[n(\mathbf{r})] = T[n(\mathbf{r})] + \frac{e^2}{2} \int \int \frac{n(\mathbf{r})n(\mathbf{r}')}{|\mathbf{r} - \mathbf{r}'|} d^3r d^3r' + \int n(\mathbf{r})V(\mathbf{r})d^3r + E^{xc}[n(\mathbf{r})], \quad (2.34)$$

where $T[n(\mathbf{r})]$ is the kinetic energy of non-interacting electrons. The second term is the Hartree energy with electrostatic interaction within the electron density. The interaction with an external potential $V(\mathbf{r})$ generated by positively charged nuclei is included in the third term. The positions of the nuclei are usually provided by experiment, but can also be evaluated by minimization of the total energy, see Eq. 2.36 below. The exchange and correlation functional $E^{xc}[n(\mathbf{r})] = \int n(\mathbf{r})\varepsilon_{xc}[n(\mathbf{r})]d^3r$ corrects the energy of the non-interacting electrons. If $E^{xc}[n(\mathbf{r})]$ was exact, DFT would provide the real electronic density of a material. Unfortunately the exact solution is not known, therefore several approximations exist, e.g. local density approximation (LDA) or generalized gradient approximation (GGA). Varying the energy functional of Eq. 2.34 results in

$$\left[-\frac{\hbar^2}{2m}\nabla^2 + V(\mathbf{r}) + \underbrace{e^2 \int \frac{n(\mathbf{r}')}{|\mathbf{r} - \mathbf{r}'|} d^3r'}_{V_{\text{eff}}} + \mu_{xc}[n(\mathbf{r})] \right] \Psi_i(\mathbf{r}) = \varepsilon_i \Psi_i(\mathbf{r}), \quad (2.35)$$

where $\mu_{xc}[n(\mathbf{r})] = \frac{\partial E^{xc}[n(\mathbf{r})]}{\partial n(\mathbf{r})}$. This equation is the Kohn-Sham equation which can be read as a single-particle Schrödinger equation with kinetic term and effective potential V_{eff} . The total energy is obtained by multiplying Eq. 2.35 by $\Psi_i^*(\mathbf{r})$, and integrating over the occupied states with subtraction of Eq. 2.34. The second Kohn-Sham equation reads

$$E = \sum_i \varepsilon_i - \frac{e^2}{2} \int \int \frac{n(\mathbf{r})n(\mathbf{r}')}{|\mathbf{r} - \mathbf{r}'|} d^3r d^3r' + \int n(\mathbf{r}) [\varepsilon_{xc}[n(\mathbf{r})] - \mu_{xc}[n(\mathbf{r})]] d^3r. \quad (2.36)$$

The Kohn-Sham equation can be solved self-consistently, starting with a test density $n(\mathbf{r})$. By using a proper approximation for $E^{xc}[n(\mathbf{r})]$, e.g. LDA, one can calculate the effective potential V_{eff} . Then the wave functions $\Psi_i(\mathbf{r})$ can be evaluated, resulting in a new density. From that one can calculate the total energy. To stabilize the iterative cycle one mixes the input density with the output density of previous iterations to generate a new density for the next cycle. We use WIEN2k [126] with an LSDA potential for band structure calculations.

2.6.2 Bloch Functions and Band Structure

The Kohn-Sham equation has the form of a Schrödinger equation for non-interacting electrons [22, 115]

$$-\frac{1}{2}\nabla^2\Psi(\mathbf{r}) + V_{\text{eff}}(\mathbf{r})\Psi(\mathbf{r}) = \varepsilon\Psi(\mathbf{r}). \quad (2.37)$$

This equation represents an eigenvalue problem for a Hermitian Hamiltonian $\hat{H} = -\frac{1}{2}\nabla^2 + V_{\text{eff}}(\mathbf{r})$, if the wave function $\Psi(\mathbf{r})$ has periodic boundary conditions at infinity and is normalizable. If the potential obeys translational symmetry

$$V_{\text{eff}}(\mathbf{r}) = V_{\text{eff}}(\mathbf{r} + \mathbf{R}), \quad (2.38)$$

where \mathbf{R} is the Bravais lattice vector, then the Bloch theorem states that the eigenfunctions can be written in terms of Bloch wave functions

$$\Psi_{n,\mathbf{k}}(\mathbf{r}) = e^{-i\mathbf{k}\cdot\mathbf{r}}u_{n,\mathbf{k}}(\mathbf{r}). \quad (2.39)$$

The function $u_{n,\mathbf{k}}(\mathbf{r})$ is an \mathbf{r} -periodic function. The index n denotes discrete bands and \mathbf{k} is a continuous vector from the first Brillouin zone. The translational operator $\hat{T}_{\mathbf{R}_l}$ commutes with the Hamiltonian \hat{H} and thus, the eigenstates of \hat{H} can be chosen to be eigenstates of $\hat{T}_{\mathbf{R}_l}$. $\hat{T}_{\mathbf{R}_l}$ shifts the Bloch wave function by the Bravais lattice vector \mathbf{R}_l to the l -th unit cell in the Bravais lattice which results into the same Bloch function with an additional phase factor

$$\hat{T}_{\mathbf{R}_l}\Psi_{n,\mathbf{k}}(\mathbf{r}) = \Psi_{n,\mathbf{k}}(\mathbf{r} - \mathbf{R}_l) = e^{i\mathbf{k}\cdot\mathbf{R}_l}\Psi_{n,\mathbf{k}}(\mathbf{r}). \quad (2.40)$$

By applying the eigenfunctions $\Psi_{n,\mathbf{k}}(\mathbf{r})$ of the translational operator into the Schrödinger equation one obtains

$$\frac{1}{2}(-i\nabla - \mathbf{k})^2u_{n,\mathbf{k}}(\mathbf{r}) + V_{\text{eff}}(\mathbf{r})u_{n,\mathbf{k}}(\mathbf{r}) = \varepsilon_{n,\mathbf{k}}u_{n,\mathbf{k}}(\mathbf{r}), \quad (2.41)$$

where the eigenvalues $\varepsilon_{n,\mathbf{k}}$ for band n are continuous and periodic in \mathbf{k} . The band structure is formed by the plotted eigenvalues $\varepsilon_{n,\mathbf{k}}$.

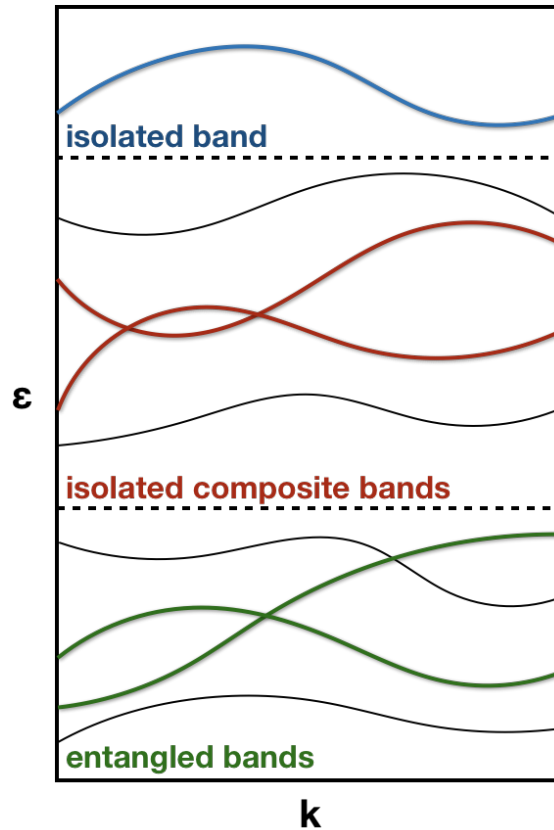


Figure 2.8: Classification of band types.

Fig. 2.8 shows a cartoon plot of eigenvalues $\varepsilon_{n,\mathbf{k}}$ forming different types of bands, where we distinguish three different kinds. The top panel of Fig. 2.8 shows an isolated band, which does not cross any other band at any \mathbf{k} : $\varepsilon_{n-1,\mathbf{k}} < \varepsilon_{n,\mathbf{k}} < \varepsilon_{n+1,\mathbf{k}}$ for each \mathbf{k} . In the center panel of Fig. 2.8 there are composite bands, which cross each other, but do not cross any other band at any \mathbf{k} : $\varepsilon_{n_{\min}-1,\mathbf{k}} < \varepsilon_{n_{\min},\mathbf{k}} \leq \varepsilon_{n_{\max},\mathbf{k}} < \varepsilon_{n_{\max}+1,\mathbf{k}}$. If bands do not obey the above criteria and cross other bands, they are called entangled bands, as shown at the bottom panel of Fig. 2.8 [22, 115].

2.6.3 Wannier Functions

Wannier functions are commonly used to link first principle band structure calculations with lattice models [12, 22, 115]. They can be seen as natural extension of atomic orbitals into the concept of solids. We use atomic-centered Wannier functions, describing a basis set which is localized and orthonormal on lattice sites. The shapes of the Wannier functions are invariant under lattice translations $T_{\mathbf{R}}$, i.e. the Wannier functions are centered on each atom forming a localized orbital. Wannier functions are constructed out of Bloch wave functions. Here we describe the construction of maximally localized Wannier functions, where the spread of the Wannier function from the center of mass at each lattice site is minimized. The

Wannierization, i.e. construction procedure of Wannier functions, depends on the band type in the band structure, see Fig. 2.8.

Wannier functions $w_n(\mathbf{r} - \mathbf{R}_l)$, obtained from isolated bands with index n , can be seen as a Fourier transform of the Bloch wave function $\Psi_{n,\mathbf{k}}(\mathbf{r}) = e^{i\mathbf{k}\mathbf{r}} u_{n\mathbf{k}}(\mathbf{r})$ [115, 127].

$$w_n(\mathbf{r} - \mathbf{R}_l) = \frac{V}{(2\pi)^3} \int_{\text{BZ}} d\mathbf{k} e^{-i\mathbf{k}\cdot\mathbf{R}_l} \Psi_{n,\mathbf{k}}(\mathbf{r}). \quad (2.42)$$

We Fourier transform the vector \mathbf{k} of the first Brillouin zone (BZ) to Bravais lattice vectors \mathbf{R}_l . The Fourier transformation is not unique, the freedom in choice of the Wannier function corresponds to the freedom of choice in the phases of Bloch orbitals as function of the wave vector \mathbf{k} [127]. Therefore a particular choice of the phases, a so-called gauge, can be realized by a gauge transformation $\Psi_{n,\mathbf{k}} \rightarrow e^{i\phi(\mathbf{k})} \Psi_{n,\mathbf{k}}$. This transformation preserves the center of mass of the Wannier functions but not the spread Ω , see Eq. 2.47 below. The inverse transformation results into Bloch functions $\Psi_{n,\mathbf{k}}(\mathbf{r})$ and reads

$$\Psi_{n,\mathbf{k}}(\mathbf{r}) = \sum_{\mathbf{R}_l} e^{i\mathbf{k}\cdot\mathbf{R}_l} w_n(\mathbf{r} - \mathbf{R}_l). \quad (2.43)$$

The orthogonality of the Wannier functions is ensured by the transformation properties of Bloch functions under lattice translations.

For composite bands, a unitary transformation for a set of isolated bands has to be determined [22, 115]

$$\mathbf{w}(\mathbf{r} - \mathbf{R}_l) = \frac{V}{(2\pi)^3} \int_{\text{BZ}} d\mathbf{k} \mathbf{U}(\mathbf{k}) \Psi_{\mathbf{k}}(\mathbf{r}), \quad (2.44)$$

where $\mathbf{w}_n(\mathbf{r} - \mathbf{R}_l)$ and $\Psi_{n,\mathbf{k}}(\mathbf{r})$ are vectors of functions corresponding to composite bands as entries

$$\mathbf{w} = \begin{pmatrix} w_{n_{min}} \\ \vdots \\ w_{n_{max}} \end{pmatrix}, \quad \Psi_{\mathbf{k}} = \begin{pmatrix} \Psi_{n_{min},\mathbf{k}} \\ \vdots \\ \Psi_{n_{max},\mathbf{k}} \end{pmatrix}. \quad (2.45)$$

The unitary matrix $\mathbf{U}(\mathbf{k})$ mixes the bands at a given wave vector \mathbf{k} . Here, the transformation does not preserve the center of mass of the individual Wannier functions, but preserves the sum of the center of masses of the composite Wannier functions, modulo the lattice vector. If $\mathbf{U}(\mathbf{k})$ can be chosen such that the product is an analytic and periodic function of \mathbf{k} , one obtains exponentially localized Wannier functions. The inverse transformation results in quasi-Bloch states and reads [22, 115]

$$\tilde{\Psi}_{\mathbf{k}}(\mathbf{r}) = \sum_{\mathbf{R}_l} e^{i\mathbf{k}\cdot\mathbf{R}_l} \mathbf{w}(\mathbf{r} - \mathbf{R}_l). \quad (2.46)$$

These quasi-Bloch wave functions preserve the transformation properties under lattice translations, but are not solutions of the Schrödinger equation anymore.

To obtain maximally localized Wannier functions for isolated and composite bands, one minimizes the spread of the Wannier functions. The spread functional reads [127]

$$\Omega = \sum_n [\langle r^2 \rangle_n - \bar{\mathbf{r}}_n^2], \quad (2.47)$$

with the center of mass for each Wannier function n

$$\bar{\mathbf{r}}_n = i \frac{V}{(2\pi)^3} \int_{\text{BZ}} d\mathbf{k} \langle w_{n,\mathbf{k}} | \nabla_{\mathbf{k}} | w_{n,\mathbf{k}} \rangle, \quad (2.48)$$

and the second moment

$$\langle r^2 \rangle_n = \frac{V}{(2\pi)^3} \int_{\text{BZ}} d\mathbf{k} |\nabla_{\mathbf{k}} w_{n,\mathbf{k}}|^2. \quad (2.49)$$

The derivation for calculating the spread functional Ω can be found in [127]. Creating Wannier functions for entangled bands fail by using only a unitary transformation. Thus, a disentanglement procedure was introduced by Souza, Marzari and Vanderbilt [128]. It also uses the minimization of the spread but in a proper subspace with fixed energy window, which encompasses the bands of interest. The obtained functions are then not Wannier functions anymore in the common sense, but they are Wannier-like functions, forming an orthonormal, localized basis set of the same Bloch subspace from which they were constructed. An important aspect of Wannier functions is, that an increase of localization can be obtained by increasing the energy window in the Wannierization, i.e. by taking more bands into account.

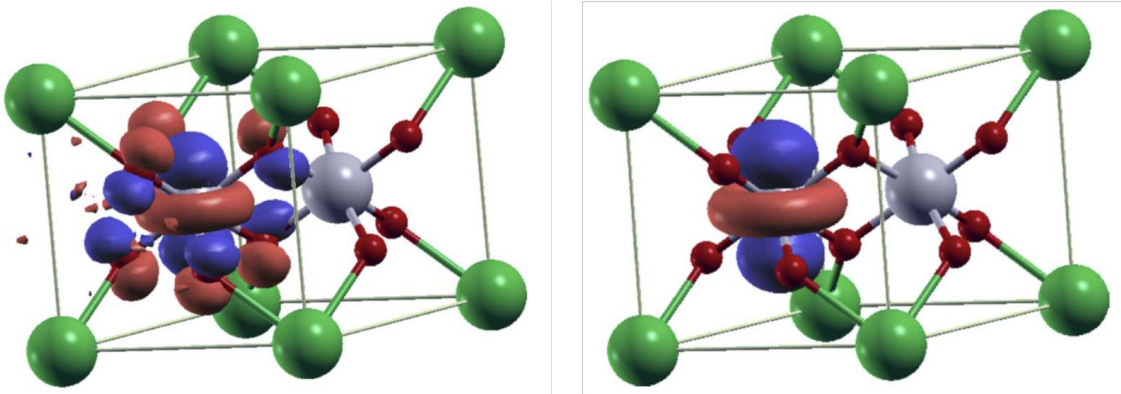


Figure 2.9: The A_{1g} Wannier function in the T_{2g} -only model (left) and T_{2g} -p model (right) of SrRu_2O_6 . The gray, red, and green circles represent Ru, O, and Sr atoms, respectively. The Wannier function in the T_{2g} -only model has a considerable weight on neighboring O sites. Figure and caption taken from [129].

Fig. 2.9 shows the Ru A_{1g} Wannier function of SrRu_2O_6 for two models, T_{2g} -only with six orbitals and T_{2g} - p model with explicit presence of the O $2p$ orbitals [129]. In the T_{2g} -only model the Ru A_{1g} Wannier function has a considerable weight on the O sites, whereas the Ru A_{1g} Wannier function of the T_{2g} - p model is more localized on the Ru site. For Wannier calculations we usually consider a full d - p model and use the WANNIER90 [130] and WIEN2WANNIER [131] packages included in WIEN2k [126].

2.6.4 Tight-Binding Representation

In solid state physics one is particularly interested in the physics happening in the low energy regime, i.e. around Fermi Energy E_F . Thus one limits oneself to proper model Hamiltonians capturing just the effects of interest. Tight-binding is a widely used representation, where only partially filled valence orbitals are taken into account explicitly. These are for example Wannier functions, generated by DFT and the Wannierization procedure.

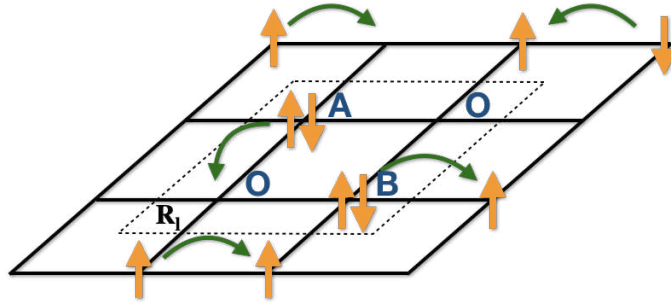


Figure 2.10: Tight-binding model with four atoms (TM A, TM B and $2 \times \text{O}$) per unit cell \mathbf{R}_l .

Fig. 2.10 shows a lattice with four atoms per unit cell. The unit cell is denoted by the Bravais lattice vector \mathbf{R}_l . Each orbital on a lattice site (TM A, TM B, or O) can either be unoccupied, occupied by up or down spin σ , or doubly occupied with up and down spin. The tight-binding representation lacks the local interaction, thus multiple electrons on the same site do not interact with each other. The energies of O $2p$ orbitals in TMOs are often near E_F , thus we include O $2p$ orbitals within our calculations to provide a realistic description of the electronic structure near E_F . The tight-binding representation contains the electron hopping between sites in the periodic lattice structure, see Fig. 2.10. Thus, the Hamiltonian of the tight-binding representation reads

$$\hat{H}_{\text{TB}} = - \sum_{i,j,\sigma} h_{ij} \hat{c}_{i,\sigma}^\dagger \hat{c}_{j,\sigma}, \quad (2.50)$$

where $\hat{c}_{i,\sigma}^\dagger$ and $\hat{c}_{j,\sigma}$ are creation and annihilation operators for electrons. The indices i and j denote the unit cells \mathbf{R}_i and \mathbf{R}'_j in the lattice and as well as the orbitals γ

and γ' of the atoms in the unit cells, respectively. The index σ denotes the spin, for simplicity we drop it in the formulas below. The hopping amplitudes h_{ij} are evaluated from the matrix elements of the Hamiltonian using Wannier functions $|w_\gamma(\mathbf{R}_l)\rangle$ as basis functions, e.g. the Hamiltonian of the first Kohn-Sham equation, see Eq. 2.35. Due to translational invariance of the Wannier functions, the hopping matrix h_{ij} can be constructed out of the distance between lattice vectors $\tilde{\mathbf{R}}_l = \mathbf{R}'_l - \mathbf{R}_0$. The lattice vector \mathbf{R}_0 denotes some fixed unit cell in the lattice. The use of maximally localized Wannier functions with fast decay from the center of mass and thus negligible overlap of Wannier functions of \mathbf{R}'_l far away from \mathbf{R}_0 enables a dramatic reduction of the size of the hopping matrix. The hopping matrix elements can be calculated by

$$h_{ij} = h_{\gamma\gamma'}(\tilde{\mathbf{R}}_l) = \langle w_\gamma(\mathbf{R}_0) | \hat{H} | w_{\gamma'}(\mathbf{R}'_l) \rangle. \quad (2.51)$$

In practice $h_{\gamma\gamma'}(\tilde{\mathbf{R}}_l)$ has a block structure corresponding to the hopping of electrons between unit cells $\tilde{\mathbf{R}}_l$. We neglect in the following the indices notation $h_{\gamma\gamma'}$ and denote matrix subblocks by an underscore. Each block corresponding to $\tilde{\mathbf{R}}_l$ has the following matrix form

$$h(\tilde{\mathbf{R}}_l) = \begin{bmatrix} \underline{h}^A(\tilde{\mathbf{R}}_l) & \underline{h}^{AB}(\tilde{\mathbf{R}}_l) & \underline{h}^{AO}(\tilde{\mathbf{R}}_l) \\ \underline{h}^{BA}(\tilde{\mathbf{R}}_l) & \underline{h}^B(\tilde{\mathbf{R}}_l) & \underline{h}^{BO}(\tilde{\mathbf{R}}_l) \\ \underline{h}^{OA}(\tilde{\mathbf{R}}_l) & \underline{h}^{OB}(\tilde{\mathbf{R}}_l) & \underline{h}^O(\tilde{\mathbf{R}}_l) \end{bmatrix}, \quad (2.52)$$

where the hopping matrix of each diagonal sub-block, e.g. \underline{h}^A , \underline{h}^B , \underline{h}^O , is constructed out of the orbital basis $\gamma \in \{\gamma_A, \gamma_B, \gamma_O\}$ of the corresponding atom (A, B, O) in the \mathbf{R}_0 unit cell and the same atoms $\gamma' \in \{\gamma'_A, \gamma'_B, \gamma'_O\}$ in the \mathbf{R}'_l unit cell, see Eq. 2.51. The block \underline{h}^O consists of two sub-blocks, corresponding to each oxygen atom in the unit cell. The diagonal elements of each sub-block on the diagonal of $h(\tilde{\mathbf{R}}_0 = 0) = \langle w_\gamma(\mathbf{R}_0) | \hat{H} | w_\gamma(\mathbf{R}_0) \rangle$ are the onsite energies of Wannier orbitals. From these one can calculate the crystal field splitting. The off-diagonal sub-blocks include the cross hopping between orbitals from different atoms in different unit cells. As an example, the element $\underline{h}_{\gamma_A\gamma'_B}^{AB}(\tilde{\mathbf{R}}_1)$ in the sub-block $\underline{h}^{AB}(\tilde{\mathbf{R}}_1)$ corresponds to the hopping amplitude of an electron in orbital γ'_B of atom B in the unit cell \mathbf{R}'_1 to an orbital γ_A of atom A in the unit cell \mathbf{R}_0 . Another important aspect is the reciprocal space \mathbf{k} representation of $h(\tilde{\mathbf{R}}_l)$. The reciprocal space representation is obtained by replacing the creation and annihilation operators by its Fourier series in the tight-binding Hamiltonian, see Eq. 2.50. The creation operator reads

$$\hat{c}_\gamma^\dagger(\mathbf{R}_l) = \frac{1}{\sqrt{N}} \sum_{\mathbf{k}} e^{-i\mathbf{k}\cdot\mathbf{R}_l} \hat{c}_\gamma^\dagger(\mathbf{k}), \quad (2.53)$$

and the annihilation operator reads

$$\hat{c}_\gamma(\tilde{\mathbf{R}}_l) = \frac{1}{\sqrt{N}} \sum_{\mathbf{k}'} e^{i\mathbf{k}' \cdot \tilde{\mathbf{R}}_l} \hat{c}_\gamma(\mathbf{k}'). \quad (2.54)$$

Then, Eq. 2.50 results in a \mathbf{k} diagonal representation of the single-particle Hamiltonian

$$h(\mathbf{k}) = \begin{bmatrix} \underline{h}^A(\mathbf{k}) & \underline{h}^{AB}(\mathbf{k}) & \underline{h}^{AO}(\mathbf{k}) \\ \underline{h}^{BA}(\mathbf{k}) & \underline{h}^B(\mathbf{k}) & \underline{h}^{BO}(\mathbf{k}) \\ \underline{h}^{OA}(\mathbf{k}) & \underline{h}^{OB}(\mathbf{k}) & \underline{h}^O(\mathbf{k}) \end{bmatrix}. \quad (2.55)$$

We note that the former discrete \mathbf{R} -dependence of $\underline{h}(\tilde{\mathbf{R}}_l)$ has a continuous \mathbf{k} -dependence in $\underline{h}(\mathbf{k})$. In practice $\mathbf{k} = \mathbf{k}_m$ are discrete vectors from the first Brillouin zone. The $h(\mathbf{k})$ is diagonal in \mathbf{k} and the sub-block structure for the atoms in the unit cell for each \mathbf{k} is consistent with the real-space representation.

2.6.5 Hubbard Model and dp Model

The Hubbard model is a paradigm model for describing electronic correlations in TMOs [22]. It captures TM atoms which are fixed on the lattice sites with a single orbital and includes the local interaction U between electrons on the same lattice site with different spin.

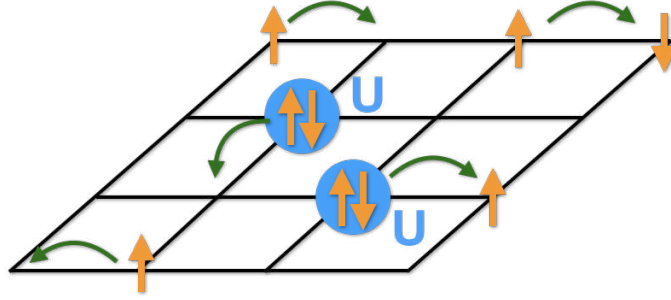


Figure 2.11: Single-band Hubbard model with local interaction U .

The Hamiltonian of the Hubbard model reads

$$\hat{H}_{\text{Hubbard}} = -t \sum_{\langle i,j \rangle, \sigma} \left(\hat{c}_{i,\sigma}^\dagger \hat{c}_{j,\sigma} + \hat{c}_{j,\sigma}^\dagger \hat{c}_{i,\sigma} \right) + U \sum_i \hat{n}_{i,\uparrow} \hat{n}_{i,\downarrow}, \quad (2.56)$$

where $\hat{c}_{i,\sigma}^\dagger$ ($\hat{c}_{i,\sigma}$) is a creation (annihilation) operator of an electron with spin σ on lattice site i . The sum over indices $\langle ij \rangle$ includes the hopping between nearest-neighbor lattice sites with amplitude t . The Coulomb term includes the occupation number $\hat{n}_{i,\sigma} = \hat{c}_{i,\sigma}^\dagger \hat{c}_{i,\sigma}$ for each lattice site i with Coulomb interaction U between

electrons with opposite spin. If the Coulomb interaction is strong compared to the band width $W \approx zt$, where z is the number of nearest-neighbors, then the electronic bands split into a lower and upper Hubbard band. However, the Hubbard model has a limited capability to describe the electronic structure of real materials, such as TMOs. Therefore, an extension to a dp model with long-distance hopping, multiple bands and also O $2p$ orbitals is necessary. The dp Hamiltonian reads [21, 22]

$$\begin{aligned} \hat{H}_{dp} &= \sum_{i,\gamma,\sigma} \varepsilon_d(\gamma) \hat{d}_{i,\gamma\sigma}^\dagger \hat{d}_{i,\gamma\sigma} + \sum_{j,\lambda\sigma} \varepsilon_p(\lambda) \hat{p}_{j,\lambda\sigma}^\dagger \hat{p}_{j,\lambda\sigma} + \hat{T}_{pd} + \hat{T}_{dd} + \hat{T}_{pp} \\ &+ \sum_i \sum_{\kappa\lambda\mu\nu} U_{\kappa\lambda\mu\nu} \hat{d}_{\kappa i}^\dagger \hat{d}_{\lambda i}^\dagger \hat{d}_{\nu i} \hat{d}_{\mu i}, \end{aligned} \quad (2.57)$$

where $\hat{d}_{i,\gamma\sigma}^\dagger$ ($\hat{p}_{j,\lambda\sigma}^\dagger$) $\hat{d}_{i,\gamma\sigma}$ ($\hat{p}_{j,\lambda\sigma}$) are creation (annihilation) operators of TM $3d$ and O $2p$ electrons, respectively. The indices γ and λ denote the TM $3d$ and O $2p$ orbitals on lattice site i and j , respectively. The $\varepsilon_d(\gamma)$ and $\varepsilon_p(\lambda)$ are the onsite energies of the TM $3d$ and O $2p$ states, respectively. The Coulomb interaction $U_{\kappa\lambda\mu\nu}$ acts on the TM $3d$ shells with orbital and spin indices $\kappa\lambda\mu\nu$ locally on each lattice site i . The operator \hat{T}_{pd} refers to the inter and intra-site hopping of electrons between TM $3d$ and O $2p$ orbitals

$$\hat{T}_{pd} = \sum_{i,\gamma,j,\lambda,\sigma} t_{pd}(i,\gamma;j,\lambda) \left(\hat{d}_{i,\gamma\sigma}^\dagger \hat{p}_{j,\lambda\sigma} + \hat{p}_{j,\lambda\sigma}^\dagger \hat{d}_{i,\gamma\sigma} \right), \quad (2.58)$$

where $t_{pd}(i,\gamma;j,\lambda)$ is the hopping amplitude. The operators \hat{T}_{dd} and \hat{T}_{pp} in Eq. 2.57 denote the inter and intra-site hopping of electrons within TM $3d$ and O $2p$ orbitals, respectively. They read

$$\hat{T}_{dd} = \sum_{i,\gamma,i',\gamma'} t_{dd}(i,\gamma;i',\gamma') \left(\hat{d}_{i,\gamma\sigma}^\dagger \hat{d}_{i',\gamma'\sigma} + \hat{d}_{i',\gamma'\sigma}^\dagger \hat{d}_{i,\gamma\sigma} \right) \quad (2.59)$$

and

$$\hat{T}_{pp} = \sum_{j,\lambda,j',\lambda'} t_{pp}(j,\lambda;j',\lambda') \left(\hat{p}_{j,\lambda\sigma}^\dagger \hat{p}_{j',\lambda'\sigma} + \hat{p}_{j',\lambda'\sigma}^\dagger \hat{p}_{j,\lambda\sigma} \right), \quad (2.60)$$

where $t_{dd}(i,\gamma;i',\gamma')$ and $t_{pp}(j,\lambda;j',\lambda')$ are the hopping amplitudes. They describe the hopping between d (p) orbitals on different atoms i (j) and i' (j'), respectively. By Fourier transforming the operators in the hopping part of Eq. 2.57 to the \mathbf{k} -space representation, the dp Hamiltonian reads [4]

$$\begin{aligned} H_{dp} &= \sum_{\mathbf{k}} \begin{pmatrix} \mathbf{d}_{\mathbf{k}}^\dagger & \mathbf{p}_{\mathbf{k}}^\dagger \end{pmatrix} \begin{pmatrix} \underline{h}_{\mathbf{k}}^{dd} - \mu_{dc} & \underline{h}_{\mathbf{k}}^{dp} \\ \underline{h}_{\mathbf{k}}^{pd} & \underline{h}_{\mathbf{k}}^{pp} \end{pmatrix} \begin{pmatrix} \mathbf{d}_{\mathbf{k}} \\ \mathbf{p}_{\mathbf{k}} \end{pmatrix} \\ &+ \sum_i \sum_{\kappa\lambda\mu\nu} U_{\kappa\lambda\mu\nu} \hat{d}_{\kappa i}^\dagger \hat{d}_{\lambda i}^\dagger \hat{d}_{\nu i} \hat{d}_{\mu i}. \end{aligned} \quad (2.61)$$

Here, $\mathbf{d}_{\mathbf{k}}$ ($\mathbf{p}_{\mathbf{k}}$) is an operator-valued vector which elements are Fourier transforms of $d_{\gamma i}$ ($p_{\gamma i}$). The double-counting energy μ_{dc} is diagonal in the subspace of the TM

$3d$ states and corrects the d - d interaction already accounted for in DFT. The μ_{dc} renormalizes the splitting of the TM $3d$ and O $2p$ energies, thus μ_{dc} is related to the charge-transfer energy Δ_{CT} [5, 31, 132].

2.6.6 Dynamical Mean-Field Theory

DMFT is used to calculate the electronic structure of correlated materials [13, 133, 134]. DMFT maps the infinite lattice model with local interaction, e.g. Hubbard (dp) model, self-consistently onto an Anderson impurity model which is coupled to an optimized non-interacting host, see Fig. 2.12. The non-interacting states of the crystal host are auxiliary bath states. They represent the former interacting valence states of the infinite crystal lattice around the impurity.

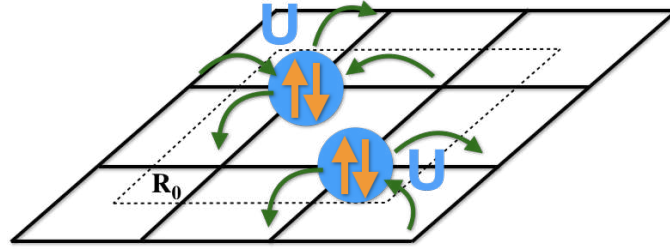


Figure 2.12: Crystal lattice with two inequivalent impurities. DMFT simultaneously captures the mapping of the crystal lattice onto the Anderson impurity model of both impurities.

DMFT is a many-body theory based on one-particle Green's functions. A one-particle Green's function describes a particle or hole added to the system at time t' and propagating in the system until its removal at time t . For finite temperatures we use imaginary time, where $it \rightarrow \tau$. The causal Green's function for finite temperatures $T > 0$ is defined as

$$\begin{aligned} G_{ij}(\tau, \tau') &\equiv -\langle \mathcal{T} \hat{c}_i(\tau) \hat{c}_j^\dagger(\tau') \rangle \\ &= -\frac{1}{Z} \Theta(\tau - \tau') \text{Tr} \left[e^{-\hat{H}(\beta - \tau)} \hat{c}_i e^{-\hat{H}(\tau - \tau')} \hat{c}_j^\dagger e^{-\hat{H}\tau'} \right] \\ &\quad \pm \frac{1}{Z} \Theta(\tau' - \tau) \text{Tr} \left[e^{-\hat{H}(\beta - \tau')} \hat{c}_j^\dagger e^{-\hat{H}(\tau' - \tau)} \hat{c}_i e^{-\hat{H}\tau} \right]. \end{aligned} \quad (2.62)$$

The operator \hat{c}_j^\dagger (\hat{c}_i) adds (removes) a particle to (from) the system. The indices i and j denote the lattice sites, orbital and spin. The sign \pm corresponds to fermionic ($-$) or bosonic ($+$) creation and annihilation operators. The operators are described in the Heisenberg picture, where $\hat{c}_i(\tau) = e^{\tau \hat{H}} \hat{c}_i e^{-\tau \hat{H}}$ and $\hat{c}_j^\dagger(\tau') = e^{\tau' \hat{H}} \hat{c}_j^\dagger e^{-\tau' \hat{H}}$. $Z = \text{Tr} \left[e^{-\beta \hat{H}} \right]$ is the partition function. The Green's function is defined on the time interval $\tau \in (0, \beta)$ and with an anti-periodic (periodic) extension to the whole real axis for fermions (bosons) $G(\tau) = \pm G(\tau)$. If the Hamiltonian is time independent

the Green's function depends only on the relative time $\tau = \tau - \tau'$. The time ordering symbol \mathcal{T} contains the Heaviside step functions Θ which sort the time arguments, starting with the largest time argument on the left. The periodicity of τ implies that we can express the Green's function as a Fourier series in Matsubara frequencies ω_n

$$G(\tau) = \frac{1}{\beta} \sum_{n=-\infty}^{\infty} e^{-i\omega_n \tau} G(i\omega_n), \quad (2.63)$$

where the Fourier coefficients are the Matsubara Green's functions

$$G(i\omega_n) = \int_0^\beta d\tau e^{i\omega_n \tau} G(\tau). \quad \begin{cases} \omega_n = (2n+1)\frac{\pi}{\beta} & \dots \text{fermions} \\ \omega_n = 2n\frac{\pi}{\beta} & \dots \text{bosons} \end{cases} \quad (2.64)$$

The Matsubara frequencies ω_n are odd for fermions and even for bosons. The relation between an interacting Green's function $G(\omega)$ and a non-interacting Green's function $G_0(\omega)$ is given by the Dyson equation

$$G(\mathbf{k}, i\omega_n) = G_0(\mathbf{k}, i\omega_n) + G_0(\mathbf{k}, i\omega_n) \Sigma(i\omega_n) G(\mathbf{k}, i\omega_n), \quad (2.65)$$

where the self-energy $\Sigma(i\omega_n)$ is assumed to be local in DMFT, i.e. the energy dependence of the self energy is explicitly taken into account, whereas the momentum dependence \mathbf{k} is neglected. DMFT is exact in the limit of infinite dimensions. However, it provides a realistic description of the electronic structure of 3- or even 2-dimensional materials [12, 14, 134, 135]. Here we show how to apply DMFT for systems with several interacting impurities in the unit cell including non-interacting ligand ions.

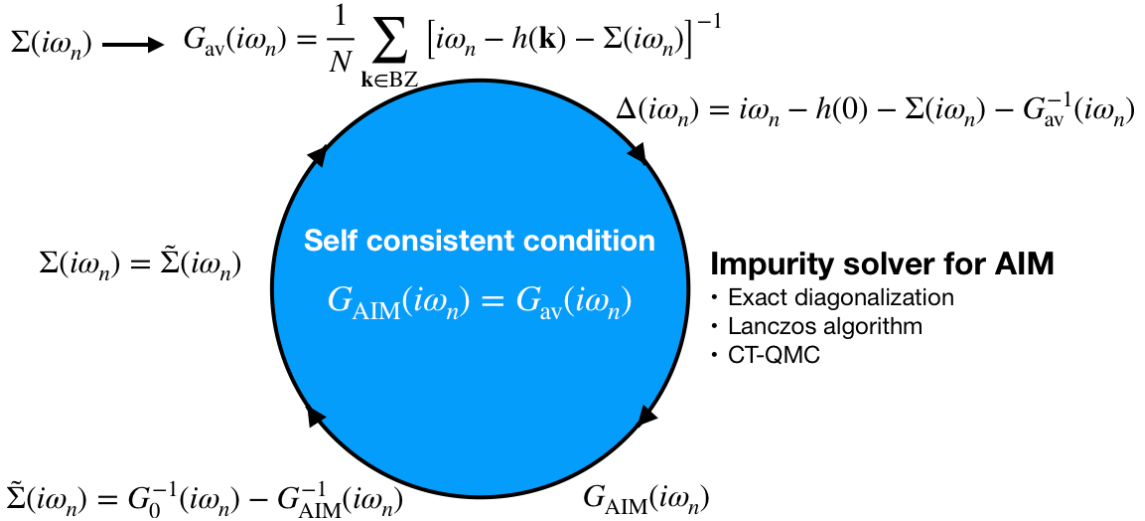


Figure 2.13: DMFT self-consistent cycle for a single impurity. Figure adapted from [22].

The self-consistent DMFT cycle follows: Initially the self-energy $\Sigma(i\omega_n)$ is guessed for the interacting orbitals γ_A and γ_B of each TM atom A and B, respectively. The

spin is included in the index γ . In this section we use the same notation as in Sec. 2.6.4. Thus, the self-energy reads

$$\Sigma(i\omega_n) = \begin{bmatrix} \underline{\Sigma}^A(i\omega_n) & \underline{0} & \underline{0} \\ \underline{0} & \underline{\Sigma}^B(i\omega_n) & \underline{0} \\ \underline{0} & \underline{0} & \underline{0} \end{bmatrix}. \quad (2.66)$$

In our approach DMFT is based on the momentum-space \mathbf{k} -representation of the tight-binding Hamiltonian, see Eq. 2.55. We calculate the local lattice Green's function G_{av} for the orbitals $\gamma \in \{\gamma_A, \gamma_B, \gamma_O\}$ ($\gamma' \in \{\gamma'_A, \gamma'_B, \gamma'_O\}$) by summing over all momenta \mathbf{k} within the Brillouin zone (BZ). The lattice Green's function averaged over all \mathbf{k} reads

$$G_{\text{av}}(i\omega_n) = \frac{1}{N} \sum_{\mathbf{k} \in \text{BZ}} [i\omega_n - h(\mathbf{k}) - \Sigma(i\omega_n)]^{-1}. \quad (2.67)$$

It is a matrix which includes all orbitals γ of all atoms in the unit cell. The hybridization functions $\underline{\Delta}^J(i\omega_n)$ of both impurities $J = \{A, B\}$ are matrix valued and read

$$\underline{\Delta}^J(i\omega_n) = i\omega_n \underline{\mathbb{I}}^J - \underline{h}^J(\tilde{\mathbf{R}}_l=0) - \underline{\Sigma}^J(i\omega_n) - [\underline{G}_{\text{av}}^{-1}(i\omega_n)]^J, \quad (2.68)$$

where $\underline{\mathbb{I}}^J$ is the identity matrix in sub-block J . The local Hamiltonian $\underline{h}^J(\tilde{\mathbf{R}}_l=0) = \frac{1}{N} \sum_{\mathbf{k}} \underline{h}^J(\mathbf{k})$ is given in Eq. 2.52. The last term in Eq. 2.68 denotes a diagonal sub-block J of $G_{\text{av}}^{-1}(i\omega_n)$. Then we construct the Green's function of the Anderson impurity model for each impurity J . The Anderson impurity model consists of the local Hamiltonian $\underline{h}^J(\tilde{\mathbf{R}}_l=0)$, the hybridization function $\underline{\Delta}^J(i\omega_n)$ and the local interaction $U_{\kappa\lambda\mu\nu}^J$, see Eq. 2.61. We use the strong coupling continuous-time quantum Monte Carlo (CT-QMC) method to calculate the interacting Anderson impurity model Green's function, where we use an in-house CT-QMC package, which implements recent improved-estimator techniques [136–138]. The new self energies $\tilde{\underline{\Sigma}}^J$ for all impurity d orbitals are calculated by the Dyson equation from the Anderson impurity model Green's function

$$\underline{G}_{\text{AIM}}^J(i\omega_n) = [i\omega_n \underline{\mathbb{I}}^J - \underline{h}_{\text{loc}}^J - \underline{\Delta}^J(i\omega_n) - \tilde{\underline{\Sigma}}^J(i\omega_n)]^{-1}. \quad (2.69)$$

After obtaining the self-energy $\tilde{\underline{\Sigma}}(i\omega_n)$ for all impurities J , we update the self-energy, see Eq. 2.66, and initiate a new cycle. The cycle is repeated until the convergence criteria

$$\underline{G}_{\text{AIM}}^J(i\omega_n) = \underline{G}_{\text{av}}^J(i\omega_n) \quad (2.70)$$

is reached. The self-energy $\Sigma(i\omega_n)$ is then analytically continued to real frequencies $\Sigma(\epsilon)$ by the maximum entropy method [139, 140].

2.6.7 Double Counting and Charge-Transfer Energy

The on-site d -energies $\varepsilon_d(\gamma) = \varepsilon_d^{\text{LDA}}(\gamma) - \mu_{dc}$ in the impurity Hamiltonian, see Eq. 2.6, are renormalized from the LDA values [1], where γ denotes orbital and spin of the TM ion. The $\varepsilon_d^{\text{LDA}}(\gamma)$ are the energies of the Wannier TM $3d$ states and μ_{dc} is the double-counting energy included in the DMFT cycle. The double-counting correction accounts for the d - d interaction implicitly present in the LDA calculation. The double-counting correction μ_{dc} renormalizes the splitting between Ni $3d$ and O $2p$ states and thus is related to the charge-transfer energy, which is introduced as $\Delta_{\text{CT}} = E(d^{n+1}\underline{L}) - E(d^n)$ in the cluster model analysis. The d^n represents the electron filling n of the TM ion in its formal valence and \underline{L} denotes a hole in the neighboring ligands. Since there is no unique mapping between the charge-transfer energy in the cluster-model picture and double-counting energy in a solid, we use a fuzzy estimate [1]

$$\Delta_{\text{CT}} = \varepsilon_d^{\text{LDA}} - \mu_{dc} + nU_{dd} - \varepsilon_p^{\text{LDA}} \quad (2.71)$$

to relate μ_{dc} with Δ_{CT} . The averaged energy of the TM $3d$ states ($\varepsilon_d^{\text{LDA}}$) is evaluated by a partial trace of the TM $3d$ energies in the tight-binding Hamiltonian as $\varepsilon_d^{\text{LDA}} = \frac{1}{N} \sum_{\gamma} \varepsilon_d^{\text{LDA}}(\gamma)$. Similarly, the averaged energy of O $2p$ states ($\varepsilon_p^{\text{LDA}}$) is evaluated by a partial trace of the O $2p$ energies. Since the O $2p$ states are not fully occupied in the LDA result and form a band, the Δ_{CT} value estimated above cannot be compared to the values used in the cluster-model analysis [1].

2.7 Computational Details of Core-Level X-ray Spectroscopy

In this section we introduce the resolvent representation of core-level spectral functions, which provides an efficient computational route using exact diagonalization. We explain the geometry of a scattering process and discuss the transition operator in more detail. Furthermore, we study the configuration-interaction scheme which provides a optimized basis set for core-level spectroscopy calculations in the resolvent formalism. Finally, we discuss an efficient way in order to treat fermionic basis sets and operators numerically.

2.7.1 Fermi's Golden Rule

Here we describe how to calculate core-level photoemission and absorption spectra based on first order perturbation theory with electron-photon coupling \hat{T}_{D} as perturbation. This first order perturbation theory results in Fermi's golden rule. Thus, the spectral functions of XPS and XAS read

$$F_{\text{XPS/XAS}}^{(n)}(\omega) = \sum_f \left| \langle f | \hat{T}_{\text{D}} | n \rangle \right|^2 \delta(E_n + \omega - E_f). \quad (2.72)$$

Using the identity $\frac{1}{\omega+i0^++E_n-E_f} = \text{p.v.} \left[\frac{1}{\omega+E_n-E_f} \right] - i\pi\delta(\omega+E_n-E_f)$, then Eq. 2.72 can be reformulated as imaginary part of a Lorentzian

$$F_{\text{XPS/XAS}}^{(n)}(\omega) = -\frac{1}{\pi} \sum_f \Im \left[\frac{\langle n|\hat{T}_D^\dagger|f\rangle \langle f|\hat{T}_D|n\rangle}{\omega^+ - E_f + E_n} \right], \quad (2.73)$$

where $\omega^+ = \omega + i0^+$. The E_f are the eigenvalues of the Hamiltonian in the subspace of the final states $|f\rangle$. We use the spectral theorem

$$\hat{H}_f = \sum_f E_f |f\rangle \langle f| \rightarrow \frac{1}{\hat{H}_f} = \sum_f \frac{1}{E_f} |f\rangle \langle f|, \quad (2.74)$$

which enables us to rewrite the spectral function in terms of a resolvent

$$F_{\text{XPS/XAS}}^{(n)}(\omega) = -\frac{1}{\pi} \Im \left[\langle n|\hat{T}_D^\dagger \frac{1}{\omega^+ - \hat{H}_f + E_n} \hat{T}_D|n\rangle \right]. \quad (2.75)$$

The resolvent representation of the spectral function allows us to formally remove the summation of the final states $|f\rangle$. The final states in the original representation, see Eq. 2.72, had to be evaluated separately. Thus, the computational efforts are substantially reduced in this representation since one does not have to compute all eigenenergies E_f and eigenvectors $|f\rangle$, but just compute the matrix element of the resolvent between the initial state $|n\rangle$. The spectral function can be calculated by a continued fraction expansion, see Appendix. A.2.

2.7.2 Kramers-Heisenberg Formula

The spectral function of RIXS is described by the Kramers-Heisenberg formula, see Eq. 2.3. Evaluating the Kramers-Heisenberg formula directly exceeds numerical limitations since the summation over all intermediate and final states would require the separate computation of each state by diagonalizing the full Hamiltonian. Thus, we introduce a way to reformulate the Kramers-Heisenberg formula where we avoid the direct evaluation of the intermediate and final states. We use the spectral theorem, see Eq. 2.74, where we apply $E_m|m\rangle = \hat{H}_m|m\rangle$, to rewrite Eq. 2.3 in terms of a resolvent

$$F_{\text{RIXS}}(\omega_{\text{in}}, \omega_{\text{out}}) = \sum_f \left| \langle f|\hat{T}_E \frac{1}{\omega_{\text{in}} + E_n - \hat{H}_m + i\Gamma_L} \hat{T}_I|n\rangle \right|^2 \delta(\omega_{\text{in}} + E_g - \omega_{\text{out}} - E_f), \quad (2.76)$$

with the operator form of the intermediate-state Hamiltonian \hat{H}_m . In practice, we calculate the initial state $|n\rangle$ by the use of the Lanczos algorithm, see Appendix. A.1. Then we apply the transition operator onto the initial state and obtain a new state

$|x\rangle = \hat{T}_I |n\rangle$. By applying the resolvent in Eq. 2.76 onto $|x\rangle$ we obtain $|y\rangle = \frac{1}{\omega_{\text{in}} + E_g - \hat{H}_m + i\Gamma_L} |x\rangle$ which can be formally rewritten as

$$(\omega_{\text{in}} + E_g - \hat{H}_m + i\Gamma_L) |y\rangle = |x\rangle. \quad (2.77)$$

We use the conjugate gradient method to evaluate state $|y\rangle$, which can be parallelized for each ω_{in} . Alternatively, one can employ the shifted conjugate gradient method [141, 142] proposed in Ref. [2], which reuses the Krylov subspace spanned for one specific ω_{in} for finding $|y\rangle$ for other energies. However, by using Eq. 2.77 we simplify Eq. 2.76 to

$$F_{\text{RIXS}}(\omega_{\text{in}}, \omega_{\text{out}}) = \sum_f \left| \langle f | \hat{T}_E | y \rangle \right|^2 \delta(\omega_{\text{in}} + E_g - \omega_{\text{out}} - E_f), \quad (2.78)$$

which resembles Fermi's golden rule, see Eq. 2.72. Here, we show a route alternative to the one introduced in Sec. 2.7.1 to calculate Eq. 2.78. In principle, we are searching for a subset of final states $\{|\tilde{f}_i\rangle\}$ which have a finite overlap $\langle \tilde{f}_i | z_0 \rangle \neq 0$ with state $|z_0\rangle = \hat{T}_E |y\rangle$. One can use the Lanczos algorithm, see Appendix. A.1, for calculating these overlaps by calculating the eigenstates of \hat{H}_f and by adopting $|z_0\rangle$ as starting vector (seed state) of the Lanczos recursion formula, see Fig. 2.14.

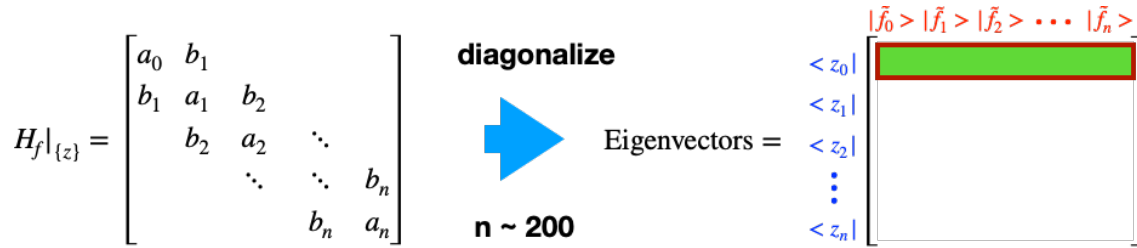


Figure 2.14: Eigenvectors obtained with Lanczos with $|z_0\rangle$ as starting vector.

The Lanczos algorithm creates a tridiagonal matrix $H_f|_{\{z\}}$ in an orthogonal Krylov basis. By diagonalizing the matrix and calculating the eigenvectors we obtain in the first row the elements with finite overlap with the seed state $|z_0\rangle$, see right panel of Fig. 2.14. Thus, the spectral function only incorporates the subset of finite overlaps and reads

$$F_{\text{RIXS}}(\omega_{\text{in}}, \omega_{\text{out}}) = \sum_i \left| \langle \tilde{f}_i | z_0 \rangle \right|^2 \delta(\omega_{\text{in}} + E_g - \omega_{\text{out}} - E_i), \quad (2.79)$$

where the overlap elements $\langle \tilde{f}_i | z_0 \rangle$ contain all states which are reachable from the initial state $|n\rangle$. E_i are the energies corresponding to the final states \tilde{f}_i .

2.7.3 Scattering Geometry

The scattering geometry of RIXS is shown in Fig. 2.15.

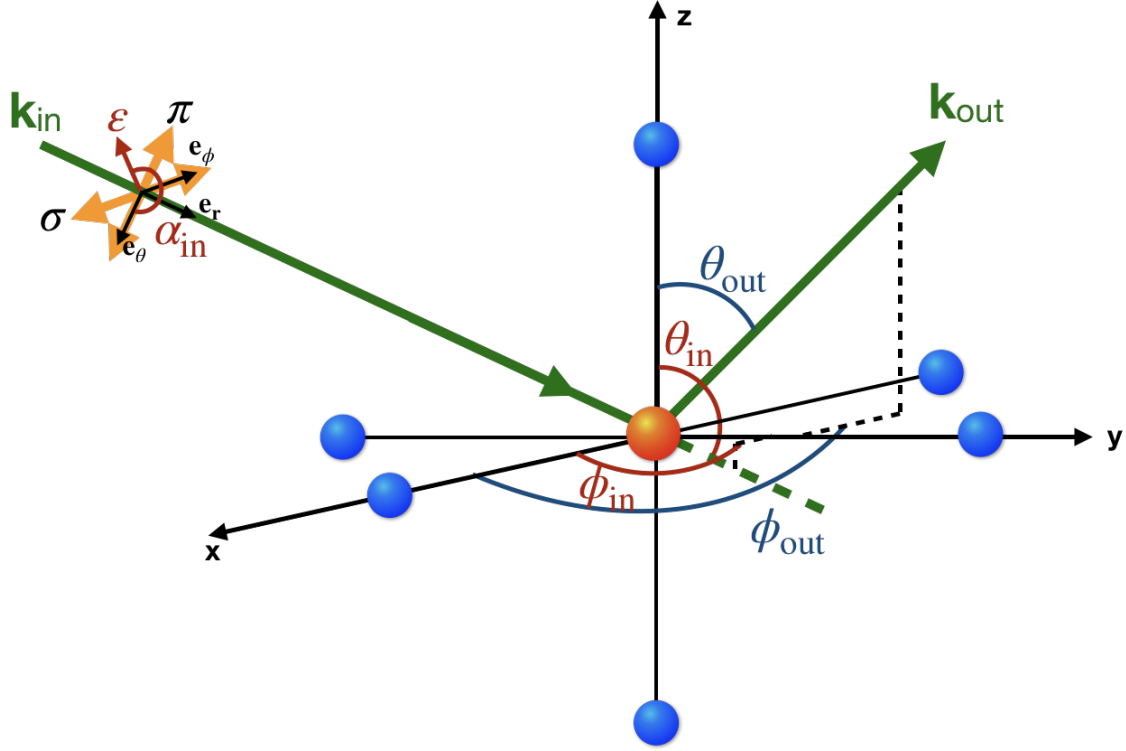


Figure 2.15: Scattering geometry of RIXS.

The orthogonal vectors \mathbf{x}, \mathbf{y} and \mathbf{z} span the global coordinate system. The scattering plane is spanned by the incident \mathbf{k}_{in} and emitted \mathbf{k}_{out} photon vectors. The angle θ_i (ϕ_i) with $i \in \{\text{in}, \text{out}\}$ is between the \mathbf{z} -axis (\mathbf{x} -axis) and the corresponding photon vector \mathbf{k}_i . For the polarization of the photons we define a local coordinate system. The transformation from the global to the local coordinate system reads

$$\begin{pmatrix} \mathbf{e}_r \\ \mathbf{e}_\theta \\ \mathbf{e}_\phi \end{pmatrix}_i = \begin{pmatrix} \sin \theta \cos \phi & \sin \theta \sin \phi & \cos \theta \\ \cos \theta \cos \phi & \cos \theta \sin \phi & -\sin \theta \\ -\sin \phi & \cos \phi & 0 \end{pmatrix}_i \begin{pmatrix} \mathbf{x} \\ \mathbf{y} \\ \mathbf{z} \end{pmatrix}, \quad (2.80)$$

where $(\mathbf{e}_r)_i$ points into the direction of the incident or emitted photon. The vectors $(\mathbf{e}_\theta)_i$ and $(\mathbf{e}_\phi)_i$ are orthogonal to $(\mathbf{e}_r)_i$ and span the polarization plane. The polarization vector is defined within the polarization plane and reads

$$(\boldsymbol{\varepsilon})_i = (\cos \alpha \mathbf{e}_\theta + \sin \alpha \mathbf{e}_\phi)_i, \quad (2.81)$$

where $(\alpha)_i$ defines the polarization direction of the photon with respect to the direction of $(\mathbf{e}_\theta)_i$. By inserting Eq. 2.80 in Eq. 2.81 we obtain an expression for the

polarization in the global coordinate system

$$\begin{pmatrix} \varepsilon_x \\ \varepsilon_y \\ \varepsilon_z \end{pmatrix}_i = \begin{pmatrix} \cos \alpha \cos \theta \cos \phi - \sin \alpha \sin \phi \\ \cos \alpha \cos \theta \sin \phi + \sin \alpha \cos \phi \\ -\cos \alpha \sin \theta \end{pmatrix}_i. \quad (2.82)$$

For RIXS we distinguish between two kinds of polarization which are defined by the polarization of the incident photon. In the case of π -polarized (also called depolarized) the polarization of the incident photon lies within the scattering plane, whereas in σ -polarized (also called polarized) the polarization is orthogonal to the scattering plane.

2.7.4 Transition Operator

The transition operator in core-level spectroscopies encodes the photoemission of a core-electron or the excitation of a core-electron to a valence state and vice versa. In terms of second quantization, the transition operator, describing an excitation of a core electron to a valence state, reads

$$\hat{T}_D = \sum_{ij} T_{ij} \hat{d}_i^\dagger \hat{p}_j, \quad (2.83)$$

where \hat{d}_i^\dagger (\hat{p}_j) is a creation (annihilation) operator of a valence (core) electron with orbital and spin indices i and j . The transition operator for a deexcitation process has the form of $\hat{T}_E = \hat{T}_D^\dagger$. In core-level photoemission spectroscopy the transition operator reads

$$\hat{T}_D = \sum_{i,j} T_{ij} \hat{q}_i^\dagger \hat{p}_j, \quad (2.84)$$

where \hat{p} annihilates a core electron and \hat{q}^\dagger creates a free electron. The transition operator is approximated as a dipole in weak field approximation, containing the position operator $\hat{\mathbf{r}}$ of the orbitals and the polarization vector $\boldsymbol{\varepsilon}$ of the photon. [30]. The transition matrix elements $T_{ij} = \langle i | \boldsymbol{\varepsilon} \cdot \hat{\mathbf{r}} | j \rangle$ can be expressed by renormalized spherical harmonics $C_q^k = \sqrt{\frac{4\pi}{2k+1}} Y_{kq}$ and by left-polarized $\boldsymbol{\varepsilon}_l = -\sqrt{\frac{1}{2}}(\varepsilon_x - i\varepsilon_y)$, right-polarized $\boldsymbol{\varepsilon}_r = \sqrt{\frac{1}{2}}(\varepsilon_x + i\varepsilon_y)$ and \mathbf{z} -polarized $\boldsymbol{\varepsilon}_z = \varepsilon_z$ photons

$$[\boldsymbol{\varepsilon} \cdot \hat{\mathbf{r}}] \sim -\sqrt{\frac{1}{2}}(\varepsilon_x - i\varepsilon_y)C_1^1 + \sqrt{\frac{1}{2}}(\varepsilon_x + i\varepsilon_y)C_{-1}^1 + \varepsilon_z C_0^1. \quad (2.85)$$

Here, we did not consider the radial part of $T_{ij} = \langle i | \hat{\mathbf{r}} | j \rangle$ because it is approximately constant and scales the spectral intensity uniformly. The selection rules lead to $\Delta q = \pm 1$ for left and right polarized light and $\Delta q = 0$ for z polarized light. The transition operator for either the incident or emitted photon in the global coordinate

system reads

$$\begin{aligned}
 [\boldsymbol{\varepsilon} \cdot \hat{\mathbf{r}}] \sim & -\sqrt{\frac{1}{2}} (\cos \alpha \cos \theta - i \sin \alpha) e^{-i\phi} C_1^1 \\
 & + \sqrt{\frac{1}{2}} (\cos \alpha \cos \theta + i \sin \alpha) e^{i\phi} C_{-1}^1 \\
 & - \cos \alpha \sin \theta C_0^1,
 \end{aligned} \tag{2.86}$$

with the photon polarization angle α , the scattering angles θ and ϕ . Here we inserted the polarization represented in the global coordinate system, see Eq. 2.82.

2.7.5 Configuration Interaction Scheme

The present configuration interaction (CI) scheme provides a convenient way to construct an optimized basis set, consisting of many-body Slater determinants for core-level spectroscopy calculations using the resolvent formalism. The CI scheme excludes Slater determinants with small contributions to ground as well as excited states reachable by X-ray excitations [1]. It is built as an expansion between the hybridization to the bath and the impurity atom. The bath is filled up to the Fermi energy E_F with electrons and is empty above E_F . Starting with the isolated-atom limit, electron-hole pairs are created by applying the impurity-bath hybridization term $\hat{H}_{\text{imp-host}}$, see Eq. 2.30, subsequently. This scheme was introduced by Gunnarsson and Schönhammer in their studies of XPS and XAS in Ce compounds [143] on the basis of a $\frac{1}{N_f}$ expansion for the Anderson impurity model. In the CI scheme for the Anderson impurity model with discretized bath levels, the choice of the total number of the electrons in the CI expansion plays an important role since it cannot be changed in the recursive procedure for creating the electron-hole pairs [1]. In a conventional CI implementation, e.g. in a cluster-model analysis, the total number of electrons is chosen such that the number of the electrons on the impurity site (with the filled bath up to E_F) is equal to the one of the target transition metal in formal valence (e.g., $|d^7\rangle$ for RNiO_3). If weakly coupled bath levels close to E_F are included, the ground state of the system does not depend on the total number of electrons in the system. I.e. if a $|d^8\rangle - |d^9 \underline{L}\rangle$ configuration represents the ground state, where \underline{L} denotes a hole in the valence bath, by choosing a different initial configuration, e.g. $|d^7\rangle - |d^8 \underline{L}\rangle - |d^9 \underline{L}^2\rangle$, the ground state is contained in $(|d^8\rangle - |d^9 \underline{L}\rangle) \underline{L}$ if the hole \underline{L} on the right hand side is located at E_F and almost decoupled from the ground state configuration. But choosing a different initial configuration is computationally more demanding. However, this treatment is not always appropriate for finding the true ground state of the Anderson impurity model with discretized bath levels since the total number of electrons in the system determines the symmetry of the wave functions in the Fock space expanded by the CI scheme.

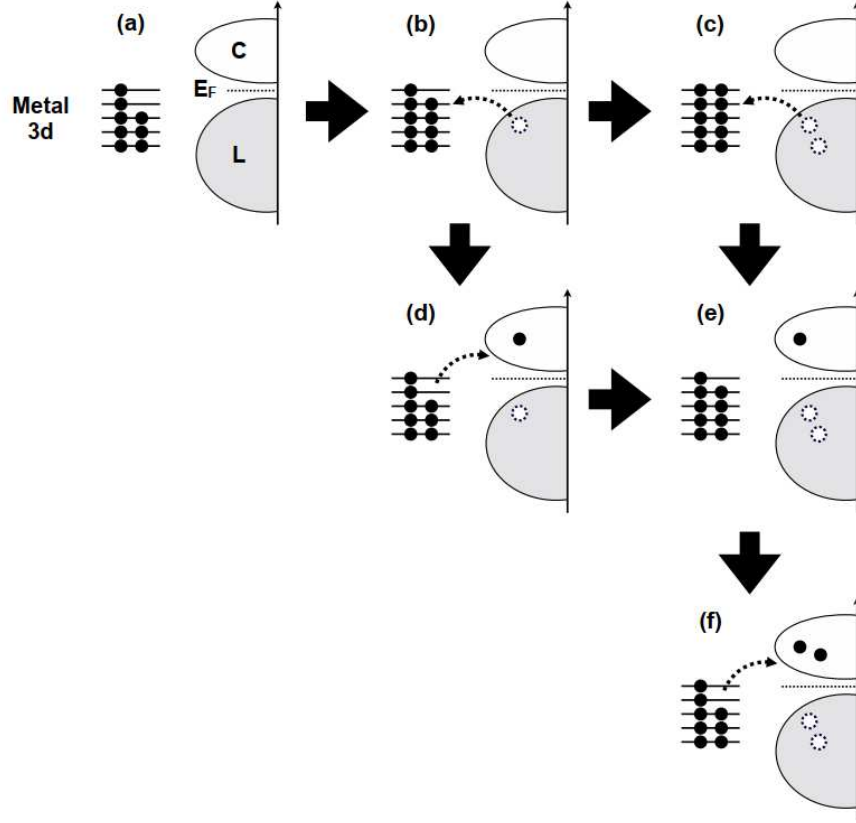


Figure 2.16: Schematic representation of basis construction in the CI scheme for a $3d$ system with 8 electrons in the $3d$ shell in the nominal valence. Starting from (a) $|d^8\rangle$ configuration, electronic configurations (b) $|d^9\underline{L}^1\rangle$, (c) $|d^{10}\underline{L}^2\rangle$, (d) $|d^8\underline{L}^1c^1\rangle$, (e) $|d^9\underline{L}^2c^1\rangle$ and (f) $|d^8\underline{L}^2c^2\rangle$ are constructed through the hybridization interaction [22]. Figure adapted from [21] with the permission of the author.

The CI scheme works as follows [21, 22, 143]: a state with $\binom{10}{n}$ electron configurations is denoted collectively as $|d^n\underline{L}^m c^l\rangle$ with n electrons in the impurity valence orbitals, $m = 0$ holes in the valence bath states and $l = 0$ electrons in the conduction bath states. We successively apply the Hamiltonian onto the state and obtain configurations with charge transfer from bath to impurity and vica versa, see Fig. 2.16. In practice, we use up to $m = 4$ holes in the valence states and $l = 2$ electrons in the conduction states and up to 30 discretized energy levels of the bath per spin and orbital, 20 for the valence bands and 10 for conduction bands. We tested even higher numbers of discretized levels which will be applied in future studies. The number of configurations in each state rises exponentially with the number of holes and electrons. The state in its full CI basis can be written as a superposition of the generated basis configurations [21, 22]

$$|n\rangle = a_0 |d^n\rangle + a_1 |d^{n+1}\underline{L}\rangle + a_2 |d^{n+2}\underline{L}^2\rangle + a_3 |d^{n-1}c^1\rangle + a_4 |d^n\underline{L}c^1\rangle \dots, \quad (2.87)$$

with weights a_i . If there is a core-hole, e.g. in the final states $|f\rangle$ of XAS, the procedure works similarly

$$|f_{\text{XAS}}\rangle = c_0 |\underline{p}d^{n+1}\rangle + c_1 |\underline{p}d^{n+2}\underline{L}\rangle + c_2 |\underline{p}d^n c^1\rangle + c_3 |\underline{p}d^{n+1}\underline{L}c^1\rangle \dots, \quad (2.88)$$

where c_i are the weights and \underline{p} denotes a hole in the core-level states.

2.7.6 Numerical Many-Body Basis

Here we provide a short introduction of the numerical treatment of fermionic states and their numerical manipulation with operators. The commutation relations for fermionic operators read

$$\{a_i, a_j^\dagger\} = \delta_{ij} \quad (2.89)$$

$$\{a_i^\dagger, a_j^\dagger\} = \{a_i, a_j\} = 0, \quad (2.90)$$

where a_i and a_i^\dagger are electron annihilation and creation operators, respectively. During the procedure of creating basis states, the order of the operators must be kept consistent. For the first orbital we use the starting index $i = 0$ and an ascending order of the operators from right to left. By adding an electron into the vacuum on orbital 3 one applies the creation operator onto the vacuum state

$$c_3^\dagger |\text{vac}\rangle = |1000\rangle. \quad (2.91)$$

By creating an additional electron in orbital 1 we sort the creation operators into the predefined order by using the anti-commutation relation of Eq. 2.90

$$c_1^\dagger |1000\rangle = c_1^\dagger c_3^\dagger |\text{vac}\rangle = -c_3^\dagger c_1^\dagger = -|1010\rangle, \quad (2.92)$$

where we obtain a negative phase factor due to the anti-commutation rules of fermionic operators. In our ordering scheme, the phase is determined by the number of electrons existing in orbitals on the left of the actual orbital. An even number of electrons on the left provides a positive phase factor, whereas an odd number of electrons on the left results in a negative phase factor. To store this information efficiently we use binary₂ numbers for the Dirac representation, which we convert into an integer form. Tab. 2.1 shows configurations in Dirac and integer representation.

Particle Number	Dirac	Integer
1	$ 0001\rangle$	1
	$ 0010\rangle$	2
	$ 0100\rangle$	4
	$ 1000\rangle$	8
2	$ 0011\rangle$	3
	$ 0101\rangle$	5
	$ 0110\rangle$	6
	$ 1001\rangle$	9
	$ 1010\rangle$	10
	$ 1100\rangle$	12
3	$ 0111\rangle$	7
	$ 1011\rangle$	11
	$ 1101\rangle$	13
	$ 1110\rangle$	14
4	$ 1111\rangle$	15

Table 2.1: Basis configurations in Dirac (binary₂) and integer notation.

Now, let us assume we have a given configuration of the TM $3d$ states (we ignore spin for the moment), where we want to calculate the number of particles in this configuration

$$|11001\rangle \hat{=} 25. \quad (2.93)$$

In this example, the particle number is easy to determine, but in practice there are configurations with $\sim 10^3$ particles, e.g. the bath states of the Anderson impurity model. Our spectroscopy code is written in FORTRAN. Thus, we use the command ‘IBITS(I,POS,LEN)’ to calculate the particle number of a given configuration. ‘IBITS’ takes an integer number ‘I’, converts it into binary form and creates a new integer with only the binaries of ‘I’ which are on the left of ‘POS’ with length ‘LEN’.

Algorithm 1 Particle Number

```

1: N = 0;
2: phase(0:5);
3: do j=0,4
4:   N = N + IBITS(25,j,1)
5:   phase(j+1)=phase(j)+IBITS(25,j,1)
6: end do

```

Alg. 1 counts the number of electrons ‘N’ in the configuration $|11001\rangle$. We set ‘LEN=1’ in ‘IBITS’ to monitor the current bit (occupation) by looping through each binary digit (orbital) of the configuration 25. Additionally, we created an array ‘phase’ which provides the number of electrons on the left of each orbital. The

output of ‘phase’ for configuration $|11001\rangle$ is $[0, 1, 1, 1, 2, 3]$, where two electrons are on the left of orbital 0. Now we can create full basis configurations for the TM $3d$ orbitals including spin. There are $2^{10} = 1024$ possible configurations if we do not restrict the particle number in the TM $3d$ orbitals. The following example, shown in Alg. 2, treats up and down spin separately. We restrict ourselves to all possible configurations with ‘nprtcl=7’ electrons in the TM $3d$ orbitals, which reduces the basis size to $\binom{10}{7} = 120$ configurations.

Algorithm 2 Basis Creation

```

1: nbit(0:1023)=(/(SUM(IBITS(j,POS(0:9),1)),j=0,1023)/)
2: mref = 2*5-1; shift=5; nprtcl = 7
3: n0=0
4: DO jd=0,mref
5:   DO ju=0,mref
6:     IF( nbit(ju)+nbit(jd) /= nprtcl ) CYCLE
7:     n0 = n0+1
8:     Shell_Conf(n0) = ju + ISHFT(jd,shift)
9:   END DO
10: END DO
11: Shell_Dim=n0

```

The array ‘nbit’ provides the number of electrons for each of the 2^{10} possible configurations. Here, we use the first 512 entries because we split up the spin configurations. The variable ‘mref’ provides the number of total configurations for each spin. Two loops, corresponding to both spins, iterate through each configuration, where ‘jd’ (‘ju’) denotes down (up) spin. The ‘IF’ statement monitors the particle number of each configuration allowing only configurations with ‘nprtcl=7’. The variable ‘n0’ counts the number of valid configurations. We use ‘ISHFT(I,SHIFT)’ to convert the integer into binary (Dirac) form and adding ‘SHIFT’ zeros on the right of the binary form of ‘I’. I.e. we assume an up spin configuration $ju = 15 \hat{=} |01111\rangle$ and a down spin configuration $jd = 11 \hat{=} |01011\rangle$. ‘ISHIFT’ manipulates the down spin configuration

$$\text{ISHIFT}(jd, 5) = 352 \hat{=} |0101100000\rangle. \quad (2.94)$$

By adding the shifted down-spin configuration 352 with the up-spin configuration 15 we obtain $\text{Shell_Conf} = 367 \hat{=} |0101111110\rangle$. This TM $3d$ configuration contains seven electrons. In Alg. 2 we store all $\text{Shell_Dim} = 120$ configurations as integers into the array ‘Shell_Conf’ which provides a fast and memory friendly basis set. Here we note, that for further purposes one should create an additional array with the position of each configuration in ‘Shell_Conf’. This is useful for the evaluation of matrix elements $\langle \text{Shell_Conf} | \hat{H} | \text{Shell_Conf} \rangle \neq 0$, where \hat{H} manipulates configurations in $|\text{Shell_Conf}\rangle$ with creation and annihilation operators. By using the

additional array with the position of each configuration we know the position of the new configuration in $\langle \text{Shell_Conf} |$.

The creation and annihilation operators of \hat{H} can also be written in binary and thus integer form. The annihilation operator for an electron in orbital 3 reads

$$c_3 \hat{=} 01000_2 = 8. \quad (2.95)$$

By applying this annihilation operator onto configuration $|11001\rangle$ we initially have to verify the existence of an electron in orbital 3 with the FORTRAN command ‘IAND(I,J)’. ‘IAND’ compares two integers ‘I’ and ‘J’ bit-wise and provides an integer with bits equal to one as output if they coincide in ‘I’ and ‘J’, e.g. $\text{IAND}(8, 25) = \text{IAND}(01000_2, 11001_2) = 8 = 01000_2$. By combining ‘IBITS’ and ‘IAND’ we obtain a small routine which monitors the existence of an electron in a given orbital, e.g. for configuration 25 at position 3: $\text{IBITS}(\text{IAND}(8, 25), 3, 1) \stackrel{!}{=} 1$. The annihilation is obtained by the exclusive-or command ‘IEOR(I,J)’, where ‘I=8’ denotes the annihilation operator and ‘J=25’ the configuration in integer form. In our example we obtain for the annihilation $\text{IEOR}(8, 25) = 17 \hat{=} |10001\rangle$, where we did not consider the phase factor

$$c_3 |11001\rangle = - |10001\rangle. \quad (2.96)$$

However, the phase factor is stored in the array ‘phase’ with one electron on the left of orbital 3, resulting in a negative sign. The creation operators are described similarly to the annihilation operators. The creation operator for an electron in orbital 2 reads

$$c_2^\dagger = 00100_2 = 4. \quad (2.97)$$

By letting c_2^\dagger act on configuration $|10011\rangle$, we obtain

$$c_2^\dagger |10011\rangle = - |10111\rangle, \quad (2.98)$$

where the condition for the creation is similar to the condition of the annihilation process with $\text{IBITS}(\text{IAND}(4, 19), 2, 1) \stackrel{!}{=} 0$. The creation of an electron is achieved by $\text{IEOR}(4, 19) = 23 \hat{=} |10111\rangle$ with consideration of the negative phase factor stored in array ‘phase’.

2.8 Workflow

Here, we elucidate the workflow of our core-level spectroscopy approach, which is based on the Anderson impurity model extended by core orbitals and a hybridization function obtained by first principle calculations, see Fig. 2.17.

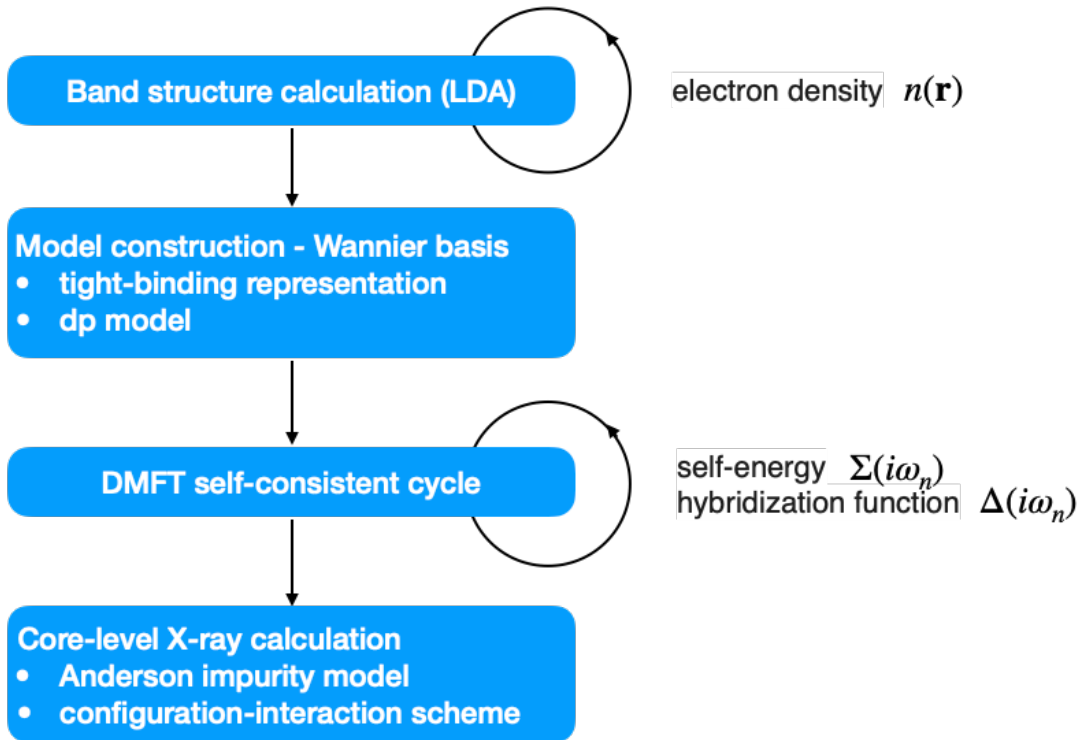


Figure 2.17: Workflow of our core-level spectroscopy approach based on the Anderson impurity model description. Figure adapted from [22].

We start our core-level X-ray studies with the crystal structure of the compound. We use WIEN2k [126] to calculate the electron density of the system. The choice of the exchange and correlation potential $E^{\text{xc}}[n(\mathbf{r})]$ used in DFT is usually not critical for our calculations. Hence, we apply the standard LDA potential. We note, that we perform paramagnetic DFT calculations without active spin-orbit coupling for most materials. The spin-orbit coupling as well as the possible antiferromagnetic ordering can be added in the DMFT calculations later on.

We use the Bloch functions from a converged DFT solution and construct Wannier functions with the WANNIER90 [130] package and the WIEN2WANNIER [131] interface, which are both included in WIEN2k [126]. For the Wannierization we use a set of local basis functions to create maximally localized Wannier functions. If bands are entangled, we apply disentanglement in a proper energy window. Then we construct the lattice model with local interaction U_{dd} . The spin-orbit coupling and the Coulomb interaction are calculated with an atomic Hartree-Fock code by Cowan [121]. The Coulomb interaction of the TM 3d shells, is parameterized by the Slater integrals F_0 , F_2 and F_4 . We fix the ratio $F_4/F_2 = 0.625$, that enables

us to determine the Coulomb vertices $U_{\kappa\lambda\mu\nu}$ using Hubbard $U = F_0$ and Hund's $J = (F_2 + F_4)/14$ parameters [115].

To obtain the electronic structure of the lattice model we use DMFT. We know the formal valence of the TM ion in the compound and thus, we can roughly determine the charge-transfer energy. The charge-transfer energy Δ_{CT} is related to the double-counting energy μ_{dc} , see Eq. 2.71. Thus, we scan μ_{dc} within a narrow energy window of a few eV. The μ_{dc} is fixed by comparison of the valence spectra to experimental (inverse) photoemission spectra. In the antiferromagnetic order, the self-energy obeys the condition $\tilde{\Sigma}_{\sigma}^A(i\omega_n) = \tilde{\Sigma}_{-\sigma}^B(i\omega_n)$ for atom A and B in the magnetic unit cell. Furthermore, we apply a magnetic field in the first few iterations of antiferromagnetic DMFT calculations. The paramagnetic phase usually contains just one TM ion in the unit cell and can be enforced with the condition $\tilde{\Sigma}_{\sigma}(i\omega_n) = \tilde{\Sigma}_{-\sigma}(i\omega_n)$, by using the same self-energy for both spins. We apply the strong coupling continuous-time quantum Monte Carlo method [136–138, 144] with density-density approximation to the Coulomb vertices to compute the self-energy of the auxiliary Anderson impurity model. After convergence of the DMFT cycle we analytically continue the self-energy with the maximum entropy method [139, 140] in order to obtain the hybridization function $\Delta(\varepsilon)$ in the real-frequency domain. Then we discretize the hybridization function and use it to construct an Anderson impurity model extended by core-orbitals. Usually we use between 25 and 30 energy levels per orbital and spin.

For the core-level spectroscopy studies we apply the same spin-orbit and Coulomb parameters for the TM $3d$ interaction as in the lattice model. The parameters of the radial parts of the Coulomb interaction, including higher-order Slater integrals, are discussed in Sec. 2.2.3. To calculate the spectral functions we perform exact diagonalization. For RIXS spectral functions we calculate the propagation of the initial states by the resolvent $(\omega_{\text{in}} + E_n - \hat{H}_{\text{AIM}} + i\Gamma)^{-1} \hat{T}_i |n\rangle$ with active core-hole. The numerical propagation is achieved by using the conjugate-gradient-based method [2]. We calculate the core-level spectra for different charge-transfer energies (= different double-counting energies) and compare them to experimental spectra if available. In case of uncertainties we additionally scan the Coulomb interaction parameters U_{dd} and U_{pd} .

Chapter 3

1s and 2p X-ray Photoemission Spectroscopy of Correlated Materials

We study 1s and 2p hard X-ray photoemission spectra (XPS) in series of late transition metal oxides, where we have chosen compounds with different initial configurations in the ground state; starting with $3d^5$ for Fe_2O_3 , $3d^6$ for FeTiO_3 , $3d^7$ for CoO and $3d^8$ for NiO . The different initial state configurations enable us to test the theoretical modelling of XPS with the Anderson impurity model approach comprehensively. We show, that 1s hard X-ray photoemission is a sensitive probe of the chemical bondings and non-local charge-transfer screening. The calculated spectra well agree with the experimental ones. This chapter is based on

[4] "Charge transfer effect in hard X-ray 1s and 2p photoemission spectra: LDA+DMFT and cluster-model analysis"

M. Ghiasi, A. Hariki, M. Winder, J. Kuneš, A. Regoutz, T.-L. Lee, Y. Hu, J.-P. Rueff, and F. M. F. de Groot
Phys. Rev. B **100**, 075146 (2019).

Extended text passages which are directly adopted from the publication are marked with a black bar.

3.1 Introduction

We compare the cluster model with the Anderson impurity model approach, where we use the hybridization function obtained by first principle calculations. Thus, we are able to distinguish the local and non-local screening contributions observed in the 1s and 2p spectra. The 2p spectra are a popular choice for the study of 3d transition-metal oxides. We demonstrate that the disentanglement of the local and non-local screening contributions in the 2p spectra is a complex task due to rich core-valence multiplets. I.e. the charge-transfer features in 2p XPS are buried in complex spectra reflecting the 2p-3d core-valence multiplets and spin-orbit coupling in the 2p shell. These effects are absent in the 1s XPS spectra. We use the 1s spectra,

where the asymmetric shape of the 1s XPS main line is found to be a fingerprint of non-local screening effects. In practice, little additional effort is required to measure 1s XPS together with valence or other core-level spectra. Despite the large life-time broadening, the absence of the core-valence multiplets and spin-orbit coupling allows 1s XPS to be used to identify charge-transfer satellites at higher binding energies. This enables an accurate estimation of material-specific parameters [42, 145]. We note, that there is a 1s–3d exchange interaction, but the interaction strength is only a few meV. Thus, this effect is not visible in the spectral shape. The accuracy of the *ab-initio* calculated material-specific parameters is examined by comparison with the present experimental 1s XPS data.

3.2 Computational Details

The experimental spectra are obtained at room temperature. We enlarge the unit cell of NiO, CoO and Fe₂O₃ for DMFT calculations to simulate the antiferromagnetic ordering observed experimentally below $T \approx 300$ K.

We used the following computational parameters for both, the cluster model and the LDA+DMFT approach: the Coulomb interaction of the 3d electrons U_{dd} ; the core-valence Coulomb interactions U_{sd} (U_{pd}) in the 1s (2p) XPS; Slater integrals representing the multipole part of the Coulomb interaction; one-particle hopping parameters; crystal-field splitting; and charge-transfer energy Δ_{CT} . The U_{dd} value is fixed by consulting with DFT-based estimates or previous XPS studies, as given in Table 3.1. The core-hole potential U_{sd} (U_{pd}) is fixed by fitting the experimental core-level spectra. Based on experimental observations, we use the same value for U_{sd} and U_{pd} . The multipole part of the core-valence interaction is determined by the Slater integrals F_k and G_k , see Eq. B.17 and Eq. B.18. The spin-orbit coupling in the 2p and 3d shell, and the Slater integrals F_k , G_k are calculated with an atomic Hartree-Fock code. The F_k and G_k values are scaled down to 80% of the Hartree-Fock values to simulate the effect of intra-atomic configuration interaction from higher basis configurations, which is a successful empirical treatment [50, 78, 121, 122, 146].

The one-particle hopping and the crystal-field parameters are obtained from the LDA bands. The double-counting correction μ_{dc} in LDA+DMFT is treated as an adjustable parameter and fixed by comparison to the valence photoemission spectra [31]. For FeTiO₃, μ_{dc} is determined to reproduce the experimental gap (≈ 2.5 eV) [147] since valence photoemission data are not reported so far. The computed XPS intensities are broadened using Gaussian function to simulate the instrumental resolution and the finite core-hole life time.

	Fe ₂ O ₃ Fe ³⁺ (<i>d</i> ⁵)	FeTiO ₃ Fe ²⁺ (<i>d</i> ⁶)	CoO Co ²⁺ (<i>d</i> ⁷)	NiO Ni ²⁺ (<i>d</i> ⁸)
10 <i>Dq</i>	0.5	0.25	0.25	0.45
Δ	3.7	3.5	4.1	4.4
<i>U</i> _{<i>sd</i>} (<i>U</i> _{<i>pd</i>})	8.4	8.0	8.6	7.8
<i>U</i> _{<i>dd</i>}	6.4	6.4	6.8	6.5
<i>V</i> _{<i>T</i>_{2<i>g</i>}}	1.3	1.3	1.2	1.2
<i>V</i> _{<i>E</i>_g}	2.5	2.1	2.0	2.1
Γ _{1<i>s</i>}	0.7	1.1	0.9	0.9
Γ _{2<i>p</i>}	0.5	0.5	0.4	0.4

Table 3.1: Summary of the parameter values in the present study: crystal-field splitting between E_g and T_{2g} states (10*Dq*), charge-transfer energy (Δ_{CT}), core-hole potential for 1*s* (U_{sd}) and 2*p* (U_{pd}) XPS, 3*d* Coulomb interaction (U_{dd}), hopping amplitude of the nearest-neighboring ligand states and transition metal E_g (V_{E_g}) and T_{2g} ($V_{T_{2g}}$) state. Γ_{1s} and Γ_{2p} are the Gaussian broadening (half width at half maximum) included in theoretical 1*s* and 2*p* spectra, respectively. In Fe₂O₃ and FeTiO₃, the triply-degenerate T_{2g} states split into double-degenerate $E_{g\pi}$ states and single A_{1g} state. The values of the T_{2g} state in the table are obtained by averaging over the ones of the $E_{g\pi}$ and A_{1g} states. In actual calculation, the splitting of the $E_{g\pi}$ and A_{1g} states is taken into account explicitly. All values are in eV. Table and caption taken from [4].

3.3 Ni 1*s* and Ni 2*p* X-ray Photoemission Spectroscopy of NiO

Figure 3.1 shows Ni 1*s* and 2*p* XPS spectra of NiO, together with the calculated spectra obtained by the cluster model and the LDA+DMFT approach. The 1*s* main line around 8311 eV corresponds to $\underline{c}d^9\underline{v}$ configuration, where \underline{c} and \underline{v} denote a 1*s* core-hole and a hole in the valence band, respectively. In addition, the charge-transfer satellite with a mixed character of $\underline{c}d^8$ and $\underline{c}d^{10}\underline{v}^2$ configurations is clearly observable around 8318 eV. The Ni 1*s* XPS spectrum is free from spin-orbit coupling in the core level, while the 2*p* spectrum is composed of 2*p*_{3/2} ($\approx 868 - 853$ eV) and 2*p*_{1/2} ($\approx 885 - 870$ eV) components. Since the spin-orbit coupling in the Ni 2*p* core level is large (≈ 11 eV), the Ni 2*p*_{3/2} and 2*p*_{1/2} components have no overlap. The 2*p*_{3/2} (2*p*_{1/2}) main line is located around 854 eV (873 eV) and the 2*p*_{3/2} (2*p*_{1/2}) charge-transfer satellite is observed around 861 eV (878 eV).

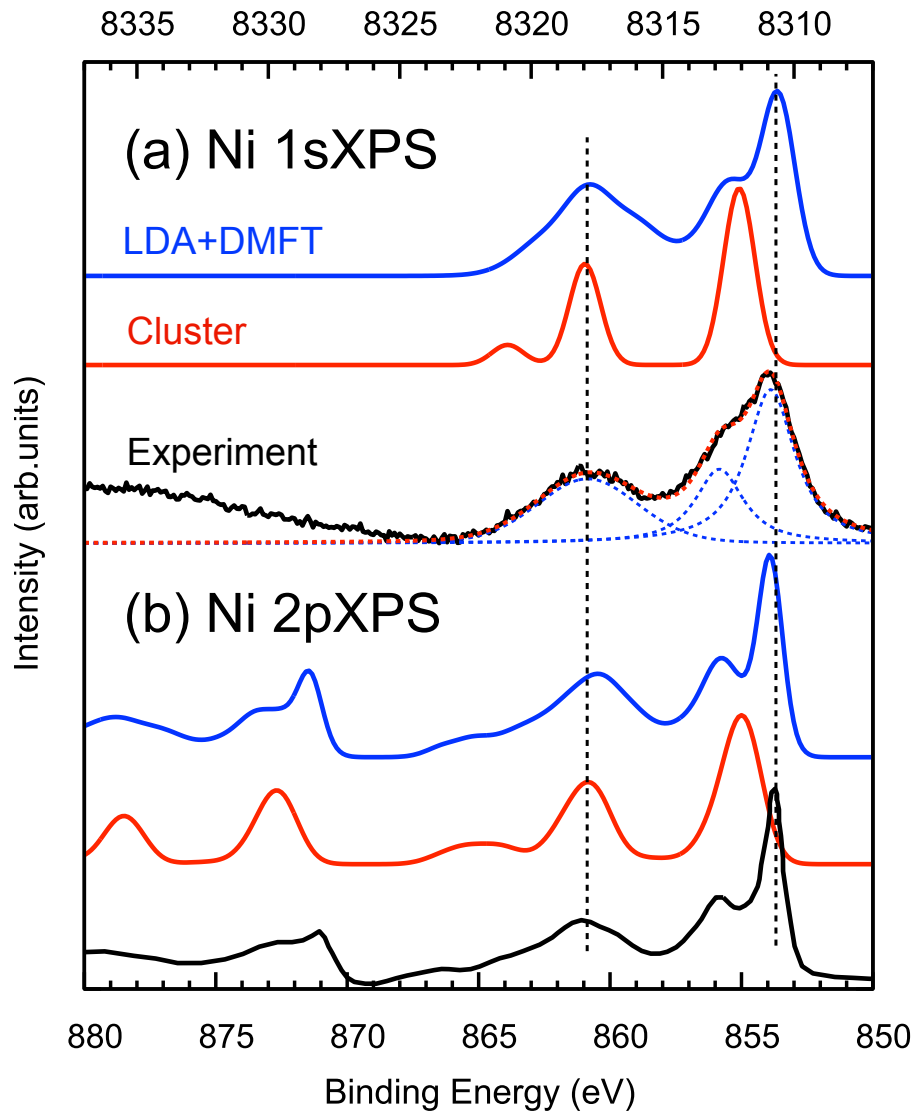


Figure 3.1: Experimental Ni $1s$ and $2p$ XPS spectra of NiO (black) are compared with LDA+DMFT in the antiferromagnetic phase (black, solid) and cluster-model (red, solid) calculations. The Gaussian spectral broadening of 0.7 (0.5) eV (HWHM) is taken into account in the calculated $1s$ ($2p$) spectra. The experimental Ni $2p$ XPS data is taken from Ref. [32]. The fitting result (red, dashed) using Voigt functions (black, dashed) for the $1s$ data is shown together. Figure and caption taken from [4].

The splittings of the main line and the charge-transfer satellite in the Ni $1s$ and $2p$ spectra are almost identical to each other (≈ 6 eV), indicating the values of the core-hole potential U_{sd} and U_{pd} are comparable. Indeed, the LDA+DMFT calculation with $U_{sd} = U_{pd} = 7.8$ eV reproduces the splitting of the main and charge-transfer satellite well, in both the $1s$ and $2p$ XPS spectra. A double-peak feature is observed in the $2p_{3/2}$ main line. The lower (higher) binding-energy

E_B side of the double peaks is due to the non-local (local) screening in the final states [31, 32, 39]. The LDA+DMFT result qualitatively reproduces the Ni 2p XPS data including the double-peak lacked in the cluster-model result. We find that a double peak is discernible in the 1s main line despite the larger core-hole broadening. The similarity to the $2p_{3/2}$ main line and its presence/absence in the LDA+DMFT/cluster-model spectra suggests its non-local screening origin. In addition, the charge-transfer satellite shows a noticeable difference in the cluster and LDA+DMFT results, indicating the non-local screening affects not only the main line but also the satellite with a higher binding energy. This is because the charge-transfer satellite has a contribution of the $cd^{10}\underline{v}^2$ configuration, the so-called over-screened states, in which the non-local screening takes part.

3.3.1 Hybridization Dependence

We study the hybridization dependence of the Ni 1s core-level spectra, where we systematically extend the hopping between impurity and its neighbors. This provides us a detailed study of the non-local screening effects observed in the core-level XPS spectra.

In contrast to the real-space approach of the multi-site cluster model [33], LDA+DMFT includes both local-screening and non-local screening effects in the hybridization function $\Delta_\gamma(\varepsilon)$ of the Anderson impurity model, see Eq. 2.31, where γ denotes orbital and spin. To see the connection between this description and the real-space one, Fig. 3.2a shows the distance dependence of the hybridization intensity $V_\gamma(\varepsilon) = \sqrt{-\frac{1}{\pi}\Im\Delta_\gamma(\varepsilon)}$ in NiO. Starting from a single peak in the $V_\gamma(\varepsilon)$ of the cluster model, which corresponds to the hybridization with nearest-neighbor oxygen atoms, $V_\gamma(\varepsilon)$ acquires a band character by taking more distant atoms into account. We note that the truncated $V_\gamma(\varepsilon)$ in panels (I)-(IV) and (V) is computed in non-interacting finite-size clusters and infinite lattice, respectively. The intensities around -2 to 2 eV correspond to the hybridization with Ni $3d$ bands. These intensities are rather weak compared to those arising from O $2p$ bands (≈ -4 eV) due to a smaller amplitude of direct metal-metal hopping as well as indirect hopping, e.g., via a metal-ligand-metal path. The electronic correlation represented by the DMFT self-energy, see Eq. 2.66, modifies the $V(\varepsilon)$ dramatically and a gap opens at the Fermi energy. Figure 3.2b shows the calculated 1s XPS spectra by the Anderson impurity model with the truncated hybridization intensities $V_\gamma(\varepsilon)$. By taking surrounding Ni ions into account, a new peak develops in the low-binding-energy side of the main line. This accompanies a noticeable shift of the local-screening peak (≈ 8312 eV) because of the following reason. In the cluster model, the main line is composed of mainly $cd^9\underline{L}$ configuration. By including the charge transfer from surrounding Ni ions, $cd^9\underline{D}$ configuration contributes the main line (here, \underline{D} denotes a hole on the neighbor Ni ion). In the impurity picture, though there is no coupling

between $cd^9\bar{L}$ and $cd^9\bar{D}$ configurations, indirect coupling via (unscreened) cd^8 configuration (i.e. $cd^9\bar{L} \leftrightarrow cd^8 \leftrightarrow cd^9\bar{D}$) gives rise to effective repulsion between the two screened configurations. However, we find a qualitative difference in the main-line shape between the experimental data and the spectra in (I)-(V). The LDA+DMFT result in the paramagnetic phase, see (VI), shows double peaks in the main line although their splitting is narrow. The LDA+DMFT result in the antiferromagnetic phase, see Fig. 3.1b, reproduces the double-peak feature qualitatively. The $V_\gamma(\varepsilon)$ in LDA, in principle, includes hybridization with all valence states in the non-interacting lattice, indicating the importance to include the correlated Ni 3d band and the magnetic ordering properly to describe the XPS spectra.

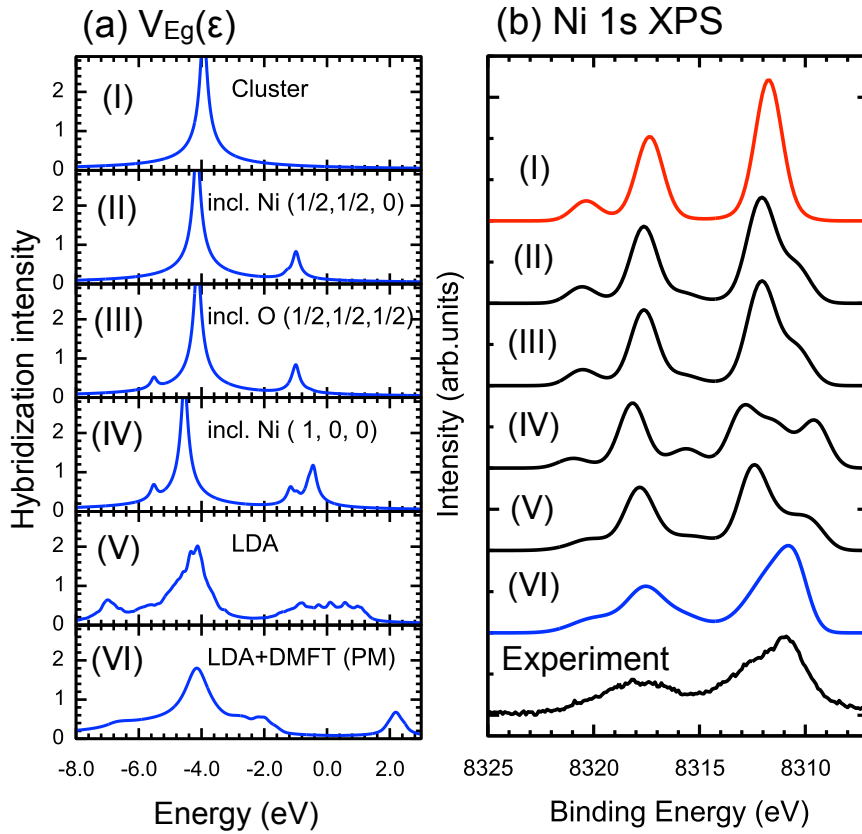


Figure 3.2: (a) Hybridization intensities for the E_g state in NiO. From top to bottom, the long-distance hoppings including the atom denoted in the bracket are taken into account. $V_{E_g}(\varepsilon)$ in panels (I)-(IV) and (V) are computed in the non-interacting finite-size clusters and infinite lattice, respectively. The $V_{E_g}(\varepsilon)$ obtained in the LDA+DMFT calculation for the paramagnetic phase is shown in panel (VI), for comparison. The $V_{E_g}(\varepsilon)$ for the antiferromagnetic phase is found in Ref. [31]. (b) Ni 1s XPS calculated by the Anderson impurity model with the hybridization intensities in Fig. (a). Figure and caption taken from [4].

3.4 Co 1s and Co 2p X-ray Photoemission Spectroscopy of CoO

Figure 3.3 shows Co 1s and 2p XPS spectra of CoO, together with the calculated spectra of the cluster model and the LDA+DMFT approach.

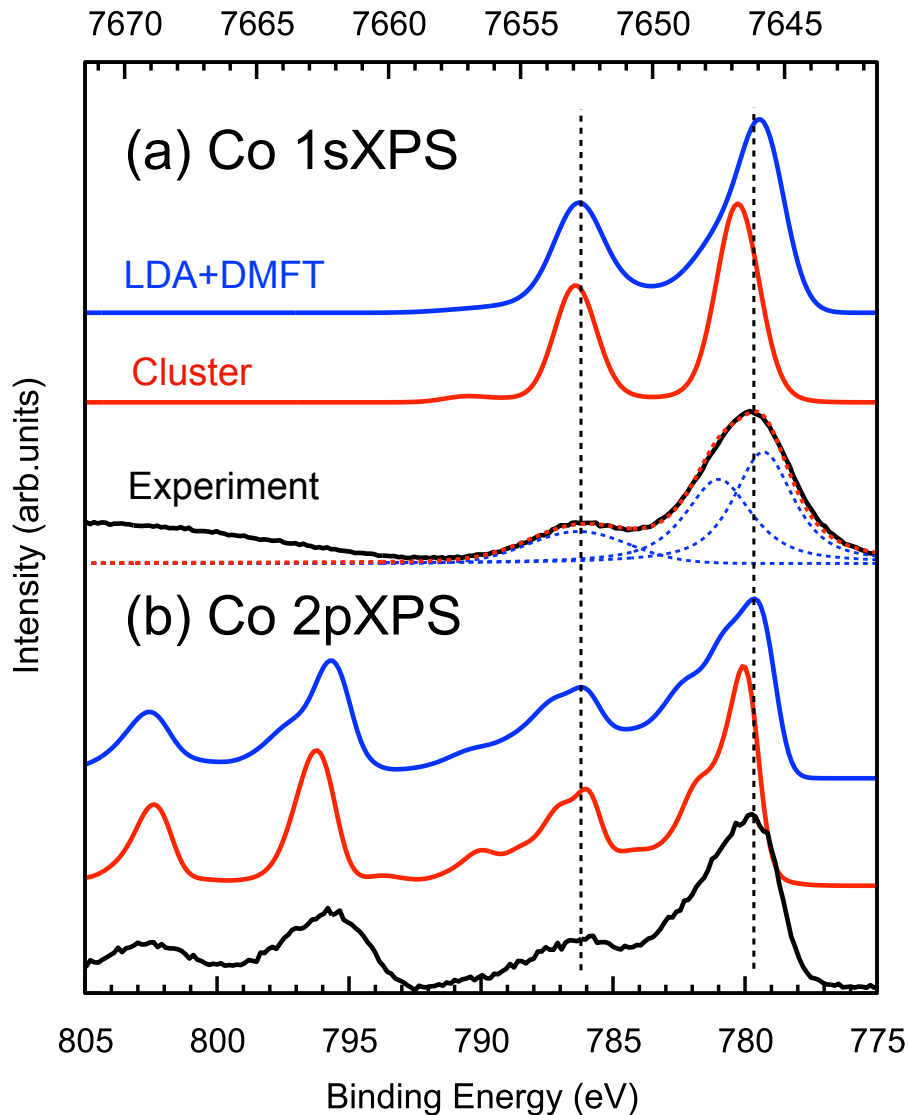


Figure 3.3: Experimental Co 1s and 2p XPS spectra of CoO (black) are compared with LDA+DMFT (black, solid) and cluster-model (red, solid) calculations. The Gaussian spectral broadening of 1.1 (0.5) eV (HWHM) is taken into account in the calculated 1s (2p) spectra. The fitting result (red, dashed) using Voigt functions (black, dashed) for the 1s data is shown together. Figure and caption taken from [4].

The Co 1s XPS, see Fig. 3.3a, shows the main line (≈ 7647 eV) corresponding to $\underline{cd^8v}$ configuration and the charge-transfer satellite (≈ 7653 eV). In the 2p spectra, $2p_{3/2}$ ($2p_{1/2}$) component is located in 794 – 778 eV (807 – 795 eV), in which the main line and satellite are observed around 780 eV (796 eV) and 787 eV (803 eV), respectively. The splitting of the main line and the charge-transfer satellite in the 1s and 2p spectra is almost identical (≈ 6 eV). The 1s main line has an asymmetric shape with a shoulder on the higher binding energy E_B side. Because of the absence of the core-valence multiplets in Co 1s spectra, the Co 1s main line is expected to be a single peak. Indeed, the cluster-model calculation yields a symmetric main line. On the other hand, the LDA+DMFT spectrum contains an asymmetric main line, suggesting the non-local screening is the origin of the asymmetry of the main line. Then, in Co 2p spectra, we find the $2p_{3/2}$ main line is rather broad, in a clear contrast to the Ni $2p_{3/2}$ main line of NiO. The LDA+DMFT result well reproduces the broad shape of the main line as well as of the charge-transfer satellite, compared to the cluster-model result. The difference between the LDA+DMFT and cluster-model results suggests that the non-local screening from Co 3d bands plays a role in the formation of the broad asymmetric main line [31]. However, the Co $2p_{3/2}$ main line in the cluster-model result has inner features due to rich 2p-3d core-valence multiplets in the $\underline{cd^8v^1}$ configuration. Thus a theoretical simulation is required to disentangle the local screening and non-local screening contributions in the Co 2p spectra [31].

3.5 Fe 1s and Fe 2p X-ray Photoemission Spectroscopy of Fe₂O₃

Figure 3.4 shows Fe 1s and 2p XPS spectra, together with the calculated spectra by LDA+DMFT and cluster model. The Fe 1s spectrum shows three peaks: main line (≈ 7118.5 eV), the first satellite (S1 : ≈ 7128 eV) and the second satellite (S2 : ≈ 7135 eV). The energy splittings of the main line and satellites are rather large (≈ 9.5 eV for S1 and ≈ 17 eV for S2) compared to those in NiO and CoO (≈ 6 eV). The large splitting in Fe₂O₃ can be explained by the value of the effective hybridization V_{eff} [30, 148, 149],

$$V_{\text{eff}} = \sqrt{(4 - N_{E_g})V_{E_g}^2 + (6 - N_{T_{2g}})V_{T_{2g}}^2},$$

where N_{E_g} ($N_{T_{2g}}$) and V_{E_g} ($V_{T_{2g}}$) are the occupation of the E_g (T_{2g}) states and the (bare) hybridization intensity between ligand and the E_g (T_{2g}) orbitals. For simplicity, octahedral symmetry is assumed and the effect of long-distance hopping (non-local screening) is not taken into account in the qualitative discussion. The V_{eff} values in NiO, CoO and Fe₂O₃, computed for high-spin ground state in formal valence, are 2.97, 3.24, and 4.19 eV, respectively. Thus the different

configurations (d^n , $d^{n+1}\underline{L}$, $d^{n+2}\underline{L}^2$, here \underline{L} denotes a hole in nearest-neighbor ligands) are split more in Fe_2O_3 as compared to NiO and CoO, yielding the large separations of the main line and satellites in Fe 1s XPS. Thus in Fe and earlier transition-metal oxides [117, 148, 149], the hybridization strength between transition metal 3d and surrounding atoms can be estimated accurately by the satellite positions since the large V_{eff} magnifies its bare value.

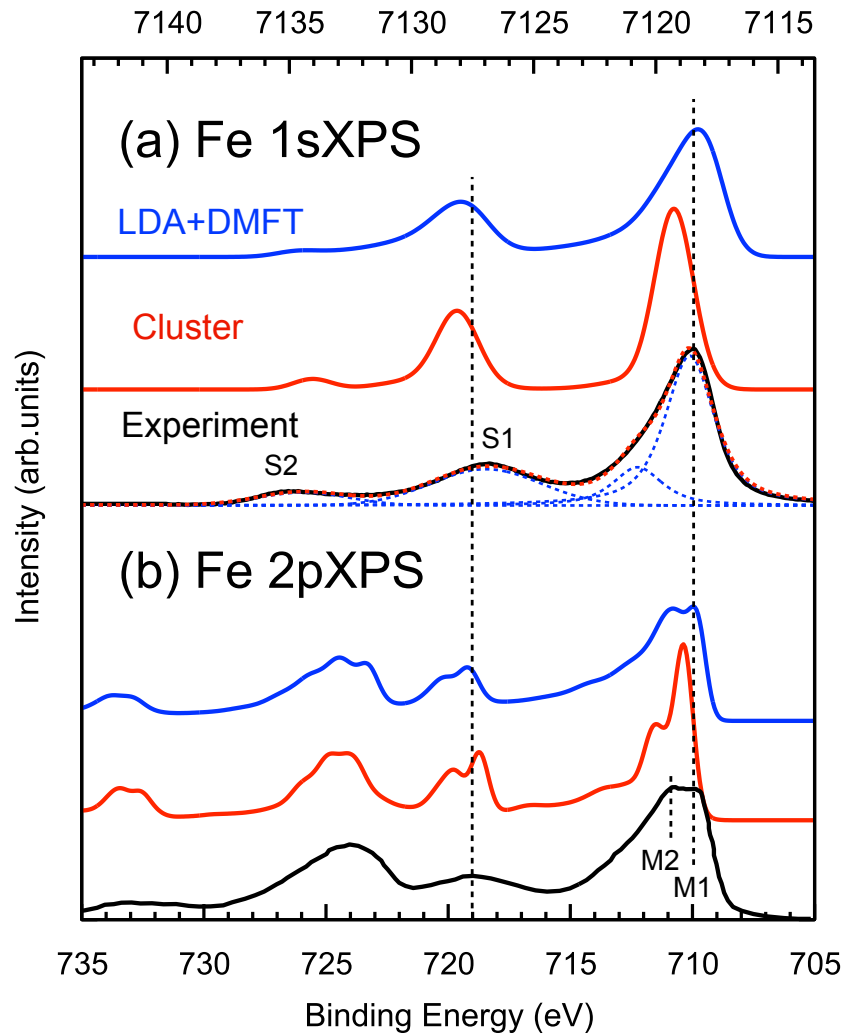


Figure 3.4: Experimental Fe 1s and 2p XPS spectra of Fe_2O_3 (black) are compared with LDA+DMFT (black, solid) and cluster-model (red, solid) calculations. The spectral broadening using a Gaussian of 0.9 (0.4) eV width (HWHM) is taken into account in the calculated 1s (2p) spectra. The experimental data of Fe 2p XPS is taken from Ref. [42]. In the 1s spectra, the first and second satellites are labeled as S1 and S2 in Fig. 3.4a, respectively. The fitting result (red, dashed) using Voigt functions (black, dashed) for the 1s data is shown together. Figure and caption taken from [4].

Both the LDA+DMFT and the cluster-model calculations reproduce the positions of the satellites reasonably well, reflecting the accuracy of hopping parameters obtained from the LDA calculation. However, in the Fe $2p$ spectrum, Fig. 3.4b, the second satellite S2 is not visible due to its overlap with the main line of the Fe $2p_{1/2}$ component (≈ 725 eV). Thus, thanks to the absence of spin-orbit coupling, $1s$ XPS complements the $2p$ XPS information about bonding. The Fe $2p_{3/2}$ main line shows a double-peak shape, marked as M1 and M2 in the figure, that is well reproduced in the LDA+DMFT result. The difference in the LDA+DMFT and cluster-model results is attributed to the contribution of the non-local screening, the M2 intensity is enhanced relative to the M1 one. However, as seen in the cluster-model spectrum, Fig. 3.4b, the main line has a rich fine structure also due to the core-valence Coulomb multiplets, which makes determination of the non-local screening contribution a difficult task. On the contrary, the asymmetry of the Fe $1s$ XPS main line, observed in the experiment, Fig 3.4a, is solely due to non-local screening. As in CoO, the $1s$ main line of the cluster model consists of a single peak due to the absence of the core-valence multiplets, while that of the LDA+DMFT shows a clear asymmetry. Thus the shape of the $1s$ XPS main line provides an unambiguous signature of the non-local screening, while it is hidden in the complex structure of $2p$ XPS.

3.6 Fe $1s$ and Fe $2p$ X-ray Photoemission Spectroscopy of FeTiO₃

Figure 3.5 shows the experimental Fe $1s$ and $2p$ XPS spectra. In the Fe $1s$ spectrum, we observe a main line (≈ 7090 eV) and a charge-transfer satellite (S1 : ≈ 7097 eV). The energy splitting between the charge-transfer satellite (S1) and main line is 7 eV which is about 2.5 eV smaller compared to that in Fe₂O₃, see Fig. 3.4a. As found in Table. 3.1, the hopping amplitude between Fe and nearest-neighboring oxygen as well as other parameters does not differ so much in the two compounds. The large difference in the main-line – charge-transfer-satellite splitting comes from the value of the V_{eff} , 4.19 eV for Fe₂O₃ and 3.49 eV for FeTiO₃. The V_{eff} value in the divalent Fe system (d^6) is smaller than that in the trivalent Fe system (d^5) due to an additional electron in the T_{2g} orbital in the high-spin ground state, resulting in the observed smaller main-satellite splitting in FeTiO₃. In FeTiO₃, a higher- E_B charge-transfer satellite (S2) is rather weak and not observed in the present data, which is due to little contribution of the $|d^8v^2\rangle$ configuration to the ground state. The position of S1 and the absence of S2 are well reproduced in the LDA+DMFT calculation.

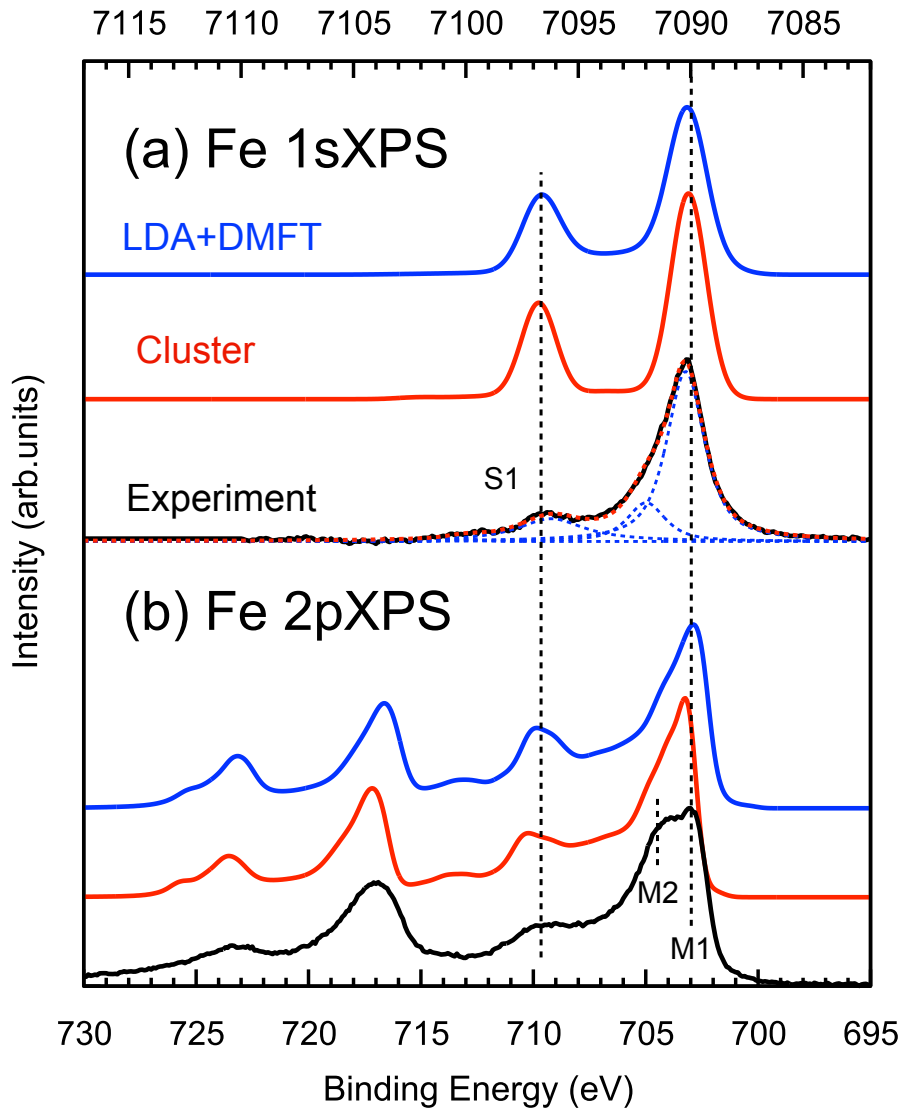


Figure 3.5: Experimental Fe 1s and 2p XPS spectra of FeTiO₃ (black) are compared with LDA+DMFT (black, solid) and cluster-model (red, solid) calculations. The spectral broadening using a Gaussian of 1.1 (0.4) eV width (HWHM) is taken into account in the calculated 1s (2p) spectra. The fitting result (red, dashed) using Voigt functions (black, dashed) for the 1s data is shown together. Figure and caption taken from [4].

We expect that the non-local screening plays a minor role in FeTiO₃ compared to Fe₂O₃ since Ti ions, formally tetravalent d^0 configuration, cannot provide electrons to screen the X-ray excited Fe ion. Simulation of the Fe 2p XPS of Fe₂O₃, Fig. 3.4b, revealed that non-local screening amplifies the intensity of M2 relative to M1. This is confirmed by comparing the experimental data of Fe₂O₃ and FeTiO₃. In FeTiO₃, Fig. 3.5b with weaker non-local screening, a smaller ratio

of M2 to M1 intensities than in Fe₂O₃ is observed. Indeed, the LDA+DMFT spectra of FeTiO₃ do not differ much from the cluster-model calculation, though the relative intensity of M1 and M2 is still noticeably modified by non-local screening. The main line of Fe 1s XPS in FeTiO₃ is rather sharp compared to that in Fe₂O₃, see the fitting analysis in Fig 3.5 and 3.4, indicating less non-local screening contribution. The intensity ratio of the low-energy peak (I_1) to the high-energy peak (I_2) in the main line is $I_1/I_2 = 3.92, 4.38$ for Fe₂O₃ and FeTiO₃, respectively. The smaller I_1/I_2 for Fe₂O₃ supports that the non-local screening is more effective in Fe₂O₃.

3.7 Conclusions

All spectral features in the studied compounds are well reproduced by the LDA+DMFT Anderson impurity model approach. This is not so for the cluster model approach. The comparison of the approaches provides information about the non-local screening effects. Despite rather large life-time broadening of the 1s spectra compared with the 2p counterparts, the charge-transfer satellites are clearly visible for the studied compounds. This holds also for charge-transfer satellites at higher binding energies, which are not obscured by the overlap of spin-orbit split edges as in the 2p spectra. Usually, the 1s charge-transfer satellites are well pronounced in the spectra of correlated insulators. Thus, they provide information about covalent bonding in these compounds. The absence of the core-valence multiplets in 1s XPS directly reveals the effect of non-local screening reflected in the asymmetry of the 1s main line. The shape of the 1s XPS spectra has implications for the interpretation of 1s (*K*-edge) X-ray absorption spectroscopy (XAS). In *K*-edge XAS, the electron excited from the 1s core-level to the broad 4p band is not bound to the excited transition-metal atom. The fact, that the 1s XPS spectra have multiple peaks implies that one X-ray photon energy creates a series of electrons with different kinetic energies. This is in contrast to the usual way to calculate *K*-edge XAS, i.e. it is assumed that the X-ray photon creates a single electron kinetic energy. To take the spectral shape of the 1s XPS spectra into account, the *K*-edge XAS spectra must be viewed as a convolution of the empty 4p density of states (as calculated from for example multiple scattering) and the 1s XPS spectrum. In other words, the detailed understanding of the *K*-edge XAS spectral shape requires the inclusion of many-body response to the core-hole potential as measured with the 1s XPS spectral shape, where we note that this approach is similar in concept to the charge-transfer satellite method as applied earlier [150–152]. If the 1s XPS spectral shape can be described by a single peak, the related *K*-edge XAS can be described from the multiple scattering of a single electron energy [153]. As shown here, charge-transfer satellites present a sizable contribution to the 1s XPS of late transition-metal oxides. Therefore a simultaneous analysis 1s XPS and 1s XAS is desirable for the detailed understanding of the 1s XAS spectral

shape.

We have studied both experimentally and theoretically the $1s$ and $2p$ hard X-ray photoemission spectra in a series of late transition metal oxides: Fe_2O_3 , FeTiO_3 , CoO and NiO . Despite the large core-hole life-time broadening, the $1s$ XPS benefits from the absence of core-valence multiplets and spin-orbit coupling effects in the spectra, which allows observation of high-energy satellites as well as the main-line asymmetry. These $1s$ XPS features can be interpreted in terms of material specific metal-ligand covalency (satellites) and non-local screening (main-line asymmetry). The $1p$ XPS is thus complementary to $2p$ XPS that has more complex spectra. Using LDA+DMFT approach we were able to reproduce the $1s$ and $2p$ XPS spectra of the studied materials, while the deviations from the cluster model allowed us to quantify the role of non-local screening. Based on the present $1s$ XPS results, we have pointed out the importance of the $1s$ XPS to interpret the $1s$ (K -edge) X-ray absorption spectra.

Chapter 4

*L*₃-Edge X-ray Absorption Spectroscopy and Resonant Inelastic X-ray Scattering of Correlated Materials

We present a computational *L*₃-edge X-ray absorption spectroscopy (XAS) and resonant inelastic X-ray scattering (RIXS) study of selected 3*d* transition-metal oxides. We have chosen the same compounds as in the previous X-ray photoemission spectroscopy study and included a few additional materials; NiO (3*d*⁸), cuprates (3*d*⁸), cobaltites (3*d*⁷ and 3*d*⁶) as well as Fe₂O₃ (3*d*⁵). Part of the study is the origin of the fluorescence-like (FL) feature, due to unbound electron-hole pair excitations and observed in the RIXS spectra of some of the compounds. There is a good agreement between calculated and experimental spectra. This chapter is based on

[2] "LDA+DMFT approach to resonant inelastic X-ray scattering in correlated materials"¹

A. Hariki, M. Winder, T. Uozumi, and J. Kuneš
Phys. Rev. B **101**, 115130 (2020),

with the exception of the *L*₃-edge XAS and RIXS study of cuprates which is based on

[5] "Continuum Charge Excitations in High-Valence Transition-Metal Oxides Revealed by Resonant Inelastic X-ray Scattering"

A. Hariki, M. Winder and J. Kuneš
Phys. Rev. Lett. **121**, 126403 (2018),

and also based on the master thesis of the author [22]. Extended text passages which are directly adopted from the publications are marked with a black bar.

¹Editors' Suggestion, A.H and M.W contributed equally to this work.

4.1 Introduction

We use the Anderson impurity model approach with a hybridization function obtained by LDA+DMFT [13, 133, 134]. This allows us to include the continuum of unbound electron-hole pairs (EHPs) as well as the charge transfer excitations in a unified and material specific manner. The Anderson impurity model approach lacks the momentum dependence of the bound electron-hole excitations such as magnons or excitons, but it allows a non-perturbative description of the initial (final) and intermediate states of the RIXS process, the continuum of unbound EHPs and many-particle excitations. Therefore, our approach provides a good description of the incident photon energy ω_{in} -dependence of the RIXS spectra. A complex situation arises when the formation of core-valence excitons compete with continuum excitations in the intermediate states at a given incident photon energy ω_{in} [5, 56]. This is manifested, for example in high-valence nickelates [57] and titanium heterostructures [56], by coexistence of the Raman-like (RL) and FL features near the X-ray absorption edge. The computational parameters of the studied compounds can be found in Sec. 3.2. The parameters of the additional compounds are explicitly discussed in the corresponding section.

4.2 Ni L_3 -Edge X-ray Absorption Spectroscopy and Resonant Inelastic X-ray Scattering of NiO

Figure 4.1a shows the valence spectra of NiO calculated by LDA+DMFT in the antiferromagnetic state at $T = 300$ K (below the experimental Néel temperature of 525 K). We employed $U = 7.0$ eV and $J = 1.1$ eV [31]. We find a fair agreement with experimental photoemission and inverse photoemission data [154] for a double-counting energy μ_{dc} in the range of 50 – 52 eV. The μ_{dc} dependence of valence, XAS and RIXS spectra is shown in Fig. 4.3. Here we present the result obtained with $\mu_{\text{dc}} = 50$ eV. Figure 4.1c shows Ni $L_{2,3}$ -edge XAS calculated using the LDA+DMFT and cluster model, together with the experimental data [43]. The Ni $L_{2,3}$ XAS is composed of the main line (ω_{in} between 850 – 855 eV), corresponding to $|\underline{c}d^9\rangle$ final-state configuration, and the weak satellite ($\omega_{\text{in}} \approx 856$ eV), corresponding to $|\underline{c}d^{10}\underline{v}\rangle$ configuration. Here, \underline{c} and \underline{v} denote a hole in $2p$ core level and valence bands, respectively. The LDA+DMFT and cluster-model results are almost identical to each other and show a good agreement with the experimental data. The match of the two is expected as the charge-transfer screening from the surrounding atoms is rather weak in the XAS final states. Figure 4.1d shows Ni L_3 -RIXS map obtained by LDA+DMFT. For comparison, Figs. 4.1e,f show the cluster-model result and the experimental data [155]. Three distinct RIXS features are observed: RL d - d excitations ($\omega_{\text{loss}} = 1 - 4$ eV); the charge transfer excitations ($\omega_{\text{loss}} = 4 - 8$ eV) showing a broad feature along ω_{loss} ; FL feature,

showing a linear increasing feature with ω_{in} . The RL and charge transfer excitations resonate mainly at the L_3 main line, while the FL feature appears for $\omega_{\text{in}} > 855$ eV. The LDA+DMFT spectrum shows a good overall agreement with the experimental data. In the cluster-model result, though the RL feature is reproduced, the charge transfer feature is found at a sharp ω_{loss} and the FL feature is missing due to the lack of the unbound EHP continuum in this description. The lowest d - d peak at 1.0 eV in the experimental data, corresponding to a single excitation from T_{2g} orbit to E_g orbit in the one-electron picture, is located at around 0.85 eV in both the LDA+DMFT and cluster-model results, see also in Sec. 4.2.1. In terms of the atomic symbols, this corresponds to ${}^3A_2 \rightarrow {}^3T_2$ excitation. The quantitative discrepancy could be attributed to underestimation of the E_g - T_{2g} splitting due to covalency in the present LDA calculation [156]. The FL feature originates from unbound EHP excitations. The low ω_{loss} -region of the FL features reflects the EHPs that involve low-energy valence bands, as demonstrated in Fig. 4.1g. There the hybridization intensity $V(\varepsilon) = \sqrt{-\frac{1}{\pi}\Im\Delta(\varepsilon)}$, see Eq. 2.31, from -2 to 0 eV is numerically removed, see Fig. 4.1b. Thus prohibiting creation of a hole in the low-energy valence bands in the RIXS process. As a result, the low- ω_{loss} part of the FL feature around $4 - 6$ eV disappears.

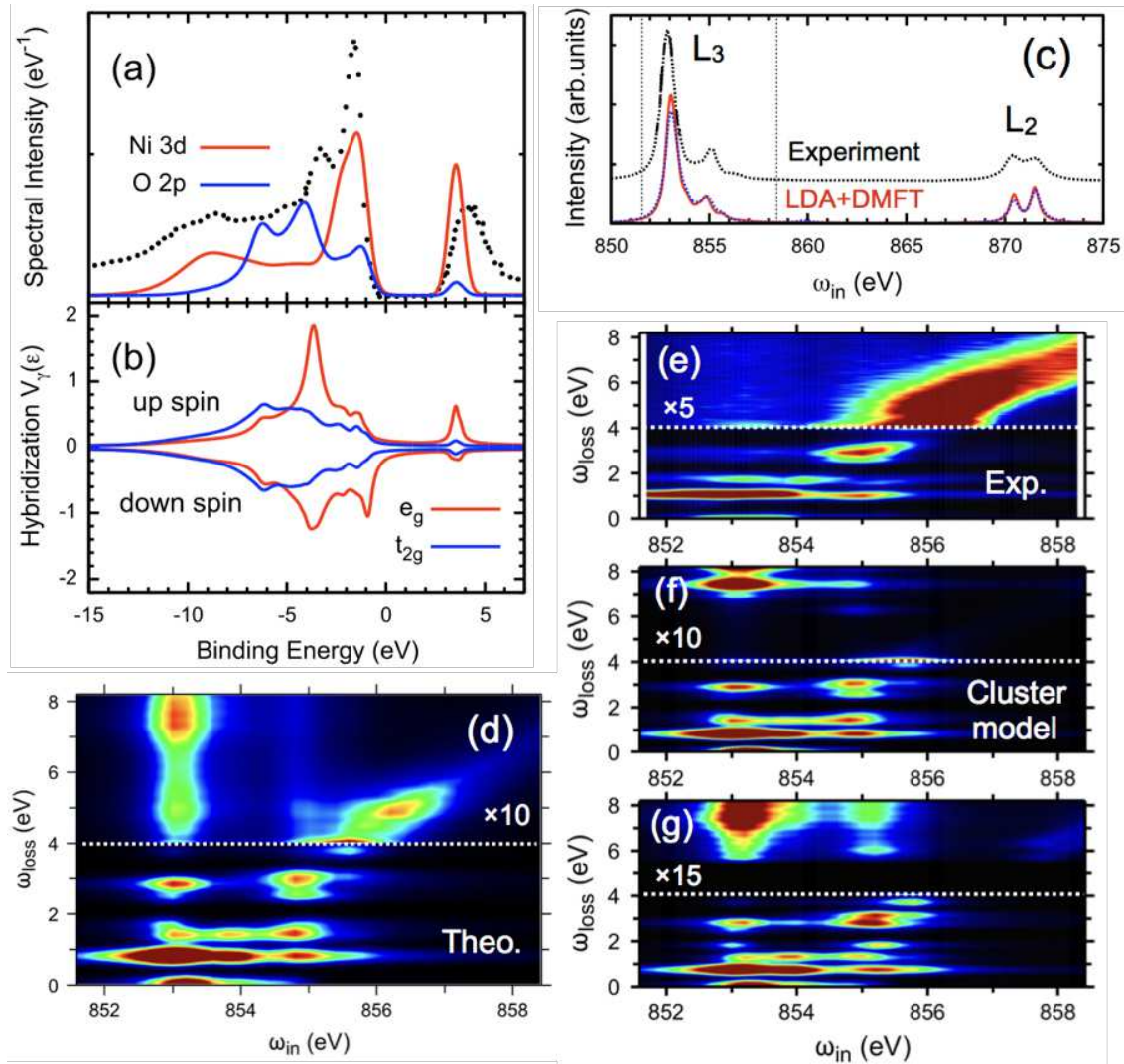


Figure 4.1: (a) LDA+DMFT valence spectra of NiO. The experimental data (black, dotted) are taken from Ref. [154]. (b) DMFT hybridization function. (c) Ni L_3 -edge XAS calculated by LDA+DMFT (solid), cluster model (blue, dashed) and the experimental data in Ref. [43]. RIXS spectra calculated by (d) LDA+DMFT. (e) experimental data [155]. (f) RIXS spectra calculated by the cluster model. (g) RIXS spectra calculated without hybridization intensities from -2.0 to 0.0 eV. The RIXS intensities above the horizontal lines (white) are magnified by a factor indicated in panels. The spectral broadening is taken into account using a Gaussian of 150 meV for RIXS, a Lorentzian 300 meV for XAS, and a Gaussian 600 meV for valence XPS. Figure and caption taken from [2].

The RIXS intensities calculated by the LDA+DMFT approach for $\mu_{dc} = 50$ eV and selected photon energies ω_{in} are shown together with the experimental data [155] in Fig. 4.2.

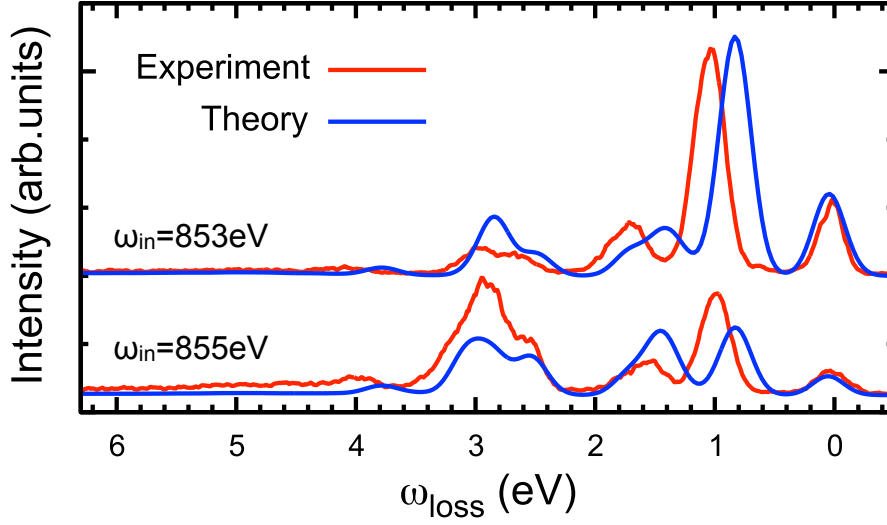


Figure 4.2: Ni L_3 -RIXS intensities calculated by LDA+DMFT ($\mu_{dc} = 50$ eV) for selected ω_{in} . The experimental data are taken from Ref. [155]. Figure and caption taken from [2].

4.2.1 Double-Counting Dependence

Figure 4.3 summarizes the μ_{dc} dependence of the LDA+DMFT result for valence, XAS and RIXS spectra in NiO.

In NiO, the one-particle gap reduces with μ_{dc} increase (corresponding to decrease of the charge-transfer energy Δ_{CT}), as expected in the charge-transfer-type insulator [23]. The satellite and lower Hubbard band are observed around 9 eV and 1 eV, respectively. We obtained a reasonable agreement with the experimental photoemission and inverse photoemission data [154] in the range of $\mu_{dc} = 50 - 52$ eV. The μ_{dc} dependence of the Ni $L_{2,3}$ -XAS spectra is rather weak since the spectral shape is mostly dominated by the local multiplet interaction and the crystal-field splitting. The onset of the FL feature in the ω_{in} - ω_{loss} plot relates to the one-particle gap in the valence spectra.

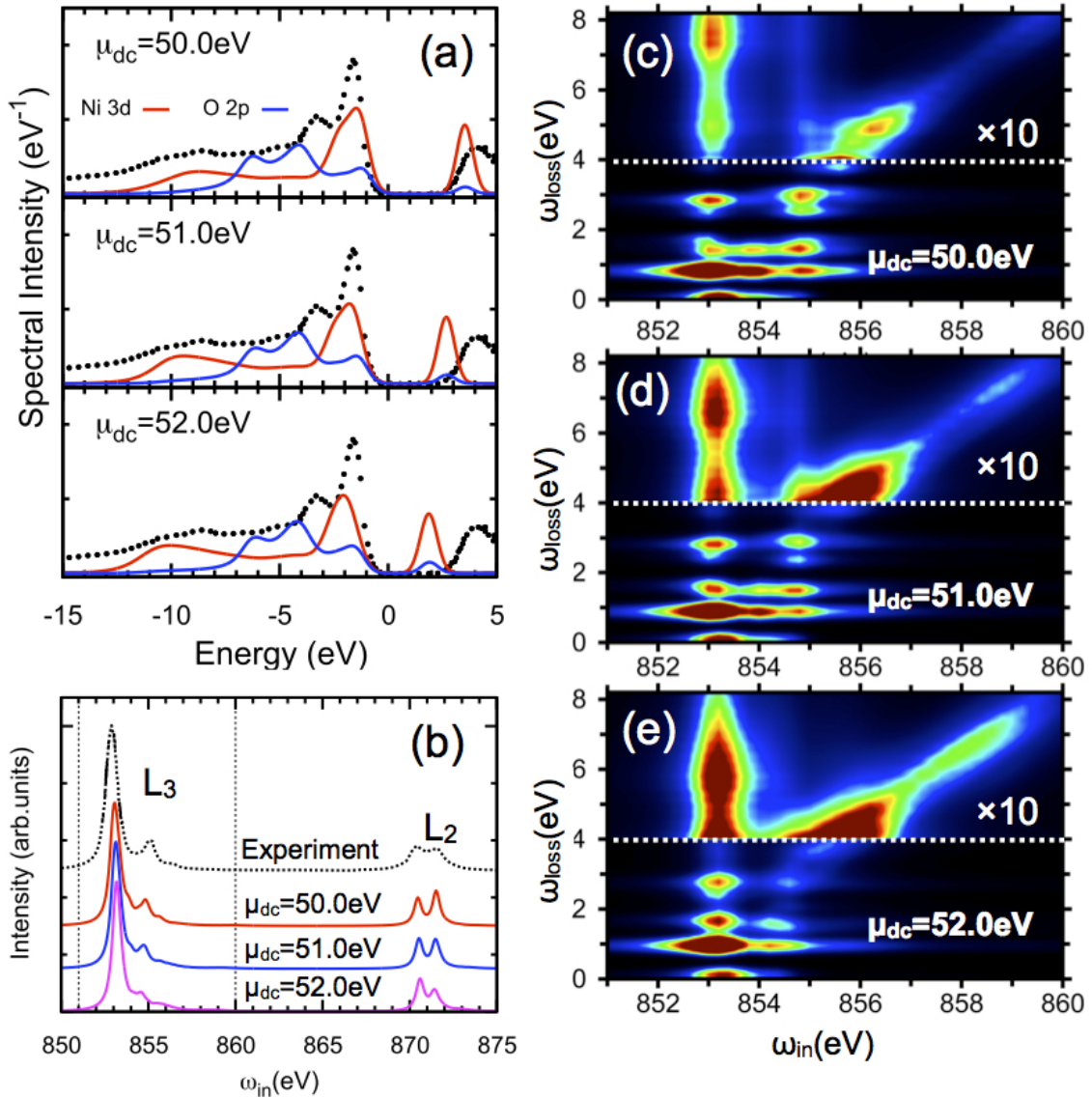


Figure 4.3: The double-counting correction μ_{dc} dependence of (a) valence spectra, (b) Ni $L_{2,3}$ -XAS spectra and (c-e) Ni L_3 -RIXS spectra of NiO calculated by LDA+DMFT. The RIXS intensities above the horizontal lines (white) are magnified by a factor indicated in panels. The $\mu_{dc} = 50.0, 51.0,$ and 52.0 eV correspond to $\Delta_{CT} = 5.4, 4.4,$ and 3.4 eV, respectively. Figure and caption taken from [2].

Finally, we comment on the character of the FL feature in a large-gap insulator. Fig. 4.4 shows the RIXS spectra calculated while artificially excluding charge transfer from X-ray excited Ni ion to the conduction bands above Fermi energy E_F . This prohibits excitation of upper Hubbard states (d^9) outside the excited Ni ion in the RIXS process. This results in only a minor intensity modulation of the FL feature, suggesting that the FL L_3 -RIXS feature of NiO reflects projected

EHP continuum with an extra d electron sitting on the excited Ni site (local upper Hubbard band state) and a hole propagating in the lower Hubbard band or O $2p$ bands. This behavior is expected to be common in large-gap systems and qualitatively differs from the behavior of FL feature in high-valence TMO with a small gap which is discussed in Sec. 4.4 [5].

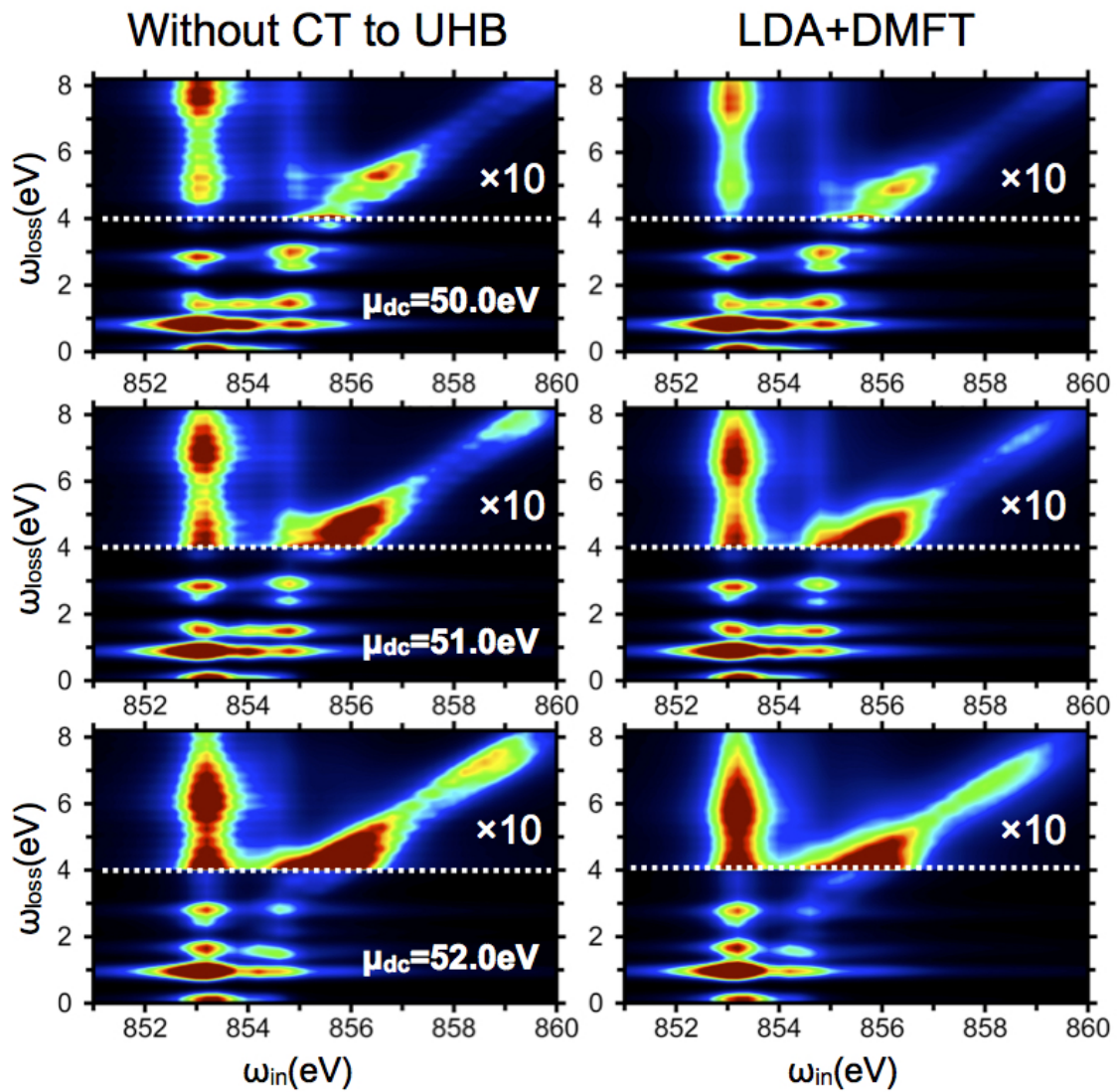


Figure 4.4: Left: Ni L_3 -RIXS map of NiO calculated by excluding a charge-transfer between X-ray-excited Ni ion and conduction states above Fermi energy E_F . Right: Ni L_3 -RIXS map of NiO calculated by LDA+DMFT. The RIXS intensities above the horizontal lines (white) are magnified by a factor indicated in panels. Figure and caption taken from [2].

4.3 Fe L_3 -Edge X-ray Absorption Spectroscopy and Resonant Inelastic X-ray Scattering of Fe_2O_3

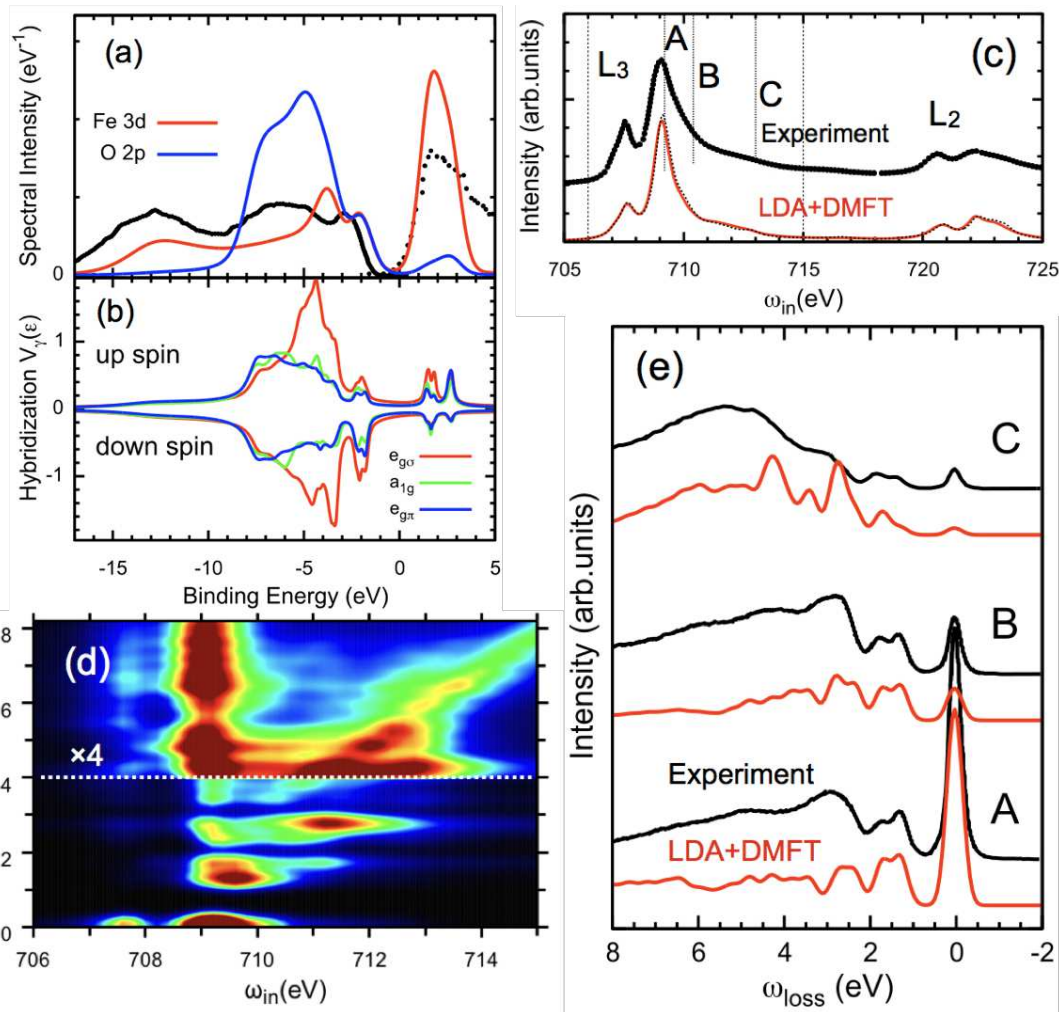


Figure 4.5: (a) LDA+DMFT valence spectra of Fe_2O_3 with the experimental data (black) [157, 158]. (b) DMFT hybridization intensity $V_\gamma(\varepsilon) = \sqrt{-\frac{1}{\pi} \Im \Delta_\gamma(\varepsilon)}$. (c) Fe $L_{2,3}$ -edge XAS spectra calculated by LDA+DMFT (solid), cluster model (dashed) and experimental data (dotted) [159]. (d) RIXS spectra calculated by LDA+DMFT. The intensities above the horizontal lines (white) are magnified by the factor indicated in panels. (e) RIXS spectra calculated at selected incident photon energies, see panel (c). The experimental data are taken from Ref. [160] (A-C corresponds to 3, 5, 7 in the reference). The spectral broadening is taken into account using a Gaussian of 200 meV for RIXS, a Lorentzian 300 meV for XAS, and a Gaussian 600 meV for valence XPS. Figure and caption taken from [2].

Fig. 4.5a shows the valence spectra of Fe_2O_3 obtained by LDA+DMFT in the experimental corundum structure [161] and antiferromagnetic state at $T = 300$ K (the experimental Néel temperature is 950 K). We employ $U = 6.8$ eV and $J = 0.86$ eV following previous DFT studies [11, 62]. A reasonable agreement with experimental photoemission and inverse photoemission data [157, 158] is found in the range $\mu_{dc} = 30.6 - 32.6$ eV. Thus we present the result obtained with $\mu_{dc} = 31.6$ eV. The hybridization intensity $V(\varepsilon) = \sqrt{-\frac{1}{\pi}\Im\Delta(\varepsilon)}$ in Fig. 4.5b shows the spin dependence reflecting the antiferromagnetic ordering. Fig. 4.5c shows Fe $L_{2,3}$ -edge XAS calculated by LDA+DMFT and the cluster model, together with the experimental data [159]. The two methods yield almost identical results and show a good agreement with the experiment. The shape of the Fe L_3 -edge main line (706 – 711 eV), that corresponds to the $|c d^6\rangle$ final state, is known to be sensitive to the local multiplet structure [78, 162], indicating the accuracy of the parameters in the present local Hamiltonian \hat{H}_{imp} , see Eq. 2.6. Fig. 4.5d shows the Fe L_3 -RIXS map obtained by the LDA+DMFT approach. The RIXS intensities calculated at selected photon energies are shown in Fig. 4.5e with recent high-resolution experimental data [160]. Fe L_3 RIXS shows rich $d-d$ features ($\omega_{loss} \approx 1 - 5$ eV) and a complex ω_{in} dependence due to a variety of multiplets in the d^5 manifolds. The LDA+DMFT result reproduces the position and ω_{in} dependence of low-energy features reasonably well.

4.3.1 Double-Counting Dependence

We find a reasonable agreement with experimental photoemission and inverse photoemission data [157, 158] in Fe_2O_3 in the range of $\mu_{dc} = 30.6 - 32.6$ eV, see Fig. 4.6a. The Fe $L_{2,3}$ -edge XAS spectra, see Fig. 4.6b, are rather insensitive to the choice of the double-counting corrections, indicating the spectral features are dominated by the local multiplets [78, 162]. We point out that in the RIXS spectra the positions of the low-energy excitations are largely renormalized by the double-counting energy μ_{dc} values. Interestingly, with decrease of the charge-transfer energy Δ_{CT} (increase of μ_{dc}), the $d-d$ feature around $\omega_{loss} \approx 1 - 2$ eV shifts to the low- ω_{loss} side sharply, while the one around $\approx 2 - 3$ eV is rather insensitive despite it is close in energy to the charge-transfer excitations. The result with $\mu_{dc} = 31.6$ eV gives the best agreement with the experimental RIXS data, see Fig. 4.5e.

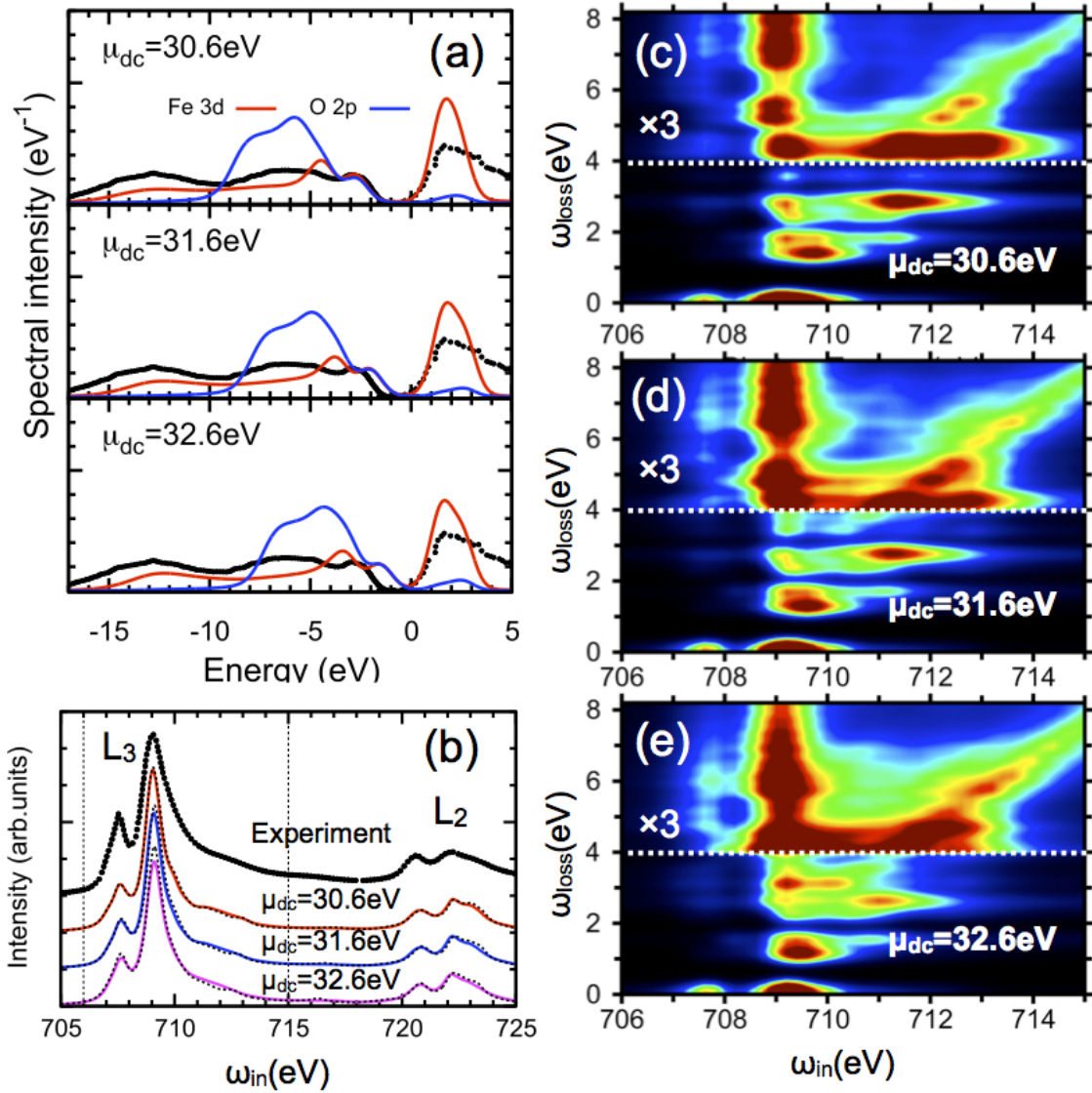


Figure 4.6: The double-counting correction μ_{dc} dependence of (a) valence spectra, (b) Fe $L_{2,3}$ -XAS spectra and (c-e) Fe L_3 -RIXS spectra of Fe_2O_3 calculated by LDA+DMFT. The RIXS intensities above the horizontal lines (white) are magnified by a factor indicated in panels. The $\mu_{dc} = 30.6, 31.6,$ and 32.6 eV correspond to $\Delta_{CT} = 4.8, 3.8,$ and 2.8 eV, respectively. Figure and caption taken from [2].

4.4 Cu L_3 -Edge X-ray Absorption Spectroscopy and Resonant Inelastic X-ray Scattering of Cuprates

We study Cu L_3 -Edge XAS and RIXS in high-valence LaCuO_3 and NaCuO_2 . We have chosen these compounds as model systems for the investigation of the origin of the FL feature observed in the RIXS spectra. Both compounds share a tiny charge-transfer energy [66–70] leading to small or no gap [66, 68, 69, 71, 72]. Part of this study is the origin of the FL feature and its connection to the crystal structure.

In Figs. 4.7a,b we show the one-particle (1P) density of states of LaCuO_3 and NaCuO_2 . The μ_{dc} in the range of 55.64 – 57.64 eV yields results consistent with Cu L -edge XAS studies [68, 163, 164]. The μ_{dc} values provide also the best match with earlier valence XPS studies [68, 70] shown in Figs. 4.7a,b. The deviations from the experimental XPS spectra may be due the uncertainty of the relative Cu $3d$ – O $2p$ cross section and the surface sensitivity of XPS. In NaCuO_2 , in particular, the surface is prone to contamination leading to the appearance of Cu^{2+} ions [74, 163]. Varying μ_{dc} within the above range has only a minor impact on the RIXS spectra for both materials and does not affect our conclusions. For LaCuO_3 , paramagnetic metal (PM) and antiferromagnetic insulator (AFI) solutions can be stabilized, similar to LDA+ U studies [69], indicating the Slater nature of the gap. Reflecting the unclear experimental situation [68, 69, 71, 72], we proceed with both states and use them later to demonstrate the effect of the small gap on RIXS. NaCuO_2 ($E_{\text{gap}} \approx 0.5$ eV) has a band-insulator character with a gap present already in the LDA solution [73, 74]. Overall, the 1P density of states suggest an existing phase space for a continuum of excitations in the few eV range.

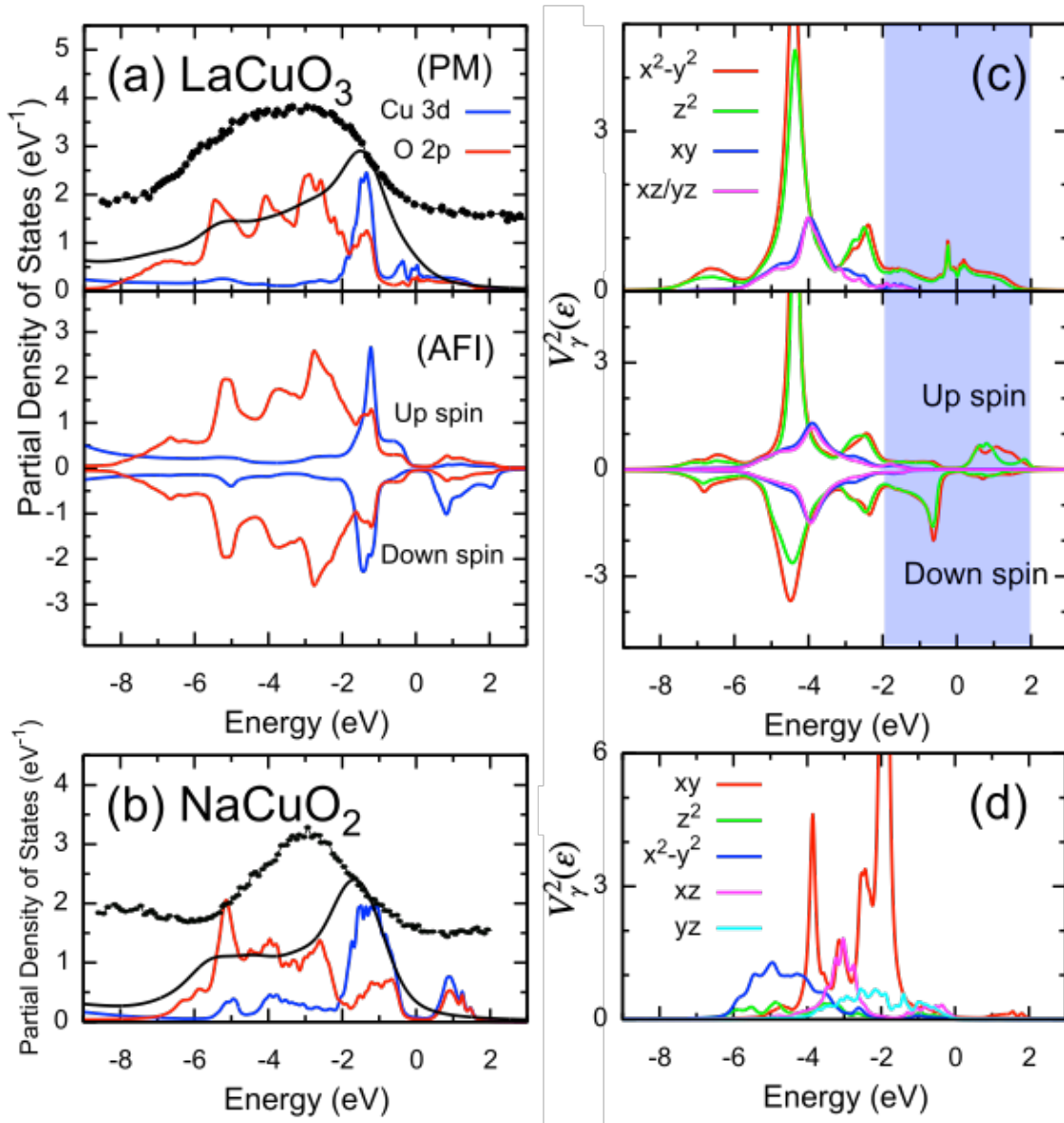


Figure 4.7: LDA+DMFT 1P density of states for (a) LaCuO₃ in the PM and AFI phases and (b) NaCuO₂. The hybridization intensity $V_\gamma^2(\epsilon) = -\frac{1}{\pi} \Im \Delta_\gamma(\epsilon)$ of LaCuO₃ (c) in the PM and AFI phases and NaCuO₂ (d). The energy origin is taken at E_F . The experimental XPS data (symbols) of LaCuO₃ [68] and NaCuO₂ [70] are compared to the theoretical ones (black line). We used the same instrumental broadening and the relative Cu 3d : O 2p cross section as in Ref. [68], where the atomic cross section is taken from Ref. [165]. $\mu_{dc}=55.64$ eV is employed in the calculation. Figure and caption taken from [5].

The calculated Cu L_3 -edge XAS and RIXS spectra are shown in Fig. 4.8. The XAS spectrum of NaCuO₂ has a single-peak (A), while that of LaCuO₃ exhibits an additional shoulder (B), which is enhanced in the PM phase and is observed also in experiment for NaCuO₂ [163] and LaCuO₃ [68]. The shoulder B is missing in the calculations on the CuO₆ cluster model [68, 166], see Fig. 4.8e, indicating that the shoulder is not of $d-d$ or charge transfer origin but due to a final state delocalized beyond the CuO₆ cluster [31].

The RIXS spectra of NaCuO₂ and LaCuO₃ are strikingly different. Tuning ω_{in} to the peak A of the XAS, two distinct $d-d$ transitions with RL behavior are found in both compounds, similar to another Cu³⁺ material Zn_{1-x}Cu_xO [167], followed by charge transfer transitions with higher ω_{loss} . However, at higher ω_{in} the RIXS of LaCuO₃ yields a linear FL feature, with little difference between the AFI and PM phase. The FL feature is suppressed in NaCuO₂ resembling the spectrum of the cluster model. The calculated RIXS spectra of LaCuO₃ reminds one of the experimental observation on NdNiO₃ [57] with the FL feature starting at the ω_{in} on the L_3 main edge and not far above it as in NiO. The continuum of unbound particle-hole pairs in the manner of Ref. [57] explains the FL feature in LaCuO₃.

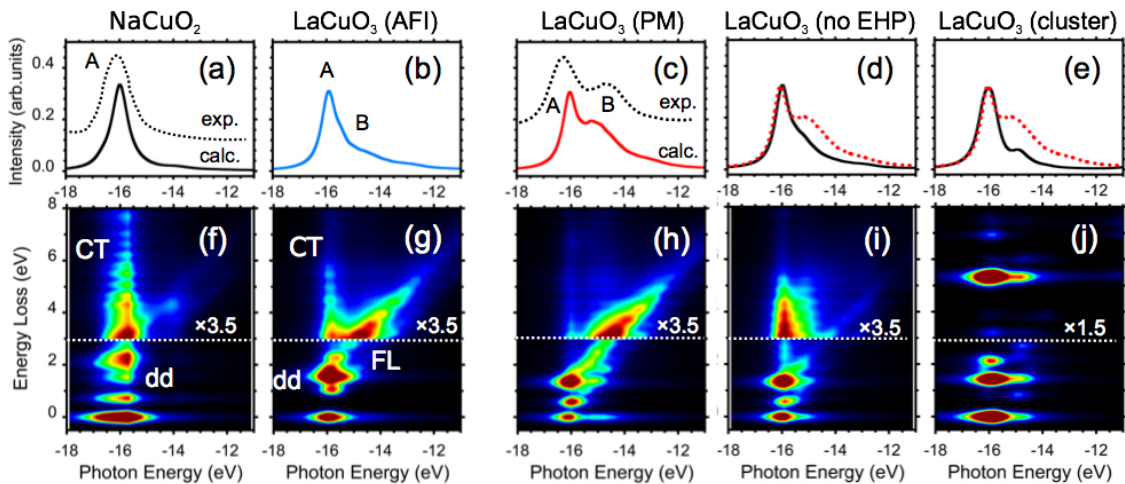


Figure 4.8: The calculated L_3 -edge XAS and RIXS spectra for (a),(f) NaCuO₂ and LaCuO₃ in (b),(g) AFI phase, (c),(h) PM phase, (d),(i) no EHP and (e),(j) CuO₆ cluster model. The RIXS intensity with $\omega_{\text{loss}} \geq 3.0$ eV (horizontal dashed line) are magnified by 3.5 times [1.5 time for (e)]. $\mu_{\text{dc}}=55.64$ eV is employed in the calculation. The LDA+DMFT spectrum for LaCuO₃ (PM) is shown by a dotted curve in (d) and (f), for comparison. The experimental XAS data (dashed line) for LaCuO₃ (PM) and NaCuO₂ are taken from Ref. [68] and Ref. [163]. The spectral broadening is considered using a Gaussian of 150 meV for RIXS and a Lorentzian 300 meV for XAS (HWHM). Figure and caption taken from [5].

4.4.1 Fluorescence-like Feature

Here we discuss the origin of the FL feature observed in the RIXS spectra of LaCuO_3 and which is absent in NaCuO_2 .

The small NaCuO_2 charge gap cannot explain the absence of visible particle-hole excitations at ω_{loss} in the 3–4 eV range. In fact, the experiment on NdNiO_3 [57] and the calculations in the PM and AFI phases of LaCuO_3 in Fig. 4.9 show that the gap opening affects the FL feature only at low ω_{loss} . Moreover, the NaCuO_2 1P density of states, see Fig. 4.7b, exhibits a noticeably higher density of states above and below the gap than LaCuO_3 , see Fig. 4.7a, which suggests a larger phase space for particle-hole excitations in NaCuO_2 . The reason for the existence of the FL feature observed in LaCuO_3 lies in the hybridization function $\Delta_\gamma(\varepsilon)$, see Eq. 2.31. The hybridization intensities $V_\gamma^2(\varepsilon) = -\frac{1}{\pi}\Im\Delta_\gamma(\varepsilon)$ of both compounds are shown in Figs. 4.7c,d.

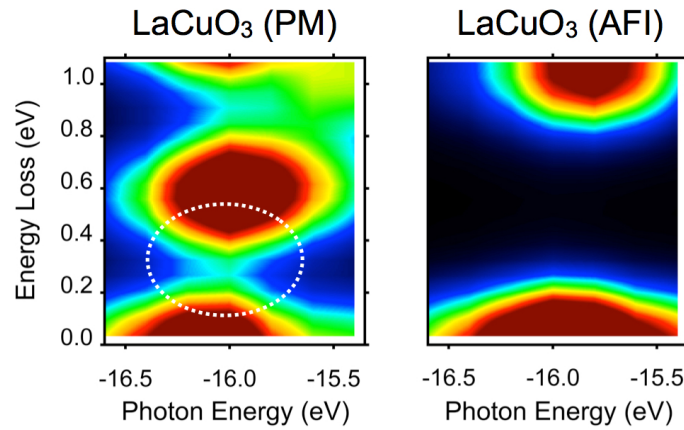


Figure 4.9: Low ω_{loss} region (< 1.0 eV) of the RIXS map in the PM and AFI phases of LaCuO_3 . The FL feature continues to zero energy loss in the PM phase. Figure and caption taken from [5].

How does the hybridization intensity affect the RIXS spectra? In the spectral function of RIXS, see Eq. 2.3, all intermediate states accessible in the XAS process contribute to RIXS in principle. We estimate that the intermediate states with $|E_m - E_n - \omega_{\text{in}}| \lesssim \Gamma_L$, which approximately conserve energy in the partial XAS process, dominate while those outside this range cancel approximately out due to the varying sign of the denominator. Such a claim cannot be directly confirmed with the resolvent formulation, see Eq. 2.76. It is, nevertheless, supported by the diagonal shape of the FL feature in the $\omega_{\text{in}}-\omega_{\text{loss}}$ plane, suggesting that a narrow range of intermediate states are ‘excited’ that ‘decay’ into a narrow range of final states with matching electron-hole excitation. The small hybridization intensity for $\varepsilon > 0$ in NaCuO_2 implies that (intermediate) states with different numbers

of conduction electrons hybridize only weakly with one another. In LaCuO₃ a RIXS process that we schematically write as $d^8 + d^9 \underline{v} \rightarrow \underline{C}d^{10} \underline{v} + \underline{C}d^9 c \underline{v} \rightarrow d^8 c \underline{v}$ ends up in a final state that can be characterized as the ground state plus an electron-hole pair in the continuum, see Fig 4.10a, where \underline{C} , \underline{v} , and c correspond to a hole in 2p core level, in valence bands, and an electron in conduction bands, respectively. Such processes in NaCuO₂ are strongly suppressed since states of the type $\underline{C}d^{10} \underline{v}$ and $\underline{C}d^9 c \underline{v}$ hybridize only weakly. This is a local expression of the fact that in NaCuO₂ a hole transferred from Cu to O has a small probability to escape the CuO₄ cluster.

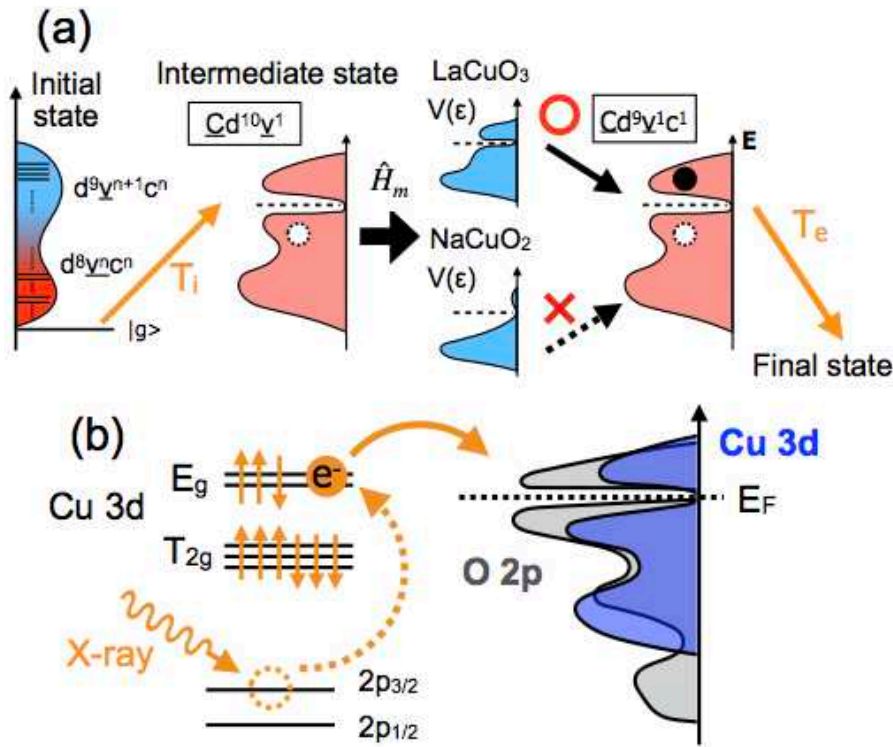


Figure 4.10: Schematic of (a) electron-hole pair creation in the RIXS process of LaCuO₃ and NaCuO₂, and (b) charge transfer to the conduction states in the intermediate state. Figure and caption taken from [5].

To test this interpretation, we switched off the hybridization to the conduction band in the intermediate states for the PM phase of LaCuO₃; see Fig. 4.8i. In practice, we have set $V_\gamma(\epsilon > 0) = 0$ in the Hamiltonian H_m of the intermediate states, see Eq. 2.3, while keeping $V_\gamma(\epsilon)$ unrestricted in the initial and final states. The intensity of the FL feature is dramatically suppressed and the structure of the RIXS spectrum resembles that of NaCuO₂. Although (unchanged) final states with excited electron-hole pairs exist, they cannot be resonantly excited by the RIXS process. This result supports the interpretation of the FL feature in

Ti L -edge spectra by Pfaff *et al.* [56] and shows that the nature of hybridization in intermediate states is the dominant factor affecting the intensity of FL feature. In Fig. 4.10b the hybridization to the conduction band is sketched. Cutting hybridization to the conduction states affects also the XAS spectrum, Fig. 4.8d, which loses the shoulder B and overlaps with that of the cluster model, Fig. 4.8e. This shows that intermediate states with localized and delocalized character coexist in this ω_{in} region, which leads to coexistence of FL and RL features in the RIXS spectrum.

4.4.2 Double-Counting Dependence

Fig. 4.11 shows Cu L -edge XAS and RIXS calculated for different double-counting corrections μ_{dc} in LaCuO_3 and NaCuO_2 . As one could find in the dp Hamiltonian, see Eq. 2.57, μ_{dc} renormalizes the p - d splitting and a larger μ_{dc} reduces the splitting, i.e. the charge-transfer energy.

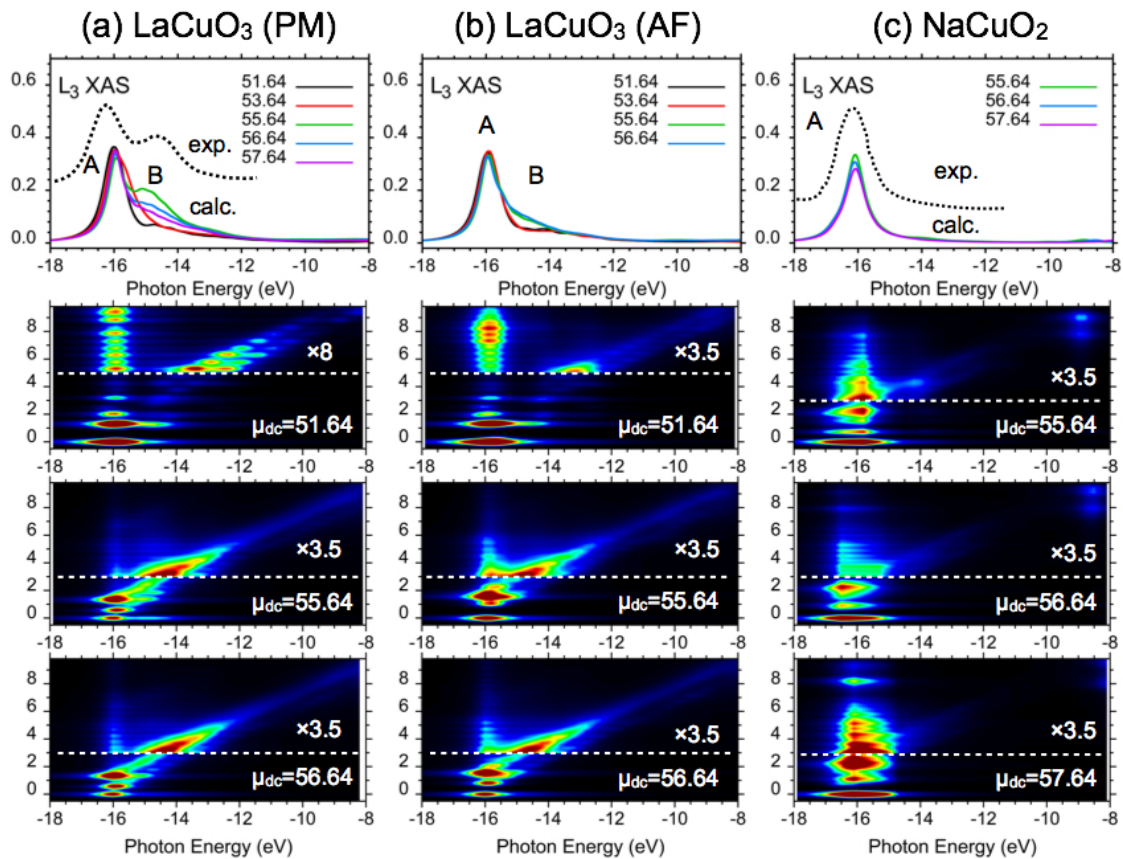


Figure 4.11: Calculated L_3 -edge XAS and RIXS for (a) LaCuO_3 (PM), (b) LaCuO_3 (AF), and (c) NaCuO_2 . The experimental XAS data (dashed line) for LaCuO_3 (PM) and NaCuO_2 are taken from Ref. [68] and Ref. [163]. Figure and caption taken from [5].

The XAS spectra of LaCuO_3 with $\mu_{\text{dc}} = 51.64$ eV, deep in the Mott insulating regime, shows a sharp main line (A) and a weak multiplet feature around the incident photon energy of $-14 - -15$ eV, resembling Ni L -edge XAS of NiO ($3d^8$ electronic configuration) [43]. With μ_{dc} increase (i.e., charge-transfer energy decrease), a new shoulder feature B develops in both, the antiferromagnetic and paramagnetic phases. The metal-insulator transition occurs at $\mu_{\text{dc}} \approx 55.64$ eV in the paramagnetic solution, while a gap survives in the antiferromagnetic solution for $\mu_{\text{dc}} \lesssim 56.74$ eV. The $\mu_{\text{dc}} = 55.64 - 57.64$ eV yields a reasonable agreement to the experimental XAS data measured using the total electron yield method [68]. The XAS of NaCuO_2 shows a rather weak μ_{dc} dependence and does not show the shoulder B , consistent with the experimental observation [163]. The estimated μ_{dc} values give similar RIXS features in LaCuO_3 , showing coexisting FL and RL features across the Cu L_3 main line, while a small μ_{dc} , see $\mu_{\text{dc}} = 51.64$ eV, gives a FL feature that appears far above the L_3 main line as in NiO [49]. The calculated valence XPS with the estimated μ_{dc} give a fair agreement to early photoemission data [68, 70], see Fig. 4.12.

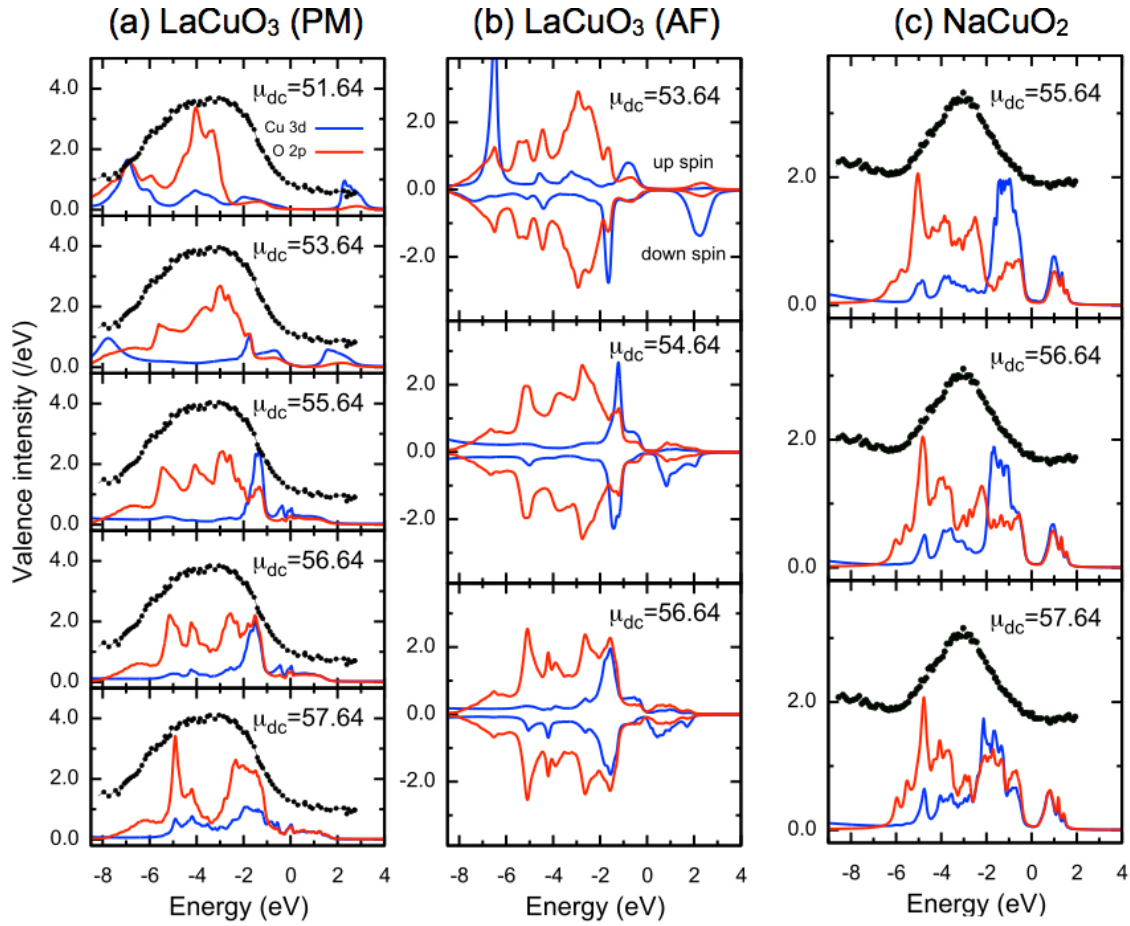


Figure 4.12: Calculated 1P density of states of (a) LaCuO_3 (PM), (b) LaCuO_3 (AF), and (c) NaCuO_2 for different double-counting corrections μ_{dc} . The calculated valence spectra (black line) are shown together. The experimental valence XPS data of LaCuO_3 and NaCuO_2 are taken from Ref [68] and [70], respectively. Figure and caption taken from [5].

4.4.3 Cluster Model

Next, we show the difference of the spectra between cluster model and Anderson impurity model approach. We use a cluster-like hybridization function with hybridization intensity to the impurity's nearest-neighbor ligands and apply it to the Anderson impurity model.

Fig. 4.13 shows the hybridization intensity $V_\gamma^2(\varepsilon) = -\frac{1}{\pi}\Im\Delta_\gamma(\varepsilon)$ of the studied compounds in the cluster model. Considering the crystal structure, see Fig. 1.12, here we assumed an CuO_6 and CuO_4 cluster for LaCuO_3 and NaCuO_2 , respectively. The $V_\gamma^2(\varepsilon)$ shows a single-peak feature, as expected, while the energy position of the peaks depends on γ because of the crystal-field splitting in O 2p states.

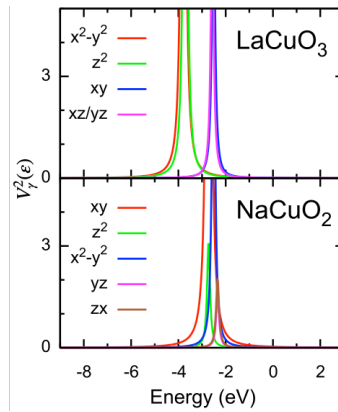


Figure 4.13: The hybridization intensity of $LaCuO_3$ and $NaCuO_2$ in the cluster model. Figure and caption taken from [5].

Fig. 4.14 shows the L_3 XAS and RIXS spectra computed by the LDA+DMFT approach and the cluster model. For comparison, a magnified RIXS map of the RL features is shown for $LaCuO_3$. We find a reasonable agreement in the energy positions of the RL features ($\lesssim 2.0$ eV) between the two methods. However, the intensities and the resonance photon energies of the RL features differ between the two methods. These depend in general on the character of the intermediate states of the RIXS process. We remind that the cluster model does not describe the intermediate states of $LaCuO_3$ properly, which leads to the absence of the shoulder B in the XAS spectrum of the cluster model (as compared to experiment).

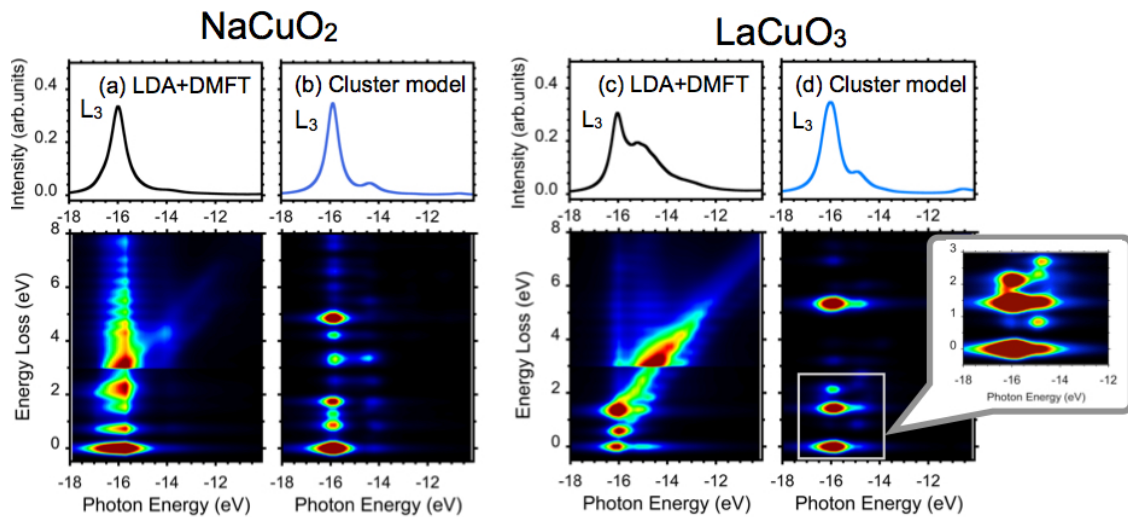


Figure 4.14: The L_3 XAS and RIXS spectra for $NaCuO_2$ and $LaCuO_3$ calculated by the LDA+DMFT approach and the cluster model. The magnification of the RL features in the cluster-model spectrum is shown, for comparison. Figure and caption taken from [5].

4.5 Co L_3 -Edge X-ray Absorption Spectroscopy and Resonant Inelastic X-ray Scattering of Cobaltites

We present Co L -edge RIXS spectra in representative cobaltites: SrCoO₃, LaCoO₃, and LiCoO₂. The comparison among the three materials allows us to explore the sensitivity of RIXS spectra to the TM valence state and lattice geometry.

SrCoO₃ and LaCoO₃ crystallize in the corner-sharing perovskite structure, while LiCoO₂ crystallizes in a quasi-two-dimensional structure with edge-sharing CoO₆ octahedra. Formally, Co ion is trivalent ($3d^6$) in LaCoO₃ and LiCoO₂, while it is tetravalent ($3d^5$) in SrCoO₃. Due to its small charge-transfer energy, SrCoO₃ possesses a dominant d^6 configuration (plus one hole in ligands) in the ground state [88, 94, 168]. The Co d^6 manifolds have rich low-energy multiplets characterized by low-spin ($S = 0$, LS), intermediate-spin ($S = 1$, IS), and high-spin ($S = 2$, HS) states. The ground states of the three compounds at low temperatures are well known; LaCoO₃ and LiCoO₂ are band insulators (insulating gap ≈ 0.5 eV) with the LS configuration, while SrCoO₃ is a ferromagnetic metal with an admixture of the HS state and charge fluctuations around it [94]. The LDA+DMFT calculations are performed in the experimental crystal structure reported well below possible spin-state transition temperatures. Following previous DFT studies for LaCoO₃ [169], we use $U = 6.0$ eV and $J = 0.8$ eV. Figures 4.15a–c show the LDA+DMFT valence spectra, together with experimental data. Due to its LS character, T_{2g} states are almost fully occupied in LaCoO₃ and LiCoO₂, while the HS character in SrCoO₃ yields considerable E_g weights below E_F in the majority-spin channel [94]. Figures 4.15d–f show the hybridization intensities $V^2(\varepsilon) = -\frac{1}{\pi}\Im\Delta(\varepsilon)$. The intensities around -8 to -2 eV (-2 to 4 eV) represent the hybridization with O $2p$ (Co $3d$) states though explicit decomposition of contributing states in the continuum bath is impossible [4]. Despite the similar LS valence spectra in LiCoO₂ and LaCoO₃, we find a clear difference in $V_\gamma^2(\varepsilon)$ for the E_g orbital between the two. LaCoO₃ shows sizable hybridization intensities above E_F , while LiCoO₂ shows only below E_F (around -2 eV). In LaCoO₃ with nearly 180° of Co-O-Co bonds, inter-orbital (E_g - T_{2g} channel) hopping between neighboring Co sites is forbidden, while it is allowed in LiCoO₂ owing to the edge-sharing CoO₆ octahedra. The E_g - E_g hopping, on the other hand, is allowed/forbidden in the former/latter geometry. This explains the presence/absence of the hybridization intensities with the empty E_g bands above E_F in LaCoO₃/LiCoO₂. In this way, the hybridization function $\Delta_\gamma(\varepsilon)$ encodes the lattice environment around the impurity site. Since an extra d electron, excited by the local X-ray absorption, goes into the empty E_g states in the LS configuration, the hybridization properties of E_g orbital is important to understand possible EHP excitations in the RIXS spectra. Figures 4.15g–i show the Co L_3 -XAS spectra calculated by LDA+DMFT. In both trivalent [77] and

tetravalent cases [168], the Co L_3 -XAS is sensitive to the spin-state character on the Co atom in the ground state. Thus, the overall good agreement with the available experimental data [77, 170, 171] suggests that the spin state in the ground state is well described within the LDA+DMFT scheme. Figures 4.15j–l show the RIXS spectra calculated across the Co L_3 edge. The d – d excitations in LaCoO₃ and LiCoO₂ resemble each other due to the similar local multiplet structures above the LS ground state, while those in SrCoO₃ are rather obscure mainly due to the thermal mixture of the HS multiplets. Despite the similarity of the d – d excitations, the FL feature in LaCoO₃/LiCoO₂ is visible/invisible. This difference originates from the hybridization of the excited Co ion with the continuum of conduction states above E_F , which differs in the two lattice geometries as mentioned above. The presence/absence of the FL feature in the corner-/edge-sharing structure, see Fig 1.12, resembles the behavior of the FL feature isoelectronic high-valence cuprates (LaCuO₃ and NaCuO₂), see Sec. 4.4 [5]. The FL feature in SrCoO₃ is more intense compared to that in LaCoO₃ despite comparable hybridization intensities above E_F between the two, see Figs. 4.15d,e. This is because, in SrCoO₃, metallicity due to negative charge-transfer energy favors EHP excitations.

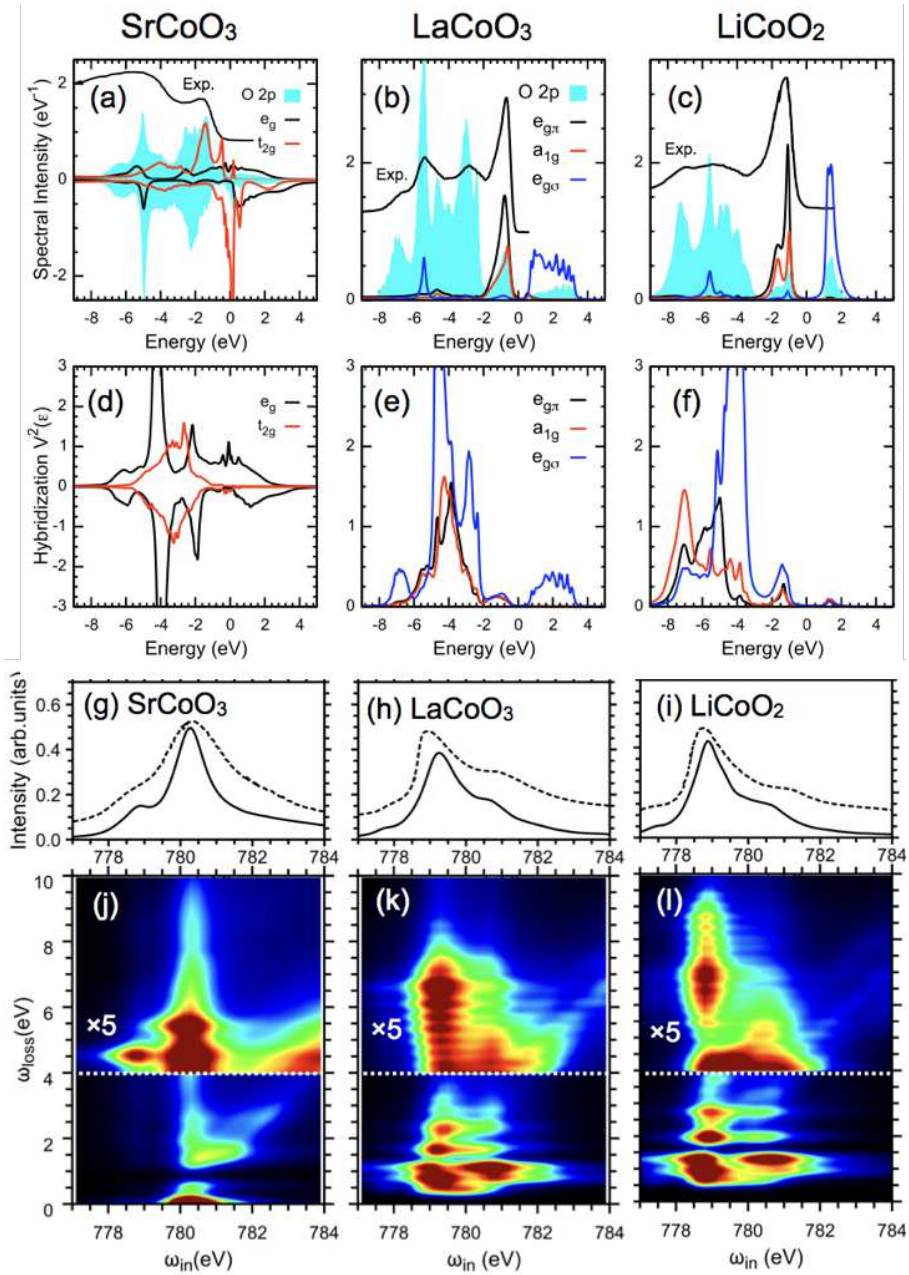


Figure 4.15: LDA+DMFT Valence spectra and hybridization intensities of (a,d) SrCoO₃, (b,e) LaCoO₃ and (c,f) LiCoO₂. Co T_{2g} orbitals split into $E_{g\pi}$ and A_{1g} orbitals due to trigonal distortion in LaCoO₃ and LiCoO₂. The experimental valence photoemission data for SrCoO_{3- δ} [170], LaCoO₃ (Sr 0.2% doped) [172] and LiCoO₂ [173] are shown together. The Co L_3 -edge XAS and RIXS spectra calculated for (g,j) SrCoO₃, (h,k) LaCoO₂ and (i,l) LiCoO₂, together with the experimental XAS data (dashed lines) [77, 171, 174]. The RIXS intensities above horizontal lines (white) are magnified by a factor indicated in panels. A small periodic oscillation of the RIXS intensities in the magnified region (charge-transfer excitation region) is due to a discretization effect in the hybridization intensity $V^2(\epsilon) = -\frac{1}{\pi} \Im \Delta(\epsilon)$. The spectral broadening is taken into account using a Gaussian of 150 meV for RIXS, a Lorentzian 300 meV for XAS. Figure and caption taken from [2].

4.6 Conclusions

We presented numerical simulations of L -edge RIXS spectra of typical $3d$ TM oxides: NiO, Fe₂O₃, cuprates and cobaltites. We used the Anderson impurity model approach with a hybridization function obtained by LDA+DMFT. This approach reproduces the experimental RIXS and XAS data of the studied materials accurately. Taking cobaltites as an example, we examined the variation of the RIXS spectra with the TM valence state and crystal geometry. We found substantial differences in RIXS spectra of isoelectronic LaCoO₃ and LiCoO₂ despite their almost identical valence photoemission and XAS spectra. The difference between the two compounds lies in the decoration of the crystal lattice with CoO₆ octahedra, which is encoded in the DMFT hybridization function. This example demonstrates that the information contained in the RIXS spectra cannot be extracted from the one-particle spectral function [2]. Furthermore we studied the coexistence of RL and FL features in RIXS spectra of high-valence transition-metal oxides e.g. cuprates. We predict that the FL feature is present in the L -edge RIXS spectra of LaCuO₃ in both the paramagnetic and antiferromagnetic insulating phases, while it is absent in the isoelectronic NaCuO₂. We have interpreted this numerical observation in terms of crystal geometry [5]. Comparing the RIXS spectra of paramagnetic and antiferromagnetic insulating LaCuO₃, we have shown that the FL feature in the low- ω_{loss} regime is sensitive to the opening of a small gap, similar to the experimental observation on NdNiO₃ [57]. The results show that the FL component of the RIXS spectra is rather material-specific, and its interpretation requires advanced many-body calculations.

The present method provides a computationally feasible material specific approach to RIXS spectra in a wide range of materials, including the strongly correlated ones. Although our approach contains a number of input parameters such as the valence-valence and core-valence interaction, these can be estimated by direct calculation or taken from other materials since they are only weakly material dependent. The only ‘real’ free parameter in the present study is the double-counting correction μ_{dc} , which is adjusted by comparison to the experimental valence photoemission spectra [2].

Chapter 5

L_3 -Edge X-ray Absorption Spectroscopy and Resonant Inelastic X-ray Spectroscopy of Rare-Earth Nickel Oxides

We present a computational study of L -edge X-ray absorption spectroscopy (XAS) and resonant inelastic X-ray scattering (RIXS) of LuNiO_3 . LuNiO_3 is a representative rare-earth nickelate exhibiting multiple phases, e.g. paramagnetic metal (PMM), paramagnetic insulating (PMI) and antiferromagnetic insulating (AFI) phase. We study the changes of the spectra across the metal-insulator transition, which is accompanied by a site-disproportionation. We address the question of site-selectivity of L -edge XAS and RIXS in the disproportionated insulating phase. Moreover, we discuss the fluorescence-like feature and the gap opening in the insulating phase, proposed by Bisogni *et al* [57]. This chapter is based on

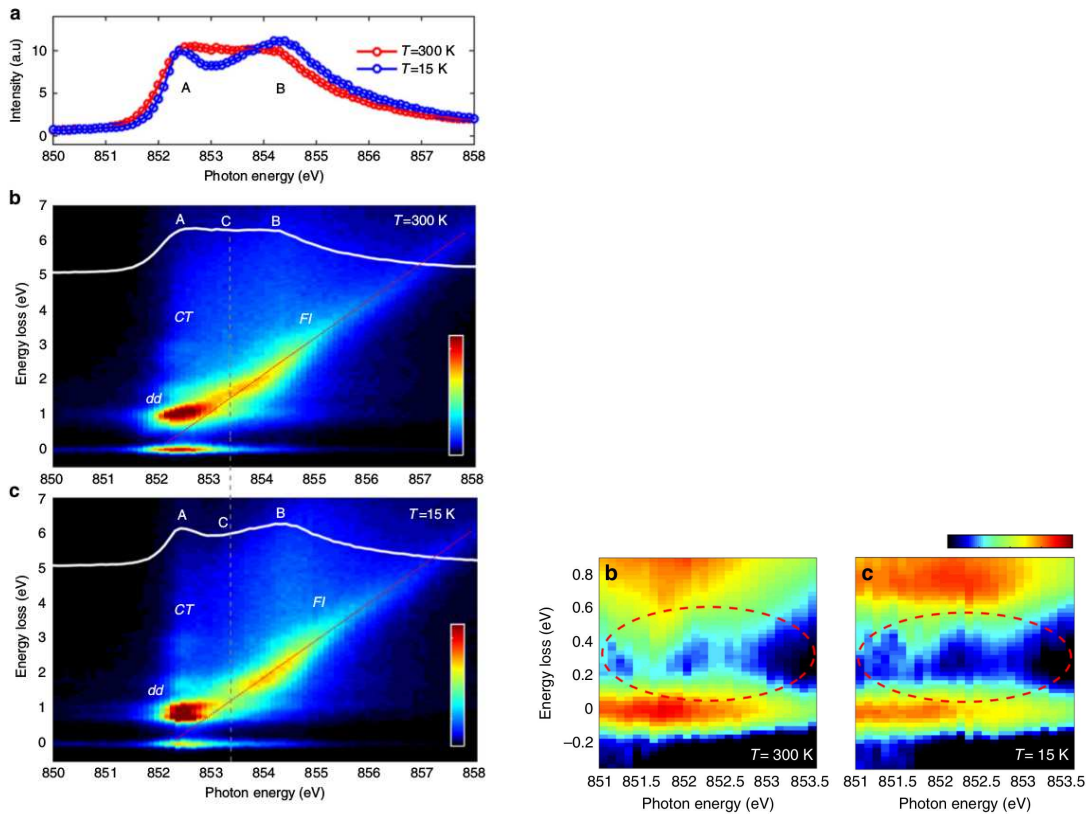
[1] "X-ray spectroscopy of rare-earth nickelate LuNiO_3 : LDA+DMFT study"

M. Winder, A. Hariki, and J. Kuneš
arXiv:2004.01428 (2020).

Extended text passages which are directly adopted from the publication are marked with a black bar.

5.1 Introduction

Rare-earth nickelates show an anomalous double-peak line of Ni L_3 -edge XAS which was observed in earlier experimental studies and was recently associated with signals from two-distinct Ni sites which show a charge disproportionation (CD) [175]. Bisogni *et al* [57] studied high-resolution RIXS across the L_3 -edge double-peak, and revealed an unusual coexistence of Raman-like (RL) and fluorescence-like (FL) features, which indicates that the 2P excitation spectra of the two Ni-sites differ qualitatively from each other, see Fig. 5.1a. The gap opening of the FL feature ($0 < \omega_{\text{loss}} < 0.5$ eV) between the CD-insulating and metallic phase was interpreted as a signature of the metal-insulator transition [57], see Fig. 5.1b. Very recently, the authors in Refs. [108, 176] succeeded in measuring low-energy magnetic excitations in the film NdNiO_3 by setting the ω_{in} to the magnetically-active Ni site, i.e. the expanded (long-bond) d^8 site. The site-selectivity in RIXS was also used to study magnetic and orbital excitations in Fe_3O_4 [177, 178].



(a) a XAS / RIXS in b PMM and c AFI phase

(b) Magnification of the FL gap

Figure 5.1: Experimental Ni L_3 -edge XAS and RIXS for NdNiO_3 , Figures taken from [57].

The study of Bisogni *et al.* [57], as well as the claimed site-selectivity achieved by

tuning the incoming photon energy ω_{in} [57, 108, 176], calls for deeper theoretical investigation. We investigate the transition from PMM to PMI phase with transition temperature of $T_{\text{MI}} \approx 600$ K. The transition is characteristic for the RNiO_3 family [104, 179–181]. The site disproportionation in the PMI phase induces a charge disproportionation. In charge disproportionated systems composed of localized and delocalized states d^8 and $d^8\bar{L}^2$ in RNiO_3 , respectively, the XAS signals between sites may show interference or an overlap. That would limit the site resolution (projection) of 2P excitations. Thus, a theory is needed that enables to simulate the site-resolved contributions in both the RIXS and XAS spectra accurately. For Ni L_3 -edge RIXS in RNiO_3 the double-cluster model (Ni_2O_{11}), which is a minimum multi-site cluster model, was applied [108, 176]. However, the small-size description dismisses the signature of the electron-hole pair continuum at the metal-insulator transition. We use the Anderson impurity model approach which includes the self-consistently coupled inequivalent Ni ions as well as the electron-hole continuum of the extended system [2, 4, 5, 31, 182].

5.2 Computational Details

RNiO_3 in PMI phase contains of two distinct Ni sites, a long bond (LB) and short bond (SB) site. These are named after the average distance between the Ni atoms and their nearest-neighboring oxygen ligands. The total Ni L_3 -edge XAS and RIXS spectra in PMI phase are obtained by summing up the LB and SB spectra

$$F_{\text{RIXS/XAS}}(\omega_{\text{out}}, \omega_{\text{in}}) = F_{\text{RIXS/XAS}}^{\text{SB}}(\omega_{\text{out}}, \omega_{\text{in}}) + F_{\text{RIXS/XAS}}^{\text{LB}}(\omega_{\text{out}}, \omega_{\text{in}}). \quad (5.1)$$

The site-resolved XAS and RIXS spectra are given by Fermi's golden rule, see Eq. 2.2, and Kramers-Heisenberg formula, see Eq. 2.3, respectively. The spectra are calculated in thermal equilibrium

$$F_{\text{RIXS/XAS}}^S = \sum_n \frac{1}{Z} e^{\frac{E_n}{k_{\text{B}}T}} F_{\text{RIXS/XAS}}^{(S,n)}, \quad (5.2)$$

where $S \in \{SB, LB\}$. The Boltzmann factor is used at simulated temperatures with the energies E_n of the relevant initial states. In our approach we use $T = 533$ K and $T = 673$ K for the PMI phase and PMM phase, respectively. In the PMM phase both sites are equivalent, and thus we drop out the site average.

The excitation of a core-level electron to a valence state is a local process, thus we use impurity models to describe the excitation process. We use the Anderson impurity model, see Eq. 2.29, for each site S

$$\hat{H}_{\text{AIM}}^S = \hat{H}_{\text{TM}}^S + \hat{H}_{\text{hyb}}^S. \quad (5.3)$$

The two sites have different occupation and different energies. In this study, we define the charge-transfer energy Δ_{CT} on the formal valence of Ni^{3+} , thus we set $n = 7$ electrons to estimate Δ_{CT} . The averaged energy of the Ni $3d$ states ($\varepsilon_d^{\text{LDA}}$) differs between the LB and SB site. The double-counting energy μ_{dc} is calculated by Eq. 2.71 and slightly varies for each site. This slight variation does not affect the spectra, i.e. by setting μ_{dc} equal for both sites (averaging them) one can estimate a slightly different Δ_{CT} for both sites, but the spectra do not change. In the following we discuss the parameters of this study, see Tab. 5.1. U_{dd} is the averaged Coulomb interaction used in the configuration interaction scheme. The F_{pd}^2 , G_{pd}^1 and G_{pd}^3 values in the core-valence (p - d) interaction, are scaled down to 75% of their actual values to simulate the effect of intra-atomic configuration interaction from higher basis configurations neglected in the atomic calculation [30, 121, 122]. We fix the isotropic part of the core-valence interaction by the relation $U_{pd} \approx 1.3 \times U_{dd}$ which is a successful empirical treatment [30, 116, 118]. The Coulomb parameters are discussed in more detail in Sec. 2.2.3. The spin-orbit coupling ζ_{2p} within the Ni $2p$ states and the anisotropic part of the $2p$ - $3d$ interaction parameters F^k , G^k are calculated by an atomic Hartree-Fock code [121]. The spin-orbit coupling within Ni $3d$ shells is ignored.

Param.	Value [eV]	Param.	Value [eV]	d^9 [eV]	Param.	Value [eV]
U	7.000	U_{pd}	8.638		$\varepsilon_d^{\text{LDA}}$ (LB)	-1.686
J	0.800	F_{pd}^2	8.350	7.721	$\varepsilon_d^{\text{LDA}}$ (SB)	-1.928
U_{dd}	6.644	G_{pd}^1	6.332	5.787	$\varepsilon_p^{\text{LDA}}$ (PMI)	-3.503
F_{dd}^2	6.892	G_{pd}^3	3.603	3.291	$\varepsilon_d^{\text{LDA}}$ (PMM)	-1.797
F_{dd}^4	4.308	ζ_{2p}	11.507		$\varepsilon_p^{\text{LDA}}$ (PMM)	-3.482

Table 5.1: (left) Coulomb interaction U and Hund's interaction J used in the present study. The corresponding isotropic (configuration averaged) U_{dd} and higher Slater integrals (F_{dd}^2 and F_{dd}^4) are shown together. The U and J parameters are used commonly in all configurations. (center) The isotropic part U_{pd} and the Slater integrals of the $2p$ - $3d$ interaction (direct: F_{pd}^2 , exchange: G_{pd}^1 , G_{pd}^3), and spin-orbit coupling ζ_{2p} in the $2p$ core-shell used in the XAS and RIXS calculation. For configurations with 9 electrons on the Ni 3-shell (e.g. $|d^9\rangle$, $|d^9\bar{\nu}\rangle$), we used the core-valence parameters shown in the d^9 column. (right) The averaged site-energies of the Wannier states, obtained by partial traces in the tight-binding Hamiltonian are shown. Table and caption taken from [1].

In practice, the hybridization function $\Delta_\gamma^S(\varepsilon)$ obtained with the LDA+DMFT calculation is represented by 25–30 discretized bath states α for each orbital and spin, collectively denoted by γ , and differs for both sites in the PMI phase. The hybridization is assumed to be orbital (and spin) diagonal, which is a good approximation in the studied compounds.

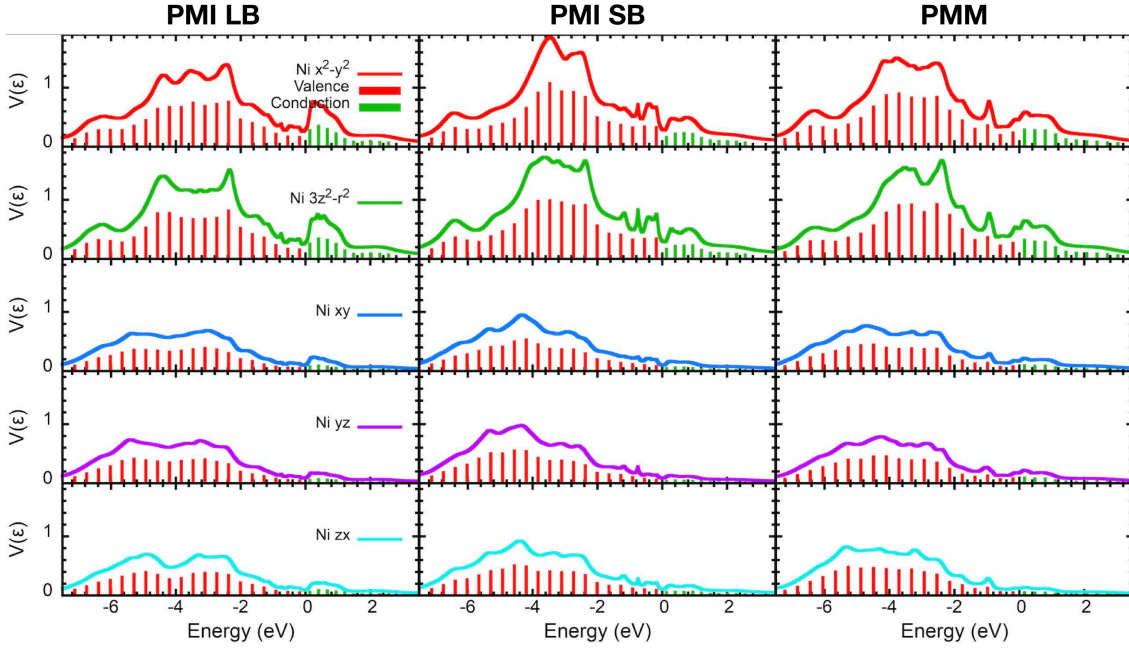


Figure 5.2: Hybridization intensities $V_\gamma^S(\varepsilon) = \sqrt{-\frac{1}{\pi}\Im\Delta_\gamma^S(\varepsilon)}$ obtained by the LDA+DMFT calculation and discretized hybridization intensities used in the XAS and RIXS calculations in the LB site (left) and the SB site (center) in the PMI phase, and PMM (right) phase for charge-transfer energy $\Delta_{CT} = 0.5$ eV. Figure and caption taken from [1].

Fig. 5.2 shows the hybridization intensities $V_\gamma^S(\varepsilon) = \sqrt{-\frac{1}{\pi}\Im\Delta_\gamma^S(\varepsilon)}$ obtained by LDA+DMFT, and the discretized intensities $V_{\alpha,\gamma}^S$, see Eq. 2.31, for the charge-transfer energy $\Delta_{CT} = 0.5$ eV. The discretized hybridization intensities are distributed uniformly with 20 levels in the valence channel ($< E_F$) and 10 levels in the conduction channel ($> E_F$). The energy window is adapted to intensities larger than $\approx 5\%$ of the peak value.

5.3 Configuration-Interaction Scheme for Different Charge Sectors

To compute Ni L_3 -edge XAS and RIXS from the Anderson impurity models, we employ the configuration-interaction (CI) scheme, see Sec. 2.7.5. Here, the CI scheme renders computational challenges because (i) the ground state wave function at LB and SB sites resides in different symmetry and the symmetry obtained by CI scheme depends on the initial configuration, and (ii) moderate charge fluctuation requires an accurate energy evaluation for the thermal average in the spectral function. We overcome these difficulties by a CI implementation

up to higher orders, while retaining a semi-continuum fashion of the bath. We perform calculations in different charge sectors of \hat{H}_{AIM} resulting in different initial states $|n\rangle$. In the XAS and RIXS spectral calculations, we use 30 (25) bath levels per spin and per orbital for the Ni^{2+} and Ni^{3+} (Ni^{4+}) charge sectors. Additionally we evaluate the energies E_n of the initial states in all three charge sectors using 30 bath levels. The CI expansion for three charge conserving series follows

$$\begin{aligned}\text{Ni}^{2+} &= \{|d^8\rangle, |d^9 \underline{v}^1\rangle, |d^{10} \underline{v}^2\rangle, |d^7 c^1\rangle, |d^8 \underline{v}^1 c^1\rangle, |d^9 \underline{v}^2 c^1\rangle, |d^6 c^2\rangle, |d^7 \underline{v}^1 c^2\rangle\} \\ \text{Ni}^{3+} &= \{|d^7\rangle, |d^8 \underline{v}^1\rangle, |d^9 \underline{v}^2\rangle, |d^{10} \underline{v}^3\rangle, |d^7 \underline{v}^1 c^1\rangle, |d^8 \underline{v}^2 c^1\rangle\} \\ \text{Ni}^{4+} &= \{|d^6\rangle, |d^7 \underline{v}^1\rangle, |d^8 \underline{v}^2\rangle, |d^9 \underline{v}^3\rangle, |d^{10} \underline{v}^4\rangle, |d^7 \underline{v}^2 c^1\rangle\}.\end{aligned}$$

Here, d^n represents Ni $3d$ states with n electrons on the Ni $3d$ shell. \underline{v}^i (c^j) denotes the number of holes (electrons) in the valence (conduction) bath states below (above) E_F . The initial states $|n\rangle$ are computed using the Lanczos method. The energies E_n of the initial states calculated in each charge sector are used to evaluate the corresponding weight of these spectra in the thermal average of the entire system. In the PMI phase, one of these charge sectors, depending on LB or SB site, provides the initial states with a dominant weight in the thermal average. The LB site has a triplet ground state in the Ni^{2+} charge sector, whereas the SB site has a singlet ground state in the Ni^{4+} charge sector. In PMM phase we obtain a mixture of all three charge sectors in thermal average, but the contributions to the spectra are mainly from Ni^{2+} and Ni^{3+} sectors which is discussed below.

In Tab. 5.2 we compare the occupation of the configurations in the ground state calculated with the CI solver with discretized bath and the CT-QMC solver.

Sector	CI			CT-QMC		
	LB	SB	PMM	LB	SB	PMM
d^6	0.3	2.4	0.4	0.4	2.0	1.0
d^7	17.9	34.3	23.2	17.6	31.1	25.5
d^8	70.9	52.7	65.2	69.5	54.4	60.5
d^9	10.7	10.3	11.0	12.2	12.1	12.5
d^{10}	0.2	0.3	0.2	0.3	0.5	0.3

Table 5.2: The atomic weights (diagonal elements of the site-reduced density matrix) integrated in the $N = 6 - 10$ sectors. The weights are calculated with the Anderson impurity model of the LB site and the SB site, and the PMM phase. The numbers estimated by the CI solver (descretized bath) and the CT-QMC solver (continuum bath) are compared. Table and caption taken from [1].

Application of the CI solver to metallic systems raises questions concerning discretization of the bath, reference state of the impurity or the size of the CI basis (degree of expansion). While the choice of the impurity reference state is crucial to minimize the computational effort (degree of CI expansion), we have checked that the same impurity dynamics (spectra) is obtained for different choices. In the present study we combine the spectra obtained from several impurity reference states (corresponding to different charge sectors of the discretized Anderson impurity model). To benchmark the CI results, we compare the equilibrium local density matrices (abundances of different Ni valence states) obtained with the CI scheme to those from CT-QMC in Table 5.2. The Ni LB site is dominated by d^8 ($S = 1$) state, expected in ionic Ni^{2+} . The SB site exhibits pronounced charge fluctuations between d^8 ($\approx 54\%$) and d^7 ($\approx 31\%$) states. The ground state of $H_{\text{ATM}}^{\text{SB}}$ is a spin singlet. This behavior matches well with the notion of site-selective Mott state in RNiO_3 [97, 101, 106].

5.4 Valence Spectra and Hybridization

Figures 5.3ac show the LDA+DMFT one-particle (1P) spectral densities in the PMI and PMM phases. The gross features of the spectra in the two phases are similar spectra to one another. The Ni $3d$ peak at -1.0 eV and O $2p$ peaks at -2.5 eV and -5.0 eV, corresponding to non- and anti-bonding states, respectively, match well with the experimental spectra of related nickelate LaNiO_3 [183], see Fig. 5.3c. The hybridization intensities $V_{\gamma,S}^2(\varepsilon) = -\frac{1}{\pi} \Im \Delta_{\gamma}^S(\varepsilon)$, the amplitude of electron hopping between the Ni $3d$ orbital γ (incl. spin) and the rest of the system at energy ε are shown in Figs. 5.3bd. Since the hybridization density is defined via the inverse of the local Green's function, the valence spectrum and $V_{\gamma,S}^2(\varepsilon)$ are not proportional to each other in general. The top of the valence band (bottom of the conduction band) is dominated by Ni LB (SB) $3d E_g$ states in Fig. 5.3a, although the total Ni d -occupation is almost identical on the two sites. The stronger Ni–O bonds at the SB site pushes the anti-bonding states above E_F , leading the sizable charge disproportionation in at low energies, that is compensated by its bonding counterpart at higher energies (around -8 eV to -4 eV). Somewhat counter-intuitively, we find larger $V_{\gamma,S}^2(\varepsilon)$ above E_F for LB than for SB site, which follows from the overall low-energy behavior of $V_{E_g,\text{LB}}$ reflecting the 1P spectral density on the SB site and vice versa. This behavior of the hybridization function is essential for the understanding of XAS and RIXS spectra.

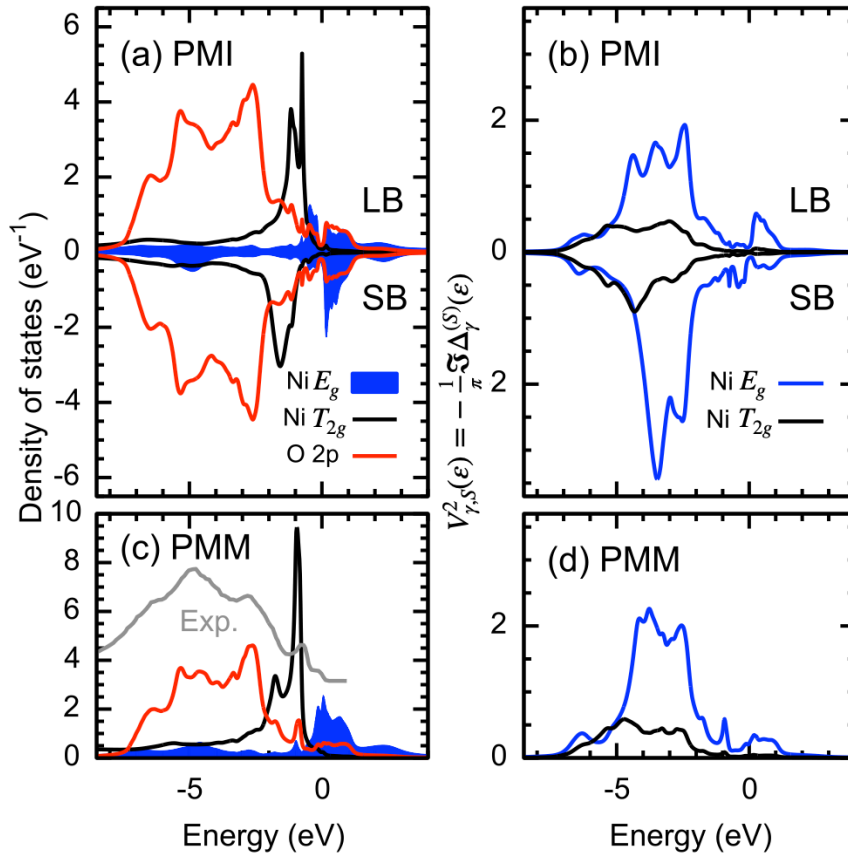


Figure 5.3: The 1P spectra calculated by LDA+DMFT in (a) PMI phase and (c) PMM phase with experimental valence photoemission spectrum (Ref [183]). DMFT hybridization intensities $V_{\gamma,S}^2(\epsilon)$ in (b) PMI phase and (d) PMM phase. In the PMI phase, the 1P spectra and $V_{\gamma,S}^2(\epsilon)$ at the Ni SB site are multiplied by -1 . Figure and caption taken from [1].

5.5 Ni 2p X-ray Absorption and Resonant Inelastic X-ray Spectroscopy of LuNiO_3

Fig. 5.4 shows the calculated Ni L_3 -XAS spectra in the PMI and PMM phases, together with the experimental data in the PMI phase of LuNiO_3 [184]. The experimental data exhibit a double-peak shape, composed of a sharp peak at low energy ω_{in} (≈ 853.5 eV) and a broader feature in high ω_{in} (≈ 855 eV). The LDA+DMFT spectra match the experiment quite well. Note that no by-hand alignment of LB and SB spectra was applied. The low- ω_{in} peak originates from a $2p - 3d$ exciton on the LB side. The broader high- ω_{in} peak originates from the excited d electron delocalized to the bath orbitals. This process is dominant on the SB site, but has a sizable contribution on the LB site as well. The

delocalization of the excited electron from the LB site is facilitated by the large hybridization intensity above E_F (Fig. 5.3b). This is demonstrated in the inset of Fig. 5.4 by setting $V_{\gamma,S}(\varepsilon > 0)$ to zero. There, the broad high- ω_{in} feature in the LB spectra vanishes. The small peak, that remains at ≈ 856 eV is due to a core-valence multiplet as observed in typical Ni²⁺ insulators like NiO [30, 43, 78]. The overlap of the LB and SB signals limits the site-selectivity of 2p XAS in RNiO₃ nickelates.

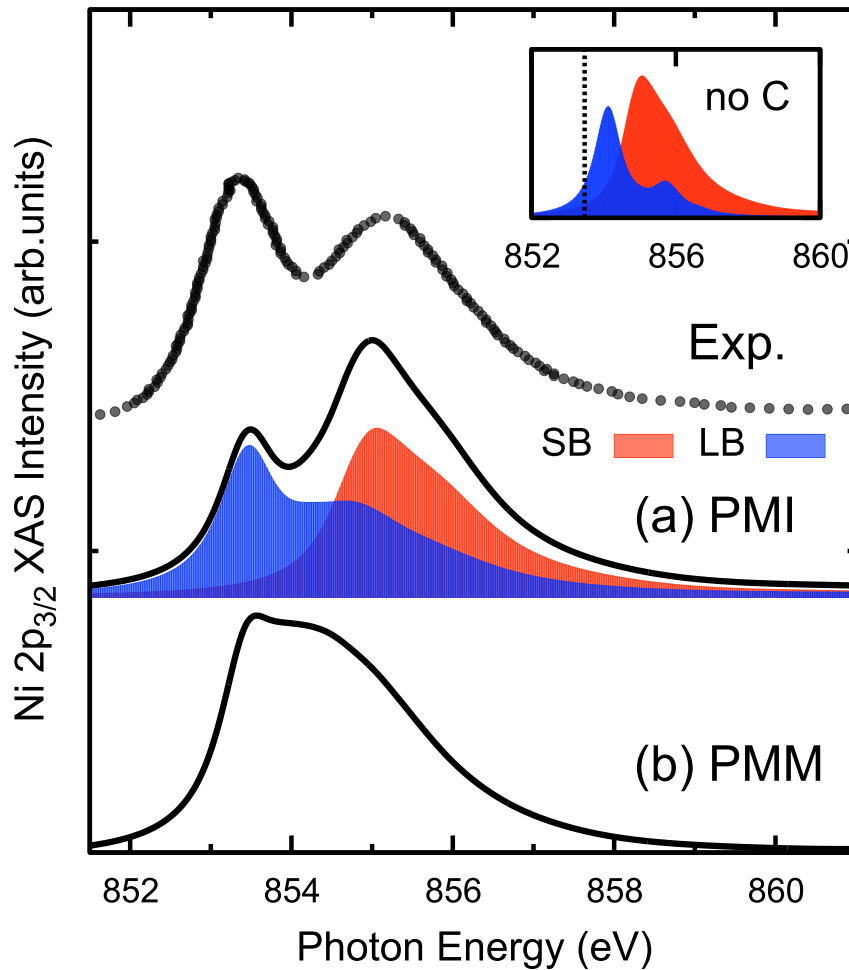


Figure 5.4: Ni L_3 -XAS in LuNiO₃ calculated by LDA+DMFT in (a) PMI phase and. (b) PMM phase. In the PMI phase, LB (SB) Ni site contribution is shown in blue (red) color. The experimental Ni L_3 -XAS data (Ref. [184]) measured in the PMI phase is shown together. The spectral broadening is considered using a Lorentzian 400 meV (HWHM). The inset shows the site contribution calculated with no a hybridization above E_F in the XAS final states. The horizontal dashed line marks the peak position of the LB XAS spectrum in the panel (a). Figure and caption taken from [1].

Figs. 5.5ab show the calculated Ni L_3 -RIXS spectra in the PMI and PMM phases, respectively. The results reproduce the experimental observations by Bisogni *et al.* [57] well: the RL feature ($\omega_{\text{loss}} \approx 1$ eV) with a constant energy loss ω_{loss} coexists with the FL feature showing a constant ω_{out} behavior, i.e., a linear dependence of ω_{loss} on ω_{in} . In the PMI phase, the FL intensity is slightly suppressed at ω_{in} between the L_3 double-peak (i.e. $\omega_{\text{in}} \approx 854$ eV) compared to the one in the PMM phase, which is also observed in the experiment [57]. Figs. 5.5cd show the site-resolved RIXS spectra in the PMI phase. As we mentioned above, the LB L_3 -XAS consists of two features marked as *A* (excitonic peak) and *B* (continuum). Their different character is reflected in the ω_{in} -dependence of the LB RIXS spectra: RL feature (due to inter-atomic dd excitations) resonates mainly at *A*, while the FL feature due to unbound electron-hole pairs gains intensity with approaching *B*. The latter can be understood as the X-ray excited electron, which leaves the LB site in the intermediate state of RIXS, giving rise to an unbound electron-hole pair in the RIXS final state, see Fig. 5.5c. The propensity of the excited electron to escape the TM site is encoded in the hybridization intensity above the Fermi level. The SB signals in Fig. 5.5d shows an intense charge-transfer excitation extending to higher ω_{loss} in addition to a less prominent FL feature, which merges with the charge-transfer excitations at $\omega_{\text{loss}} \approx 3$ eV. The bright and (vertically) broad charge-transfer feature reflects stronger Ni–O hybridization on the SB site. Since the *B*-peak signal from the LB site largely overlaps with the SB signal, Fig. 5.4, the site-selectivity cannot be achieved for the corresponding ω_{in} . In RNiO_3 , only the d – d excitations at the *A*-peak can be associated with the LB site.

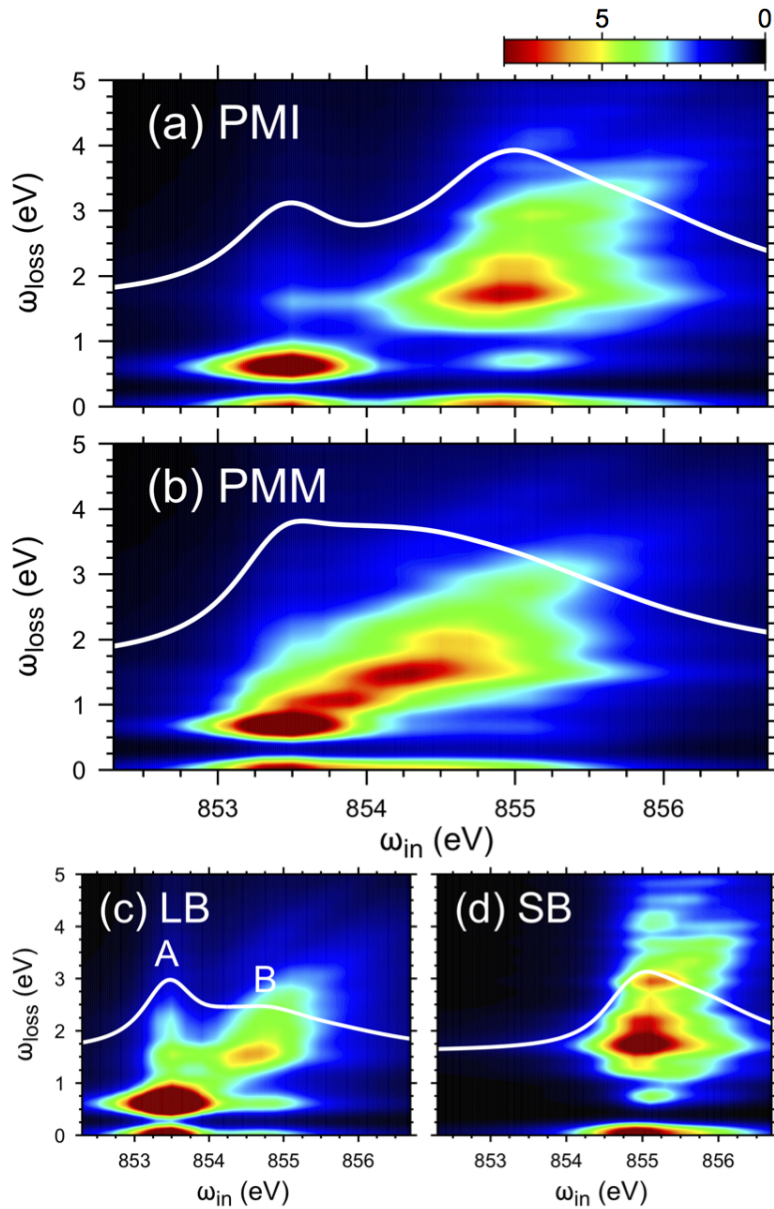


Figure 5.5: Ni L_3 -RIXS in LuNiO₃ calculated by LDA+DMFT in (a) PMI phase and (b) PMM phase. (c) LB and (d) SB Ni site contribution to the RIXS spectra in the PMI phase. White lines in panels are Ni L_3 -XAS spectra calculated in the corresponding phase or Ni site. The spectral broadening is considered using a Gaussian 150 meV (HWHM). Figure and caption taken from [1].

5.5.1 Metal-Insulator Transition

Then, we zoom at very low ω_{loss} to address the behavior reported in Ref. [57]. Figs. 5.6ab show the calculated low- ω_{loss} RIXS spectra in the PMI phase and the PMM phase, respectively. The photon energies ω_{in} are set to around the main

peak at the LB site. We find a significant difference, gap closing, between the CD-insulating and metallic phases, which matches the experimental observation of Bisogni *et al* [57]. Thus, RIXS can be used to study the reconstruction of the low-energy electron-hole continuum due to the metal-insulator transition and LDA+DMFT provides an accurate description of it.

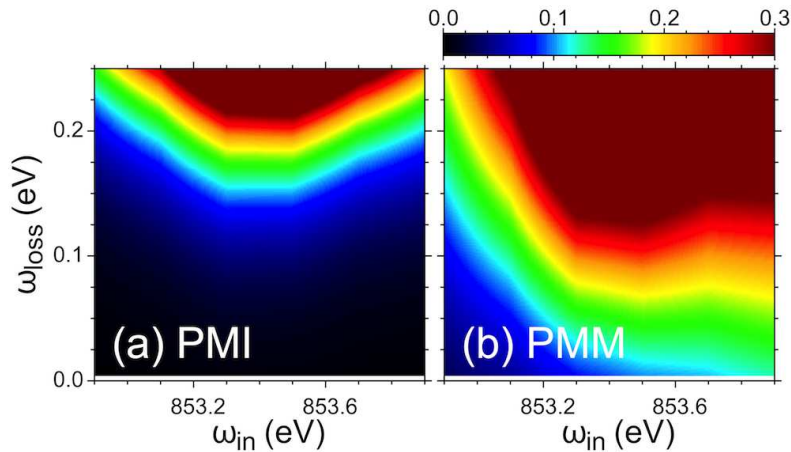


Figure 5.6: Low-energy Ni L_3 -RIXS features in LuNiO_3 in (a) PMI phase and (b) PMM phase. Note that the calculated elastic peak ($\omega_{\text{loss}}=0.0$ eV) is removed. Figure and caption taken from [1].

5.5.2 Charge Sector Resolved Spectra

In the following we show the XAS and RIXS spectra for PMI and PMM phase for each charge sector with a charge-transfer energy of $\Delta_{\text{CT}} = 0.5$ eV. This corresponds to a double-counting energy of $\mu_{\text{dc}} = -47.8278$ eV for LB and $\mu_{\text{dc}} = -47.5858$ eV for SB in PMI phase and in PMM phase to $\mu_{\text{dc}} = -47.6960$ eV. Fig. 5.7 shows the Ni L_3 -edge XAS and RIXS spectra of three charge sectors (Ni^{2+} , Ni^{3+} , Ni^{4+}) for PMI (SB, LB) and PMM phase. The total spectra of the LB site consists purely of the triplet state in the Ni^{2+} charge sector due to the high energies of the doublet Ni^{3+} states and singlet Ni^{4+} states. In the SB spectra only the singlet state of the Ni^{4+} charge sector contributes to the total spectra. The final spectra in PMI phase are the sum of thermal averaged LB and SB spectra, see Fig. 5.5a. In PMM phase all three charge sectors contribute in thermal average to the total spectra, with 75 % Ni^{2+} , 15 % Ni^{3+} and 10 % Ni^{4+} , see Fig. 5.5b.

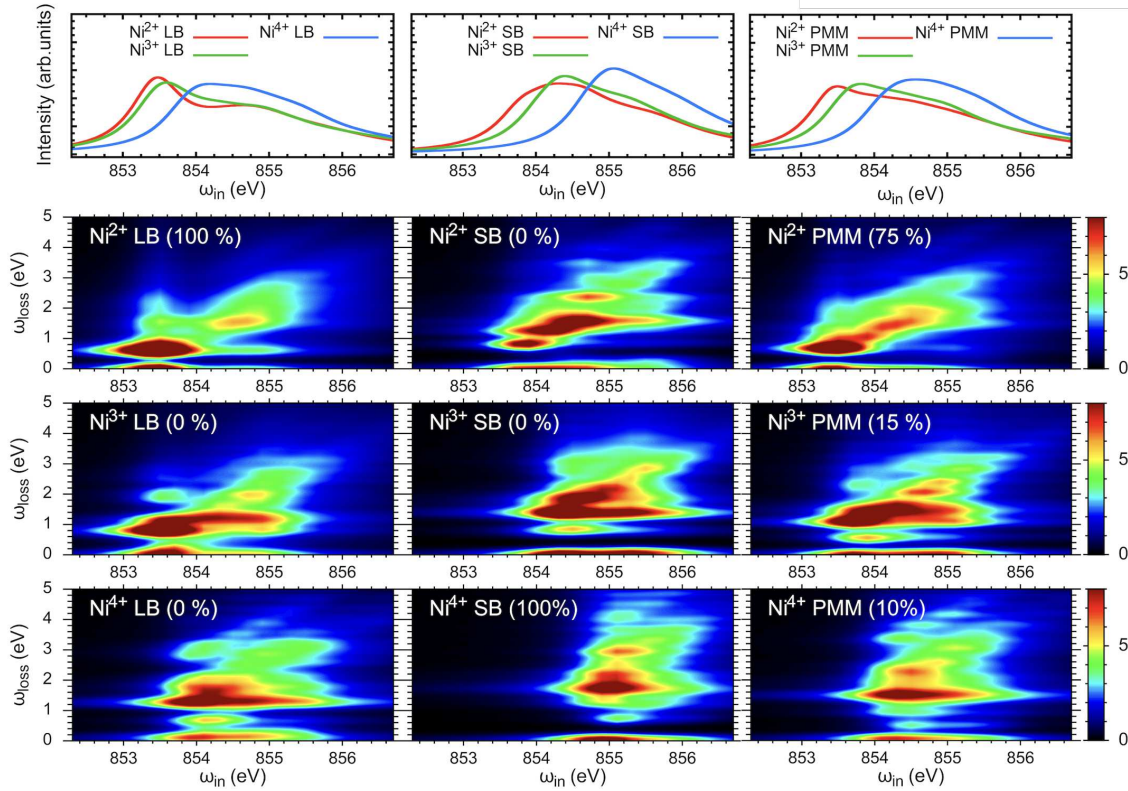


Figure 5.7: Ni L_3 -edge XAS and RIXS spectra of each charge sector for LB (left) and SB (right) site. The XAS and RIXS spectra of LB site Ni^{2+} and SB site Ni^{4+} contribute to the final spectra of PMI phase. Figure and caption taken from [1].

5.6 Double-Counting Dependence

We show briefly the Ni L_3 -edge XAS and RIXS spectra for different charge transfer energies $\Delta_{\text{CT}} = \{-1.0, 0.0, 0.5, 1.0\}$ eV in PMI phase, see Fig. 5.8. The spectra are calculated with 20 discrete hybridization levels below E_{F} and 5 above E_{F} . The LB site with $\Delta_{\text{CT}} = 0.5$ eV has 10 discrete levels above E_{F} .

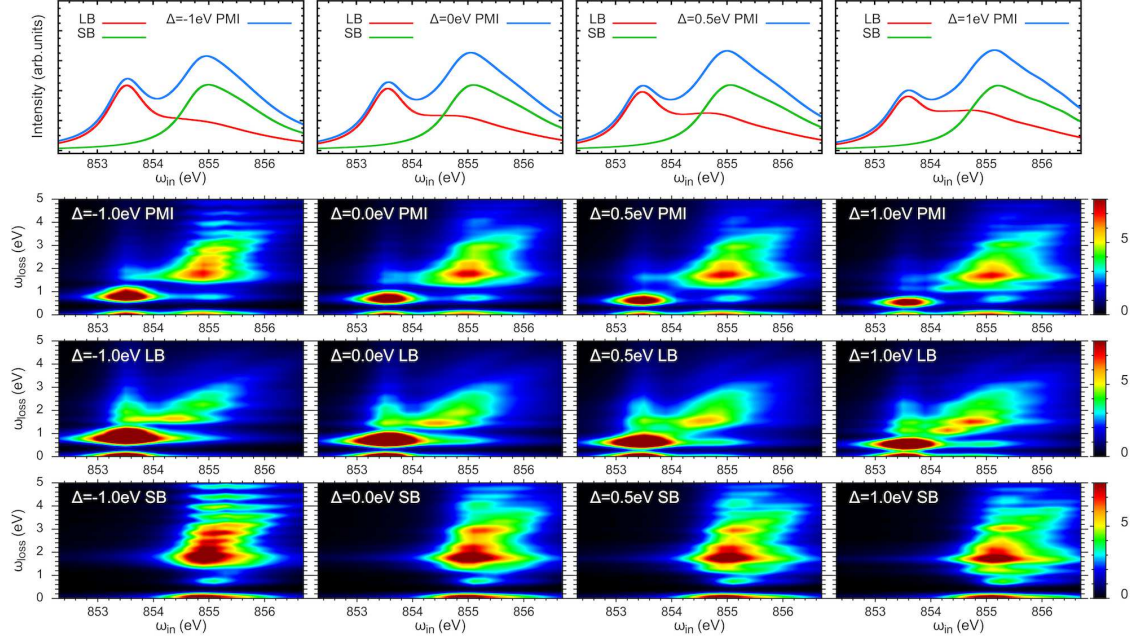


Figure 5.8: Ni L_3 -edge XAS and RIXS spectra for different charge transfer energies $\Delta_{CT} = \{-1.0, 0.0, 0.5, 1.0\}$ eV in PMI phase. Figure and caption taken from [1].

5.7 Conclusions

We presented a computational study of L -edge X-ray absorption spectroscopy and resonant inelastic X-ray scattering of the representative rare-earth nickelate LuNiO_3 . LuNiO_3 shows a charge disproportionation within the PMI phase with a triplet and singlet ground state for LB and SB site, respectively. Our approach enabled us to capture the charge disproportionation in the PMI phase and also the strong charge fluctuations in the PMM phase. We discussed the spectra across the CD/metal-insulator transition in LuNiO_3 and reflected on the possibility of site-selectivity of XAS and RIXS in the PMI phase of the compound. Our results showed, that the two peaks, present in XAS spectra and reflected in RIXS of the CD insulating phase, cannot be uniquely associated with the LB and SB sites. While the low-energy peak originates from the LB site, the high-energy peak combines signals from both sites. We showed that the shoulder above the main line observed in the XAS spectra of the LB site consists of unbound electron-hole pairs which are propagating within the crystal host. Thus, the shoulder is not only due to Coulomb multiplet excitations, which provide only minor intensities. Furthermore, we studied the FL feature observed in the RIXS spectra of the studied compound. There are subtle changes in the FL features at the low- ω_{loss} regime which can be used to identify the metal-insulator transition as proposed in Ref. [57]. We also studied the charge resolved spectra and the double-counting dependence of the spectra, to which especially the gap in the low- ω_{loss} regime of the FL feature is sensitive.

Chapter 6

Summary and Outlook

We studied the application of the new core-level spectroscopy framework based on the Anderson impurity model to a variety of transition metal oxides. We have chosen transition metal compounds with different occupation number of valence electrons in the ground state to test its wide applicability. The studies contain the simulation of several core-level spectroscopies, X-ray photoemission spectroscopy (XPS), X-ray absorption spectroscopy (XAS) and resonant inelastic X-ray scattering (RIXS). In core-level spectroscopy calculations, we were able to include the band character of the bath states in the Anderson impurity model description. This is important to understand the core-level spectra of transition metal compounds. For example, we captured the non-local screening effects observed in XPS spectra. In XAS spectra we observed pronounced delocalization effects of electrons which were formally attributed to Coulomb multiplet effects. Our approach provided an accurate description of both bound (dd) and unbound (electron-hole pair) excitations in the RIXS spectra. We also studied charge disproportionated systems with two inequivalent NiO_6 octahedra. The spectra are intriguing and have a quantitative agreement with experimental spectra.

In general, we confirmed that our approach provides a quantitative description of core-level spectroscopies of transition metal oxides. We are even able to study complex systems at relatively low computational cost. But there are still remaining tasks concerning our approach. Although one is able to study a broad variety of materials, the code is still not user friendly. A detailed knowledge and experience is needed to generate inputs for the study of complex materials, which often includes minor modifications of the code. Thus, a user friendly interface which automatically generates input for at least simple systems should be provided for future studies. The extension of the possible basis size of the Hamiltonian is always an important aspect. We are limited by available memory size, but we can reduce the memory demands by a further parallelization of the code. The study of large f -electron systems, e.g. uranium compounds, would need an adjustment of the code, although the foundation is already provided. Another idea is the application of the code

for X-ray magnetic linear dichroism (XMLD), which would be of great interest to obtain an even more comprehensive understanding of the electronic structure. A more extensive project would be the implementation of momentum-dependent RIXS on the basis of the existing code.

Appendices



Die approbierte gedruckte Originalversion dieser Dissertation ist an der TU Wien Bibliothek verfügbar.
The approved original version of this doctoral thesis is available in print at TU Wien Bibliothek.

Appendix A

Methods

A.1 Lanczos Algorithm

When dealing with Hamiltonian's of large rank the knowledge of a 'few' lowest (or largest) eigenvalues is for many calculations sufficient. Contrary to simply diagonalizing the matrix, which is often computationally not feasible, the Lanczos algorithm provides a clever alternative. Let us consider a Hamiltonian \hat{H} of rank N and orthonormal basis states $|\Phi_j\rangle$ with $j = 0, 1, 2, \dots, N$. The Lanczos algorithm transforms the Hamiltonian with the initial basis set $\{|\Phi_j\rangle\}$ iteratively into a tridiagonal form with a new basis $\{|x_i\rangle\}$ and $i = 0, 1, 2, \dots, k; k \leq N$. Basis vectors $\{|x_i\rangle\}$ are generated by applying the Hamiltonian \hat{H} to a randomly chosen starting vector $|x_0\rangle$, also called seed state. This creates Krylov basis states $\{|k_N\rangle = \prod_{i=0}^N \hat{H}^i |x_0\rangle\}$, which are not orthogonal. The Lanczos algorithm builds up on the Krylov states by including the orthonormalization. The orthogonalization of a state $|x_i\rangle$ depends only on its two preceding states ($|x_{i-1}\rangle, |x_{i-2}\rangle$). By normalizing these states $\{|x_i\rangle\}$ one obtains $\{|f_i\rangle\}$. If $k < N$ the true eigenvalues of \hat{H} can be approximated by the eigenvalues of the tridiagonal matrix. It turns out, that after a few iterations the eigenvalues of the tridiagonal matrix converge to the lowest (or largest) eigenvalue of the Hamiltonian. This is due to the analogy of the Lanczos algorithm to the power method. Let us consider a Hamiltonian with eigenspectrum of $|E_0| > |E_1| > \dots > |E_N|$. Successive application of the Hamiltonian onto any state not orthogonal to the ground state results in

$$|x_k\rangle = \hat{H}^k |x_0\rangle = \sum_{j=0}^N E_j^k c_j |\Phi_j\rangle = E_0^k \left[c_0 |\Phi_0\rangle + \sum_{j=1}^N \left(\frac{E_j}{E_0} \right)^k c_j |\Phi_j\rangle \right] \xrightarrow{k \rightarrow \infty} E_0^k c_0 |\Phi_0\rangle. \tag{A.1}$$

Thus as long as the seed state $|x_0\rangle$ contains the ground state $|\Phi_0\rangle$, only the ground state 'survives' [21, 185].

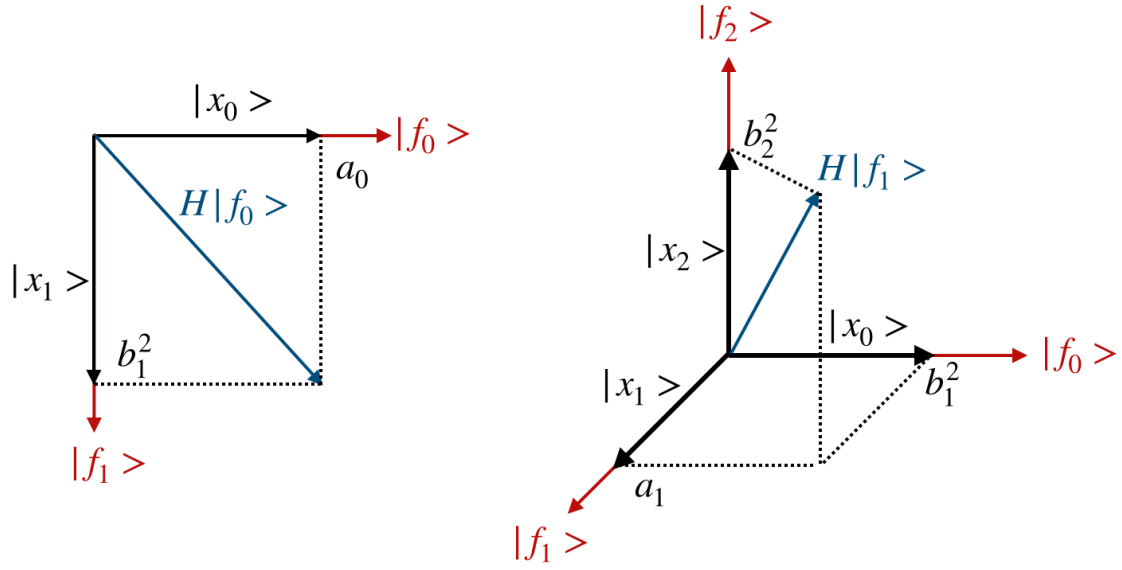


Figure A.1: Scheme of the Lanczos algorithm. Figure adapted from [185].

The Lanczos algorithm operates like follows: First a random seed state $|x_0\rangle$ state must be generated and normalized $|f_0\rangle$. To obtain a subsequent state $|x_1\rangle$, we apply the Hamiltonian \hat{H} onto the seed state $\hat{H}|f_0\rangle$ and orthogonalize this state by subtracting its projection onto the initial state, see left panel of Fig. (A.1),

$$|x_1\rangle = \hat{H}|f_0\rangle - \langle f_0|\hat{H}|f_0\rangle|f_0\rangle. \quad (\text{A.2})$$

By subsequent normalizing of $|x_1\rangle$ we obtain a state $|f_1\rangle = \frac{|x_1\rangle}{b_1}$ which is orthonormal to $|f_0\rangle$. In the next iteration, state $|x_2\rangle$ is obtained by applying the Hamiltonian \hat{H} onto state $|f_1\rangle$ and by orthogonalization to the two preceding states $|f_1\rangle$ and $|f_0\rangle$, see right panel of Fig. (A.1),

$$|x_2\rangle = \hat{H}|f_1\rangle - \langle f_1|\hat{H}|f_1\rangle|f_1\rangle - \langle f_0|\hat{H}|f_1\rangle|f_0\rangle. \quad (\text{A.3})$$

By normalization of $|x_2\rangle$ we obtain $|f_2\rangle$. The essence of the Lanczos algorithm is, that by orthogonalizing the next state $|x_3\rangle$ to the previous states, the projection $\langle f_0|\hat{H}|f_2\rangle \equiv 0$ vanishes, which is valid for all succeeding iterations. Thus, this procedure results in

$$|x_{i+1}\rangle = \hat{H}|x_i\rangle - a_i|x_i\rangle - b_i^2|x_{i-1}\rangle, \quad (\text{A.4})$$

where

$$a_i = \frac{\langle x_i|\hat{H}|x_i\rangle}{\langle x_i|x_i\rangle} \quad (\text{A.5})$$

and

$$b_i^2 = \frac{\langle x_{i-1}|\hat{H}|x_i\rangle}{\langle x_{i-1}|x_{i-1}\rangle}, \quad (\text{A.6})$$

with $b_0 = 0$. The approximate Hamiltonian \hat{H} in the basis $\{|f_i\rangle\}$ reads

$$\hat{H} = \sum_{i=0}^k a_i |f_i\rangle \langle f_i| + b_{i+1} [|f_i\rangle \langle f_{i+1}| + |f_{i+1}\rangle \langle f_i|], \quad (\text{A.7})$$

which is a tridiagonal matrix

$$H = \begin{bmatrix} a_0 & b_1 & & & \\ b_1 & a_1 & b_2 & & \\ & b_2 & a_2 & \ddots & \\ & & \ddots & \ddots & b_k \\ & & & b_k & a_k \end{bmatrix}. \quad (\text{A.8})$$

This procedure is continued until the convergence of the lowest (or highest) eigenvalue. The ground state $|\text{GS}\rangle$ in its initial basis $|\Phi_j\rangle$ can be reconstructed from the entries c_i of the eigenvector $|\tilde{f}_i\rangle$ of the corresponding lowest eigenvalue

$$|\text{GS}\rangle = \sum_{i=0}^n c_i |\tilde{f}_i\rangle. \quad (\text{A.9})$$

To obtain the first excited state, one creates a new seed state, where the ground state $|\text{GS}\rangle$ is projected out, e.g. by Gram-Schmidt, and rerun the procedure of the Lanczos algorithm. This process can be done repeatedly to obtain multiple excited states.

A.2 Continued Fraction Expansion

The continued fraction expansion is related to the inversion of tridiagonal matrices. Here we consider the inverse of a tridiagonal matrix $\frac{1}{H}$, where H is obtained by e.g. the Lanczos algorithm. We want to calculate the first diagonal element of the inverse of the matrix, e.g. $(\frac{1}{H})_{00}$. To evaluate this element we split the tridiagonal Matrix H into various subspaces and use of a set of special determinants D_i . D_0 is the determinant of the whole tridiagonal matrix H ; D_1 is the determinant of H , where the first row and first column are removed from the matrix; D_2 is the determinant of H when additionally the second row and second column are removed, and so on. We use Cramers rule to obtain the diagonal element $(\frac{1}{H})_{00} = \frac{D_1}{D_0}$. By using the introduced determinants, this results in [185]

$$\left(\frac{1}{H}\right)_{00} = \frac{1}{a_0 - b_1^2 \frac{1}{D_1/D_2}}, \quad (\text{A.10})$$

where H is represented by Eq. A.8. We inserted $D_0 = a_0 D_1 - b_1^2 D_2$ by developing the determinant D_0 along the first row. The expression D_1/D_2 can be evaluated

with $D_1 = a_1 D_2 - b_2^2 D_3$. By iterating over all expressions D_i/D_{i+1} we obtain a continued fraction expansion

$$\left(\frac{1}{H}\right)_{00} = \frac{1}{a_0 - \frac{b_1^2}{a_1 - \frac{b_2^2}{a_2 - \dots}}}, \quad (\text{A.11})$$

which is a convenient way to calculate objects like spectral functions of the form

$$F(\omega) = -\frac{1}{\pi} \Im \left[\langle x | \frac{1}{\omega^+ - \hat{H}} | x \rangle \right], \quad (\text{A.12})$$

where \hat{H} is the Hamiltonian and $\omega^+ = \omega + i0^+$. The term in the brackets has the form

$$\langle x | \frac{1}{\omega^+ - \hat{H}} | x \rangle = \frac{\langle x | x \rangle}{\omega^+ - a_0 - \frac{b_1^2}{\omega^+ - a_1 - \frac{b_2^2}{\omega^+ - a_2 - \dots}}}, \quad (\text{A.13})$$

where we consider that the Hamiltonian is calculated by the Lanczos algorithm with $|x\rangle$ as seed state. Usually, the continued fraction expansion converges after a few hundred iterations, depending on the system size.

A.3 Resolvent Formalism of Electronic Systems

The resolvent formalism of electronic systems provides a systematic way to obtain the electronic structure of a system with initially large or even infinite number of basis functions. The number of basis functions is reduced progressively within this scheme by creating subsequently new basis states describing an effective model. We start the procedure with a Hamiltonian \hat{H} with dimension N which describes the electronic structure of the system. Then we divide the system into two sub-blocks \hat{H}^A and \hat{H}^B with dimension N_A and $N_B = N - N_A$, respectively [21, 185]. The Hamiltonian of the system reads

$$\hat{H} = \hat{H}_0 + \hat{W} = \begin{bmatrix} \hat{H}^A & 0 \\ 0 & \hat{H}^B \end{bmatrix} + \begin{bmatrix} 0 & \hat{H}^{AB} \\ \hat{H}^{BA} & 0 \end{bmatrix}, \quad (\text{A.14})$$

where \hat{H}^{AB} and \hat{H}^{BA} connects the two Hamiltonians \hat{H}^A and \hat{H}^B in subspace A and B . The diagonal blocks of \hat{H} are contained in the operator \hat{H}_0 . The Hamiltonian can be further transformed into additional subspaces which are only connected by their preceding and succeeding subspaces. I.e. by iteratively transforming subspace B into e.g. subspace B' and subspace C , or transforming \hat{H}^B into two blocks $\hat{H}^{B'}$

and \hat{H}^C , and so on, one obtains a tridiagonal shape of \hat{H} which is an implicit characteristic of the Lanczos algorithm. For pedagogical reasons we stick in this section to two sub-blocks. We use the identity

$$\varepsilon - \hat{H}_0 = (\varepsilon - \hat{H}_0 - \hat{W}) + \hat{W}, \quad (\text{A.15})$$

where we multiply from left $\frac{1}{\varepsilon - \hat{H}_0}$ and from right $\frac{1}{\varepsilon - \hat{H}_0 - \hat{W}}$ which results in

$$\frac{1}{\varepsilon - \hat{H}_0 - \hat{W}} = \frac{1}{\varepsilon - \hat{H}_0} + \frac{1}{\varepsilon - \hat{H}_0} \hat{W} \frac{1}{\varepsilon - \hat{H}_0 - \hat{W}}. \quad (\text{A.16})$$

This equation reminds of the Dyson equation, see Eq. 2.65. We note that the expressions here are operators, compared to the scalar (matrix) valued form of the Dyson equation used in DMFT. We rewrite Eq. A.16 in terms of resolvents \hat{F} and \hat{F}_0

$$\hat{F} = \hat{F}_0 + \hat{F}_0 \hat{W} \hat{F}. \quad (\text{A.17})$$

By using the Hamiltonian in its sub-block shape, Eq. A.17 reads

$$\begin{bmatrix} \hat{F}^A & \hat{F}^{AB} \\ \hat{F}^{BA} & \hat{F}^B \end{bmatrix} = \begin{bmatrix} \hat{F}_0^A & 0 \\ 0 & \hat{F}_0^B \end{bmatrix} + \begin{bmatrix} \hat{F}_0^A & 0 \\ 0 & \hat{F}_0^B \end{bmatrix} \begin{bmatrix} 0 & \hat{H}^{AB} \\ \hat{H}^{BA} & 0 \end{bmatrix} \begin{bmatrix} \hat{F}^A & \hat{F}^{AB} \\ \hat{F}^{BA} & \hat{F}^B \end{bmatrix}, \quad (\text{A.18})$$

where \hat{W} connects the two sub-blocks \hat{H}^A and \hat{H}^B . The matrix elements of Eq. A.18 provide the following four equations

$$\hat{F}^A = \hat{F}_0^A + \hat{F}_0^A \hat{H}^{AB} \hat{F}^{BA} \quad (\text{A.19})$$

$$\hat{F}^B = \hat{F}_0^B + \hat{F}_0^B \hat{H}^{BA} \hat{F}^{AB} \quad (\text{A.20})$$

$$\hat{F}^{AB} = \hat{F}_0^A \hat{H}^{AB} \hat{F}^B \quad (\text{A.21})$$

$$\hat{F}^{BA} = \hat{F}_0^B \hat{H}^{BA} \hat{F}^A. \quad (\text{A.22})$$

These equations can be solved to provide an expression for the resolvent in subspace A

$$\hat{F}^A = \frac{1}{\varepsilon - \hat{H}^A - \hat{H}^{AB} \frac{1}{\varepsilon - \hat{H}^B} \hat{H}^{BA}}. \quad (\text{A.23})$$

One can now repeat this splitting for \hat{H}^B . This can be done repeatedly which leads to a continued fraction expansion. In practice, the splitting of the sub-blocks is continued until the expansion converges. Now let us focus on the term in the denominator of Eq. A.23. This term can be viewed as effective or renormalized Hamiltonian

$$\hat{H}_{\text{eff}} = \hat{H}^A - \hat{H}^{AB} \frac{1}{\varepsilon - \hat{H}^B} \hat{H}^{BA}. \quad (\text{A.24})$$

The effective Hamiltonian $\hat{H}_{\text{eff}} = \hat{H}^A + \hat{V}^A$ consists of \hat{H}^A and an operator \hat{V}^A

$$\hat{V}^A = \hat{H}^{AB} \frac{1}{\varepsilon - \hat{H}^B} \hat{H}^{BA}. \quad (\text{A.25})$$

\hat{V}^A describes an effective interaction of the remaining system \hat{H}^B with the subsystem \hat{H}^A [185]. In physical terms \hat{V}^A describes the hopping of a particle from subspace A into subspace B , followed by the propagation of the particle within subspace B and the returning into subspace A . This scheme formally decouples the resolvent \hat{F}^A in Eq. A.23 from subspace B . In practice one applies a state, e.g. ground state, from left and right to the resolvent. The resolvent formalism is connected to the zero temperature Green's function by

$$G_{ij}^A(\varepsilon) = \langle \text{GS} | c_i \hat{F}^A(\varepsilon) c_j^\dagger | \text{GS} \rangle, \quad (\text{A.26})$$

where c_i^\dagger and c_j are creation and annihilation operators, where the indices i and j denote to e.g. site, orbital and spin. In practice, Lanczos algorithm is used to transform the Hamiltonian \hat{H} into sub-blocks with a tridiagonal shape. The continued fraction expansion combined with the orthogonal Krylov basis is used iteratively to increase the number of subspaces until the convergence of the continued fraction expansion. Usually around 200–500 iterations are used.

Appendix B

Tensor Operators

B.1 Crystal Field Potential

The crystal field potential $v_{\text{cf}}(\mathbf{r}) = v_{\text{cf}}(r, \theta, \phi)$ is generated in the most general case by a charge density $\rho(\mathbf{R}) = \rho(R, \Theta, \Phi)$ describing electrons of the crystal host [21, 112, 113, 186, 187]

$$O(\mathbf{r}) = v_{\text{cf}}(\mathbf{r}) = \int d^3R \frac{\rho(\mathbf{R})}{|\mathbf{R} - \mathbf{r}|}. \quad (\text{B.1})$$

Since the basis functions can be expressed in terms of atomic-like orbitals and thus spherical harmonics, we expand the Coulomb potential $v_{\text{cf}}(\mathbf{r})$ in terms of Legendre polynomials

$$\frac{1}{|\mathbf{R} - \mathbf{r}|} = \sum_k \frac{r_{<}^k}{r_{>}^{k+1}} P_k(\cos \omega), \quad (\text{B.2})$$

where ω is the angle between \mathbf{R} and \mathbf{r} . The $r_{<} = \min(|\mathbf{R}|, |\mathbf{r}|)$ and $r_{>} = \max(|\mathbf{R}|, |\mathbf{r}|)$ are the lesser and greater ones of $R = |\mathbf{R}|$ and $r = |\mathbf{r}|$. The addition-theorem for spherical harmonics, which is a generalization of the trigonometric relation $\cos \omega \equiv \cos \Theta \cos \theta + \sin \Theta \sin \theta \cos \Phi - \phi$, provides an expression for Legendre polynomials in terms of spherical harmonics

$$P_k(\cos \omega) = \frac{4\pi}{2k+1} \sum_{q=-k}^k Y_{kq}^*(\Theta, \Phi) Y_{kq}(\theta, \phi), \quad (\text{B.3})$$

with the identity of spherical harmonics $Y_{kq} = (-1)^q Y_{kq}^*$. This expansion and the expression of renormalized spherical harmonics

$$C_q^k(\theta, \phi) = \sqrt{\frac{4\pi}{2k+1}} Y_{kq}(\theta, \phi), \quad (\text{B.4})$$

result in the crystal field potential

$$v_{\text{cf}}(\mathbf{r}) = \sum_k \sum_{q=-k}^k C_q^k(\theta, \phi) \int d^3R \rho(\mathbf{R}) \frac{r_{<}^k}{r_{>}^{k+1}} C_q^k(\Theta, \Phi)^*. \quad (\text{B.5})$$

The renormalized spherical harmonics provide a practical way to evaluate the crystal field potential in spherical symmetry. In practice, either further simplifications are applied, e.g. using point charges with fixed positions or the crystal field potential is obtained by first principle calculations.

B.2 Spin-Orbit Coupling

The matrix elements of the spin-orbit coupling read $\langle lm\frac{1}{2}s|\mathbf{l}\cdot\mathbf{s}|lm'\frac{1}{2}s'\rangle$, where m and s are the magnetic quantum number and the secondary spin quantum number, respectively. We express the angular momentum operator \mathbf{l} and the spin momentum operator \mathbf{s} in terms of ladder operators

$$l_1 = -\frac{l_x + il_y}{\sqrt{2}} \equiv -\frac{l_+}{\sqrt{2}}, \quad (\text{B.6})$$

$$l_{-1} = \frac{l_x - il_y}{\sqrt{2}} \equiv \frac{l_-}{\sqrt{2}}, \quad (\text{B.7})$$

$$l_0 = l_z, \quad (\text{B.8})$$

where the spin momentum operator \mathbf{s} is defined equivalently. The inner product of vector operators reads

$$\mathbf{l}\cdot\mathbf{s} = \sum_q (-1)^q l_{-q} s_q = -l_{-1} s_1 + l_0 s_0 - l_1 s_{-1}, \quad (\text{B.9})$$

where $l_0 s_0$ are diagonal elements with no change of magnetic m and spin s quantum numbers. The off-diagonal elements $l_{-1} s_1$ and $l_1 s_{-1}$ change the magnetic and spin quantum number by ± 1 . This results in a total angular momentum conservation $J = l + s$. The matrix elements

$$\langle lm, \frac{1}{2}s|\mathbf{l}\cdot\mathbf{s}|lm', \frac{1}{2}s'\rangle = \sum_q (-1)^q \langle lm|l_{-q}|lm'\rangle \langle \frac{1}{2}s|s_q|\frac{1}{2}s'\rangle \quad (\text{B.10})$$

of the angular momentum tensor operators $T_q^1 \in \{l_q, s_q\}$ are calculated by the use of the Wigner-Eckhart theorem which can be used for both, angular and spin momentum

$$\langle lm|T_q^1|l'm'\rangle = (-1)^{l-m_l} \langle l||\mathbf{T}^1||l'\rangle \begin{pmatrix} l & 1 & l' \\ -m & q & m' \end{pmatrix}, \quad (\text{B.11})$$

with the reduced matrix elements for the angular momentum operator (spin momentum operator)

$$\langle l||\mathbf{T}^1||l'\rangle = \delta_{ll'} \sqrt{l(l+1)(2l+1)}. \quad (\text{B.12})$$

The selection rules of $3J$ symbols $\begin{pmatrix} A & B & C \\ a & b & c \end{pmatrix}$ provide finite values for

$$|A - B| \leq C \leq A + B, \quad (\text{B.13})$$

$$a + b + c = 0. \quad (\text{B.14})$$

B.3 Coulomb Interaction

The two-particle matrix element of the Coulomb interaction reads

$$\langle l_1 m_1 l_2 m_2 | \frac{1}{|\mathbf{r}' - \mathbf{r}|} | l_3 m_3 l_4 m_4 \rangle = \sum_k F^k(\text{shell}_1, \text{shell}_2) \times f^k(l_1 m_1 l_2 m_2, l_3 m_3 l_4 m_4), \quad (\text{B.15})$$

where we factorized the potential in radial and angular part in the basis of spherical harmonics. The m_i are magnetic moments of the corresponding angular momentum. The radial parts of the valence-valence Coulomb interaction read

$$F^k(3d, 3d) = \int_0^\infty \int_0^\infty dr dr' R_{3d}^2(r) R_{3d}^2(r') \frac{r^k}{r^{k+1}} r^2 r'^2, \quad (\text{B.16})$$

which are so-called Slater integrals. The $R_{3d}(r)$ are the radial parts of the TM $3d$ orbitals. The radial part of the direct core-valence interaction reads

$$F^k(2p, 3d) = \int_0^\infty \int_0^\infty dr dr' R_{2p}^2(r) R_{3d}^2(r') \frac{r^k}{r^{k+1}} r^2 r'^2. \quad (\text{B.17})$$

The exchange part reads

$$G^k(2p, 3d) = \int_0^\infty \int_0^\infty dr dr' R_{2p}(r) R_{3d}(r) R_{2p}(r') R_{3d}(r') \frac{r^k}{r^{k+1}} r^2 r'^2. \quad (\text{B.18})$$

The R_{2p} and R_{3d} correspond to the radial part of the TM $2p$ and TM $3d$ orbitals, respectively. The angular integrals of the Coulomb interaction read

$$f^k(l_1 m_1 l_2 m_2, l_3 m_3 l_4 m_4) = \sum_q (-1)^q \langle l_1 m_1 | C_{-q}^k | l_3 m_3 \rangle \langle l_2 m_2 | C_q^k | l_4 m_4 \rangle, \quad (\text{B.19})$$

which can be evaluated by the Wigner-Eckhart theorem, see Eq. B.11,

$$\begin{aligned} f^k(l_1 m_1 l_2 m_2, l_3 m_3 l_4 m_4) &= \delta_{s_1, s_3} \delta_{s_2, s_4} (-1)^{l_1 + l_2 - m_2 - m_4} \langle l_1 || \mathbf{C}^k || l_3 \rangle \langle l_2 || \mathbf{C}^k || l_4 \rangle \\ &\times \begin{pmatrix} l_1 & k & l_3 \\ -m_1 & m_1 - m_3 & m_3 \end{pmatrix} \begin{pmatrix} l_2 & k & l_4 \\ -m_2 & m_2 - m_4 & m_4 \end{pmatrix}. \end{aligned} \quad (\text{B.20})$$

The reduced matrix elements $\langle l || \mathbf{C}^k || l' \rangle$ of the tensor operators of the Coulomb interaction are represented by

$$\langle l || \mathbf{C}^k || l' \rangle = (-1)^l \sqrt{(2l+1)(2l'+1)} \begin{pmatrix} l & k & l' \\ 0 & 0 & 0 \end{pmatrix}, \quad (\text{B.21})$$

where the selection rules of the $3J$ symbol provide finite values for

$$|l - l'| \leq k \leq l + l', \quad (\text{B.22})$$

and

$$l + k + l' \stackrel{!}{=} \text{even}. \quad (\text{B.23})$$

Bibliography

- [1] M. Winder, A. Hariki, and J. Kuneš. X-ray spectroscopy of rare-earth nickelate LuNiO_3 : LDA+DMFT study (2020).
- [2] A. Hariki, M. Winder, T. Uozumi, and J. Kuneš. LDA + DMFT approach to resonant inelastic x-ray scattering in correlated materials. Phys. Rev. B **101**, 115130 (2020).
- [3] A. Hariki, M. Winder, and J. Kuneš. Metal-insulator transition in $\text{CaCu}_3\text{Fe}_4\text{O}_{12}$ (2019).
- [4] M. Ghiasi, A. Hariki, M. Winder, J. Kuneš, A. Regoutz, T.-L. Lee, Y. Hu, J.-P. Rueff, and F. M. F. de Groot. Charge-transfer effect in hard x-ray $1s$ and $2p$ photoemission spectra: LDA + DMFT and cluster-model analysis. Phys. Rev. B **100**, 075146 (2019).
- [5] A. Hariki, M. Winder, and J. Kuneš. Continuum Charge Excitations in High-Valence Transition-Metal Oxides Revealed by Resonant Inelastic X-Ray Scattering. Phys. Rev. Lett. **121**, 126403 (2018).
- [6] R. Feynman, R. Leighton, and M. Sands. The Feynman Lectures on Physics: Volume 3, volume 3 of The Feynman Lectures on Physics. Addison-Wesley, Boston (1963).
- [7] P. Hohenberg and W. Kohn. Inhomogeneous Electron Gas. Phys. Rev. **136**, B864 (1964).
- [8] W. Kohn and L. J. Sham. Self-Consistent Equations Including Exchange and Correlation Effects. Phys. Rev. **140**, A1133 (1965).
- [9] R. O. Jones and O. Gunnarsson. The density functional formalism, its applications and prospects. Rev. Mod. Phys. **61**, 689 (1989).
- [10] J. P. Perdew, K. Burke, and M. Ernzerhof. Generalized Gradient Approximation Made Simple. Phys. Rev. Lett. **77**, 3865 (1996).
- [11] V. I. Anisimov, J. Zaanen, and O. K. Andersen. Band theory and Mott insulators: Hubbard U instead of Stoner I. Phys. Rev. B **44**, 943 (1991).

- [12] J. Kuneš, I. Leonov, P. Augustinský, V. Křápek, M. Kollar, and D. Vollhardt. LDA+DMFT approach to ordering phenomena and the structural stability of correlated materials. *The European Physical Journal Special Topics* **226**, 2641 (2017).
- [13] A. Georges, G. Kotliar, W. Krauth, and M. J. Rozenberg. Dynamical mean-field theory of strongly correlated fermion systems and the limit of infinite dimensions. *Rev. Mod. Phys.* **68**, 13 (1996).
- [14] J. Kuneš, I. Leonov, M. Kollar, K. Byczuk, V. I. Anisimov, and D. Vollhardt. Dynamical mean-field approach to materials with strong electronic correlations. *Eur. Phys. J. Spec. Top.* **180**, 5 (2009).
- [15] M. Imada, A. Fujimori, and Y. Tokura. Metal-insulator transitions. *Rev. Mod. Phys.* **70**, 1039 (1998).
- [16] S. Maekawa, T. Tohyama, S. Barnes, S. Ishihara, W. Koshibae, and G. Khalullin. Physics of Transition Metal Oxides. Springer Series in Solid-State Sciences. Springer Berlin Heidelberg (2004).
- [17] D. I. Khomskii. Transition Metal Compounds. Cambridge University Press (2014).
- [18] J. H. D. BOER and E. J. W. VERWEY. SEMI-CONDUCTORS WITH PARTIALLY AND COMPLETELY FILLED 3d-LATTICE BANDS. *Proc. Phys. Soc. London* **49** (1937).
- [19] N. F. Mott and R. Peierls. Discussion of the paper by de Boer and Verwey. *Proc. Phys. Soc. London* **49** (1937).
- [20] L. F. Mattheiss. Electronic Structure of the 3d Transition-Metal Monoxides. I. Energy-Band Results. *Phys. Rev. B* **5**, 290 (1972).
- [21] A. Hariki. New theoretical framework for core-level X-ray spectroscopy analysis based on dynamical mean-field theory and its application. Ph.D. thesis, Osaka Prefecture University (2016).
- [22] M. Winder. Numerical simulation of core-level spectroscopies.
- [23] J. Zaanen, G. A. Sawatzky, and J. W. Allen. Band gaps and electronic structure of transition-metal compounds. *Phys. Rev. Lett.* **55**, 418 (1985).
- [24] C. S. Fadley. Hard X-ray Photoemission: An Overview and Future Perspective, pp. 1–34. Springer International Publishing, Cham (2016).

- [25] Y. Takata, K. Tamasaku, T. Tokushima, D. Miwa, S. Shin, T. Ishikawa, M. Yabashi, K. Kobayashi, J. J. Kim, T. Yao, T. Yamamoto, M. Arita, H. Namatame, and M. Taniguchi. A probe of intrinsic valence band electronic structure: Hard x-ray photoemission. *Applied Physics Letters* **84**, 4310 (2004).
- [26] K. Kobayashi. *Nucl. Instrum. Methods. Phys. Res. A.* **601**, 32 (2009).
- [27] M. Taguchi, Y. Takata, and A. Chainani. *J. Electron. Spectrosc. Relat. Phenom.* **190**, 242 (2013).
- [28] M. Taguchi, A. Chainani, S. Ueda, M. Matsunami, Y. Ishida, R. Eguchi, S. Tsuda, Y. Takata, M. Yabashi, K. Tamasaku, Y. Nishino, T. Ishikawa, H. Daimon, S. Todo, H. Tanaka, M. Oura, Y. Senba, H. Ohashi, and S. Shin. Temperature Dependence of Magnetically Active Charge Excitations in Magnetite across the Verwey Transition. *Phys. Rev. Lett.* **115**, 256405 (2015).
- [29] M. Taguchi and G. Panaccione. Depth-Dependence of Electron Screening, Charge Carriers and Correlation: Theory and Experiments, pp. 197–216. Springer International Publishing, Cham (2016).
- [30] F. De Groot and A. Kotani. Core Level Spectroscopy of Solids. *Advances in Condensed Matter Science*. Taylor & Francis Group (2008).
- [31] A. Hariki, T. Uozumi, and J. Kuneš. LDA+DMFT approach to core-level spectroscopy: Application to 3d transition metal compounds. *Phys. Rev. B* **96**, 045111 (2017).
- [32] M. Taguchi, M. Matsunami, Y. Ishida, R. Eguchi, A. Chainani, Y. Takata, M. Yabashi, K. Tamasaku, Y. Nishino, T. Ishikawa, Y. Senba, H. Ohashi, and S. Shin. Revisiting the Valence-Band and Core-Level Photoemission Spectra of NiO. *Phys. Rev. Lett.* **100**, 206401 (2008).
- [33] M. A. van Veenendaal and G. A. Sawatzky. Nonlocal screening effects in 2p x-ray photoemission spectroscopy core-level line shapes of transition metal compounds. *Phys. Rev. Lett.* **70**, 2459 (1993).
- [34] M. van Veenendaal. Competition between screening channels in core-level x-ray photoemission as a probe of changes in the ground-state properties of transition-metal compounds. *Phys. Rev. B* **74**, 085118 (2006).
- [35] K. Horiba, M. Taguchi, A. Chainani, Y. Takata, E. Ikenaga, D. Miwa, Y. Nishino, K. Tamasaku, M. Awaji, A. Takeuchi, M. Yabashi, H. Namatame, M. Taniguchi, H. Kumigashira, M. Oshima, M. Lippmaa, M. Kawasaki, H. Koinuma, K. Kobayashi, T. Ishikawa, and S. Shin. Nature of the

- Well Screened State in Hard X-Ray Mn 2p Core-Level Photoemission Measurements of $\text{La}_{1-x}\text{Sr}_x\text{MnO}_3$ Films. *Phys. Rev. Lett.* **93**, 236401 (2004).
- [36] R. Eguchi, M. Taguchi, M. Matsunami, K. Horiba, K. Yamamoto, Y. Ishida, A. Chainani, Y. Takata, M. Yabashi, D. Miwa, Y. Nishino, K. Tamasaku, T. Ishikawa, Y. Senba, H. Ohashi, Y. Muraoka, Z. Hiroi, and S. Shin. Photoemission evidence for a Mott-Hubbard metal-insulator transition in VO_2 . *Phys. Rev. B* **78**, 075115 (2008).
- [37] M. Obara, A. Sekiyama, S. Imada, J. Yamaguchi, T. Miyamachi, T. Balashov, W. Wulfhekel, M. Yabashi, K. Tamasaku, A. Higashiya, T. Ishikawa, K. Fujiwara, H. Takagi, and S. Suga. V-V dimerization effects on bulk-sensitive hard x-ray photoemission spectra for Magnéli phase vanadium oxides. *Phys. Rev. B* **81**, 113107 (2010).
- [38] N. Kamakura, M. Taguchi, A. Chainani, Y. Takata, K. Horiba, K. Yamamoto, K. Tamasaku, Y. Nishino, D. Miwa, E. Ikenaga, M. Awaji, A. Takeuchi, H. Ohashi, Y. Senba, H. Namatame, M. Taniguchi, T. Ishikawa, K. Kobayashi, and S. Shin. Hard X-ray core-level photoemission of V 2 O 3. *Europhys Lett.* **68**, 557 (2004).
- [39] A. Hariki, Y. Ichinozuka, and T. Uozumi. Dynamical Mean-Field Approach to Ni 2p X-ray Photoemission Spectra of NiO: A Role of Antiferromagnetic Ordering. *J. Phys. Soc. Jpn.* **82**, 043710 (2013).
- [40] M. Taguchi, A. Chainani, K. Horiba, Y. Takata, M. Yabashi, K. Tamasaku, Y. Nishino, D. Miwa, T. Ishikawa, T. Takeuchi, K. Yamamoto, M. Matsunami, S. Shin, T. Yokoya, E. Ikenaga, K. Kobayashi, T. Mochiku, K. Hirata, J. Hori, K. Ishii, F. Nakamura, and T. Suzuki. Evidence for Suppressed Screening on the Surface of High Temperature $\text{La}_{2-x}\text{Sr}_x\text{CuO}_4$ and $\text{Nd}_{2-x}\text{Ce}_x\text{CuO}_4$ Superconductors. *Phys. Rev. Lett.* **95**, 177002 (2005).
- [41] C. F. Chang, T. C. Koethe, Z. Hu, J. Weinen, S. Agrestini, L. Zhao, J. Gerner, H. Ott, G. Panaccione, H. Wu, M. W. Haverkort, H. Roth, A. C. Komarek, F. Offi, G. Monaco, Y.-F. Liao, K.-D. Tsuei, H.-J. Lin, C. T. Chen, A. Tanaka, and L. H. Tjeng. c-Axis Dimer and Its Electronic Breakup: The Insulator-to-Metal Transition in Ti_2O_3 . *Phys. Rev. X* **8**, 021004 (2018).
- [42] P. Miedema, F. Borgatti, F. Offi, G. Panaccione, and F. [de Groot]. Iron 1s X-ray photoemission of Fe_2O_3 . *Journal of Electron Spectroscopy and Related Phenomena* **203**, 8 (2015).
- [43] D. Alders, L. H. Tjeng, F. C. Voogt, T. Hibma, G. A. Sawatzky, C. T. Chen, J. Vogel, M. Sacchi, and S. Iacobucci. Temperature and thickness dependence of magnetic moments in NiO epitaxial films. *Phys. Rev. B* **57**, 11623 (1998).

- [44] L. J. P. Ament, M. van Veenendaal, T. P. Devereaux, J. P. Hill, and J. van den Brink. Resonant inelastic x-ray scattering studies of elementary excitations. *Rev. Mod. Phys.* **83**, 705 (2011).
- [45] D. Betto, Y. Y. Peng, S. B. Porter, G. Berti, A. Calloni, G. Ghiringhelli, and N. B. Brookes. Three-dimensional dispersion of spin waves measured in NiO by resonant inelastic x-ray scattering. *Phys. Rev. B* **96**, 020409(R) (2017).
- [46] G. Fabbris, D. Meyers, L. Xu, V. M. Katukuri, L. Hozoi, X. Liu, Z.-Y. Chen, J. Okamoto, T. Schmitt, A. Uldry, B. Delley, G. D. Gu, D. Prabhakaran, A. T. Boothroyd, J. van den Brink, D. J. Huang, and M. P. M. Dean. Doping Dependence of Collective Spin and Orbital Excitations in the Spin-1 Quantum Antiferromagnet $\text{La}_{2-x}\text{Sr}_x\text{NiO}_4$ Observed by X Rays. *Phys. Rev. Lett.* **118**, 156402 (2017).
- [47] J. Kim, D. Casa, M. H. Upton, T. Gog, Y.-J. Kim, J. F. Mitchell, M. van Veenendaal, M. Daghofer, J. van den Brink, G. Khaliullin, and B. J. Kim. Magnetic Excitation Spectra of Sr_2IrO_4 Probed by Resonant Inelastic X-Ray Scattering: Establishing Links to Cuprate Superconductors. *Phys. Rev. Lett.* **108**, 177003 (2012).
- [48] L. Braicovich, L. J. P. Ament, V. Bisogni, F. Forte, C. Aruta, G. Balestrino, N. B. Brookes, G. M. De Luca, P. G. Medaglia, F. M. Granozio, M. Radovic, M. Salluzzo, J. van den Brink, and G. Ghiringhelli. Dispersion of Magnetic Excitations in the Cuprate La_2CuO_4 and CaCuO_2 Compounds Measured Using Resonant X-Ray Scattering. *Phys. Rev. Lett.* **102**, 167401 (2009).
- [49] G. Ghiringhelli, M. Matsubara, C. Dallera, F. Fracassi, R. Gusmeroli, A. Piazzalunga, A. Tagliaferri, N. B. Brookes, A. Kotani, and L. Braicovich. NiO as a test case for high resolution resonant inelastic soft x-ray scattering. *J. Phys. Condens. Matter.* **17**, 5397 (2005).
- [50] M. Matsubara, T. Uozumi, A. Kotani, and J. C. Parlebas. Charge Transfer Excitation in Resonant X-ray Emission Spectroscopy of NiO. *J. Phys. Soc. Jpn.* **74**, 2052 (2005).
- [51] M. Guarise, B. Dalla Piazza, M. Moretti Sala, G. Ghiringhelli, L. Braicovich, H. Berger, J. N. Hancock, D. van der Marel, T. Schmitt, V. N. Strocov, L. J. P. Ament, J. van den Brink, P.-H. Lin, P. Xu, H. M. Rønnow, and M. Grioni. Measurement of Magnetic Excitations in the Two-Dimensional Antiferromagnetic $\text{Sr}_2\text{CuO}_2\text{Cl}_2$ Insulator Using Resonant X-Ray Scattering: Evidence for Extended Interactions. *Phys. Rev. Lett.* **105**, 157006 (2010).
- [52] M. Rossi, R. Arpaia, R. Fumagalli, M. Moretti Sala, D. Betto, K. Kummer, G. M. De Luca, J. van den Brink, M. Salluzzo, N. B. Brookes, L. Braicovich,

- and G. Ghiringhelli. Experimental Determination of Momentum-Resolved Electron-Phonon Coupling. *Phys. Rev. Lett.* **123**, 027001 (2019).
- [53] A. Kotani and S. Shin. Resonant inelastic x-ray scattering spectra for electrons in solids. *Rev. Mod. Phys.* **73**, 203 (2001).
- [54] K.-J. Zhou, M. Radovic, J. Schlappa, V. Strocov, R. Frison, J. Mesot, L. Patthey, and T. Schmitt. Localized and delocalized Ti 3d carriers in LaAlO₃/SrTiO₃ superlattices revealed by resonant inelastic x-ray scattering. *Phys. Rev. B* **83**, 201402 (2011).
- [55] T. Schmitt, L.-C. Duda, M. Matsubara, M. Mattesini, M. Klemm, A. Augustsson, J.-H. Guo, T. Uozumi, S. Horn, R. Ahuja, A. Kotani, and J. Nordgren. Electronic structure studies of V₆O₁₃ by soft x-ray emission spectroscopy: Band-like and excitonic vanadium states. *Phys. Rev. B* **69**, 125103 (2004).
- [56] F. Pfaff, H. Fujiwara, G. Berner, A. Yamasaki, H. Niwa, H. Kiuchi, A. Gloskovskii, W. Drube, J. Gabel, O. Kirilmaz, A. Sekiyama, J. Miyawaki, Y. Harada, S. Suga, M. Sing, and R. Claessen. Raman and fluorescence contributions to the resonant inelastic soft x-ray scattering on LaAlO₃/SrTiO₃ heterostructures. *Phys. Rev. B* **97**, 035110 (2018).
- [57] V. Bisogni, S. Catalano, R. J. Green, M. Gibert, R. Scherwitzl, Y. Huang, V. N. Strocov, P. Zubko, S. Balandeh, J.-M. Triscone, G. Sawatzky, and T. Schmitt. Ground-state oxygen holes and the metal–insulator transition in the negative charge-transfer rare-earth nickelates. *Nature Communications* **7**, 13017 (2016).
- [58] J. Vinson, J. J. Rehr, J. J. Kas, and E. L. Shirley. Bethe-Salpeter equation calculations of core excitation spectra. *Phys. Rev. B* **83**, 115106 (2011).
- [59] K. Gilmore, J. Vinson, E. Shirley, D. Prendergast, C. Pemmaraju, J. Kas, F. Vila, and J. Rehr. Efficient implementation of core-excitation Bethe–Salpeter equation calculations. *Comput. Phys. Commun.* **197**, 109 (2015).
- [60] K. Momma and F. Izumi. VESTA3 for three-dimensional visualization of crystal, volumetric and morphology data. *J. Appl. Crystall.* **44**, 1272 (2011).
- [61] K. Terakura, T. Oguchi, A. R. Williams, and J. Kübler. Band theory of insulating transition-metal monoxides: Band-structure calculations. *Phys. Rev. B* **30**, 4734 (1984).
- [62] J. Kuneš, D. M. Korotin, M. A. Korotin, V. I. Anisimov, and P. Werner. Pressure-Driven Metal-Insulator Transition in Hematite from Dynamical Mean-Field Theory. *Phys. Rev. Lett.* **102**, 146402 (2009).

- [63] M. P. Pasternak, G. K. Rozenberg, G. Y. Machavariani, O. Naaman, R. D. Taylor, and R. Jeanloz. Breakdown of the Mott-Hubbard State in Fe_2O_3 : A First-Order Insulator-Metal Transition with Collapse of Magnetism at 50 GPa. *Phys. Rev. Lett.* **82**, 4663 (1999).
- [64] E. Greenberg, I. Leonov, S. Layek, Z. Konopkova, M. P. Pasternak, L. Dubrovinsky, R. Jeanloz, I. A. Abrikosov, and G. K. Rozenberg. Pressure-Induced Site-Selective Mott Insulator-Metal Transition in Fe_2O_3 . *Phys. Rev. X* **8**, 031059 (2018).
- [65] J. G. Bednorz and K. A. Müller. Possible high T_c superconductivity in the Ba-La-Cu-O system. *Zeitschrift für Physik B Condensed Matter* **64**, 189 (1986).
- [66] T. Mizokawa, H. Namatame, A. Fujimori, K. Akeyama, H. Kondoh, H. Kuroda, and N. Kosugi. Origin of the band gap in the negative charge-transfer-energy compound NaCuO_2 . *Phys. Rev. Lett.* **67**, 1638 (1991).
- [67] D. Khomskii. Unusual valence, negative charge-transfer gaps and self-doping in transition-metal compounds. eprint arXiv:cond-mat/0101164 (2001).
- [68] T. Mizokawa, A. Fujimori, H. Namatame, Y. Takeda, and M. Takano. Electronic structure of tetragonal LaCuO_3 studied by photoemission and x-ray-absorption spectroscopy. *Phys. Rev. B* **57**, 9550 (1998).
- [69] M. T. Czyżyk and G. A. Sawatzky. Local-density functional and on-site correlations: The electronic structure of La_2CuO_4 and LaCuO_3 . *Phys. Rev. B* **49**, 14211 (1994).
- [70] T. Mizokawa, A. Fujimori, H. Namatame, K. Akeyama, and N. Kosugi. Electronic structure of the local-singlet insulator NaCuO_2 . *Phys. Rev. B* **49**, 7193 (1994).
- [71] J. F. Bringley, B. A. Scott, S. J. La Placa, T. R. McGuire, F. Mehran, M. W. McElfresh, and D. E. Cox. Structure and properties of the $\text{LaCuO}_{3-\delta}$ perovskites. *Phys. Rev. B* **47**, 15269 (1993).
- [72] S. Darracq, S. Matar, and G. Demazeau. Correlations between the structural distortion of LaCuO_3 lattice and the resulting physical properties. *Solid State Commun.* **85**, 961 (1993).
- [73] D. J. Singh. Electronic structure of NaCuO_2 . *Phys. Rev. B* **49**, 1580 (1994).
- [74] D. Choudhury, P. Rivero, D. Meyers, X. Liu, Y. Cao, S. Middey, M. J. Whitaker, S. Barraza-Lopez, J. W. Freeland, M. Greenblatt, and J. Chakhalian. Anomalous charge and negative-charge-transfer insulating state in cuprate chain compound KCuO_2 . *Phys. Rev. B* **92**, 201108 (2015).

- [75] N. E. Brese, M. O’Keeffe, R. B. V. Dreele, and V. G. Young. Crystal structures of NaCuO₂ and KCuO₂ by neutron diffraction. *J. Solid State Chem* **83**, 1 (1989).
- [76] R.-P. Wang, A. Hariki, A. Sotnikov, F. Frati, J. Okamoto, H.-Y. Huang, A. Singh, D.-J. Huang, K. Tomiyasu, C.-H. Du, J. Kuneš, and F. M. F. de Groot. Excitonic dispersion of the intermediate spin state in LaCoO₃ revealed by resonant inelastic x-ray scattering. *Phys. Rev. B* **98**, 035149 (2018).
- [77] M. W. Haverkort, Z. Hu, J. C. Cezar, T. Burnus, H. Hartmann, M. Reuther, C. Zobel, T. Lorenz, A. Tanaka, N. B. Brookes, H. H. Hsieh, H.-J. Lin, C. T. Chen, and L. H. Tjeng. Spin State Transition in LaCoO₃ Studied Using Soft X-ray Absorption Spectroscopy and Magnetic Circular Dichroism. *Phys. Rev. Lett.* **97**, 176405 (2006).
- [78] F. M. F. de Groot, J. C. Fuggle, B. T. Thole, and G. A. Sawatzky. 2p x-ray absorption of 3d transition-metal compounds: An atomic multiplet description including the crystal field. *Phys. Rev. B* **42**, 5459 (1990).
- [79] C. Zobel, M. Kriener, D. Bruns, J. Baier, M. Grüniger, T. Lorenz, P. Reutler, and A. Revcolevschi. Evidence for a low-spin to intermediate-spin state transition in LaCoO₃. *Phys. Rev. B* **66**, 020402 (2002).
- [80] A. Ishikawa, J. Nohara, and S. Sugai. Raman Study of the Orbital-Phonon Coupling in LaCoO₃. *Phys. Rev. Lett.* **93**, 136401 (2004).
- [81] M. A. Korotin, S. Y. Ezhov, I. V. Solovyev, V. I. Anisimov, D. I. Khomskii, and G. A. Sawatzky. Intermediate-spin state and properties of LaCoO₃. *Phys. Rev. B* **54**, 5309 (1996).
- [82] J.-Q. Yan, J.-S. Zhou, and J. B. Goodenough. Bond-length fluctuations and the spin-state transition in LCoO₃ (L = La, Pr, and Nd). *Phys. Rev. B* **69**, 134409 (2004).
- [83] Z. Ropka and R. J. Radwanski. ⁵D term origin of the excited triplet in LaCoO₃. *Phys. Rev. B* **67**, 172401 (2003).
- [84] A. Podlesnyak, S. Streule, J. Mesot, M. Medarde, E. Pomjakushina, K. Conder, A. Tanaka, M. W. Haverkort, and D. I. Khomskii. Spin-State Transition in LaCoO₃: Direct Neutron Spectroscopic Evidence of Excited Magnetic States. *Phys. Rev. Lett.* **97**, 247208 (2006).
- [85] S. Noguchi, S. Kawamata, K. Okuda, H. Nojiri, and M. Motokawa. Evidence for the excited triplet of Co³⁺ in LaCoO₃. *Phys. Rev. B* **66**, 094404 (2002).

- [86] G. Maris, Y. Ren, V. Volotchaev, C. Zobel, T. Lorenz, and T. T. M. Palstra. Evidence for orbital ordering in LaCoO_3 . Phys. Rev. B **67**, 224423 (2003).
- [87] T. Vogt, J. A. Hriljac, N. C. Hyatt, and P. Woodward. Pressure-induced intermediate-to-low spin state transition in LaCoO_3 . Phys. Rev. B **67**, 140401 (2003).
- [88] T. Saitoh, T. Mizokawa, A. Fujimori, M. Abbate, Y. Takeda, and M. Takano. Electronic structure and temperature-induced paramagnetism in LaCoO_3 . Phys. Rev. B **55**, 4257 (1997).
- [89] R. A. Bari and J. Sivardière. Low-Spin-High-Spin Transitions in Transition-Metal-Ion Compounds. Phys. Rev. B **5**, 4466 (1972).
- [90] K. Knížek, Z. c. v. Jiráček, J. c. v. Hejtmánek, P. Novák, and W. Ku. GGA + U calculations of correlated spin excitations in LaCoO_3 . Phys. Rev. B **79**, 014430 (2009).
- [91] J. Kuneš and V. Křápek. Disproportionation and Metallization at Low-Spin to High-Spin Transition in Multiorbital Mott Systems. Phys. Rev. Lett. **106**, 256401 (2011).
- [92] M. Karolak, M. Izquierdo, S. L. Molodtsov, and A. I. Lichtenstein. Correlation-Driven Charge and Spin Fluctuations in LaCoO_3 . Phys. Rev. Lett. **115**, 046401 (2015).
- [93] A. Hariki, R.-P. Wang, A. Sotnikov, K. Tomiyasu, D. Betto, N. B. Brookes, Y. Uemura, M. Ghiasi, F. M. F. de Groot, and J. Kuneš. Melting of excitonic dispersion in LaCoO_3 : theory and experiment (2019).
- [94] J. Kuneš, V. Křápek, N. Parragh, G. Sangiovanni, A. Toschi, and A. V. Kozhevnikov. Spin State of Negative Charge-Transfer Material SrCoO_3 . Phys. Rev. Lett. **109**, 117206 (2012).
- [95] I. I. Mazin, D. I. Khomskii, R. Lengsdorf, J. A. Alonso, W. G. Marshall, R. M. Ibberson, A. Podlesnyak, M. J. Martínez-Lope, and M. M. Abd-Elmeguid. Charge Ordering as Alternative to Jahn-Teller Distortion. Phys. Rev. Lett. **98**, 176406 (2007).
- [96] S. Lee, R. Chen, and L. Balents. Landau Theory of Charge and Spin Ordering in the Nickelates. Phys. Rev. Lett. **106**, 016405 (2011).
- [97] H. Park, A. J. Millis, and C. A. Marianetti. Site-Selective Mott Transition in Rare-Earth-Element Nickelates. Phys. Rev. Lett. **109**, 156402 (2012).
- [98] B. Lau and A. J. Millis. Theory of the Magnetic and Metal-Insulator Transitions in $R\text{NiO}_3$ Bulk and Layered Structures. Phys. Rev. Lett. **110**, 126404 (2013).

- [99] S. Johnston, A. Mukherjee, I. Elfimov, M. Berciu, and G. A. Sawatzky. Charge Disproportionation without Charge Transfer in the Rare-Earth-Element Nickelates as a Possible Mechanism for the Metal-Insulator Transition. *Phys. Rev. Lett.* **112**, 106404 (2014).
- [100] R. Jaramillo, S. D. Ha, D. M. Silevitch, and S. Ramanathan. Origins of bad-metal conductivity and the insulator–metal transition in the rare-earth nickelates. *Nat. Phys.* **10**, 304 EP (2014).
- [101] A. Subedi, O. E. Peil, and A. Georges. Low-energy description of the metal-insulator transition in the rare-earth nickelates. *Phys. Rev. B* **91**, 075128 (2015).
- [102] A. Mercy, J. Bieder, J. Íñiguez, and P. Ghosez. Structurally triggered metal-insulator transition in rare-earth nickelates. *Nature Communications* **8**, 1677 (2017).
- [103] J. Varignon, M. N. Grisolia, J. Íñiguez, A. Barthélémy, and M. Bibes. Complete phase diagram of rare-earth nickelates from first-principles. *npj Quantum Materials* **2**, 21 (2017).
- [104] S. Catalano, M. Gibert, J. Fowlie, J. Íñiguez, J.-M. Triscone, and J. Kreisel. Rare-earth nickelates RNiO₃: thin films and heterostructures. *Reports on Progress in Physics* **81**, 046501 (2018).
- [105] P. Seth, O. E. Peil, L. Pourovskii, M. Betzinger, C. Friedrich, O. Parcollet, S. Biermann, F. Aryasetiawan, and A. Georges. Renormalization of effective interactions in a negative charge transfer insulator. *Phys. Rev. B* **96**, 205139 (2017).
- [106] J. Ruppen, J. Teyssier, O. E. Peil, S. Catalano, M. Gibert, J. Mravlje, J.-M. Triscone, A. Georges, and D. van der Marel. Optical spectroscopy and the nature of the insulating state of rare-earth nickelates. *Phys. Rev. B* **92**, 155145 (2015).
- [107] A. Agui, T. Uozumi, M. Mizumaki, and T. Käämbre. Intermetallic charge transfer in FeTiO₃ probed by resonant inelastic soft x-ray scattering. *Phys. Rev. B* **79**, 092402 (2009).
- [108] K. Fürsich, Y. Lu, D. Betto, M. Bluschke, J. Porras, E. Schierle, R. Ortiz, H. Suzuki, G. Cristiani, G. Logvenov, N. B. Brookes, M. W. Haverkort, M. Le Tacon, E. Benckiser, M. Minola, and B. Keimer. Resonant inelastic x-ray scattering study of bond order and spin excitations in nickelate thin-film structures. *Phys. Rev. B* **99**, 165124 (2019).
- [109] J. Vinson, J. J. Rehr, J. J. Kas, and E. L. Shirley. Bethe-Salpeter equation calculations of core excitation spectra. *Phys. Rev. B* **83**, 115106 (2011).

- [110] K. Gilmore, J. Vinson, E. Shirley, D. Prendergast, C. Pemmaraju, J. Kas, F. Vila, and J. Rehr. Efficient implementation of core-excitation Bethe–Salpeter equation calculations. *Comput. Phys. Commun.* **197**, 109 (2015).
- [111] H. A. Kramers and W. Heisenberg. Über die Streuung von Strahlung durch Atome. *Zeitschrift für Physik* **31**, 681 (1925).
- [112] S. Sugano. Multiplets of Transition-Metal Ions in Crystals. Elsevier Science (2012).
- [113] M. van Veenendaal. Theory of Inelastic Scattering and Absorption of X-rays. Cambridge University Press (2015).
- [114] S. Hüfner. Photoelectron Spectroscopy: Principles and Applications. Springer Series in Solid-State Sciences. Springer Berlin Heidelberg (2013).
- [115] E. Pavarini, E. Koch, A. Lichtenstein, and D. E. Vollhardt. The LDA+DMFT approach to strongly correlated materials, volume 1 of Schriften des Forschungszentrums Jülich : Modeling and Simulation (2011). Record converted from VDB: 12.11.2012.
- [116] J. Zaanen, C. Westra, and G. A. Sawatzky. Determination of the electronic structure of transition-metal compounds: 2p x-ray photoemission spectroscopy of the nickel dihalides. *Phys. Rev. B* **33**, 8060 (1986).
- [117] A. E. Bocquet, T. Mizokawa, K. Morikawa, A. Fujimori, S. R. Barman, K. Maiti, D. D. Sarma, Y. Tokura, and M. Onoda. Electronic structure of early 3d-transition-metal oxides by analysis of the 2p core-level photoemission spectra. *Phys. Rev. B* **53**, 1161 (1996).
- [118] A. E. Bocquet, T. Mizokawa, T. Saitoh, H. Namatame, and A. Fujimori. Electronic structure of 3d-transition-metal compounds by analysis of the 2p core-level photoemission spectra. *Phys. Rev. B* **46**, 3771 (1992).
- [119] J. Park, S. Ryu, M.-s. Han, and S.-J. Oh. Charge-transfer satellites in the 2p core-level photoelectron spectra of heavy-transition-metal dihalides. *Phys. Rev. B* **37**, 10867 (1988).
- [120] E. Pavarini. Electronic Structure Calculations with LDA+DMFT, p. 321 (2014).
- [121] R. D. Cowan. The Theory of Atomic Structure and Spectra (Los Alamos Series in Basic and Applied Sciences). University of California Press (1981).
- [122] J. Sugar. Potential-Barrier Effects in Photoabsorption. II. Interpretation of Photoabsorption Resonances in Lanthanide Metals at the 4d-Electron Threshold. *Phys. Rev. B* **5**, 1785 (1972).

- [123] M. W. Haverkort. Spin and orbital degrees of freedom in transition metal oxides and oxide thin films studied by soft x-ray absorption spectroscopy (2005).
- [124] J. C. Slater and G. F. Koster. Simplified LCAO Method for the Periodic Potential Problem. Phys. Rev. **94**, 1498 (1954).
- [125] A. Agui, T. Uozumi, M. Mizumaki, and T. Käämbre. Intermetallic charge transfer in FeTiO₃ probed by resonant inelastic soft x-ray scattering. Phys. Rev. B **79**, 092402 (2009).
- [126] P. Blaha, K. Schwarz, G. Madsen, D. Kvasnicka, and J. Luitz. WIEN2k, An Augmented Plane Wave + Local Orbitals Program for Calculating Crystal Properties. Karlheinz Schwarz, Techn. Universitat Wien, Austria, 2001, ISBN 3-9501031-1-2 (2001).
- [127] N. Marzari and D. Vanderbilt. Maximally localized generalized Wannier functions for composite energy bands. Phys. Rev. B **56**, 12847 (1997).
- [128] I. Souza, N. Marzari, and D. Vanderbilt. Maximally localized Wannier functions for entangled energy bands. Phys. Rev. B **65**, 035109 (2001).
- [129] A. Hariki, A. Hausoel, G. Sangiovanni, and J. Kuneš. DFT+DMFT study on soft moment magnetism and covalent bonding in SrRu₂O₆. Phys. Rev. B **96**, 155135 (2017).
- [130] A. A. Mostofi, J. R. Yates, G. Pizzi, Y.-S. Lee, I. Souza, D. Vanderbilt, and N. Marzari. An updated version of wannier90: A tool for obtaining maximally-localised Wannier functions. Comput. Phys. Commun. **185**, 2309 (2014).
- [131] J. Kuneš, R. Arita, P. Wissgott, A. Toschi, H. Ikeda, and K. Held. Wien2wannier: From linearized augmented plane waves to maximally localized Wannier functions. Comput. Phys. Commun. **181**, 1888 (2010).
- [132] M. Karolak, G. Ulm, T. Wehling, V. Mazurenko, A. Poteryaev, and A. Lichtenstein. Double counting in LDA+DMFT—The example of NiO. J. Electron. Spectrosc. Relat. Phenom. **181**, 11 (2010).
- [133] W. Metzner and D. Vollhardt. Correlated Lattice Fermions in $d = \infty$ Dimensions. Phys. Rev. Lett. **62**, 324 (1989).
- [134] G. Kotliar, S. Y. Savrasov, K. Haule, V. S. Oudovenko, O. Parcollet, and C. A. Marianetti. Electronic structure calculations with dynamical mean-field theory. Rev. Mod. Phys. **78**, 865 (2006).

- [135] J. Kuneš, V. I. Anisimov, A. V. Lukoyanov, and D. Vollhardt. Local correlations and hole doping in NiO: A dynamical mean-field study. Phys. Rev. B **75**, 165115 (2007).
- [136] P. Werner, A. Comanac, L. de' Medici, M. Troyer, and A. J. Millis. Continuous-Time Solver for Quantum Impurity Models. Phys. Rev. Lett. **97**, 076405 (2006).
- [137] L. Boehnke, H. Hafermann, M. Ferrero, F. Lechermann, and O. Parcollet. Orthogonal polynomial representation of imaginary-time Green's functions. Phys. Rev. B **84**, 075145 (2011).
- [138] H. Hafermann, K. R. Patton, and P. Werner. Improved estimators for the self-energy and vertex function in hybridization-expansion continuous-time quantum Monte Carlo simulations. Phys. Rev. B **85**, 205106 (2012).
- [139] X. Wang, E. Gull, L. de' Medici, M. Capone, and A. J. Millis. Antiferromagnetism and the gap of a Mott insulator: Results from analytic continuation of the self-energy. Phys. Rev. B **80**, 045101 (2009).
- [140] M. Jarrell and J. Gubernatis. Bayesian inference and the analytic continuation of imaginary-time quantum Monte Carlo data. Phys. Rep. **269**, 133 (1996).
- [141] S. Yamamoto, T. Sogabe, T. Hoshi, S.-L. Zhang, and T. Fujiwara. Shifted Conjugate-Orthogonal-Conjugate-Gradient Method and Its Application to Double Orbital Extended Hubbard Model. J. Phys. Soc. Jpn. **77**, 114713 (2008).
- [142] T. Sogabe, T. Hoshi, S.-L. Zhang, and T. Fujiwara. A Numerical Method for Calculating the Green's Function Arising from Electronic Structure Theory. In Y. Kaneda, H. Kawamura, and M. Sasai (eds.), Frontiers of Computational Science, pp. 189–195. Springer Berlin Heidelberg, Berlin, Heidelberg (2007).
- [143] O. Gunnarsson and K. Schönhammer. Electron spectroscopies for Ce compounds in the impurity model. Phys. Rev. B **28**, 4315 (1983).
- [144] E. Gull, A. J. Millis, A. I. Lichtenstein, A. N. Rubtsov, M. Troyer, and P. Werner. Continuous-time Monte Carlo methods for quantum impurity models. Rev. Mod. Phys. **83**, 349 (2011).
- [145] J. Rubio-Zuazo, A. Chainani, M. Taguchi, D. Malterre, A. Serrano, and G. R. Castro. Electronic structure of FeO, γ -Fe₂O₃, and Fe₃O₄ epitaxial films using high-energy spectroscopies. Phys. Rev. B **97**, 235148 (2018).
- [146] A. Tanaka and T. Jo. Temperature Dependence of 2p-Core X-Ray Absorption Spectra in 3d Transition-Metal Compounds. J. Phys. Soc. Jpn. **61**, 2040 (1992).

- [147] D. S. Ginley and M. A. Butler. The photoelectrolysis of water using iron titanate anodes. *Journal of Applied Physics* **48**, 2019 (1977).
- [148] T. Uozumi, K. Okada, A. Kotani, Y. Tezuka, and S. Shin. Ti 2p and Resonant 3d Photoemission Spectra of Ti₂O₃. *J. Phys. Soc. Jpn.* **65**, 1150 (1996).
- [149] T. Uozumi, K. Okada, A. Kotani, R. Zimmermann, P. Steiner, S. Hüfner, Y. Tezuka, and S. Shin. Theoretical and experimental studies on the electronic structure of M₂O₃ (M = Ti, V, Cr, Mn, Fe) compounds by systematic analysis of high-energy spectroscopy. *J. Electron. Spectrosc. Relat. Phenom.* **83**, 9 (1997).
- [150] R. A. Bair and W. A. Goddard. Ab initio studies of the x-ray absorption edge in copper complexes. I. Atomic Cu²⁺ and Cu(ii)Cl₂. *Phys. Rev. B* **22**, 2767 (1980).
- [151] E. Collart, A. Shukla, J.-P. Rueff, P. Leininger, H. Ishii, I. Jarrige, Y. Q. Cai, S.-W. Cheong, and G. Dhalenne. Localized and Delocalized Excitons: Resonant Inelastic X-Ray Scattering in La_{2-x}Sr_xNiO₄ and La_{2-x}Sr_xCuO₄. *Phys. Rev. Lett.* **96**, 157004 (2006).
- [152] H. Tolentino, M. Medarde, A. Fontaine, F. Baudelet, E. Dartyge, D. Guay, and G. Tourillon. Anisotropy of the core-hole relaxation in x-ray-absorption spectroscopy as probed in square planar cuprates. *Phys. Rev. B* **45**, 8091 (1992).
- [153] Z. Y. Wu, D. C. Xian, T. D. Hu, Y. N. Xie, Y. Tao, C. R. Natoli, E. Paris, and A. Marcelli. Quadrupolar transitions and medium-range-order effects in metal *K*-edge x-ray absorption spectra of 3d transition-metal compounds. *Phys. Rev. B* **70**, 033104 (2004).
- [154] G. A. Sawatzky and J. W. Allen. Magnitude and Origin of the Band Gap in NiO. *Phys. Rev. Lett.* **53**, 2339 (1984).
- [155] G. Ghiringhelli, A. Piazzalunga, C. Dallera, T. Schmitt, V. N. Strocov, J. Schlappa, L. Patthey, X. Wang, H. Berger, and M. Grioni. Observation of Two Nondispersive Magnetic Excitations in NiO by Resonant Inelastic Soft-X-Ray Scattering. *Phys. Rev. Lett.* **102**, 027401 (2009).
- [156] M. W. Haverkort, M. Zwierzycki, and O. K. Andersen. Multiplet ligand-field theory using Wannier orbitals. *Phys. Rev. B* **85**, 165113 (2012).
- [157] F. Ciccacci, L. Braicovich, E. Puppini, and E. Vescovo. Empty electron states in Fe₂O₃ by ultraviolet inverse-photoemission spectroscopy. *Phys. Rev. B* **44**, 10444 (1991).

- [158] R. J. Lad and V. E. Henrich. Photoemission study of the valence-band electronic structure in Fe_xO , Fe_3O_4 , and $\alpha\text{-Fe}_2\text{O}_3$ single crystals. Phys. Rev. B **39**, 13478 (1989).
- [159] W. L. Yang, A. P. Sorini, C.-C. Chen, B. Moritz, W.-S. Lee, F. Vernay, P. Olalde-Velasco, J. D. Denlinger, B. Delley, J.-H. Chu, J. G. Analytis, I. R. Fisher, Z. A. Ren, J. Yang, W. Lu, Z. X. Zhao, J. van den Brink, Z. Hussain, Z.-X. Shen, and T. P. Devereaux. Evidence for weak electronic correlations in iron pnictides. Phys. Rev. B **80**, 014508 (2009).
- [160] J. Miyawaki, S. Suga, H. Fujiwara, M. Urasaki, H. Ikeno, H. Niwa, H. Kiuchi, and Y. Harada. Dzyaloshinskii-Moriya interaction in $\alpha\text{-Fe}_2\text{O}_3$ measured by magnetic circular dichroism in resonant inelastic soft x-ray scattering. Phys. Rev. B **96**, 214420 (2017).
- [161] L. W. Finger and R. M. Hazen. Crystal structure and isothermal compression of Fe_2O_3 , Cr_2O_3 , and V_2O_3 to 50 kbars. Journal of Applied Physics **51**, 5362 (1980).
- [162] F. M. F. de Groot, P. Glatzel, U. Bergmann, P. A. van Aken, R. A. Barrea, S. Klemme, M. Hävecker, A. Knop-Gericke, W. M. Heijboer, and B. M. Weckhuysen. 1s2p Resonant Inelastic X-ray Scattering of Iron Oxides. J. Phys. Chem. B **109**, 20751 (2005).
- [163] D. D. Sarma, O. Strebel, C. T. Simmons, U. Neukirch, G. Kaindl, R. Hoppe, and H. P. Müller. Electronic structure of high- T_c superconductors from soft-x-ray absorption. Phys. Rev. B **37**, 9784 (1988).
- [164] A. Webb, K. Kim, and C. Bouldin. The valence of copper in LaCuO_3 : An x-ray absorption study. Solid State Commn. **79**, 507 (1991).
- [165] J. Scofield. Hartree-Slater subshell photoionization cross-sections at 1254 and 1487 eV. J. Electron. Spectrosc. Relat. Phenom. **8**, 129 (1976).
- [166] K. Okada and A. Kotani. Large-Cluster Effects on Core-Level Photoabsorption Spectrum of LaCuO_3 . J. Phys. Soc. Jpn **68**, 666 (1999).
- [167] P. Thakur, V. Bisogni, J. C. Cezar, N. B. Brookes, G. Ghiringhelli, S. Gautam, K. H. Chae, M. Subramanian, R. Jayavel, and K. Asokan. Electronic structure of Cu-doped ZnO thin films by x-ray absorption, magnetic circular dichroism, and resonant inelastic x-ray scattering. J. Appl. Phys. **107**, 103915 (2010).
- [168] R. H. Potze, G. A. Sawatzky, and M. Abbate. Possibility for an intermediate-spin ground state in the charge-transfer material SrCoO_3 . Phys. Rev. B **51**, 11501 (1995).

- [169] V. Křápek, P. Novák, J. Kuneš, D. Novoselov, D. M. Korotin, and V. I. Anisimov. Spin state transition and covalent bonding in LaCoO_3 . *Phys. Rev. B* **86**, 195104 (2012).
- [170] J. Zhao, Y. Luo, J.-O. Wang, H. Qian, C. Liu, X. He, Q. Zhang, H. Huang, B. Zhang, S. Li, E. Guo, C. Ge, T. Yang, X. Li, M. He, L. Gu, K.-J. Jin, K. Ibrahim, and H. Guo. Electronic structure evolutions driven by oxygen vacancy in SrCoO_{3-x} films. *Sci. China Mater.* **62**, 1162 (2019).
- [171] T. Mizokawa, Y. Wakisaka, T. Sudayama, C. Iwai, K. Miyoshi, J. Takeuchi, H. Wadati, D. G. Hawthorn, T. Z. Regier, and G. A. Sawatzky. Role of Oxygen Holes in Li_xCoO_2 Revealed by Soft X-Ray Spectroscopy. *Phys. Rev. Lett.* **111**, 056404 (2013).
- [172] D. Takegami, L. Nicolai, T. C. Koethe, D. Kasinathan, C. Y. Kuo, Y. F. Liao, K. D. Tsuei, G. Panaccione, F. Offi, G. Monaco, N. B. Brookes, J. Minár, and L. H. Tjeng. Valence band hard x-ray photoelectron spectroscopy on 3d transition-metal oxides containing rare-earth elements. *Phys. Rev. B* **99**, 165101 (2019).
- [173] V. R. Galakhov, N. A. Ovechkina, A. S. Shkvarin, S. N. Shamin, E. Z. Kurmaev, K. Kuepper, A. F. Takács, M. Raekers, S. Robin, M. Neumann, G.-N. Gavrilă, A. S. Semenova, D. G. Kellerman, T. Käämbre, and J. Nordgren. Electronic structure and x-ray spectra of defective oxides Li_xCoO_2 . *Phys. Rev. B* **74**, 045120 (2006).
- [174] Z. Jiali, L. Yi, J. Wang, Q. Haijie, L. Chen, H. Xu, Z. Qinghua, H. Heyi, Z. Bingbing, L. Shunfang, G. Erjia, C. Ge, Y. Tieying, L. Xiaolong, H. Meng, G. Lin, J. Kui-Juan, K. Ibrahim, and H. Guo. Electronic structure evolutions driven by oxygen vacancy in SrCoO_{3-x} **62**, 1162 (2019).
- [175] R. J. Green, M. W. Haverkort, and G. A. Sawatzky. Bond disproportionation and dynamical charge fluctuations in the perovskite rare-earth nickelates. *Phys. Rev. B* **94**, 195127 (2016).
- [176] Y. Lu, D. Betto, K. Fürsich, H. Suzuki, H.-H. Kim, G. Cristiani, G. Logvenov, N. B. Brookes, E. Benckiser, M. W. Haverkort, G. Khaliullin, M. Le Tacon, M. Minola, and B. Keimer. Site-Selective Probe of Magnetic Excitations in Rare-Earth Nickelates Using Resonant Inelastic X-ray Scattering. *Phys. Rev. X* **8**, 031014 (2018).
- [177] H. Elnaggar, R. Wang, S. Lafuerza, E. Paris, A. C. Komarek, H. Guo, Y. Tseng, D. McNally, F. Frati, M. W. Haverkort, M. Sikora, T. Schmitt, and F. M. F. de Groot (2018).

- [178] H. Elnaggar, P. Sainctavit, A. Juhin, S. Lafuerza, F. Wilhelm, A. Rogalev, M.-A. Arrio, C. Brouder, M. van der Linden, Z. Kakol, M. Sikora, M. W. Haverkort, P. Glatzel, and F. M. F. de Groot. Noncollinear Ordering of the Orbital Magnetic Moments in Magnetite. *Phys. Rev. Lett.* **123**, 207201 (2019).
- [179] J. B. Torrance, P. Lacorre, A. I. Nazzal, E. J. Ansaldo, and C. Niedermayer. Systematic study of insulator-metal transitions in perovskites $RNiO_3$ ($R=Pr,Nd,Sm,Eu$) due to closing of charge-transfer gap. *Phys. Rev. B* **45**, 8209 (1992).
- [180] J. A. Alonso, M. J. Martínez-Lope, M. T. Casais, M. A. G. Aranda, and M. T. Fernández-Díaz. Metal–Insulator Transitions, Structural and Microstructural Evolution of $RNiO_3$ ($R = Sm, Eu, Gd, Dy, Ho, Y$) Perovskites: Evidence for Room-Temperature Charge Disproportionation in Monoclinic $HoNiO_3$ and $YNiO_3$. *J. of the Am. Chem. Soc.* **121**, 4754 (1999).
- [181] G. Catalan. Progress in perovskite nickelate research. *Phase Transitions* **81**, 729 (2008).
- [182] J. Kolorenč. Theory of resonant x-ray emission spectra in compounds with localized f electrons. *Physica B: Condensed Matter* **536**, 695 (2018).
- [183] R. Eguchi, Y. Okamoto, Z. Hiroi, S. Shin, A. Chainani, Y. Tanaka, M. Matsunami, Y. Takata, Y. Nishino, K. Tamasaku, M. Yabashi, and T. Ishikawa. Structure and photoemission spectroscopy of strain-controlled metal-insulator transition in $NdNiO_3$ thin films. *Jour. of App. Phys.* **105**, 056103 (2009).
- [184] C. Piamonteze, F. M. F. de Groot, H. C. N. Tolentino, A. Y. Ramos, N. E. Massa, J. A. Alonso, and M. J. Martínez-Lope. Spin-orbit-induced mixed-spin ground state in $RNiO_3$ perovskites probed by x-ray absorption spectroscopy: Insight into the metal-to-insulator transition. *Phys. Rev. B* **71**, 020406 (2005).
- [185] G. Grosso and G. P. Parravicini. Solid State Physics (Second Edition). Academic Press, Amsterdam, second edition edition (2014).
- [186] M. Tinkham. Group Theory and Quantum Mechanics. Dover Books on Chemistry and Earth Sciences. Dover Publications (2003).
- [187] E. König and S. Kremer. Ligand field energy diagrams. Plenum Press (1977).

Curriculum Vitae

Mathias Winder

E-mail: winder.mathias@gmail.com

Date of birth: 9 July 1989

Nationality: Austria

Main areas of research

- Theory of X-ray photoemission, X-ray absorption and X-ray emission spectroscopy
- Theory of electronic correlations and magnetism in transition metal systems
- Numerical many-body methods and ab-initio calculations

Academic career

- **Project assistant** (September 2018 – September 2020)
TU Wien, the group of Prof. Jan Kuneš
ERC project "Excitonic Magnetism in Strongly Correlated Materials" (No.646807-EXMAG), project leader Prof. Jan Kuneš
- **Master thesis** (September 2017 – July 2018)
TU Wien, the group of Prof. Jan Kuneš
ERC project "Excitonic Magnetism in Strongly Correlated Materials" (No.646807-EXMAG), project leader Prof. Jan Kuneš

Work experience

- **System administrator** (August 2009 – August 2012)
Meusburger Georg GmbH & Co KG, Wolfurt, Austria
- **Laborer** (April 2009 – July 2009)
Hinteregger Baumeister GmbH, Bregenz, Austria
- **Military service** (October 2008 – April 2009)

Education

- **Doctoral programme** (September 2018 – September 2020)
in Natural Sciences Technical Physics, Wien, Austria
- **Dipl.-Ing.** (March 2016 – July 2018)
Master programme in Technical Physics, TU Wien, Austria
- **B. Sc.** (October 2012 – January 2016)
Bachelor programme in Technical Physics, University of Technology Graz, Austria
- **Information technologist** (September 2009 – January 2012)
Apprenticeship, Landesberufsschule Feldkirch, Austria
- **Academy of Commerce** (September 2003 – July 2008)
Matura, concentration in information management and information technology, Bezauer Wirtschaftsschulen, Austria

List of presentations

Poster, Conference: "New Generation in Strongly Correlated Electrons Systems", Silvi Marina (2019)

Talk, Conference: "Theory Meets Experiment in Low-Dimensional Structures with Correlated Electrons", Prague (2019)

Poster, Conference: "DPG Spring Meeting", Regensburg (2019)

Poster, Autumn school: "DMFT: From Infinite Dimensions to Real Materials", Jülich (2018)

Poster, Summer school: "Bandstructure meets quantum field theory", Vienna (2018)